THÈSE

Pour l'obtention du grade de
DOCTEUR DE L'UNIVERSITÉ DE POITIERS
UFR des sciences fondamentales et appliquées
Pôle poitevin de recherche pour l'ingénieur en mécanique, matériaux et énergétique - PPRIMME (Poitiers)
(Diplôme National - Arrêté du 25 mai 2016)

École doctorale : Sciences et Ingénierie des Matériaux, Mécanique, Énergétique (Poitiers)
Secteur de recherche : Génie mécanique

Cotutelle : Harbin Institute of Technology, China

Présentée par :
Shuhui Cui

Research on the start-stop wear and thermal slip behavior at film-coating interface of high-speed and heavy-load journal bearings

Directeur(s) de Thèse :
Le Gu, Michel Fillon

Soutenue le 09 décembre 2021 devant le jury

Jury :

Président	**Yongda Yan**	Professor, Harbin Institute of Technology, Harbin, China
Rapporteur	**Benyebka Bou-Saïd**	Professeur, LaMCoS, INSA, Lyon
Rapporteur	**Qiuying Chang**	Professor, Jiaotong University, Beijing, China
Membre	**Le Gu**	Professor, Harbin Institute of Technology, Harbin, China
Membre	**Michel Fillon**	Directeur de recherche CNRS, Pprime, Université de Poitiers
Membre	**Francesco Massi**	Professore, Università La Sapienza, Roma, Italia
Membre	**Wen Wang**	Associate professor, Shanghai University, China

Pour citer cette thèse :
Shuhui Cui. *Research on the start-stop wear and thermal slip behavior at film-coating interface of high-speed and heavy-load journal bearings* [En ligne]. Thèse Génie mécanique. Poitiers : Université de Poitiers, 2021. Disponible sur Internet <http://theses.univ-poitiers.fr>

THESE

UNIVERSITE OF POITIERS
&
HARBIN INSTITUTE OF TECHNOLOGY

DOCTORAL THESIS

****

RESEARCH ON THE START-STOP WEAR AND THERMAL SLIP BEHAVIOR AT FILM-COATING INTERFACE OF HIGH-SPEED AND HEAVY-LOAD JOURNAL BEARINGS

****

Author:

Shuhui CUI

Supervisors:

Michel FILLON CNRS Director of Research
&
Le GU Professor

****

Jury members:

Benyebka	BOU-SAÏD	Professor	INSA de Lyon	Reviewer
Qiuying	CHANG	Professor	Beijing Jiaotong university	Reviewer
Yongda	YAN	Professor	Harbin Institute of Technology	Examiner
Francesco	MASSI	Professor	Sapienza Universita di Roma	Examiner
Wen	WANG	Associate professor	Shanghai University	Examiner
Michel	FILLON	Directeur de Recherche	Université de Poitiers	Examiner
Le	GU	Professor	Harbin Institute of Technology	Examiner

A thesis submitted in fulfilment of the requirements
for the degree of Doctor of Engineering

in the
Doctoral School of Materials, Mechanics and Energetics Science and Engineering
and the
School of Mechatronics Engineering of HIT

9 December 2021

THESE

Pour l'obtention du Grade de

DOCTEUR DE L'UNIVERSITE DE POITIERS

(Faculté des Sciences Fondamentales et Appliquées)
(Diplôme National - Arrêté du 25 mai 2016)

École Doctorale : Sciences et ingénierie en matériaux, mécanique, énergétique et aéronautique - SIMMEA

Secteur de Recherche : Génie mécanique.

Présentée par :

Shuhui CUI

****

RECHERCHE SUR L'USURE START-STOP ET LE COMPORTEMENT DE GLISSEMENT THERMIQUE À L'INTERFACE DE REVÊTEMENT DE FILM DES ROULEMENTS À GRANDE VITESSE ET À FORTE CHARGE

****

Directeur de Thèse : Michel FILLON
Co-directeur de Thèse : Le GU

****

Soutenance prévue le 9 décembre 2021

devant la Commission d'Examen

****

Membres du jury:

Benyebka	BOU-SAÏD	Professeur	INSA de Lyon	Rapporteur
Qiuying	CHANG	Professeur	Beijing Jiaotong university	Rapporteur
Yongda	YAN	Professeur	Harbin Institute of Technology	Examinateur
Francesco	MASSI	Professeur	Sapienza Universita di Roma	Examinateur
Wen	WANG	Professeur agrégé	Shanghai University	Examinateur
Michel	FILLON	Directeur de Recherche	Université de Poitiers	Examinateur
Le	GU	Professeur	Harbin Institute of Technology	Examinateur

Abstract

In special cases, the hydrodynamic bearings used in high-power gas turbines own compact size and micro relative clearance, and often start up and shut down frequently under heavy load without hydrostatic supporting system, which easily cause bearing seizure and worn failure. Self-lubrication coatings are becoming an alternative way to improve the friction performance of the bearing. The slip properties at lubricant-coating interface are quite different from those of traditional bearing friction pairs. In the thesis, a mixed lubrication model is established by considering both surface contact and hydrodynamic lubrication during startup and shutdown of plain journal bearings. The transient contact behavior and worn problem of the bearing under applied load are analyzed. The influences of surface roughness, acceleration, and relative clearance on the contact behavior are discussed. A thermoelastohydrodynamic (TEHD) model considering wall slip is established. The influence of slip zone on the hydrodynamic (HD) force and friction coefficient are studied to determine the optimal slip zone for high eccentricity ratios (heavy loads) in isothermal case. Then the influence of the coating (slip) position on the thermal behavior and minimum film thickness is analyzed. The selection criteria of the coating position are given. Aimed at coated tilting pad journal bearing used on marine gas turbine, the experimental research on both the steady state and startup process are conducted. The wear and thermal characteristics of the PTFE, graphite and silver (Ag) coatings are tested. The influence of relative clearance, acceleration and initial temperature on the temperature rise during startup is explored.

Résumé

Dans des cas particuliers, les paliers hydrodynamiques démarrent et s'arrêtent souvent sous une charge élevée mais sans l'aide d'un système de support hydrostatique, ce qui provoque facilement des grippages et des défaillances par usure. Les revêtements autolubrifiants deviennent une alternative pour améliorer les performances de frottement des paliers hydrodynamiques. Les propriétés de glissement à l'interface lubrifiant-revêtement sont assez différentes de celles existantes dans les paliers à revêtements traditionnels. Dans la thèse, un modèle de lubrification mixte est établi en considérant à la fois le contact de surface et la lubrification hydrodynamique pendant le démarrage et l'arrêt des paliers lisses. Le comportement transitoire du contact lubrifié et le problème d'usure du palier chargé sont analysés. Les influences de la rugosité de surface, de l'accélération et du jeu relatif sur le comportement du contact lubrifié sont discutées. Un modèle thermoélastohydrodynamique (TEHD) considérant le glissement aux parois est établi. L'influence de la zone de glissement sur la force hydrodynamique et sur le coefficient de frottement est étudiée afin de déterminer la zone de glissement optimale pour des excentricités relatives élevées (charges lourdes) en régime isotherme. Ensuite, l'influence de la position du revêtement (glissement) sur le comportement thermique et l'épaisseur minimale du film est analysée. Les critères de sélection de la position de revêtement sont donnés. Des recherches expérimentales sur le fonctionnement à l'état stationnaire et en phase de démarrage sont menées sur des paliers à patins oscillants utilisés sur les turbines à gaz marines. L'usure et les caractéristiques thermiques des revêtements PTFE, graphite et argent (Ag) sont analysées. L'influence du jeu relatif, de l'accélération et de la température initiale sur l'élévation de température au démarrage est explorée.

Acknowledgements

At the moment of the accomplish of my thesis, firstly, I would like to thank my supervisors Dr. Michel Fillon and Prof. Le Gu for their careful and patient guidance and helpful and important advice to my Ph.D study. And both of them are kindness, humorous, energetic and knowledgeable. I am very fortunate to meet two such excellent mentors in my Ph.D career, and I appreciate it very much.

In the French side, many thanks to professors of Jean Bouyer and Noël Brunetière et al. and the staff of Laurence Artus, Mathieu Maillet, Estelle Ferdinand et. al. in the research group for their help in my study and daily life. I want to give my special thanks to Samia Dahite and Hiba Jendoubi for their help in communication of everything (bank call, renting…etc.). Thanks to Tran Anh Vo and Prasanth Kumar for their discussion of my research and revision of my paper.

In the Chinese side, I am deeply grateful to Prof. Chuanwei Zhang for his selfless help and meticulous guidance in my research. I want to thank professors of Liqin Wang, Dezhi Zheng and Xiaoli Zhao for their selfless guidance in the group meeting. In addition, I would like to thank the doctoral candidates of Kun Shu, Pingping Hou, Zhen Li, Jiqiang Wu, Che Wang et al. and the masters of Huijie Tang, Ruoshui Liu, Cheng Lu, Yaqian Wang et. al. for creating a friendly, active and diligent laboratory atmosphere to help me study in a good shape.

I also give my great thanks to the jury members for their constructive comments to my dissertation.

Finally, I am especially grateful to my parents for their selfless devotion and support without any pressure on me. I also thank my husband, Mr. Mukai Wang, for standing with me all the time. Also thanks and wishes to my lovely little baby, my new born daughter Yoyo, for everything.

Contents

Abstract I

Résumé II

Acknowledgements III

Contents IV

List of Figures VII

List of tables XII

Chapter 1 Introduction 1

1.1 Objective and significance of the research 1

1.2 The startup and shutdown behavior of hydrodynamic bearings 2

1.3 Self-lubricated coatings in hydrodynamic bearings 5

1.4 Slip behavior of hydrodynamic bearing 8

1.4.1 Slip model 8

1.4.2 Wall slip in hydrodynamic bearings 9

1.5 Research content of present study 12

Chapter 2 Contact behavior of loaded hydrodynamic journal bearings during startup and shutdown 14

2.1 Introduction 14

2.2 Contact model during startup and shutdown 14

2.2.1 Geometry model of hydrodynamic journal bearing 14

2.2.2 Asperity contact model of surface roughness 15

2.2.3 Average Reynolds equation 16

2.2.4 Motion equation during startup and shutdown 18

2.2.5 Solution method 18

2.3 Contact behavior during startup and shutdown 24

2.3.1 Contact behavior during startup 24

2.3.2 Contact behavior during shutdown 26

2.4 Effect of surface roughness on the contact behavior 27

2.4.1 Contact and wear performance during startup 27

2.4.2 Contact and wear performance during shutdown 31

2.5 Effect of relative clearance on the contact behavior 34

2.5.1 Contact and wear performance during startup 34

2.5.2 Contact and wear performance during shutdown 36

2.6 Effect of acceleration/deceleration on the contact behavior 37

2.6.1 Contact and wear performance during startup 37
2.6.2 Contact and wear performance during shutdown 38
2.7 Conclusions 40

Chapter 3 Thermoelastohydrodynamic model of partly coated journal bearings considering wall slip 42
3.1 Introduction 42
3.2 Geometry model 42
3.3 Governing equations of the fluid 43
3.3.1 Generalized Reynolds equation considering slip 43
3.3.2 Film velocity 44
3.3.3 Wall slip velocity 47
3.4 Governing equation of temperature 49
3.4.1 Governing equation of film temperature 49
3.4.2 Governing equation of bush 50
3.4.3 Boundary conditions for temperature calculation 51
3.4.4 Deformation of the bush 52
3.5 Solution method of Finite Element Method 53
3.5.1 Solution of thermal deformation 53
3.5.2 Up-wind FEM for the solution of film temperature 56
3.5.3 Solution procedure 58
3.5.4 Model verification 59
3.6 Effect of operating conditions on thermal slip behavior 61
3.6.1 TEHDS behavior in different relative clearances 61
3.6.2 TEHDS behavior in different feeding temperatures 63
3.6.3 TEHDS behavior in different shaft speeds 64
3.7 Conclusions 66

Chapter 4 Coating zone optimization and thermal slip behavior of the coated journal bearings 68
4.1 Introduction 68
4.2 Geometry model 68
4.3 Optimization of slip (coating) zone in isothermal case 69
4.3.1 Effect of eccentricity ratio ε on the slip behavior 70
4.3.2 Optimization of slip zone in high eccentricity ratios 70
4.3.3 Optimal slip zone selection under heavy loads 73
4.4 Selection of PTFE coating position in thermal case 75
4.5 Effect of coating parameters on the thermal behavior 78
4.5.1 Thermal behavior in different coating thickness 78

4.5.2 Thermal behavior in different coating materials 80
4.6 Conclusions 82
Chapter 5 Experimental tests of the thermal properties of the coated tilting pad journal bearings 83
5.1 Introduction 83
5.2 Test rig and instrumentation 83
5.2.1 The construction of test rig 83
5.2.2 The geometry of the tilting pad journal bearing 84
5.2.3 Sensors position on the pads 85
5.3 Geometry model of the coated tilting pad journal bearing 86
5.4 Thermal properties of the large-clearance coated bearings 88
5.4.1 TEHD behavior in different relative clearances 89
5.4.2 TEHD behavior in different coating materials 91
5.4.3 Effect of operating conditions on temperature 93
5.5 Thermal and wear properties of micro-clearance coated bearings 93
5.5.1 Test of PTFE coated bearing 94
5.5.2 Test of Graphite coated bearing 95
5.5.3 Test of silver (Ag) coated bearing 96
5.6 Thermal behavior of the coated bearings during startup 97
5.6.1 Temperature rise in different relative clearances 97
5.6.2 Temperature rise in different accelerations 98
5.6.3 Temperature rise in different initial temperatures 99
5.7 Conclusions 99
Conclusions 101
Reference 103
Extended Abstract 113
Résumé étendu 130
Publications 149

List of Figures

Fig. 1-1 The (a) worn and (b)burn [3]pads 1
Fig. 1-2 The safe startup process considering TEHD lubrication [6] 2
Fig. 1-3 Wall slip models at fluid-sold interface 9
Fig. 2-1 (a) The coordinate system and (b) the movement and the asperity contact during startup and shutdown 15
Fig. 2-2 The contact shape of surface roughness asperity in different surface pattern 17
Fig. 2-3 Isoperimetric transformation for the quadrilateral element, (a) irregular element in Cartesian coordinate, and (b) regular isoperimetric element in parametric coordinate system 20
Fig. 2-4 (a) The contact time and (b) shaft center locus in different applied loads during startup 24
Fig. 2-5 Variation of the contact force F_c and HD force F_h during startup 25
Fig. 2-6 Influence of σ on (a) shaft center locus, (b) transient peak HD pressure, (c) HD pressure and (d) contact pressure during startup 26
Fig. 2-7 The variation of the transient parameters during shutdown (a) shaft center locus, (b) eccentricity ratio and attitude angle, (c) HD force and contact force, (d) HD force and contact force in x and y directions 27
Fig. 2-8 Influence of σ on (a) the HD force F_h and contact force F_c and (b) volume wear during startup 28
Fig. 2-9 Influence of σ on (a) shaft center locus, (b) eccentricity ratio and attitude angle, (c) peak HD pressure and (d) Stribeck ratio of h_{min}/σ during startup 28
Fig. 2-10 Influence of surface pattern on (a) shaft center locus, (b) eccentricity ratio ε, (c) HD force F_h and contact force F_c, and (d) peak HD pressure during startup 31
Fig. 2-11 Influence of surface pattern on the volume wear during startup 31
Fig. 2-12 Influence of σ on (a) HD force F_h and contact force F_c, and (b) volume wear V_f during shutdown 32
Fig. 2-13 Influence of σ on (a) shaft center locus and (b) eccentricity ratio and attitude angle during shutdown. 33
Fig. 2-14 Influence of σ on the (a) transient peak HD pressure, HD pressure distribution at (b) t=0, (c) t=t_{pmax} and (d) at t=0.6s 33
Fig. 2-15 Influence of surface pattern on the (a) HD force and contact force and (b) shaft center locus during startup 34

Fig. 2-16 Influence of the relative clearance on (a) HD force and contact force, (b) shaft center locus, (c) eccentricity ratio and attitude angle, (d) transient peak HD pressure during startup 35
Fig. 2-17 Influence of relative clearance on the volume wear during startup 35
Fig. 2-18 Influence of relative clearance on (a) HD force and contact force, (b) eccentricity ratio and attitude angle (c) shaft center locus and (d) maximum HD pressure and velocity of shaft center during shutdown 36
Fig. 2-19 Influence of relative clearance on the (a) contact time and contact zone and (b) volume wear V_f during shutdown 37
Fig. 2-20 Influence of acceleration on the transient parameters during startup, (a)transient HD force and contact force, (b) shaft center locus, (c) eccentricity ratio and attitude angle, (b) transient peak HD pressure 38
Fig. 2-21 Influence of acceleration on (a) contact time and zone and (b) volume wear V_f 38
Fig. 2-22 Influence of deceleration on transient parameters, (a) HD force and contact force, (b) eccentricity ratio and attitude angle, (c) shaft center locus and (d) contact zone 39
Fig. 2-23 Influence of deceleration on (a) contact time, (b) contact zone and (c) volume wear V_f during shutdown 40
Fig. 3-1. (a) Coating, interlayer and basement, (b) structure at middle plane and (c) coordinate system of the coated journal bearings considering partial wall slip 42
Fig. 3-2 The mechanical analysis of the fluid microcell 45
Fig. 3-3 The heat exchange in the oil groove 52
Fig. 3-4 The constrain of thermal deformation of the bush 53
Fig. 3-5 The freedom of the element node 54
Fig. 3-6 Flow chart of the calculation procedure 58
Fig. 3-7 Verification of the HD pressure distribution consider wall slip in the middle plane 59
Fig. 3-8 Comparison of the thermal deformation of PTFE coating in radial direction at inner surface of bush 61
Fig. 3-9 Present result of film-bush (bronze) interface temperature compared with Kucinchi's [116] 61
Fig. 3-10 Influence of relative clearance on (a) T_{max}, (b) h_{min}, (c) $\triangle T_{max}$ and $\triangle h_{min}$ and (d) inlet flow rate 62
Fig. 3-11 Influence of relative clearance on temperature distribution in TEHDS regime 62
Fig. 3-12 Influence of relative clearance on (a) mechanical deformation and (b)

thermal deformation of the coating in radial direction 62
Fig. 3-13 Influence of inlet temperature on (a) T_{max}, (b) h_{min} (c) T_{max} and h_{min} 63
Fig. 3-14 Influence of feeding temperature on (a) mechanical and (b) thermal deformation of coating deformations in radial direction and (c) thermal expansion of shaft 64
Fig. 3-15 Influence of feeding temperature on temperature distribution in TEHDS regime 64
Fig. 3-16 Influence of shaft speed on (a) maximum temperature, (b) minimum film thickness and (c) T_{max} and h_{min} 65
Fig. 3-17 Influence of shaft speed on (a) mechanical and (b) thermal deformations of the coating in radial direction and (c) shaft expansion in TEHDS regime 66
Fig. 3-18 Influence of shaft speed on temperature distribution in TEHDS regime .. 66
Fig. 4-1. Coating (slip) zone at bush surface (a) unfolded drawing and (b) section view 68
Fig. 4-2 The slip zone and the nondimensional slip velocities in circumferential direction U_s and axial direction W_s at ε=0.9 69
Fig. 4-3 Effect of eccentricity ratio ε on (a) the HD force gain F_G, friction coefficient decrease f_D and friction torque decrease T_D, and (b) the nondimensional circumferential slip velocity U_s in the middle plane 70
Fig. 4-4 Effect of slip zone coefficient α on the hydrodynamic behavior under high eccentricity ratio of ε=0.9, (a) the HD force gain F_G and friction coefficient decrease f_D, (b) the HD force gain F_G and friction coefficient decrease f_D in positive region, and (c) friction torque T_D decrease in positive region 71
Fig. 4-5 Effect of slip zone coefficient λ on the hydrodynamic (HD) behavior of journal bearings, (a) the HD force gain F_G, friction coefficient decrease f_D, (b) the HD pressure, and (c) the slip velocity U_s in the middle 72
Fig. 4-6 Effect of slip zone coefficient γ on (a) the HD force gain F_G, friction coefficient decrease f_D and friction torque decrease T_D, (b) the HD pressure, (c) the slip velocity U_s and (d) the distribution of U_s at film-bush interface in high eccentricity ratio 72
Fig. 4-7 Effect of high eccentricity ratio on (a) HD force gain F_G, friction coefficient decrease f_D, (b) HD pressure, and (c) slip velocity U_s in the middle plane 73
Fig. 4-8 The performance of journal bearing in partial slip zone in different eccentricity ratios, (a) the HD force gain F_G, (b) the friction coefficient decrease f_D, (c) the decrease percentage of attitude angle 74
Fig. 4-9 Influence of coefficient α of PTFE coating on (a) shaft and maximum temperature T_{max}, (b) minimum film thickness h_{min} and (c) maximum pressure

P_{max} 76
Fig. 4-10 Temperature distribution of the film-bush (coating, interlayer, basement) area 77
Fig. 4-11 Slip velocity in the middle plane in TEHDS regime 77
Fig. 4-12 Influence of coating coefficient α on (a) mechanical and (b) thermal deformations of the coating and (d) the temperature distribution of bush in middle plane in TEHDS regime 78
Fig. 4-13 (a) Maximum temperature T_{max}, (b) minimum film thickness h_{min} and (c) maximum pressure p_{max} in different coating thicknesses in TEHDS regime 79
Fig. 4-14 The influence of coating thickness on (a) mechanical deformation and (b) thermal deformation in TEHDS regime 80
Fig. 4-15 Thermal distribution with different coating materials 81
Fig. 4-16 Influence of coating material on (a) maximum temperature T_{max} and (b) minimum film thickness h_{min} 81
Fig. 4-17 Influence of coating material on thermal deformation at (a) $\alpha \approx 1.0$ and (b) full coating 82
Fig. 5-1 Schematic representation of the test rig 83
Fig. 5-2 Photo of the test rig of the journal bearings 84
Fig. 5-3 (a) assembly drawing and (b) photo of the mechanical system of the test rig of the journal bearings 84
Fig. 5-4 Photo of the six-pad CTPJB, (a) single coated pad, (b) pads in the loading ring and (c) loading mode 85
Fig. 5-5 Location of the sensors in the pad 85
Fig. 5-6 Geometry of the tilting pad journal bearing 86
Fig. 5-7 Mechanics analysis of the shaft 87
Fig. 5-8 Mechanics analysis of each pad (a) 3D view and (b) front view 88
Fig. 5-9 Solution process of the CTPJBs 89
Fig. 5-10 Effect of relative clearance on temperature of each pad 90
Fig. 5-11 Effect of relative clearance on (a) film thickness and (b) pressure of the CTPJB 90
Fig. 5-12 Effect of relative clearance on the thermal deformation in radial direction 91
Fig. 5-13 Thermal deformation (μm) of each Ag coated pad in the clearance of C2, (a) in radial direction, (b) in circumferential direction and (c) total deformation . 91
Fig. 5-14 Effect of coating materials on (a) temperature, (b) radial thermal deformation, (c) film thickness and (d) HD pressure of CTPJBs 92
Fig. 5-15 Temperature distribution in the middle plane of CTPJBs 92

Fig. 5-16 (a) Temperature and (b) HD pressure of CTPJBs at different shaft speeds 93
Fig. 5-17 (a) Temperature and (b) HD pressure of CTPJBs under different applied loads 93
Fig. 5-18 Temperature and pressure of the PTFE coated pads under 6k rpm and 4 kN 94
Fig. 5-19 Surface topography of the PTFE coated pads after several tests 95
Fig. 5-20 Temperature of different Graphite coated pads at (a) 6k rpm and (b) 7k rpm 95
Fig. 5-21 Surface topography of graphite coated pads after several test 96
Fig. 5-22 Temperature of different Ag coated pads 96
Fig. 5-23 Surface topography of Ag coated pads after several test 96
Fig. 5-24 Temperature rise of (a) pad 3 and (b) pad 4 during startup in different relative clearances 97
Fig. 5-25 Effect of acceleration on temperature rise of pad 3 and pad 4, (a) shaft speed, (b) temperature rise of pad 3 and (c) temperature rise of pad 4 98
Fig. 5-26 Effect of acceleration mode on temperature rise of pad 4 99
Fig. 5-27 Influence of initial temperature on temperature rise during startup, (a) high initial temperature and (b) low initial temperature 99

List of tables

Table 2-1 Coefficients of Φ_θ, Φ_z and Φ_s (H'>0.5) [108] 17
Table 2-2 The simulation parameters 24
Table 3-1 Structure parameters of the bearing 60
Table 3-2 Properties of the coating, interlayer and basement [117] 60
Table 3-3 Simulation parameters 60
Table 4-1 Parameters of simulation 69
Table 5-1 Geometrical parameters of the bearing at 20°C 85
Table 5-2 Lubricant characteristics (ISO T32) 86
Table 5-3 Parameters of bearing clearance 89

Chapter 1 Introduction

1.1 Objective and significance of the research

Hydrodynamic bearings normally run in hydrodynamic lubrication regime, and the rotating shaft and the bush surface are completely separated by the lubricant film. In this case the bearing life is assumed to be infinite, but in some extreme conditions, constrained by the bearing constructers, the bearings start up and shut down frequently under heavy load without hydrostatic support system, and this leads to the mixed lubrication, in which the surface contact of the shaft and bush surface generates [1] and results in the serious wear of the bush surface as shown in Fig. 1-1(a). Meanwhile, the bearing could be seizure in the very early period during startup process [2] and leads to the burn pads in Fig. 1-1 (b). The bearing failures cause the machine breakdown, and the costs of the maintenance or replacement is huge compared to the initial design cost. In order to improve the worn and seizure, it is necessary to investigate the wear and thermal properties of the journal bearings during startup and shut down.



Fig. 1-1 The (a) worn and (b)burn [3] pads

Nowadays, composite plastic coating is an alternative way to improve the bearing wear. Some of the coatings is still under the test in the lab, and some have been widely used in the hydrodynamic bearings, such as polytetrafluoroethylene (PTFE) and polyetheretherketone (PEEK). This kind of coatings expresses excellent anti-wear properties, but it also easily causes bearing seizures because of the heat insulation properties. Therefore, the influence of the composite coatings on the bearings is necessary to be understood. Moreover, the coatings have lower surface energy and non-sticky property, which are very different from the metal ones [4]. For heavily loaded hydrodynamic journal bearings under high speed, wall slip is easier to occur, and the traditional nonslip boundary condition is not appropriate in the condition of

high-speed sliding bearing with small gap [5]. Therefore, the influence of wall slip at fluid-solid interfaces is necessary to be discussed.

This work aims at the wear and thermal properties of the coated journal bearing during startup and shutdown to explore the operating conditions that can improve the wear and thermal performance, in order to provide some guidance to the engineering practice.

1.2 The startup and shutdown behavior of hydrodynamic bearings

Due to the transient thermoelastohydrodynamic (TEHD) behavior, there are two possibilities for hydrodynamic bearings during the startup phase: safe startup and rapid seizure. The safe startup process is shown in Fig. 1-2. Seizure usually occurs in the first few minutes of startup period, especially when the bearing starts from a cold state [6]. The rapid rise of the temperature will cause thermal expansion of the bush and shaft, so the bearing clearance decreases and seizure will occur when the clearance decreases to zero [7].

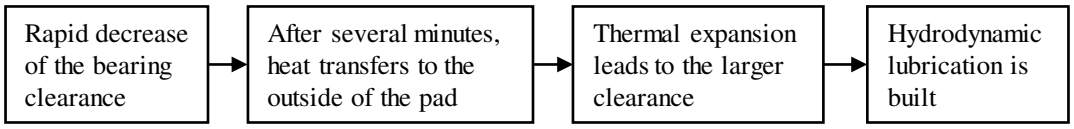


Fig. 1-2 The safe startup process considering TEHD lubrication [6]

In the early 1960s, the start-stop behavior of hydrodynamic bearings had begun to be conducted. In 1967, the U.S. Naval Fleet Engineering Laboratory [8] measured the oil film thickness, hydrodynamic (HD) pressure, friction torque, and hydrodynamic force of the tilting pad thrust bearing during startup, and found that if the static loading time exceeded a certain value, the breakaway torque would not be affected by the loading time. In 1975, Conway et al. [7] conducted the acceleration test of tilting pad journal bearing and found that low speed and high inlet temperature were beneficial to the safe startup; while the high speed and low inlet temperature made the bearing clearance smaller and caused seizure. In 1977, Mokhtar et al. tested the initial and evolution of wear of journal bearings during startup and shutdown [9]. The wear location was mainly caused by the sliding of the shaft along the bush surface without or with very little pure rolling during startup and was affected by the bearing clearance, surface finish, and bearing roundness. The hydrodynamic pressure formed quickly during startup [10], then the shaft would reach the steady position in the whirl way. During shutdown, the shaft reached the end position along the squeezed film trajectory. In 1989, Dufrane et al. [2] established a simple model

considering seizure time to analyze the seizure problems of journal bearings caused by insufficient lubrication, and they found at high speeds the seizure would occur within a few seconds.

In 1990s, Fillon et al. did a series of studies on the transient thermal effects of sliding bearings. In 1992, they tested the temperature of tilting pad bearings under different loads and speeds [11]. They found that the operating conditions had a large impact on temperature rise, and the impact of the speed was greater than the load. Affected by the oil feeding position, the highest temperature of each pad appeared at 70% to 90% of the circumferential length, and the lowest temperature appeared at the front edge of the pad. In 1994, they built a nonlinear elastic model considering bush deformation under static and unbalanced forces in isothermal condition, and found the bush deformation had little influence on the on the trajectory of the shaft center [12]. In 1997, they studied the temperature rise of the tilting pad journal bearings during startup by both simulations and experiments [13]. They found the temperature needed longer time to reach the steady value than the shaft speed during startup. The effect of heat conduction should be considered in the simulations because the thermoelastic deformation could reduce the radial clearance by about 20%. In 1999, they tested the friction torque and instantaneous temperature of hydrodynamic bearings in different operating conditions [14]. The friction torque experienced two stages: in the initial period, the bearing run in boundary lubrication, and the friction torque increases rapidly. Then the full film was built and the bearing turned to hydrodynamic lubrication, and the friction torque decreased. The temperature curve of rapid startup was obviously different from that of slow startup. For slow startup, the temperature raised slowly but it took almost the same time to reach stable temperature. In 1995, Harnoy et al. [15] established a model to evaluate the dynamic friction coefficient of the hydrodynamic bearings during startup process. They presented that the large acceleration and the flexible bearing support could reduce the maximum friction and energy loss.

In 2000, Fillon et al. studied the safe startup using a TEHD model [6]. They presented that the longer acceleration time, higher feeding temperature and larger bearing clearance were conducive to safe startup. However, the initial eccentricity of the bearing was nil, i.e. the applied load was zero, and the shaft did not contact with the bush. They also proposed a two-dimensional model considering realistic boundary conditions and deformations to calculate the temperature of journal bearings in rapid and slow startup [16]. Compared with thermal deformation, the mechanical deformation caused by hydrodynamic pressure was very small and could be neglected [13].

In 2003, Ettles et al. [17] proposed a two-dimensional (2D) TEHD model to study the start-stop process of the thrust bearing of a hydroelectric generator. They and proposed using jacking oil thrust to avoid the seizures. In 2005, Wang et al. studied the transient thermal behavior of tilting pad thrust bearings during startup based on a three-dimensional (3D) transient TEHD model [18]. They found that the temperature of rapid startup was lower than that of slow startup, but the acceleration has almost no effect on the pressure distribution. Lu et al.[19,20][19] tested the lift-off speed of journal bearings, and analyzed the influence of applied load, oil temperature and lubricant type on Stribeck curve.

From 2007 to 2011, Fillon et al. experimentally studied the friction torque during startup of journal bearings [21-24]. They found that the friction torque was greatly affected by the feeding temperature, and the maximum friction torque was linear to the static applied load [21,22]. During startup, the friction coefficient increased with the increasing in roughness, and was obviously influenced by the feeding temperature and the surface finish[23]. In addition, they also observed the stick-slip phenomenon during startup[24]. In 2008, Durak et al. [25] experimentally found that the friction coefficient and wear could be reduced by adding suitable additives to the lubricating oil during the start-stop process of journal bearings.

In 2014, Mehala et al. [26] used the finite volume method to analyze the lubrication mechanism of the bearing during startup. At low startup speed and applied load, the bearing would be in mixed lubrication regime, so it was necessary to increase the speed quickly. In 2016, Liu et al. [27] studied the variations of film thickness and thickness changing rate ($\mathrm{d}h/\mathrm{d}t$) of bearings during the start-stop process, and analyzed the acceleration and deceleration processes using a new optical slider-disk system.

Sang et al. studied the wear of the journal bearing of a single-cylinder engine during start-stop process [28]. They determined whether the bearing was in mixed lubrication based on the lift-off speed. They also established a mixed lubrication model considering wear and surface roughness contact, and calculated the capacity coefficient of roughness peak using the modified Archard wear equation. In 2016, Cristea et al. [29] firstly measured the transient pressure field and temperature field of a grooved journal bearing from initial startup to thermal stability. They found that the pressure field built faster than the temperature field, and the film rupture was mainly caused by the cavitation nucleus moving down to the position of minimum film thickness and absorbing the gas in the environment. In addition, the high pressure in the convergent region stabilized faster than the low pressure in the divergent region. Xiang et al. [30-32] proposed the transient mixed lubrication

behavior during startup largely depended on the elastic modulus and harness of the material, and the contact force may be underestimated in isothermal case.

Generally speaking, in the aspect of experiments, the influences of the applied load, journal speed, acceleration, feeding temperature, surface roughness and bearing structure on the motion of shaft center, transient film thickness, transient temperature, friction torque, friction coefficient, startup torque, lift-off speed are separately studied during startup. In terms of simulations, the elastohydrodynamic (EHD) model taking into account the elastic deformation of solids, the thermohydrodynamic (THD) model considering the effect of temperature, and the thermoelastichydrodyanmic (TEHD) model that considers both thermal deformation and solid elastic deformation are separately built to study the startup and shutdown behavior of hydrodynamic bearings. In summary, the experimental study is sufficient enough, but few models consider the influence of transient surface contact during startup and shutdown.

1.3 Self-lubricated coatings in hydrodynamic bearings

Bearings are prone to be in boundary or mixed lubrication regime under extreme conditions such as start-stop period, heavy load or starved lubrication. In these cases, traditional metal alloy bush materials, such as Babbitt, copper-based and aluminum-based alloy etc. can cause severe surface wear and burn resulting in catastrophic bearing failure [33]. The application of self-lubricated coatings is an alternative way to cope with the various extreme conditions.

The excellent performance of the composite coatings, such as polytetrafluoroethylene (PTFE) AND polyetheretherketone (PEEK), used in hydrodynamic bearings has been confirmed by many researchers [34,35]. Compared with the traditional babbitted bush, the application of polymer coatings shows great advantages, such as the low stiffness which causes favorable bush deformation, the plasticity which enables the applied load to better distribute on the bush, the vibration absorption capacity, abrasive grain embedding, the high corrosion resistance, and low wear rate, etc.[36].

Researches have shown that the hydrodynamic (HD) force of polymer coated bearings is 1.5 [37] to 3.0 [38] times higher than that of babbitted bearings. Lan et al.[39] simulated contact state in the mixed lubrication of sliding bearings used pin-on-disk wear test to study the properties of PTFE, PEEK and aromatic thermosetting polyester (ATSP) based coatings. Tests showed that, compared to steel, the three coatings obviously improved the wear properties; ATSP based coating demonstrated lowest friction coefficient and wear rate. In high temperature and dry friction condition, the coating with pure ATSP, PTFE and graphene nanosheets sharply

decreased the friction coefficient and improved the wear properties [40].

Glavatskih et al. [41-45] experimentally studied the PTFE coated thrust bearings. Compared with babbitted bearings, the polymer coatings increased the film temperature, reduced the maximum HD pressure. During start-stop process, the performance of the PTFE based coating was superior to that of the pure PTFE coating. The friction coefficient of the babbitted coating was twice of the polymer coating [43]. When the PTFE coating thickness increased, the maximum HD pressure increased, and the minimum film thickness at the leading and trailing edges also raised, and the thermal insulation properties of the coating leaded to higher film temperature [45].

Mahieux [46] experimentally compared the hydrodynamic behavior of tilting pad thrust bearing with coatings of Babbitt, PTFE and PFA. Compared to the babbitted bush, the coatings of PTFE and PFA reduced the bearing internal temperature by 15℃, but the PTFE and PFA still exhibited very different hydrodynamic behavior. Ettles et al. [17] studied the thermal characteristics, energy loss, and creep behavior of tilting pad thrust bearings with PTFE coating. Katsaros et al. [47] established a parameterized iterative algorithm based on the energy equation, the continuity equation and the Naiver-Stokes equation. The thermal fluid hydrodynamic behavior of Babbitt, PTFE and DLC coated tilting pad thrust bearings was compared. The PTFE and DLC coatings exhibited low friction. The impact of DLC coating on the flow rate and thermal area of the bearing was smaller than that of PTFE. Weißbacher et al. [48] tested the PEEK coatings for hydrodynamic bearings were not prone to creep at high temperatures, and the robustness was similar to tin-based coatings.

In addition, the application of other polymer coatings in hydrodynamic bearings was also carried out. The DLC coatings showed excellent anti-wear properties with low friction coefficient in mixed lubrication [49,50]. Rodriguez-Lelis et al. [51] found that low HD pressure distribution can be obtained when DLC coating is applied to the journal of a thrust hydrodynamic bearing, which they believe is due to the change of the shear stress between the interfaces. Rodriguez-Lelis et al. [51] experimentally found that the thrust hydrodynamic bearing with DLC coating owned a lower HD pressure, which leaded to the change of the shear stress at the interface. Prase et al. [52] tested the wear properties of the plastic coating (GL92) in the operating conditions of start-stop process, sudden oil cut, intermittent oil supply and gradually reduced oil supply. The results showed that plastic coated bearings exhibited excellent anti-wear performance in mixed lubrication conditions, had high HD force and were not easy to be worn during start-stop period. In dry friction (no oil supply) condition, seizure was prone to occur in high temperature but without no

wear. Thomsen et al. [53] theoretically studied the dynamic response, maximum HD pressure, minimum film thickness, wear, energy loss and temperature response of journal bearings with polymer bush. They found that the polymer bush was beneficial to reduce the peak HD pressure under heavy dynamic loads, but accompanied with smaller film thickness on the edges of the bush.

The polymer coatings show excellent performance in the mixed lubrication state, but its mechanical properties are easily affected by temperature [17], and the bush temperature can be reduced by its adiabatic property, which will make the traditional temperature diagnosis method invalid [36]. In engineering applications, the polymer coatings also cause seizure failure during startup and shutdown. Pap et al. [54] demonstrated the seizure failure of PTFE coating by journal bearing test bench, and analyzed the phenomenon by establishing pseudo transient TEHD model. They found that the temperature rise of PTFE coating was faster than that of bush and shaft, which limits the thermal expansion of PTFE coating, but does not affect the thermal expansion of journal.

Novel metal alloy coatings and metal based composite coatings for hydrodynamic bearings are also studied. Summer et al. [55] developed the alloy materials, including Cu-Pb-Sn as lining material, steel as matrix, and metal alloys as coating, to reduce the friction coefficient of bearings. Koß [56] prepared the metal matrix composite coating (316L+TiC/316L+SiC) by Extreme High-Speed Laser Material Depositions (EHLA). The coating owns good fretting and abrasive wear resistance, and the bonding ability at film-substrate interface was strong enough to bear large mechanical and thermal stresses. Vandoni et al. [57] compared the properties of Laser Surface Texturing (LST) tin coating, plain tin coating and WC/C coating under boundary lubrication by pin-on-disc friction test. They found that the average wear volume and maximum wear depth of LST Tin coating were significantly lower than that of plain Tin coating. For WC/C, the wear resistance gains were lower, but LST Tin kept this advantage for longer wear runs. Zhang et al. [58] tested the friction and wear properties of Ni-Cu-Ag based PVD coating for hydrodynamic and hydrostatic bearings at low temperature with the lubricants of liquid nitrogen and liquid oxygen. Mubarok et al. [59] studied the application of SiC coating in marine wind turbine bearings.

In total, most researchers study the coating properties in mixed lubrication using pin-on-disk friction test; some of the research use bearing bench test. The tests show that the polymer coatings have excellent performance and promising application prospect in hydrodynamic bearing. However, in the engineering application, the operation conditions are quite complex, which is greatly affected by pressure,

temperature, deformation and oil condition, so various failure problems will appear. Present researches mainly focused on the pin-on-disk friction and wear test which simplify the real operating condition of the bearings. The theoretical analysis is rare, especially for the analysis of the journal bearings in complex working conditions.

1.4 Slip behavior of hydrodynamic bearing

1.4.1 Slip model

Wall slip, also known as interface slip or boundary slip, refers to the relative motion at fluid-solid interface. The non-slip hypothesis is applied in classical fluid mechanics, i.e. the fluid velocity at fluid-solid surface is zero. In fact, as long as the shear stress is large enough, it is possible to overcome the molecules interaction between solid and liquid to produce slip.

Wall slip has almost no effect on macroscopic fluids due to the quite small scale, which is between a few nanometers and several micrometers for Newtonian fluids [61]. The measurement method mainly includes two types: direct method, such as fluorescence bleaching recovery technology and Particle image velocimetry, and indirect method, such as atomic force microscope (AFM), surface force meter (SFA) method, and quartz crystal resonator (QCM) method, etc.

The non-slip model was firstly proposed by Bernoulli, as shown in Fig. 1-3a). Girard et al. [62] and Prony et al. [63] believed that there is a certain thickness of fluid layer named Stagnant Layer on the solid surface, where the fluid has no relative movement at the solid surface, and the slip occurs at the interface of the fluid and Stagnant layer as shown in Fig. 1-3(b). Navier proposed slip length model (SLM), as shown in Fig. 1-3c), which considers that the slip velocity is proportional to the local shear rate as

$$v_s = b\left.\frac{\partial v_x}{\partial z}\right|_{wall} \quad \text{or} \quad v_s = b\dot{\gamma} \tag{1-1}$$

where, $\dot{\gamma}$ is local shear rate. v_s is slip velocity. b is slip length.

The slip length is the length extending from the fluid-solid interface to the point where the fluid velocity is zero. It is an imaginary fixed value that has no relation with the shear stress. When the shear stress is greater than zero, wall slip occurs. At low shear stress, SLM is in good agreement with the experimental results. However, at high shear stress the slip velocity is in strongly nonlinear relationship with the stress, and it can be described by the critical shear stress model (CSM). This model

considers that there is a critical shear stress at the fluid-solid interface and slip occurs when the surface shear stress exceeds the critical shear stress [64].

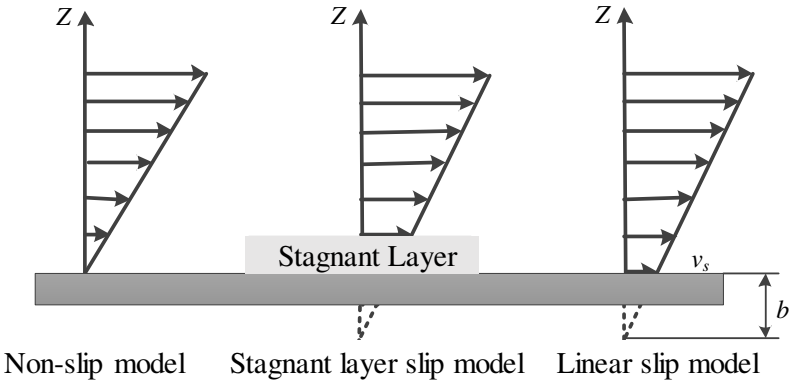


Fig. 1-3 Wall slip models at fluid-sold interface

$$\tau_L = \tau_0 + \kappa p \tag{1-2}$$

where τ_L is the limited shear stress. τ_0 is initial limited shear stress. κ is the plastic pressure coefficient. p is the pressure.

Thompson and Troian [65] proposed a nonlinear slip length model based on the molecular dynamics

$$b / b_0 = (1 - \dot{\gamma} / \dot{\gamma}_C)^{-1/2} \tag{1-3}$$

where b_0 is initial slip length, $\dot{\gamma}$ is shear rate, $\dot{\gamma} = \partial v_x / \partial v_z$, and $\dot{\gamma}_C$ is critical shear rate.

In low shear stress, the slip length is constant in the nonlinear slip length model, which is similar to the SLM, but in high shear stress, this model is similar to the CSM. The constitutive relationship of this model is complicated, and presently it can be only used to simple models. In addition, Spikes et al. [66] proposed a two-component model, which considers the effects of slip length and critical shear stress at the same time.

1.4.2 Wall slip in hydrodynamic bearings

Wall slip is affected by temperature, solid surface wettability and roughness etc. [67,68], and it is hard to be detected at macro scale. For the bearings applied in extreme operating conditions of high speed, heavy load and small clearance, kinds of polymer coatings on the bearing bush surface have become an important way to improve the friction performance of bearings. These self-lubricated coating materials

have advantages of low surface energy and non-sticky property [5], which are very different from those of the metal and wall slip is easier to occur at the surface of the coatings.

Experimental studies have been conducted to investigate the occurrence and influence of wall slip at the fluid-coating interface [69]. Yu et al. [70] developed a rheometer and tested the perfluoropolyethers (PFPE) coated sample with the slip length in the order of 10 μm. They indicated that the critical shear rate of water was higher than that of PC and 3# mineral oil. Jin et al. [5] tested that the critical shear stress at the oil-PTFE interface of a plastic journal bearing was about 1126.94 Pa. Wang [71] tested the slip phenomenon of the journal hydrodynamic bearing under low and high viscosity lubricants by the target velocity tracking method. Kalin et al. [72] studied the Stribeck curve of the friction pairs of steel-steel, steel-DLC, and DLC-DLC in nonslip and slip conditions. In hydrodynamic lubrication, the slip would decrease the friction coefficient, and this effect would be weaken in mixed lubrication. Evens et al. [73] studied the Stribeck curve of the coated/uncoated steel with a ball-on-flat test. They observed that when the film thickness was small, the micro-texture and coatings would affect the traction coefficient. With PAO oil, the Cr_xN coatings could decrease the traction coefficient more significantly than DLC coatings. Choo et al. [74] found slip would occur at hydrophobic smooth surface and could decrease friction coefficient in hydrodynamic lubrication.

Some slip models have been applied in the studies of hydrodynamic bearings. The modified Reynolds equation is deduced based on the Navier-Stokes equation [75,76], critical shear stress slip model [77-79] and two-component slip model [66,80-81]. Rao et al. [82] derived a model for hydrodynamic bearing considering slip and permeation based on the microcontinuum theory. The slip at bush surface of three-layered journal bearing would reduce the stability, but the partial slip was beneficial to increase the stability[83]. Bhattacharya et al.[84] studied the influence of multiple non-slip/slip interval areas on the oil film/bearing shell interface of a radial hydrodynamic bearing. The pressure distribution in the circumferential direction was similar to that of multi-lobe bearings. Cheng et al. [85] presented a slip model between cavitation air and lubricant oil to solve the problem of slip occurring in the cavitation zone. Jao et al. [86] studied the effect of anisotropy slip combined with roughness on the lubrication behavior of journal bearings. They concluded that the wall slip could offset part effect of roughness. Moreover, it was found that wall slip was easier to occur in the zones owning high shear stress gradient and small film thickness. The special oil wedge and high eccentricity ratio could decrease the influence of wall slip. In addition, the rupture zone and the maximum pressure are

also affected by wall slip [79]. Song et al. [87] and Zhu et al. [88] respectively presented that for tilting pad thrust bearings, the slip zone close to the inner ring or at the radial center is beneficial to improve the bearing performance. The homogeneous slip zone would reduce the minimum HD pressure and power loss.

For journal bearings, the performance of slip zone is significantly affected by working conditions, so the optimal designs of wall slip parameters are conducted. Ma et al. [64] systematically investigated and obtained the optimal parameters of the slip zone for the eccentricity ratios from 0 to 0.8. They also indicated that if wall slip occurring on the oil-shaft interface, there were almost no extra bearing load. Chen et al.[89] believed that when the slip occurring at the whole bush surface, both the HD force and friction coefficient would decrease. The slip effect became more obvious in small critical shear stress [90]. Zhang et al. [91] studied the effects of wall slip at water-bush interface of the high-speed water lubricated journal bearings under low eccentricity ratios. They found it would decrease the HD force in full slip configuration on the bush, but an appropriate partial slip zone could improve the performance of the bearing. Rao [92] analyzed the effect of partial slip immediately followed by a single grooved on the journal bearing and found that the maximum hydrodynamic pressure was larger in partial slip condition. Also, the shear stress was large before the slip/nonslip interface and obviously decreased in the nonslip zone. Fortier et al. [93] concluded that for low and moderate eccentricity ratios, wall slip had an advantage for the improvement of HD force and friction coefficient. However, for the eccentricity ratios larger than 0.92, the effect of slip became much smaller. Lv et al.[80] demonstrated that wall slip occurring at thin polymer film coated on metallic bush could decrease the HD force and increase the friction coefficient in mixed lubrication. Wang et al. [94] found that wall slip was more difficult to occur in high eccentricity and spiral oil wedge, and it affects the cavitation zone, pressure peak of the journal bearings.

The slip behavior with the effect of surface texture is also investigated on [95,96], The hydrodynamic behavior of the bearing is affected by both wall slip and surface texture [92,97]. Tauviqirrahman et al. [98] found that the wall slip would reduce the cavitation area in the bearing. The texture would decrease the HD force, and wall slip would further aggravate this negative effect in high eccentricity [99]. The HD force and friction coefficient could be improved when slip and texture were considered simultaneously on two parallel sliding surfaces [77]. There is an optimal speed that maximizes the effect of the slip zone [100]. Feng et al. [101] studied the influence of the micro-texture shape on the hydrodynamic performance of water-lubricated bearings considering slip by the two-component slip model. Jin et al. [102] optimized

the slip and texture zones of journal bearings. They found the front slip zone and the rear texture zone had significant influence on the HD force. The effect was most obvious when the junction point of the slip zone and the texture zone is near the position of maximum pressure. Li et al. [103] studied the dynamic and static characteristics of journal hydrodynamic bearings considering the effect of anisotropic slip and surface roughness. The direction of the rough peak would significantly affect the effect of slip.

Summarily, Present studies of experiments mainly focuses on discovering the wall slip phenomenon for various fluid-solid interface and then establishing the wall slip model. The numerical analysis for bearings are focused on deriving the Reynolds equation considering wall slip, and then analyzing the influence of wall slip on the hydrodynamic behavior. There are few studies on the thermal slip behavior of coated journal bearings, and the comprehensive mechanism of coating and slip is not clear yet due to the complexity of the operating conditions of journal bearings.

1.5 Research content of present study

This paper focuses on the research of the contact behavior of the shaft and bush surfaces during startup and shut down. And the thermal slip behavior of the coated journal bearing. The experimental and theoretical research on the coated tilting pad journal bearing are carried out to explore the operating conditions for safe running.

The main contents of this subject are as follows:

(1) Contact behavior of the loaded hydrodynamic journal bearings during startup and shutdown

A mixed lubrication model considering both surface contact and hydrodynamic lubrication during startup and shutdown of plain journal bearings is established. The contact time, lift-off speed, transient hydrodynamic pressure, contact pressure and minimum film thickness are obtained. The influences of surface roughness, acceleration, and relative clearance on the contact and wear behavior are discussed.

(2) Thermoelastohydrodynamic model of coated hydrodynamic bearing considering wall slip

A thermoelastohydrodynamic (TEHD) model considering wall slip is established. The heat conduction characteristics among the film, coating, interlayer and basement are presented. The influence of operating conditions on the thermal slip behavior is analyzed.

(3) Optimization of coating (slip) zones and thermal slip behavior of the coated bearing

The influence of the slip zone on the HD force and friction coefficient are systematically analyzed, and the selection criteria of slip zone parameters under

heavy load is given. The influence of the coating (slip) position on the thermal behavior and minimum film thickness under constant load conditions is analyzed, and the selection criteria of the coating position are given. Finally, the influences of coating parameters on the thermal behavior of the coated bearings are discussed.

(4) Experimental study of coated tilting pad journal bearings

Aimed at coated tilting pad journal bearing (CTPJB), the experimental research on both steady-state and start-stop process are conducted. The wear and thermal properties of the PTFE, graphite and silver (Ag) coatings for micro-clearance bearings are tested. Then the influence of operating conditions and relative clearance on the startup behavior is explored. The appropriate operating conditions for safe startup are proposed.

Chapter 2 Contact behavior of loaded hydrodynamic journal bearings during startup and shutdown

2.1 Introduction

At the beginning of startup and the end of shutdown, the hydrodynamic bearing is in mixed lubrication state, and the bush surface is easily worn. It is necessary to understand the influence of contact behavior on the shaft and bush surfaces. This chapter will establish a transient model considering surface contact of journal bearings during startup and shutdown. The transient parameters of hydrodynamic pressure, contact pressure and minimum oil film thickness are theoretically determined. The contact time, lift-off speed, contact zone and volume wear are given. The effects of surface roughness, relative clearance and acceleration on the contact and wear behavior are discussed.

2.2 Contact model during startup and shutdown

2.2.1 Geometry model of hydrodynamic journal bearing

Fig. 2-1 shows the schematic of the startup and shutdown behavior of journal bearings. θ is the circumferential angle. R_s is the shaft radius. The relative clearance is defined as the ratio of radius clearance and the shaft radius, $\psi=C/R_s$. Eccentricity ratio is defined as the ratio of eccentric distance and the radius clearance, $\varepsilon=e/C$. The film thickness is $h=C(1+\varepsilon\cos(\theta-\varphi))$. φ is the attitude angle.

The rotational speed of the shaft ω increases linearly during startup. At beginning, the hydrodynamic (HD) force F_h is insufficient to sustain the shaft, leading to the asperity contact. The HD force and film thickness increase with an increasing shaft speed. The corresponding asperity contact force F_c decreases. The shaft is completely separated with the bearing surface when the contact force reaches to zero. Shutdown is a reverse process, i.e. the bearing runs from hydrodynamic lubrication to the mixed lubrication. The contact time t_c is defined as the period during which two surfaces are in contact [10].

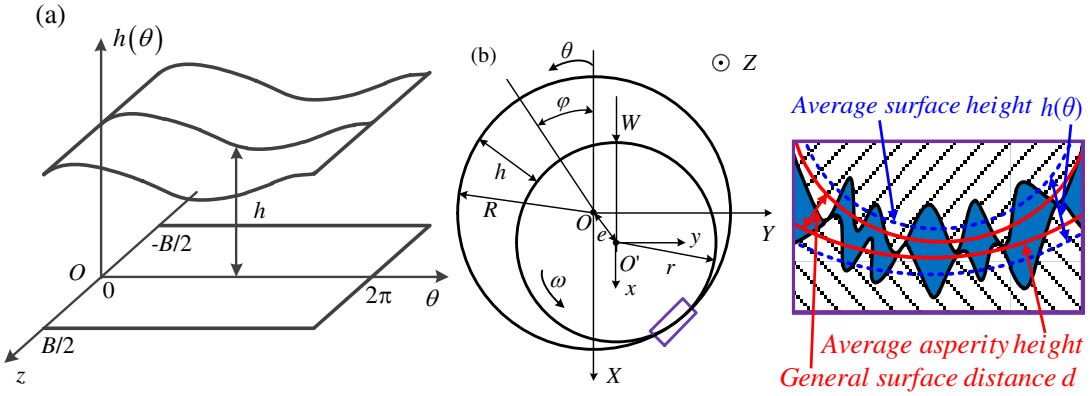


Fig. 2-1 (a) The coordinate system and (b) the movement and the asperity contact during startup and shutdown

2.2.2 Asperity contact model of surface roughness

For calculating the asperity contact pressure, the Greenwood-Williamson (GW) contact model is applied [104]. The Gaussian distribution function of the asperity height is

$$f\left(\overline{z}_r\right)=\frac{1}{\sqrt{2\pi}\sigma}\exp\left(-\frac{\overline{z}_r^2}{2\sigma^2}\right) \tag{2-1}$$

where σ is the standard deviation of roughness distribution, $\sigma=\sqrt{\sigma_1^2+\sigma_2^2}$, the subscripts of 1 and 2 represent shaft and bush respectively. The contact between the bush and the shaft is converted into a smooth rigid surface and a rough surface with σ. As shown in Fig. 2-1(b), $\overline{z}_r$ is the asperity height, $h(\theta)$ is the film thickness. When $\overline{z}_r > h$, the rough asperities are in contact. The normal contact force per unit area, i.e., the conformal contact pressure $\rho(\theta, z)$ is [105]

$$\rho\left(\theta,\ z\right)=D_{sum}\int_d^{+\infty}\overline{P}(\overline{z}_r-d)f\left(\overline{z}_r\right)\mathrm{d}\overline{z}_r \tag{2-2}$$

where D_{sum} is the density of the surface asperity; d is the general surface distance; $\overline{P}$ is the individual asperity contact force, $\overline{P}=\frac{4}{3}E'\sqrt{R_p}\left(\varpi\right)^{3/2}$, and E' is equivalent elasticity modulus, $1/E'=\left(1-\nu_1^2\right)/E_1+\left(1-\nu_2^2\right)/E_2$, E_1, ν_1 and E_2, ν_2 are the elasticity modulus and Poisson's ratios of the shaft and bush, respectively; R_p is radius of the asperity; $\varpi=\overline{z}_r-d$ is the inference of asperities.

The contact forces in X and Y directions are

$$\begin{cases} F_{cx} = R_s \int_0^{2\pi} \int_{-L/2}^{L/2} \rho(\theta, z) \cos\theta \mathrm{d}z\mathrm{d}\theta \\ F_{cy} = R_s \int_0^{2\pi} \int_{-L/2}^{L/2} \rho(\theta, z) \sin\theta \mathrm{d}z\mathrm{d}\theta \end{cases} \tag{2-3}$$

where L is the bearing width. The total contact force is $F_c = \sqrt{F_{cx}^2 + F_{cy}^2}$.

The volume wear can be obtained by the Achard model

$$\frac{\mathrm{d}V_f}{\mathrm{d}s_f} = P_f \frac{F_c}{H_{BS}} \tag{2-4}$$

where V_f is the volume wear, s_f is the sliding distance, P_f is the nondimensional wear coefficient, and H_{BS} is the hardness.

2.2.3 Average Reynolds equation

In the model, the lubricant is laminar Newtonian fluid and incompressible. The modified average Reynolds equation [106] of Eq.(2-5) is used for calculating the hydrodynamic pressure.

$$\frac{\partial}{R_s\partial\theta}\left(\Phi_\theta \frac{h^3}{\mu}\frac{\partial p}{R_s\partial\theta}\right) + \frac{\partial}{\partial z}\left(\Phi_z \frac{h^3}{\mu}\frac{\partial p}{\partial z}\right) = 6u\Phi_c \frac{\partial h}{R_s\partial\theta} + 6u\sigma \frac{\partial \Phi_s}{R_s\partial\theta} + 12\Phi_c \frac{\partial h}{\partial t} \tag{2-5}$$

where p is the hydrodynamic (HD) pressure, μ is the dynamic viscosity of the lubricant, u is the surface velocity of the shaft, $u=R_s\omega$, ω is the rotational speed of the shaft, t is time.

For simplification, the nondimensional parameters are used as

$$\bar{z} = \frac{z}{L}, \quad H = \frac{h}{C}, \quad \psi = \frac{C}{R_s}, \quad \frac{p}{P} = \frac{2\mu\omega_0}{\psi^2}, \quad \bar{\sigma} = \frac{\sigma}{C}, \quad U = \frac{u}{R_s\omega_0}, \quad \tau = \omega_0 t$$

where ω_0 is the shaft velocity at steady state. The nondimensional form of Eq.(2-5) is

$$\frac{\partial}{\partial\theta}\left(\Phi_\theta H^3 \frac{\partial P}{\partial\theta}\right) + \left(\frac{R_s}{L}\right)^2 \frac{\partial}{\partial\bar{z}}\left(\Phi_z H^3 \frac{\partial P}{\partial\bar{z}}\right) = 3U\Phi_c \frac{\partial H}{\partial\theta} + 3\bar{\sigma}U \frac{\partial \Phi_s}{\partial\theta} + 6\Phi_c \frac{\partial H}{\partial\tau} \tag{2-6}$$

where Φ_θ and Φ_z are the pressure flow factors in circumferential and axial directions, Φ_s is the shear flow factor [107,108], Φ_c is the contact factor [106], which are given by

$$\Phi_\theta = \Phi_z\left(H', 1/\gamma_s\right) = \begin{cases} 1 - c' e^{-r' H'}, \gamma_s \le 1 \\ 1 + c' e^{-r'}, \ \gamma_s > 1 \end{cases} \tag{2-7}$$

$$\Phi_s = V_{r1}\phi_s\left(H', \gamma_1\right) - V_{r2}\phi_s\left(H', \gamma_2\right) \tag{2-8}$$

$$\Phi_c = \begin{cases} e^{-0.6912 + 0.782H' - 0.304H'^2 + 0.0401H'^3}, 0 \le H' \le 3 \\ 1 \qquad\qquad\qquad\qquad\qquad\qquad , H' > 3 \end{cases} \tag{2-9}$$

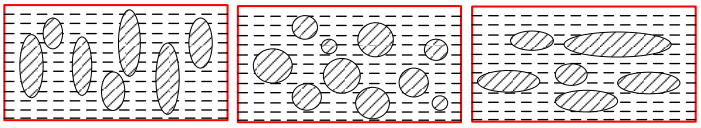
The parameters of V_{r1} and V_{r2} in Eq.(2-7) is calculated by

$$V_{r1} = 1 - V_{r2} = \left(\frac{\sigma_1}{\sigma}\right)^2$$

The parameters of ϕ_s in Eq.(2-8) can be obtained by

$$\phi_s = \begin{cases} A_1 H'^{\alpha_1} e^{-\alpha_2 H' + \alpha_3 H'^2}, H' \le 5 \\ A_2 e^{-0.25H'} \qquad\qquad , H' > 5 \end{cases} \tag{2-10}$$

where $H' = h/\sigma$ is the Stribeck ratio, γ' represents the surface pattern; $\gamma' < 1$ represents the transversal rough surface; $\gamma_s = 1$ represents isotropic rough surface; $\gamma_s < 1$ represents the longitudinal rough surface. The contact shapes of the three surface patterns are shown in Fig. 2-2. c', r', A_1, A_2, α_1, α_2 and α_3 are constant, which are related to H' and γ'. Table 2-1 shows the coefficients of different surface patterns.



a) Transversal b) Isotropic c) Longitudinal

Fig. 2-2 The contact shape of surface roughness asperity in different surface pattern

Table 2-1 Coefficients of Φ_θ, Φ_z and Φ_s (H'>0.5) [108]

Surface pattern	γ_s	c'	r'	A_1	A_2	α_1	α_2	α_3
Transverse	1/6	1.38(H'>1)	0.42(H'>1)	1.962	1.754	1.08	0.77	0.03
Isotropic	1	0.90	0.56	1.899	1.126	0.98	0.92	0.05
Longitudinal	6	0.520	1.5	1.290	0.388	0.62	1.09	0.08

The hydrodynamic (HD) force in the x and y directions are expressed as F_{hx} and F_{hy}

$$\begin{cases} F_{hx} = R_s \int_0^{2\pi} \int_{-L/2}^{L/2} p(\theta, z) \cos\theta \mathrm{d}z\mathrm{d}\theta \\ F_{hy} = R_s \int_0^{2\pi} \int_{-L/2}^{L/2} p(\theta, z) \sin\theta \mathrm{d}z\mathrm{d}\theta \end{cases} \tag{2-11}$$

2.2.4 Motion equation during startup and shutdown

The motion equation of the shaft center in x and y directions can be expressed by

$$\begin{cases} m\ddot{x} = F_{cx}(t) + F_{hx}(t) + F_{fx}(t) + W \\ m\ddot{y} = F_{cy}(t) + F_{hy}(t) + F_{fy}(t) \end{cases} \tag{2-12}$$

where F_c, F_h and F_f respectively represent contact force, HD force and friction force. The subscripts of x and y represent in X and Y directions. m is the equivalent mass, $m=W/g$; W is the applied force, g is acceleration of gravity.

The friction force caused by the shear stress of the oil is

$$F_f = \int_{-L/2}^{L/2} \int_0^{2\pi} \tau_{\theta z} \mathrm{d}\theta \mathrm{d}z \tag{2-13}$$

where $\tau_{\theta Z}$ is the shear stress, $\tau_{\theta z} = \frac{\mu u}{h}\left(\phi_f + \phi_{fs}\right) + \phi_{fp} \frac{h}{2} \frac{\partial p}{R_s \partial \theta}$; ϕ_f, ϕ_{fs} and ϕ_{fp} is the coefficients considering surface roughness and they can be obtained by Ref.[106].

2.2.5 Solution method

2.2.5.1 Solution method of the hydrodynamic pressure

The nondimensional Reynolds equation of Eq.(2-6) is calculated by finite element method, and the Reynolds boundary condition is applied. The weak elemental formation of Reynolds equation is deduced by Galerkin method. The weighted residual method is used to integrate Eq.(2-5) as

$$\iint_{\Omega_e} \nabla\left(\ell H^3 \nabla P\right) \cdot \Re \mathrm{d}\Omega_e = \iint_{\Omega_e} \left[3U\Phi_c \frac{\partial H}{\partial \theta} + 3\bar{\sigma} U \frac{\partial \Phi_s}{\partial \theta} + 6\Phi_c \frac{\partial H}{\partial \tau} \right] \cdot \Re \mathrm{d}\Omega_e \tag{2-14}$$

where ∇ is the differential operator, Ω_e is the domain of the element, $\Re$ is the weight function. ℓ represents the factor Φ_θ and $\Phi_z\left(\frac{R_s}{L}\right)^2$ which are the coefficients of $\frac{\partial P}{\partial \theta}$ and $\frac{\partial P}{\partial \bar{z}}$ respectively.

Eq.(2-14) can be modified by the Green's Formula as

$$\begin{aligned}&\iint_{\Omega_e}\left(-\ell H^3\nabla P\cdot\nabla\Re\right)\mathrm{d}\Omega_e+\oint_s\left(\ell H^3\nabla P\cdot\Re\right)\mathrm{d}s\\&-\iint_{\Omega_e}\left[3U\Phi_c\frac{\partial H}{\partial\theta}+3\bar{\sigma}U\frac{\partial\Phi_s}{\partial\theta}+6\Phi_c\frac{\partial H}{\partial\tau}\right]\cdot\Re\mathrm{d}\Omega_e=0\end{aligned}\tag{2-15}$$

Because the pressure at the boundary is fixed, the integral term along the closed curve of s is zero and Eq.(2-15) becomes

$$\begin{aligned}&\iint_{\Omega_e}\left(-\ell H^3\nabla P\cdot\nabla\Re\right)\mathrm{d}\Omega_e\\&-\iint_{\Omega_e}\left[3U\Phi_c\frac{\partial H}{\partial\theta}+3\bar{\sigma}U\frac{\partial\Phi_s}{\partial\theta}+6\Phi_c\frac{\partial H}{\partial\tau}\right]\cdot\Re\mathrm{d}\Omega_e=0\end{aligned}\tag{2-16}$$

The pressure can be linearized based on the first-order Taylor expansion

$$P=P_0+\mathrm{d}P,\ \nabla P=\nabla P_0+\nabla\mathrm{d}P\tag{2-17}$$

where ∇ is the differential operator. dP is the change in pressure between consecutive iterations.

Submitting Eq.(2-17) to Eq.(2-15) and replacing ℓ with the original terms, it can be obtain

$$\begin{aligned}&-\iint_{\Omega_e}\left[\Phi_\theta H^3\frac{\partial\mathrm{d}P}{\partial\theta}\frac{\partial\Re}{\partial\theta}+\left(\frac{R_s}{L}\right)^2\Phi_z H^3\frac{\partial\mathrm{d}P}{\partial\bar{z}}\frac{\partial\Re}{\partial\bar{z}}\right]\mathrm{d}\Omega_e\\&=\iint_{\Omega_e}\left[\Phi_\theta H^3\frac{\partial P_0}{\partial\theta}\frac{\partial\Re}{\partial\theta}+\left(\frac{R_s}{L}\right)^2\Phi_z H^3\frac{\partial P_0}{\partial\bar{z}}\frac{\partial\Re}{\partial\bar{z}}\right]\mathrm{d}\Omega_e\\&+\iint_{\Omega_e}\left[3U\Phi_c\frac{\partial H}{\partial\theta}+3\bar{\sigma}U\frac{\partial\Phi_s}{\partial\theta}+6\Phi_c\frac{\partial H}{\partial\tau}\right]\cdot\Re\mathrm{d}\Omega_e\end{aligned}\tag{2-18}$$

The quadrilateral element is used to discretize the solution domain. Isoperimetric transformation processing is used to regularize the element as shown in Fig. 2-3. The shape functions of the four-node element are

$$\Re_i(\xi,\eta)=\frac{1}{4}(1+\xi_i\xi)(1\text{-}\eta_i\eta),\ i=1,2,3,4\tag{2-19}$$

where i is the node number in Fig. 2-3. ξ and η and are the normalized coordinates of the element with -1≤ ξ , η ≤1. ξ_i and η_i are set to be (ξ_i, η_i)=(1,-1), (-1,-1), (-1, 1) and

(1, 1) which are corresponding to the node of 1, 2, 3, 4 in Fig. 2-3(b).

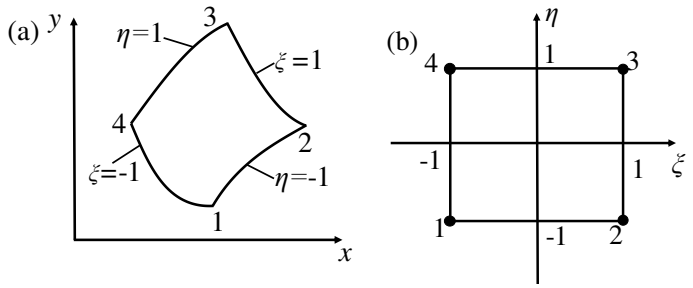


Fig. 2-3 Isoperimetric transformation for the quadrilateral element, (a) irregular element in Cartesian coordinate, and (b) regular isoperimetric element in parametric coordinate system

The parameters χ_e and $\mathrm{d}\chi_e$ of each element (χ_e can represents coordinates x_e, y_e, HD pressure P_e or film thickness H_e etc.) can be obtained by the interpolation of the values χ_i and $\mathrm{d}\chi_i$ of the four nodes belonging to the element

$$\chi_e = \sum_{i=1}^{4} \Re_i(\xi,\eta)\chi_i, \quad \text{and} \quad \mathrm{d}\chi_e = \sum_{i=1}^{4} \Re_i(\xi,\eta)\mathrm{d}\chi_i \tag{2-20}$$

The gradient of χ of each element in x and y directions can be expressed as

$$\frac{\partial\chi}{\partial x} = \sum_{i=1}^{4} \frac{\partial\Re_i}{\partial x}\chi_i, \quad \frac{\partial\chi}{\partial y} = \sum_{j=1}^{4} \frac{\partial\chi_j}{\partial y}\chi_j \tag{2-21}$$

The element in x-y space can be transformed to the isoperimetric element in ξ-η space by

$$\begin{Bmatrix} \mathrm{d}x \\ \mathrm{d}y \end{Bmatrix} = \begin{bmatrix} \dfrac{\partial x}{\partial\xi} & \dfrac{\partial x}{\partial\eta} \\ \dfrac{\partial y}{\partial\xi} & \dfrac{\partial y}{\partial\eta} \end{bmatrix} \begin{Bmatrix} \mathrm{d}\xi \\ \mathrm{d}\eta \end{Bmatrix} = \begin{bmatrix} \displaystyle\sum_{i=1}^{4} \frac{\partial\Re_i}{\partial\xi} x_i & \displaystyle\sum_{i=1}^{4} \frac{\partial\Re_i}{\partial\eta} x_i \\ \displaystyle\sum_{i=1}^{4} \frac{\partial\Re_i}{\partial\xi} y_i & \displaystyle\sum_{i=1}^{4} \frac{\partial\Re_i}{\partial\eta} y_i \end{bmatrix} \begin{Bmatrix} \mathrm{d}\xi \\ \mathrm{d}\eta \end{Bmatrix} = \boldsymbol{J} \cdot \begin{Bmatrix} \mathrm{d}\xi \\ \mathrm{d}\eta \end{Bmatrix} \tag{2-22}$$

where $\boldsymbol{J}$ is the Jacobian matrix.

Based on (2-22), it can be deduced as

$$\begin{Bmatrix} \mathrm{d}\xi \\ \mathrm{d}\eta \end{Bmatrix} = \frac{1}{\det \boldsymbol{J}} \cdot \begin{bmatrix} \dfrac{\partial y}{\partial\eta} & -\dfrac{\partial x}{\partial\eta} \\ -\dfrac{\partial y}{\partial\xi} & \dfrac{\partial x}{\partial\xi} \end{bmatrix} \begin{Bmatrix} \mathrm{d}x \\ \mathrm{d}y \end{Bmatrix} \tag{2-23}$$

where det $\boldsymbol{J}$ is the determinant of the Jacobian matrix.

$$\det \boldsymbol{J} = \left(\sum_{i=1}^{4} \frac{\partial \Re_i}{\partial \xi} x_i \cdot \sum_{i=1}^{4} \frac{\partial \Re_i}{\partial \eta} y_i \right) - \left(\sum_{i=1}^{4} \frac{\partial \Re_i}{\partial \xi} y_i \cdot \sum_{i=1}^{4} \frac{\partial \Re_i}{\partial \eta} x_i \right) \tag{2-24}$$

The inverse transformation from ξ-η space to x-y space is

$$\begin{Bmatrix} \mathrm{d}\xi \\ \mathrm{d}\eta \end{Bmatrix} = \begin{bmatrix} \dfrac{\partial \xi}{\partial x} & \dfrac{\partial \xi}{\partial y} \\ \dfrac{\partial \eta}{\partial x} & \dfrac{\partial \eta}{\partial y} \end{bmatrix} \begin{Bmatrix} \mathrm{d}x \\ \mathrm{d}y \end{Bmatrix} \tag{2-25}$$

Combining Eq.(2-23) and Eq.(2-25), it obtains

$$\begin{cases} \dfrac{\partial \xi}{\partial x} = \dfrac{1}{\det \boldsymbol{J}} \dfrac{\partial y}{\partial \eta} & \dfrac{\partial \xi}{\partial y} = -\dfrac{1}{\det \boldsymbol{J}} \dfrac{\partial x}{\partial \eta} \\ \dfrac{\partial \eta}{\partial x} = -\dfrac{1}{\det \boldsymbol{J}} \dfrac{\partial y}{\partial \xi} & \dfrac{\partial \eta}{\partial y} = \dfrac{1}{\det \boldsymbol{J}} \dfrac{\partial x}{\partial \xi} \end{cases} \tag{2-26}$$

Then the partial derivatives can be gotten as

$$\begin{cases} \dfrac{\partial}{\partial x} = \dfrac{\partial}{\partial \xi} \dfrac{\partial \xi}{\partial x} + \dfrac{\partial}{\partial \eta} \dfrac{\partial \eta}{\partial x} = \dfrac{\partial}{\partial \xi} \cdot \dfrac{1}{\det \boldsymbol{J}} \dfrac{\partial y}{\partial \eta} - \dfrac{\partial}{\partial \eta} \cdot \dfrac{1}{\det \boldsymbol{J}} \dfrac{\partial y}{\partial \xi} \\ \dfrac{\partial}{\partial y} = \dfrac{\partial}{\partial \xi} \dfrac{\partial \xi}{\partial y} + \dfrac{\partial}{\partial \eta} \dfrac{\partial \eta}{\partial y} = -\dfrac{\partial}{\partial \xi} \cdot \dfrac{1}{\det \boldsymbol{J}} \dfrac{\partial x}{\partial \eta} + \dfrac{\partial}{\partial \eta} \cdot \dfrac{1}{\det \boldsymbol{J}} \dfrac{\partial x}{\partial \xi} \end{cases} \tag{2-27}$$

The partial derivatives of the shape function $\Re(\xi, \eta)$ is

$$\begin{Bmatrix} \dfrac{\partial \Re}{\partial x} \\ \dfrac{\partial \Re}{\partial y} \end{Bmatrix} = \frac{1}{\det \boldsymbol{J}} \begin{bmatrix} \displaystyle\sum_{i=1}^{4} \frac{\partial \Re_i}{\partial \eta} y_i & -\displaystyle\sum_{i=1}^{4} \frac{\partial \Re_i}{\partial \xi} y_i \\ -\displaystyle\sum_{i=1}^{4} \frac{\partial \Re_i}{\partial \eta} x_i & \displaystyle\sum_{i=1}^{4} \frac{\partial \Re_i}{\partial \xi} x_i \end{bmatrix} \begin{Bmatrix} \dfrac{\partial \Re_i}{\partial \xi} \\ \dfrac{\partial \Re_i}{\partial \eta} \end{Bmatrix} \tag{2-28}$$

Applying the isoperimetric transformation to Eq.(2-18), the complex double integration can be simplified and calculated by Gauss integration. The selected Gauss points are expressed by (ξ_m, η_n), and the integration can be calculated by the sum of the function values at Gauss points as

$$\int_{-1}^{-1} \int_{-1}^{-1} f(\xi, \eta) \mathrm{d}\xi \mathrm{d}\eta = \sum_{m=1}^{N} \sum_{n=1}^{N} f(\xi_m, \eta_n) w_m w_n \equiv \underset{N \times N}{\mathbf{I}} f(\xi, \eta) \tag{2-29}$$

where w_m and w_n are the weight factors of the Gauss points of (ξ_m, η_n). N is the number

of the Gauss points.

The matrix equation for calculating the HD pressure over each quadrilateral element is

$$\left[K_{4\times4}\right]\left\{\mathrm{d}P_{4\times1}\right\}=\left\{R_{4\times1}\right\} \tag{2-30}$$

where the matrix elements of Eq.(2-30) are

$$k_{ij}=-\underset{2\times2}{\mathbf{I}}\left\{\Phi_\theta\bar{H}^3\frac{\partial\Re_i}{\partial\theta}\frac{\partial\Re_j}{\partial\theta}+\Phi_z\bar{H}^3\left(\frac{R_s}{L}\right)^2\frac{\partial\Re_i}{\partial\bar{z}}\frac{\partial\Re_j}{\partial\bar{z}}\right\}\det\boldsymbol{J} \tag{2-31}$$

$$R_i=\underset{2\times2}{\mathbf{I}}\left\{\begin{array}{l}\Phi_\theta\bar{H}^3\dfrac{\partial P_0}{\partial\theta}\dfrac{\partial\Re_i}{\partial\theta}+\left(\dfrac{R_s}{L}\right)^2\Phi_z\bar{H}^3\dfrac{\partial P_0}{\partial\bar{z}}\dfrac{\partial\Re_i}{\partial\bar{z}}\\+\left(3U\Phi_c\dfrac{\partial H}{\partial\theta}+3\bar{\sigma}U\dfrac{\partial\Phi_s}{\partial\theta}+6\Phi_c\dfrac{H_{t+\triangle t}-H_t}{\triangle\tau}\right)\Re_i\end{array}\right\}\det\boldsymbol{J} \tag{2-32}$$

Combining the stiffness matrices at each element can obtain the stiffness matrix of the entire solution area. By solving the linear equation, the pressure increment of dP can be obtained. Repeat it until dP approaches less than the imposed error, then the pressure result at present time step can be obtained.

2.2.5.2 Solution method of the motion equation

Due to the highly nonlinear Reynolds equation, the Newmark method is used to solve Eq.(2-12) which can be expressed by

$$\left\{\begin{array}{l}\dot{x}_{t+\triangle t}=\dot{x}_t+\left[\left(1-\alpha_{\mathrm{N}}\right)\ddot{x}_t+\alpha_{\mathrm{N}}\ddot{x}_{t+\triangle t}\right]\triangle t\\x_{t+\triangle t}=x_t+\dot{x}_t\triangle t+\left[\left(\dfrac{1}{2}-\beta_{\mathrm{N}}\right)\ddot{x}_t+\beta_{\mathrm{N}}\ddot{x}_{t+\triangle t}\right]\triangle t^2\\\dot{y}_{t+\triangle t}=\dot{y}_t+\left[\left(1-\alpha_{\mathrm{N}}\right)\ddot{y}_t+\alpha_{\mathrm{N}}\ddot{y}_{t+\triangle t}\right]\triangle t\\y_{t+\triangle t}=y_t+\dot{y}_t\triangle t+\left[\left(\dfrac{1}{2}-\beta_{\mathrm{N}}\right)\ddot{y}_t+\beta_{\mathrm{N}}\ddot{y}_{t+\triangle t}\right]\triangle t^2\end{array}\right. \tag{2-33}$$

where x, $\dot{x}$, $\ddot{x}$ and y, $\dot{y}$, $\ddot{y}$ are the displacements, velocities and accelerations of the shaft center in the x and y directions respectively. Δt is the time step. The subscripts t and $t+\Delta t$ are the present and next moments. The constant coefficients α_{N} and β_{N} are set to be 0.5 and 0.25.

Bellowing is the solution procedure of the model:

1. At beginning of t=0, the shaft is in a steady-state position, and the initial average

film thickness is determined according to the balance of contact force and applied load for startup, or the balance of HD force and applied load for shutdown.

2. With the increasing/decreasing shaft speed during startup/shutdown, the HD pressure and HD force are obtained by calculating Eq.(2-6) and Eq.(2-11). Meanwhile, the contact pressure and the contact force are obtained by calculating the contact model (Eq.(2-2) and Eq.(2-3)).

3. The displacements, velocities and accelerations of the shaft center at each time step are calculated using the motion equations (Eq.(2-12) and Eq.(2-33)). Then the film thickness is refreshed.

4. The HD force, contact force and the motion properties are calculated iteratively until the end of the acceleration/deceleration of the bearing during startup/shutdown.

At the very early initial stage of startup, the friction force drives the shaft to roll along the bush surface in the opposite direction of rotation, then the shaft falls back and forms a very small minimum film thickness. With the increase in the shaft speed, there is a small HD pressure, and the influence of the friction force is not significant. Therefore, we mainly focus on the center locus in the rotating direction after the very beginning period. As a consequence, the friction force between the two contacted surfaces and the hydrodynamic shear stresses which occur on the body surface are neglected.

2.2.5.3 Model Verification

Fig. 3 shows the comparison of the present results with Mokhtar's [10] experiments for the contact time and the shaft center locus during startup in different applied loads. The mean diameter and the length of the bearing are 74.653 mm and 76.20 mm respectively. The diametral clearance is 0.121 mm. The surface roughness of the shaft and the bush are 0.12 μm and 1.473 μm respectively. The oil viscosity is 0.074 Pa·s. The shaft speed increases linearly from 0 to 850 rpm in 0.3 s. The result shows that both the contact time and the shaft center locus calculated by present model are in accordance with that tested by Mokhtar et al.

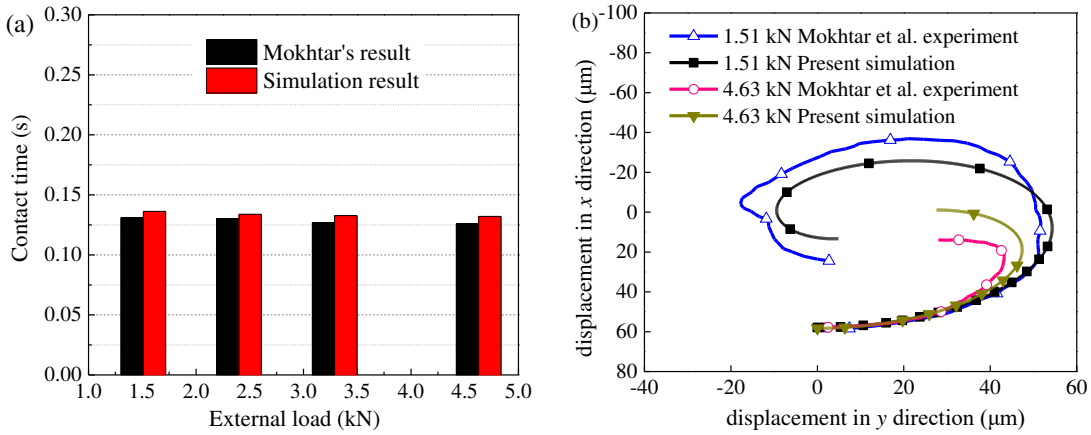


Fig. 2-4 (a) The contact time and (b) shaft center locus in different applied loads during startup

2.3 Contact behavior during startup and shutdown

The parameters of the journal bearing are listed in Table 2-2. The surface pattern is isotropic. The shaft speed accelerates from zero to 1000 rpm in 0.1 s, or decelerate from 1000 rpm to zero in 0.1 s.

Table 2-2 The simulation parameters

Parameters	Symbols	Values	Parameters	Symbols	Values
Shaft radius, mm	Rs	50	Areal asperity density, asp/m^2	D_{sum}	5e11
Bearing length, mm	B	60	Standard deviation of surface roughness, μm	σ	1.0
Density of oil, kg/m^3	ρ	860	Equivalent modulus, GPa	$E_{1,2}$	210
Oil viscosity at 20℃, Pa·s	μ	0.027	Poisson's ratio	$v_{1,2}$	0.29
Asperity radius, μm	R_p	2	Applied load, kN	W	4

2.3.1 Contact behavior during startup

Fig. 2-5 shows the variations of hydrodynamic (HD) force and asperity contact force during startup. The negative of the scale represents the inverse direction of the coordinate system (Fig. 2-1(b)). We observe that the shaft lifts off at time of t=0.057 s, corresponding to the lift-off speed of ω=570 rpm. The period before the shaft separates with the bush surface is named as contact time [10]. During the contact time, the HD force and contact force in the x direction (F_{hx} and F_{cx}) are larger than that in the y direction (F_{hy} and F_{cy}). This is because that the applied load is in the x direction and the contact force and HD force are mainly used to support the applied load.

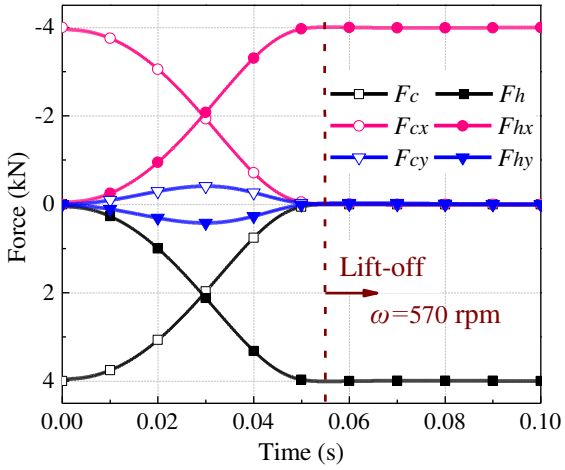


Fig. 2-5 Variation of the contact force F_c and HD force F_h during startup

Fig. 2-6 shows the transient behavior of the journal bearing during startup. In initial period of startup, the shaft mainly slides along the bearing surface with a quickly increasing attitude angle φ and a slightly increasing eccentricity ratio ε. The attitude angle of φ=38° at the contact time of t_c=0.057 s is named as contact zone which can express the wear zone of the bush surface (Fig. 2-6(a)). During startup, the minimum film thickness ($h_{\min}$) keeps increasing, while the transient HD pressure first increases and then decreases (Fig. 2-6 (b)). The maximum HD pressure appears at the time of t_{pmax}=0.047 s (Fig. 2-6 (b)) before the shaft separates with the bearing surface (Fig. 2-6 (a)). This is due to the effect of both the film thickness and the increasing shaft speed. Until the time t_{pmax}=0.047 s, $h_{\min}$ rises quite small (Fig. 2-6 (b)). The slow rotating shaft squeezes the oil into the small clearance between the two surfaces causing an increase in the HD pressure. After t_{pmax}=0.047 s, $h_{\min}$ increases quickly, and this squeeze effect decreases leading to a decrease in the HD pressure. In addition, the active zone of HD pressure keeps increasing (Fig. 2-6 (c)), while the active zone of the contact pressure always keeps being about 20° which is determined by the curvature of the two surfaces (Fig. 2-6 (d)).

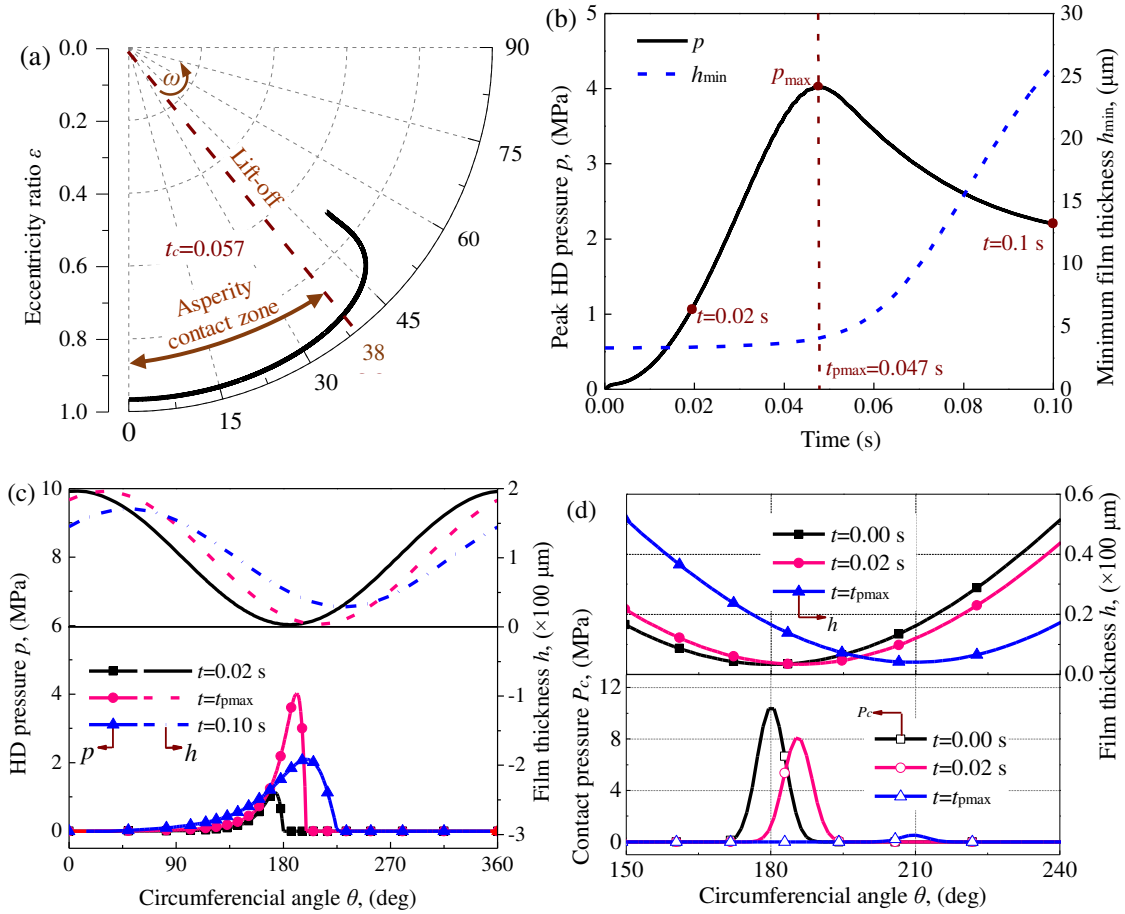


Fig. 2-6 Influence of σ on (a) shaft center locus, (b) transient peak HD pressure, (c) HD pressure and (d) contact pressure during startup

2.3.2 Contact behavior during shutdown

Fig. 2-7 shows the variation of transient parameters of the journal bearing during shutdown. The shaft speed decreases linearly from 1000 rpm to zero in 0.1 s. In Fig. 2-7 (a) and (b), during the first 0.28 s the eccentricity ratio increases sharply and the attitude angle decreases rapidly. At 0.1 s, the eccentricity ratio reaches to 0.83 and the attitude angel decreases to 21°. However, the HD force almost remains stable as shown in Fig. 2-7(c). This means that when the shaft stops rotating, the HD force can still support the shaft because of the HD pressure caused by squeeze effect. At 0.28 s, the two surfaces begin to contact, and the period from the two surfaces beginning to contact until the shaft being static is noted as contact time t_c. The corresponding contact zone is 4.0° as shown in Fig. 2-7(a). From 0.28 s to 0.4 s, the contact force sharply increases and the HD decreases rapidly (Fig. 2-7(c)), while the variations of the eccentric ratio and attitude angle during this period changes sharply (Fig. 2-7(b)). The HD force and contact force in the x direction are much smaller than that in the y

direction which mainly balances the applied load (Fig. 2-7(d)).

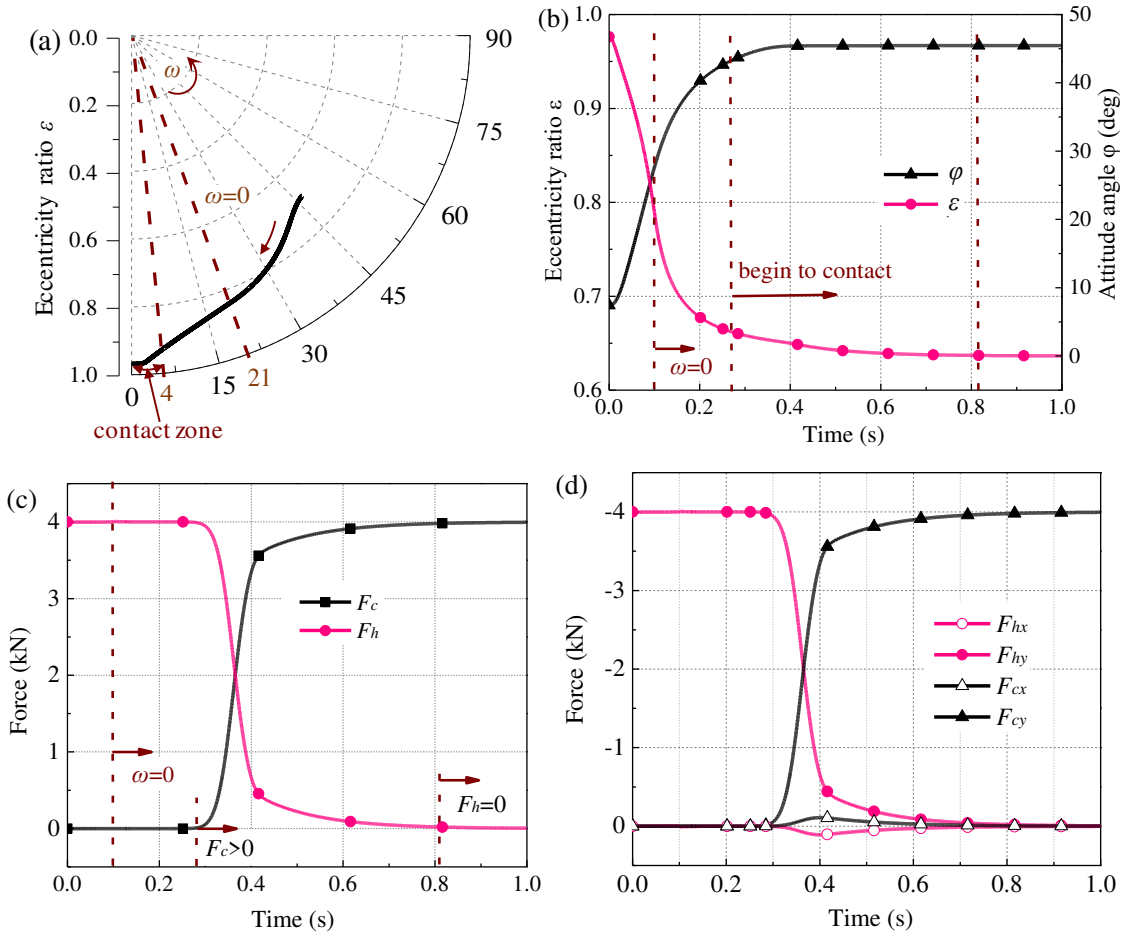


Fig. 2-7 The variation of the transient parameters during shutdown (a) shaft center locus, (b) eccentricity ratio and attitude angle, (c) HD force and contact force, (d) HD force and contact force in x and y directions

2.4 Effect of surface roughness on the contact behavior

2.4.1 Contact and wear performance during startup

2.4.1.1 Influence of standard deviation of asperity height σ

Fig. 2-8 shows the effect of standard deviation of asperity height σ on the hydrodynamic (HD) force F_h and contact force F_c and volume wear V_f during startup. The shaft speed rises linearly up to 1000 rpm within 0.1 second. The surface pattern is in isotropic. σ is set to be 0.50 μm, 0.75 μm and 1.0 μm respectively. It is observed that high σ leads to a slow increase in HD force, resulting in a large transient contact force. The corresponding contact time is 0.051 s, 0.054 s and 0.057 s and the lift-off speed is 507 rpm, 541 rpm and 570 rpm respectively, which means it owns a long contact time and a high lift-off speed in large σ. Meanwhile, the small σ leads to the

less volume wear, so the smooth surface is beneficial to reduce wear during startup.

Fig. 2-9 describes the influence of standard deviation of asperity height σ on the transient characteristics during startup. Small σ leads to large eccentricity ratio but

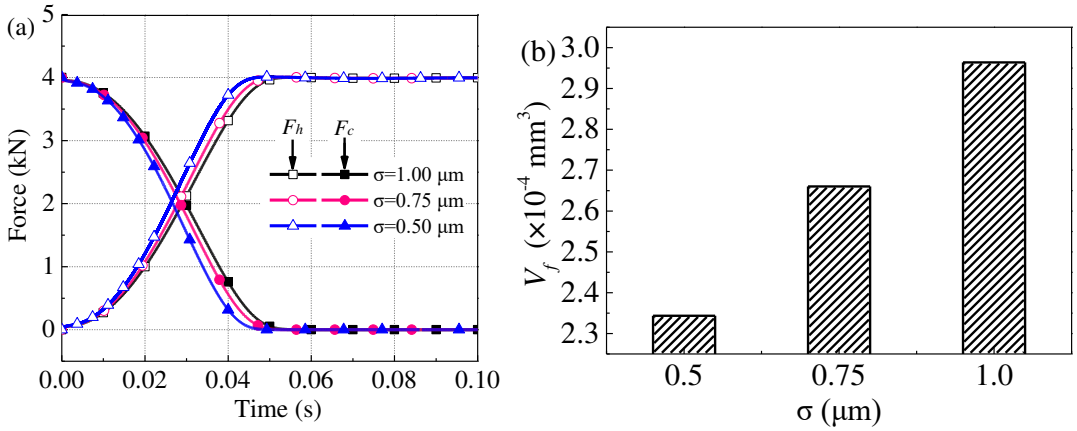


Fig. 2-8 Influence of σ on (a) the HD force F_h and contact force F_c and (b) volume wear during startup

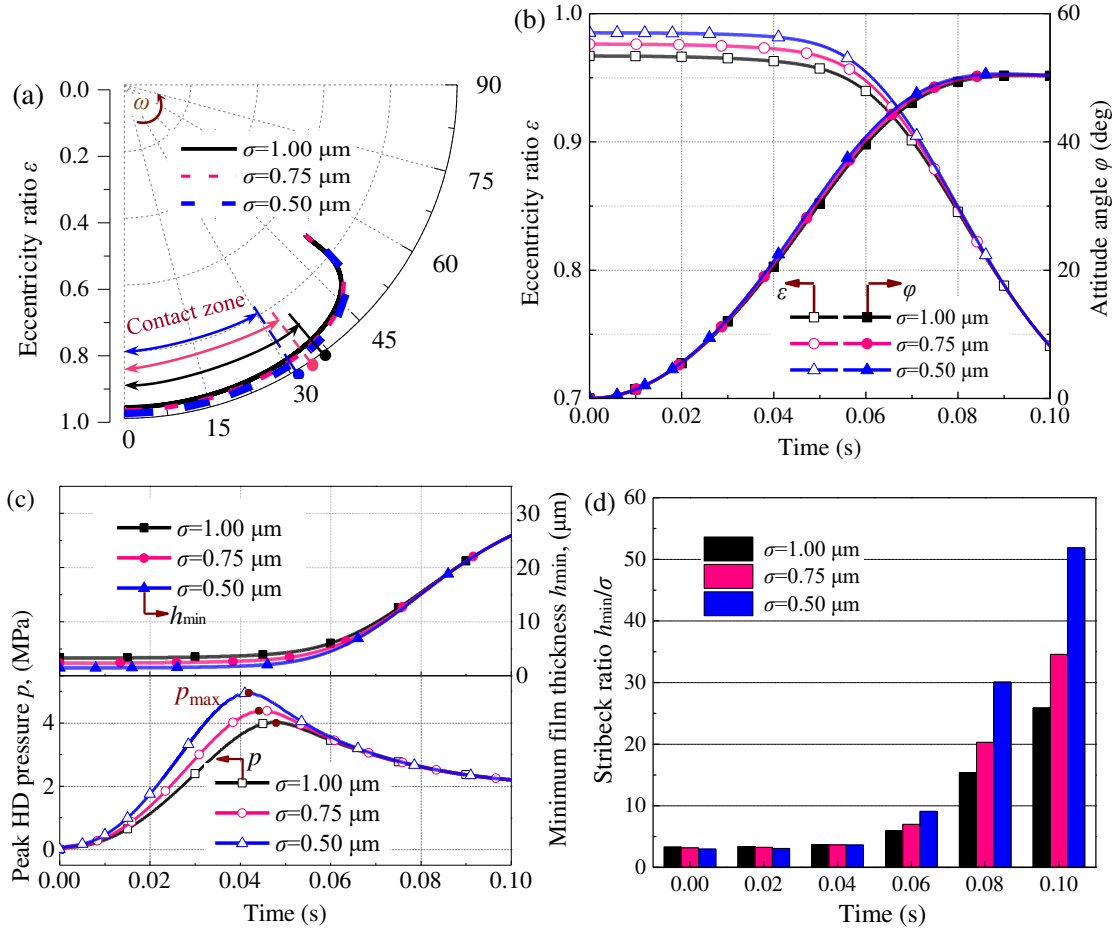


Fig. 2-9 Influence of σ on (a) shaft center locus, (b) eccentricity ratio and attitude angle, (c) peak HD pressure and (d) Stribeck ratio of h_{min}/σ during startup

small contact zone (Fig. 2-9(a) and (b)). The minimum film thickness (h_{min}) decreases with an increasing eccentricity ratio (Fig. 2-9(b)), leading to an increasing HD pressure (Fig. 2-9(c)). Interestingly, in the mixed lubrication during contact time, the Stribeck ratio h_{min}/σ changes quite small (Fig. 2-9(d)), while the HD pressure is significantly influenced by σ (Fig. 2-9(c)). However, in the hydrodynamic lubrication when the shaft lifts up, the Stribeck ratio h_{min}/σ decreases rapidly with an increase in σ (Fig. 2-9(d)), while the HD pressure changes slowly (Fig. 2-9(c)). This is because that in mixed lubrication σ has a significant effect on the contact factor Φ_c (Eq.(2-6)). In addition, the small σ generates the large maximum HD pressure in Fig. 2-9(c).

Fig. 2-11 depicts the influence of standard deviation of asperity height σ on the distributions of HD pressure and contact pressure in the plane of z=0 of the bearing. At the initial time t=0 s, high peak contact pressure is caused by low σ. The maximum contact pressure reaches 14 MPa in σ=0.5 μm (Fig. 2-11 (a)). At the time of $t=t_{pmax}$ (the moment of maximum HD pressure) (Fig. 2-11 (c)), the locations of both the

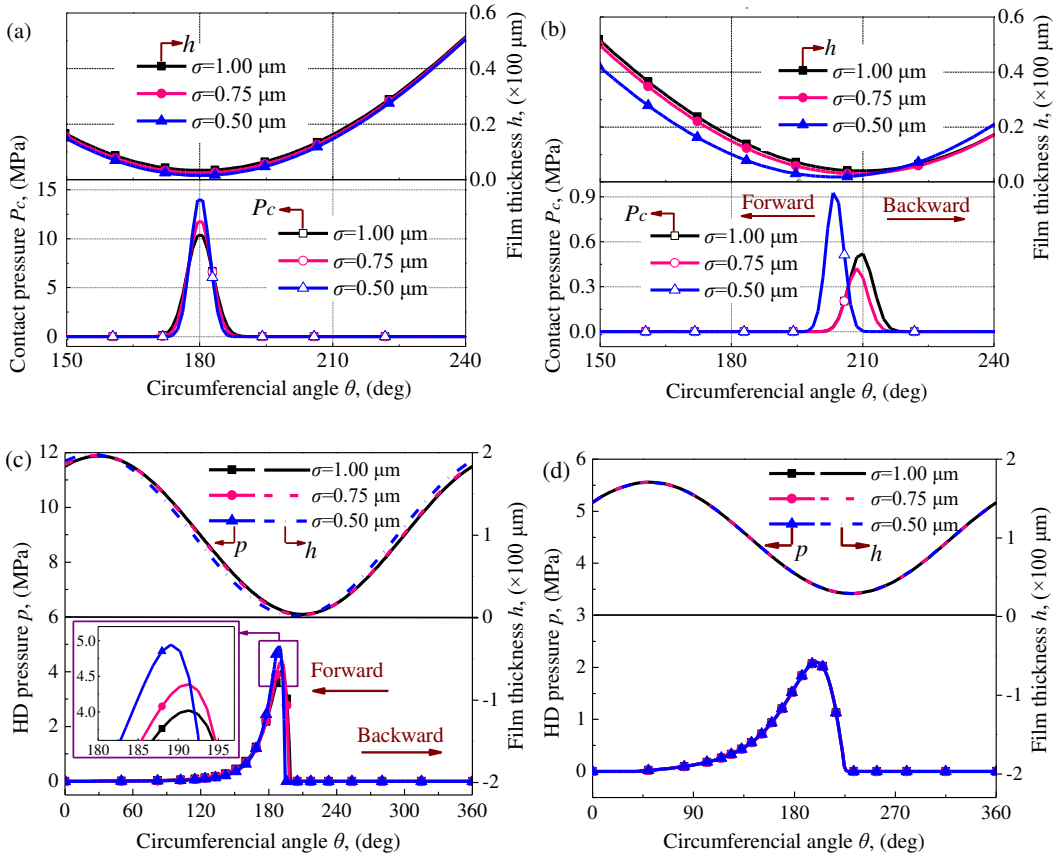


Fig. 2-11 Influence of σ on contact pressure distribution at (a) t=0 s and (b) the moment of maximum HD pressure, i.e. $t=t_{pmax}$, and HD pressure distribution at (c) $t=t_{pmax}$ and (d) t=0.1 s during startup

maximum contact pressure (Fig. 2-11 (b)) and the maximum HD pressure (Fig. 2-11 (c)) moves forward at a small σ. At t=0.1 s, σ has a very slight effect on the HD pressure (Fig. 2-11 (d)), because the micro-surface texture has little influence in large film thickness.

2.4.1.2 Influence of surface pattern

The surface pattern parameters are 1/6, 1 and 6 in transverse, isotropic and longitudinal orientations respectively, as shown in Table 2-1. σ is set to be 1.0 μm. The shaft speed rises up to 1000 rpm in 0.1 second. Other parameters are listed in Table 2-2.

Fig. 2-10 shows the influence of surface pattern on the transient characteristics of hydrodynamic journal bearings during startup. It is obvious that the surface pattern has slight effect on both the motion of the shaft center and the HD forces of the bearing during startup. Comparing to the transverse and isotropic patterns, the longitudinal pattern generates a slight increase in the eccentricity ratio (Fig. 2-10 (b)) and a slow decrease in the HD force (Fig. 2-10 (c)). Also, $h_{\min}$ in longitudinal pattern is the smallest, while the peak HD pressure is the lowest (Fig. 2-10 (d)). This means that the longitudinal pattern can decrease the carrying capacity slightly, which agrees with the conclusion of Dobrica et al.[109]. This is due to the micro-hydrodynamic effect generated by the micro-textures of surface roughness.

In general, the influence of surface pattern on the transient characteristics of the bearing during startup is slight enough to be ignored. The reason is that the initial Stribeck ratio of the rough surfaces under the present applied load is about 3.3. At such a large Stribeck ratio, the effects of the factors Φ_θ, Φ_z and Φ_s in the average Reynolds equation can be neglected. However, if a heavy load is applied, $h_{\min}$ is small, generating a low Stribeck ratio. The effects of the surface pattern will be more obvious [108].

Fig. 2-11 shows the influence of surface pattern on the volume wear during startup. The volume wear is largest in the longitudinal pattern and smallest in the transverse pattern, but the difference of the volume wear in the two patterns is quite small, which is only 0.07×10^{-4} mm^3 (2.4%).

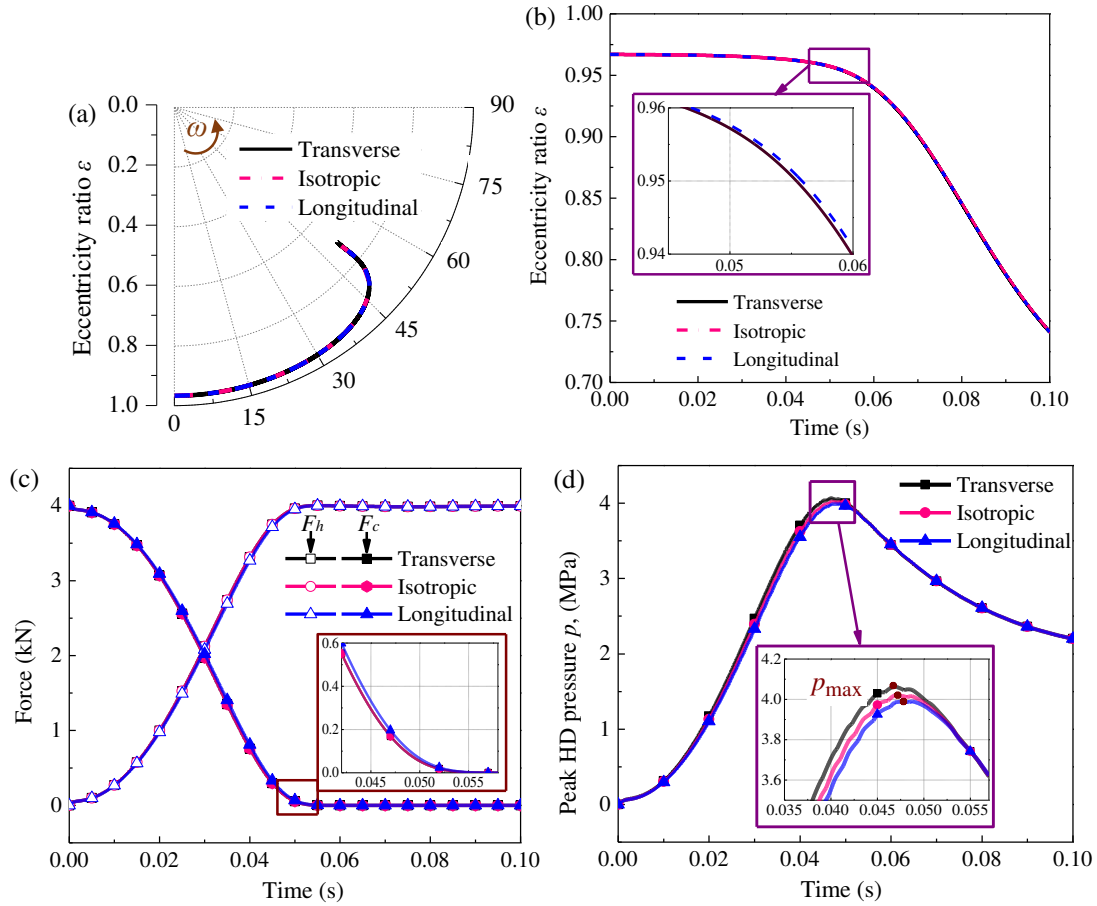


Fig. 2-10 Influence of surface pattern on (a) shaft center locus, (b) eccentricity ratio ε, (c) HD force F_h and contact force F_c, and (d) peak HD pressure during startup

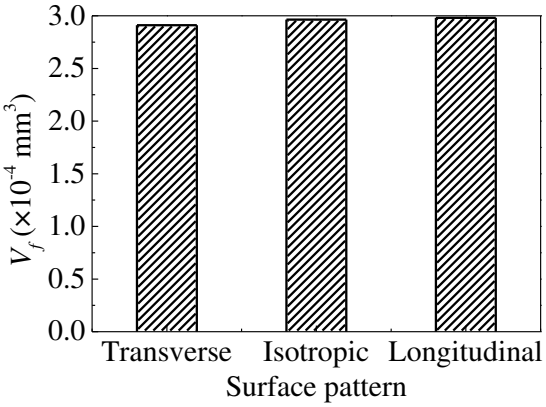


Fig. 2-11 Influence of surface pattern on the volume wear during startup

2.4.2 Contact and wear performance during shutdown

2.4.2.1 Influence of standard deviation of asperity height σ

During shutdown, the shaft speed decreases from 1000 rpm to 0 in 0.1 s. The surface

pattern is in isotropic orientation. The standard deviations of asperity height σ are set to be 1.0 μm, 0.75 μm and 0.5 μm. The other parameters are set in Table 2-2.

Fig. 2-12 shows the variation of hydrodynamic (HD) force and contact force as a function of σ during shutdown. In Fig. 2-12(a), it takes a short time for high σ to get contacted, about 0.28 s, 0.37 s and 0.51 s for σ=1.0, 0.75 and 0.5 μm respectively. The high σ causes a sharp decrease of the HD force, which generates a rapid increase of the contact force. Meanwhile, it takes a short time in large σ to arrive the standstill position. Fig. 2-12 (b) shows the volume wear increases obviously in large σ. The volume wear at σ=1.0 μm is about 4 times of that at σ=0.5 μm. The volume wear during startup is in the order of 10^{-7} mm^3, which can be neglected compared to that during startup (in the order of 10^{-4} mm^3 in Fig. 2-8 (b)).

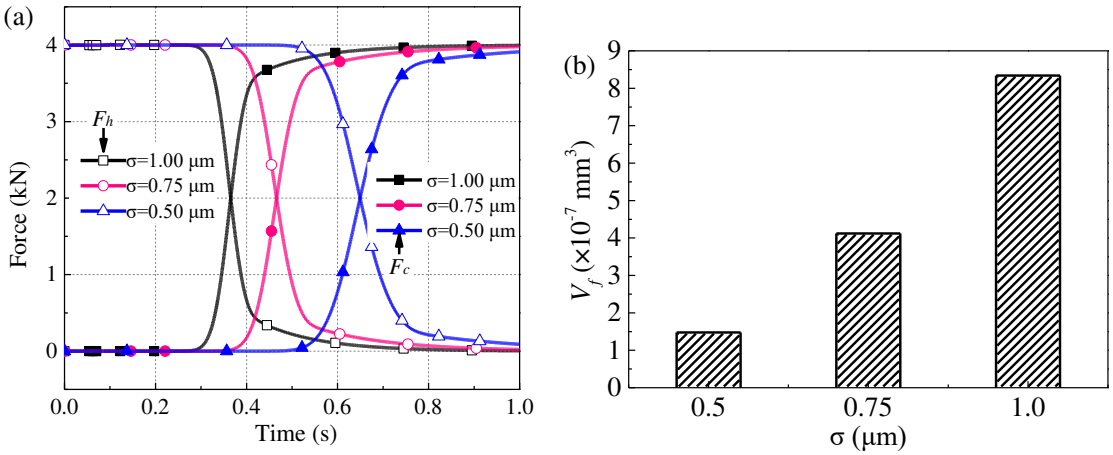


Fig. 2-12 Influence of σ on (a) HD force F_h and contact force F_c, and (b) volume wear V_f during shutdown

Fig. 2-13 shows the influence of σ on the transient behavior of the journal bearing during shutdown. Before contact, σ has almost no effect on the transient eccentricity ratio and attitude angle. After the contact of two surfaces, the eccentricity ratio of large σ is small, but it experiences a large contact zone. This is because σ has a greater impact on the contact coefficient Φ_c in the mixed lubrication. A large σ represents a high contact possibility for a single asperity, which generates a larger h_{min} between two rough surfaces.

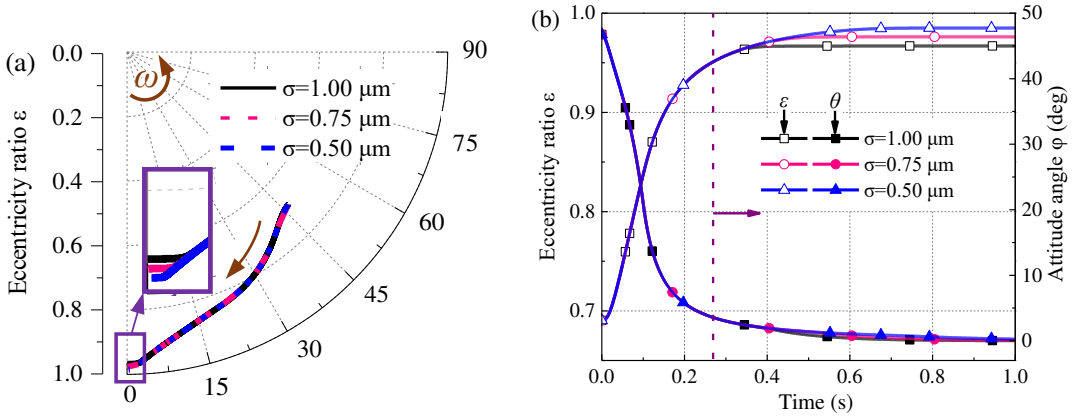


Fig. 2-13 Influence of σ on (a) shaft center locus and (b) eccentricity ratio and attitude angle during shutdown.

Fig. 2-14 shows the influence of σ on the peak HD pressure and pressure distributions. As shown in Fig. 2-14(a), the small σ leads to the large maximum HD pressure by generating a small $h_{\min}$ when the two surfaces are in contact, but it has almost no effect on the peak HD pressure before 0.3 s, which means it has little influence in hydrodynamic lubrication. Fig. 2-14 (c) shows the maximum transient HD pressure appears around θ=180° where is the standstill position of the shaft. Comparing Fig. 2-14 (b), (c) and (d), σ has very little effect on the active pressure zone.

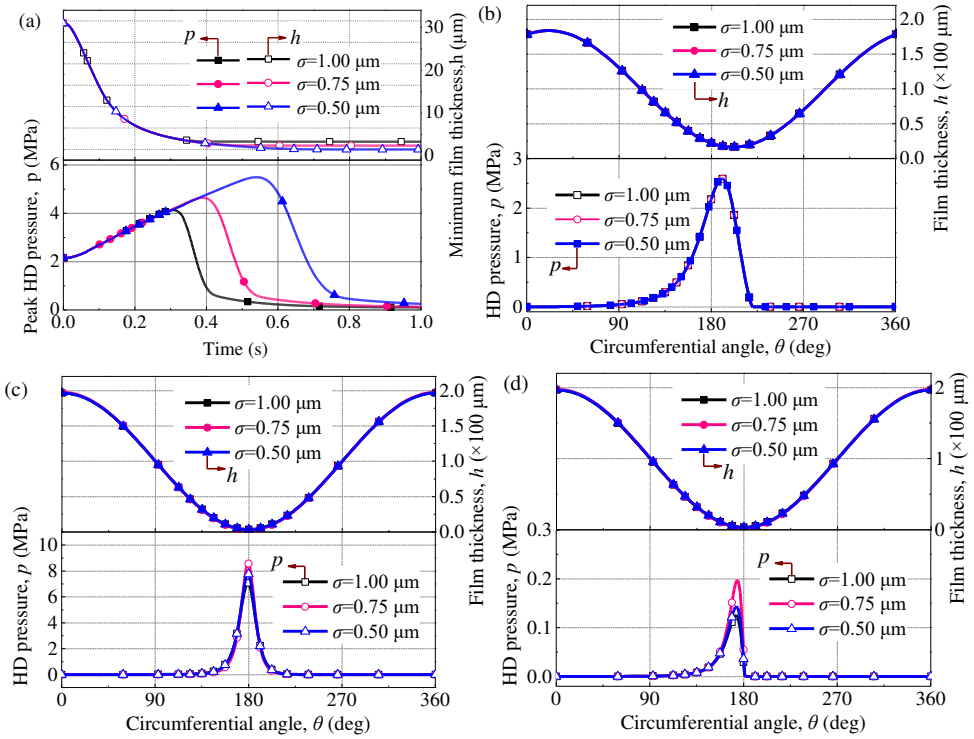


Fig. 2-14 Influence of σ on the (a) transient peak HD pressure, HD pressure distribution at (b) t=0, (c) t=t_{pmax} and (d) at t=0.6s

2.4.2.2 Influence of surface pattern

Fig. 2-15 shows the influence of surface pattern on the transient forces and shaft center locus during startup. The surface pattern has a very small effect on the transient parameters. In Fig. 2-15(a), it shows that the contact time in the longitudinal pattern is slightly earlier than the other two patterns, but the difference is so small that can be neglected. Therefore, it is not further discussed.

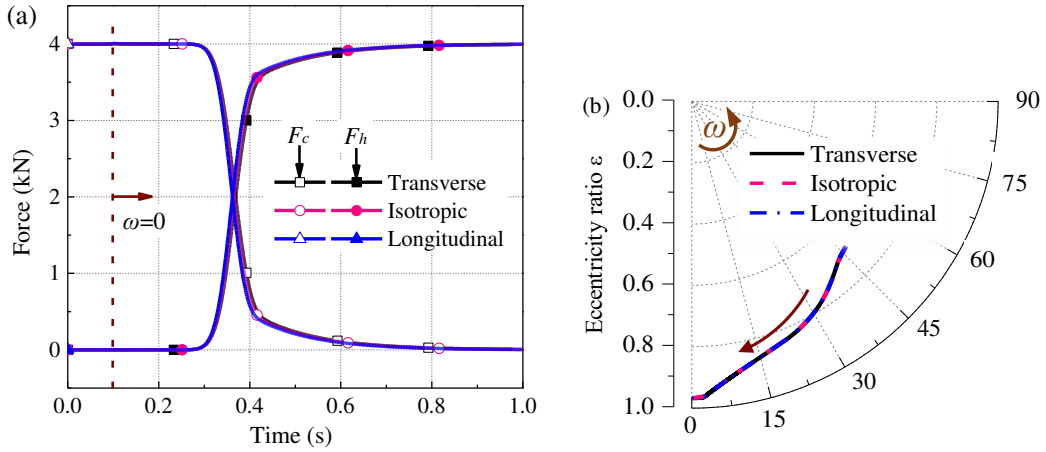


Fig. 2-15 Influence of surface pattern on the (a) HD force and contact force and (b) shaft center locus during startup

2.5 Effect of relative clearance on the contact behavior

2.5.1 Contact and wear performance during startup

Fig. 2-16 shows the influence of relative clearance on the transient behavior during startup. During early startup, the hydrodynamic (HD) force rises faster leading to a sharp decrease in contact force in large relative clearance (Fig. 2-16(a)). δ=1‰, 2‰, and 3‰ correspond to the contact time of 0.065 s, 0.057 s and 0.052 s, and lift-off speed of 520 rpm, 570 rpm and 645 rpm respectively. The large relative clearance leads to the small contact zone, which is 53°, 38° and 29° in the three clearances (Fig. 2-16(b)). The eccentricity ratio is high in large relative clearance (Fig. 2-16(c)), resulting in a large maximum HD pressure (Fig. 2-16(d)). This is due to the large conformal curvature of the shaft and bush, there are less asperities to support the applied load leading to a large deformation of the asperities, as well as a small h_{min}. In addition, a large relative clearance causes a small attitude angle (in Fig. 2-16(d)). In total, the large relative clearance can reduce the contact time and contact zone with decreasing the h_{min} and enlarging maximum HD pressure.

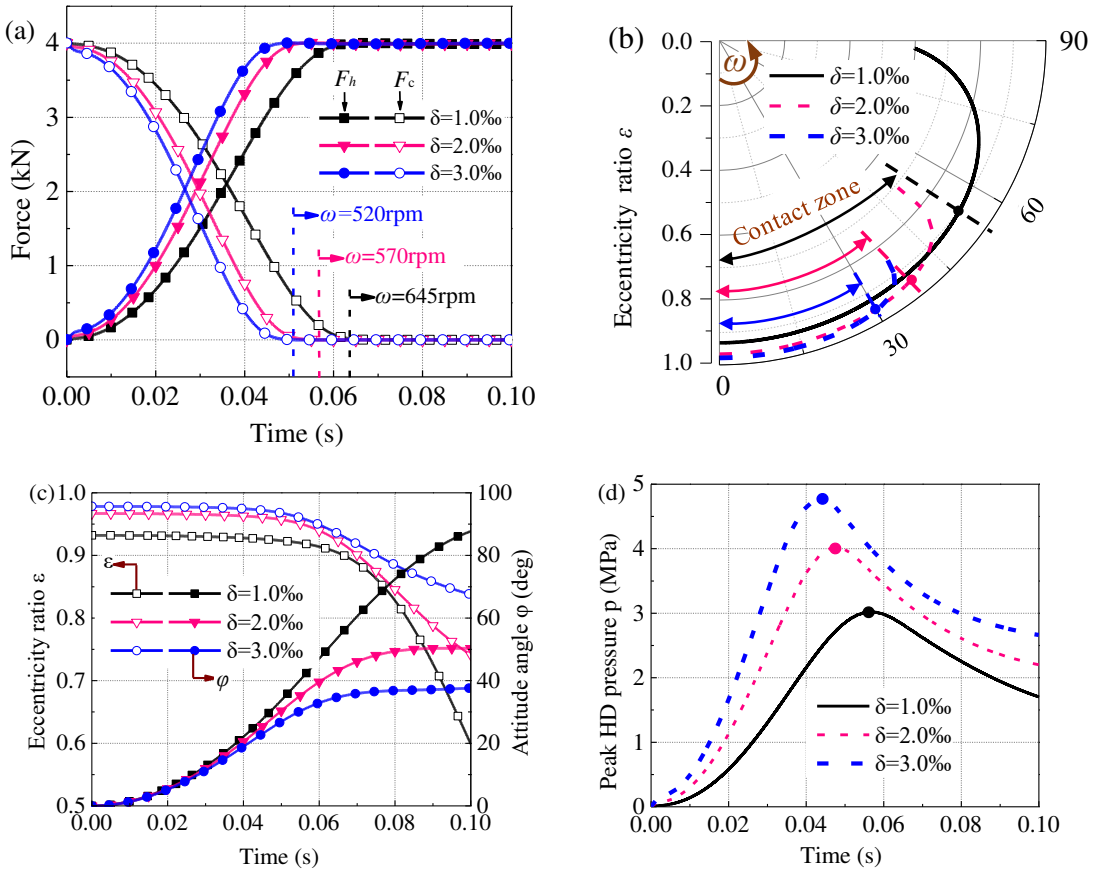


Fig. 2-16 Influence of the relative clearance on (a) HD force and contact force, (b) shaft center locus, (c) eccentricity ratio and attitude angle, (d) transient peak HD pressure during startup

Fig. 2-17 demonstrates the influence of relative clearance on the volume wear during startup. It can be seen that with the increase of the relative clearance, the amount of wear decreases significantly. When the relative clearance increases from 1.0‰ to 3.0‰, the volume wear decreases by 41.19%. Therefore, the large relative clearance is beneficial to reduce wear.

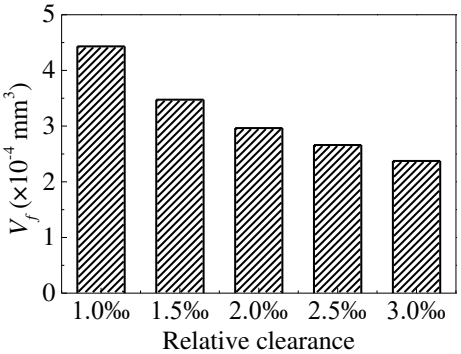


Fig. 2-17 Influence of relative clearance on the volume wear during startup

2.5.2 Contact and wear performance during shutdown

Fig. 2-18 shows the influence of relative clearance on transient parameters during shutdown. The shaft speed linearly decelerates from 1000 rpm to zero in 0.1 s. It can be seen from Fig. 2-18 (a) that the large relative clearance causes the HD force rising fast leading to the sharp decrease in contact force and the early contact of the two surfaces. The beginning contact time for δ=1‰, δ=2‰, and δ=3‰ is 0.588 s, 0.307 s and 0.211 s respectively. The small relative clearance generates a low stable eccentricity and large attitude angle which lead to the obvious difference of the shaft center locus (in Fig. 2-18(b) and (c)). Fig. 2-18d) shows the large relative clearance enlarges the maximum velocity of the shaft center which leads to a rise in maximum HD pressure.

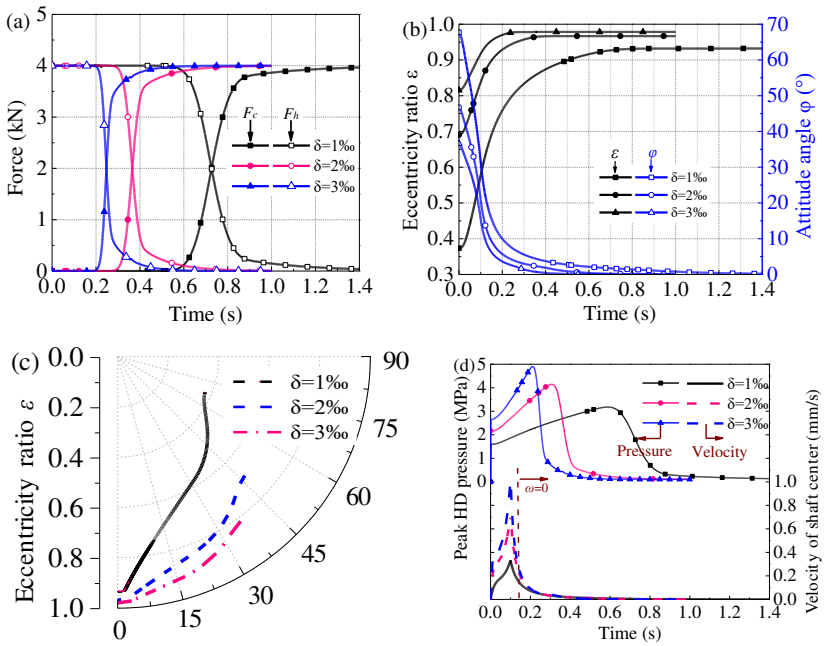


Fig. 2-18 Influence of relative clearance on (a) HD force and contact force, (b) eccentricity ratio and attitude angle (c) shaft center locus and (d) maximum HD pressure and velocity of shaft center during shutdown

Fig. 2-19 shows the influence of the relative clearance on the contact and wear behavior during shutdown. Unlike startup, the contact zone and volume wear that are far less than that during startup grows with the increase in relative clearance. The contact zone and volume wear at the relative of 3‰ are 30° and 2.66×10^{-4} mm^3 respectively during startup, while the two values are 4.53° and 15.14×10^{-7} mm^3 during shutdown. In addition, it is late for the appearance of the maximum HD pressure and the beginning contact time in small relative clearance.

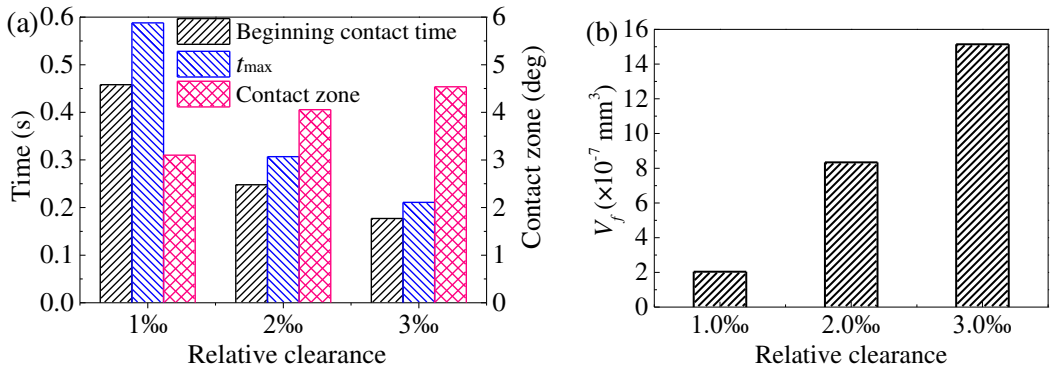


Fig. 2-19 Influence of relative clearance on the (a) contact time and contact zone and (b) volume wear V_f during shutdown

2.6 Effect of acceleration/deceleration on the contact behavior

2.6.1 Contact and wear performance during startup

Fig. 2-20 shows the influence of acceleration on the transient parameters during startup. The shaft speed increases linearly from zero to 1000 rpm in 0.1 s, 0.2 s and 0.3 s respectively. Short acceleration time means large acceleration of the shaft speed. The relative clearance is 2‰. The high acceleration generates the sharp increase in the HD force, which results in the sharp decrease in the contact force, as well as short contact time of 0.057 s, 0.082 s and 0.102 s respectively (Fig. 2-20(a)) due to the sharp increase in shaft speed. Before lifting off, the shaft slides along the same locus in different accelerations as shown in Fig. 2-20(b). The high acceleration causes the fast change of the eccentricity and attitude angle in the early stage (Fig. 2-20(c)), as well as a sharp increase in HD pressure (Fig. 2-20(d)).

Fig. 2-21 shows the effect of acceleration on the contact and wear during startup. In Fig. 2-21(a), as the acceleration time increases from 0.1 s to 0.5 s, the contact zone decreases from 37° to 30.6°, meanwhile the contact time increases from 0.057 s to 0.129 s. This indicates that with the decrease in acceleration, although the contact time increases, the wear zone decreases. In Fig. 2-21(b), the relationship between wear and acceleration time is not monotonous. When the acceleration time is 0.3 s, the volume wear is 2.91×10^{-4} mm which is the lowest, so there is an optimal acceleration to minimize the volume wear during startup.

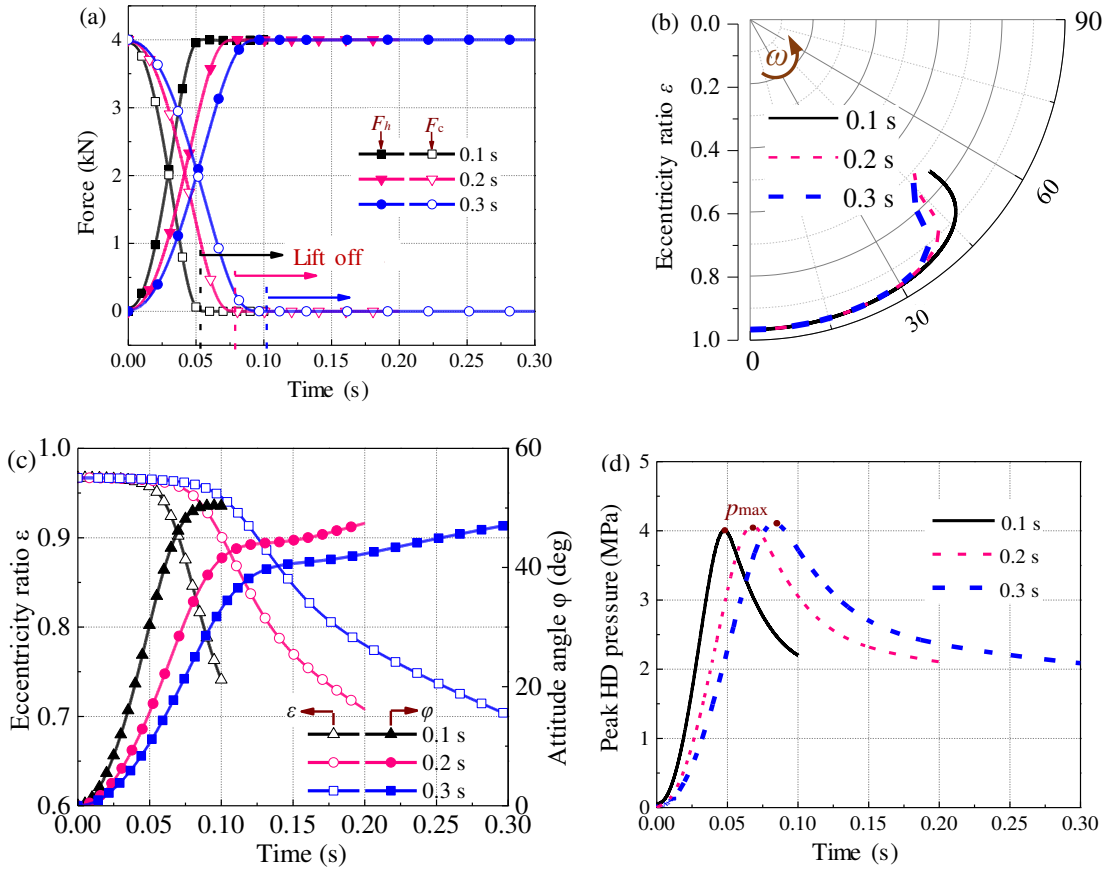


Fig. 2-20 Influence of acceleration on the transient parameters during startup, (a)transient HD force and contact force, (b) shaft center locus, (c) eccentricity ratio and attitude angle, (b) transient peak HD pressure

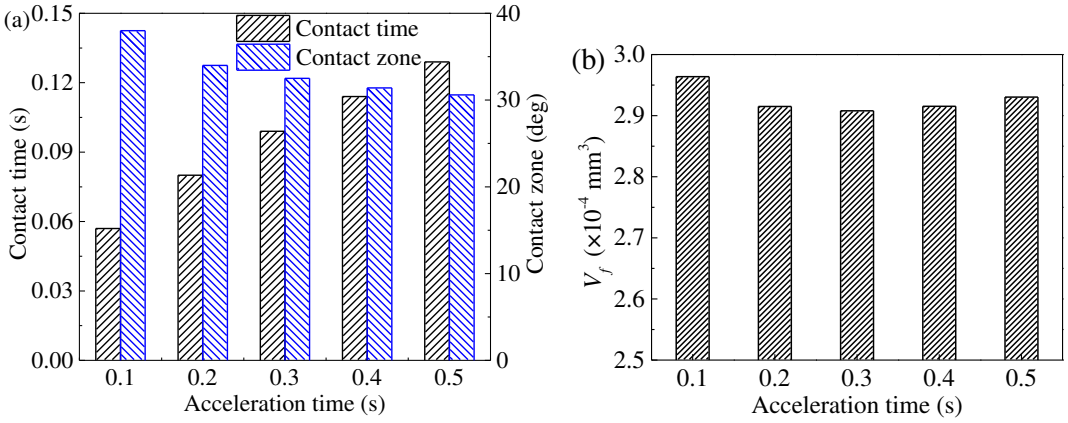


Fig. 2-21 Influence of acceleration on (a) contact time and zone and (b) volume wear V_f

2.6.2 Contact and wear performance during shutdown

Fig. 2-22 shows the effect of deceleration on transient parameters during shutdown. The shaft decelerates from 1000 rpm to zero in 0.1 s, 0.3 s and 1.0 s respectively, and the deceleration decreases consecutively. In Fig. 2-22(a), the beginning contact time

of the two surfaces in the three decelerations is 0.248 s, 0.407 s, and 1.024 s respectively, which means the large deceleration leads to the early contact of the two surfaces. The eccentricity ratio increases rapidly and the attitude angle decreases rapidly in large deceleration (Fig. 2-22(b)), meanwhile the locus is steep and the shaft will reach the standstill position faster (Fig. 2-22 (c)). The maximum velocity of the shaft center is high in large deceleration, which means the shaft moves more slowly, leading to the more obvious squeeze effect of the oil film, so the maximum HD pressure is more likely to appear after the speed decreasing to ω=0, i.e. the contact occurs after the speed drops to zero.

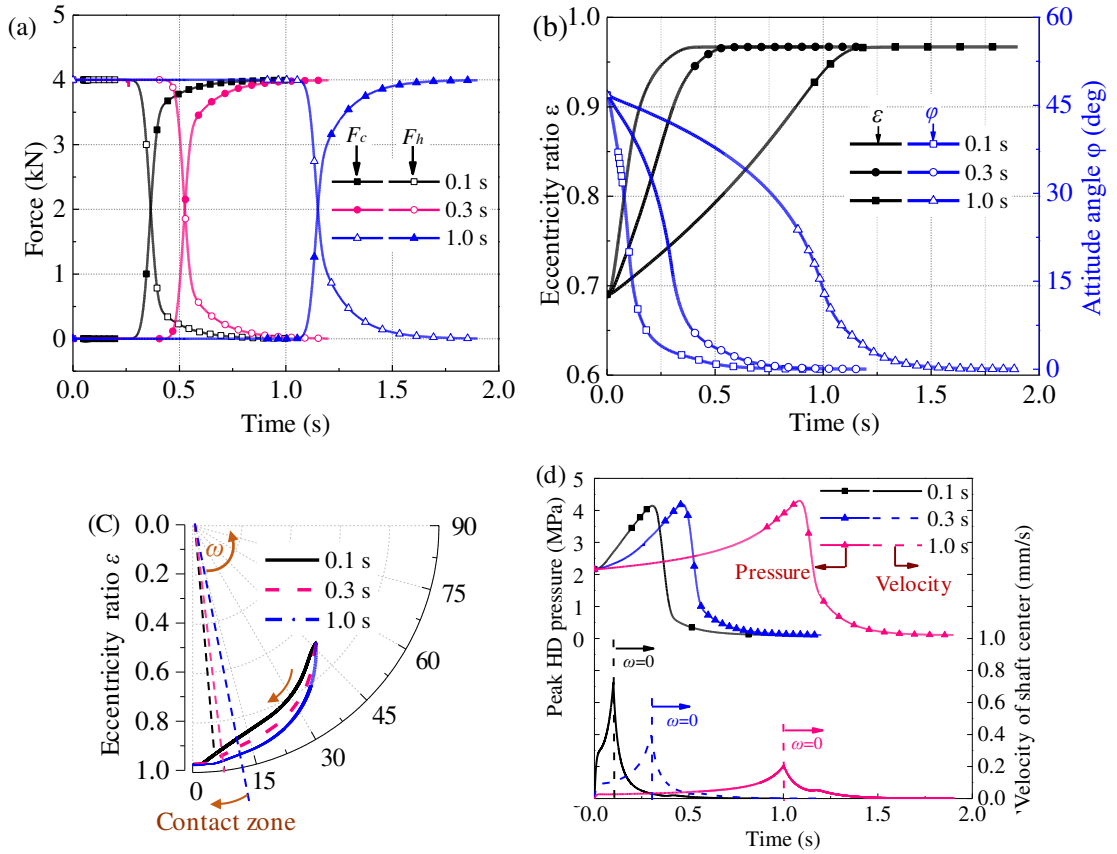


Fig. 2-22 Influence of deceleration on transient parameters, (a) HD force and contact force, (b) eccentricity ratio and attitude angle, (c) shaft center locus and (d) contact zone

Fig. 2-23 shows the influence of deceleration on contact and wear behavior during shutdown. The shaft speed decelerates from 1000 rpm to zero in the deceleration time. When the deceleration time climbs up to 10 s, the surface contact occurs at 9.268 s and maximum HD pressure appears at t_{pmax}=9.268 s which are before the time of the shaft speed decreasing to zero as shown in Fig. 2-23(a). In this case, the squeeze effect of the film is weak, and the shaft will slide along the bush surface for a while then roll to the standstill position. The contact zone and volume wear increase with

the decrease in deceleration, and the contact zone and the volume wear will be as large as 20.48° and 1.415×10^{-4} mm^3 at the deceleration time of 10 s. This indicates that when the deceleration time is long, i.e. the deceleration is small, the contact zone and volume wear during shutdown can be in the same order with that during startup, so the wear cannot be neglected during shutdown in this case.

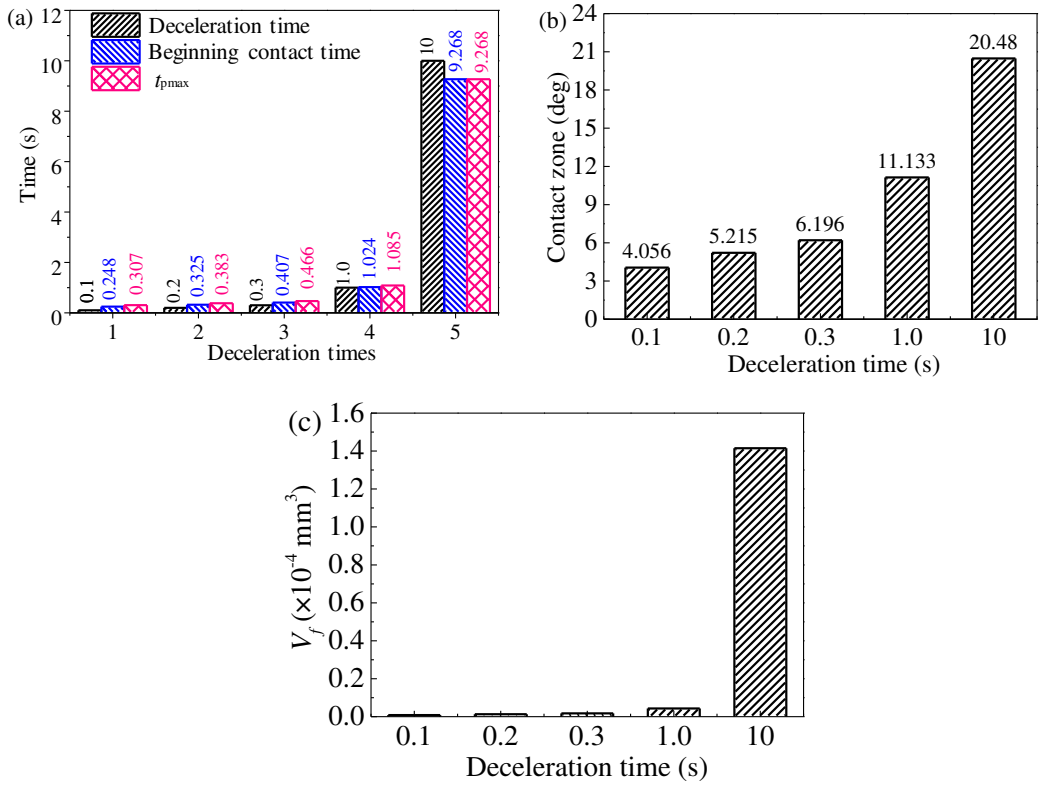


Fig. 2-23 Influence of deceleration on (a) contact time, (b) contact zone and (c) volume wear V_f during shutdown

2.7 Conclusions

In this chapter, a transient mixed lubrication model considering both hydrodynamic pressure and surface asperity contact of the loaded journal bearing during startup and shutdown is established. The contact behavior of the shaft-bush surface is presented. The effect of surface roughness, relative clearance and acceleration/deceleration on the contact and wear behavior during startup and shutdown are discussed. The main conclusions are as follows:

In the same conditions, the contact zone during startup can be more than 8 times of that during shutdown, and the volume wear (in the order of 10^{-4} mm^3) can reach 10^3 times of that during shutdown. Contact and wear mainly occur in the initial stage of the startup process. During startup, the smooth surface and the large relative clearance are beneficial to reduce the contact zone and volume wear. During

shutdown, the smooth surface and the small relative clearance are helpful.

The effects of acceleration/deceleration on the startup/shutdown contact behavior are quite obvious. During startup, the contact zone is small in low acceleration, but there exists an optimal acceleration that can minimize the volume wear. During shutdown, the low deceleration results in the large contact zone and volume wear. When the deceleration is low enough, the shaft will slide along the bush surface and then roll to the standstill position. Meanwhile, the contact zone and volume wear will be in the same order with that during startup. When the deceleration is high enough, the contact occurs after the shaft speed drops to zero, and the shaft will purely roll to the standstill position where the wear usually appears.

Chapter 3 Thermoelastohydrodynamic model of partly coated journal bearings considering wall slip

3.1 Introduction

Compared to metal bush, the PTFE coated bush surface owns low surface energy and non-sticky property, wall slip is easier to occur for heavy-load and high-speed journal bearings. The heat conductivity of PTFE coating is much lower than that of metals, which results in high temperature of the film. In this chapter, a thermoelastohydrodynamic (TEHD) model considering wall slip (TEHDS) is built to analyze the effects of partial coating (slip) zone on the TEHD behavior of journal bearings. A two-component slip model is applied to calculate the slip velocity. The model is solved by finite element method to obtain the temperatures of the film, coating, interlayer and basement. The influence of coating parameters on the thermal behavior is discussed.

3.2 Geometry model

Fig. 3-1 shows a partial slip zone of the partly coated journal bearings in nondimensional and cylindrical coordinates. An interlayer is used to enhance the bonding force between the coating and basement. Because the slip occurs at the film-coating interface, the slip zone is consistent with the coating zone at the bush surface. In Fig. 3-1c), Θ is the fixed coordinate system, θ is the dynamic coordinate system, and $\theta=\Theta-\varphi$, where φ is the attitude angle. The oil inlet groove is located at $\Theta=0$, and the groove angle is A_{Groove}.

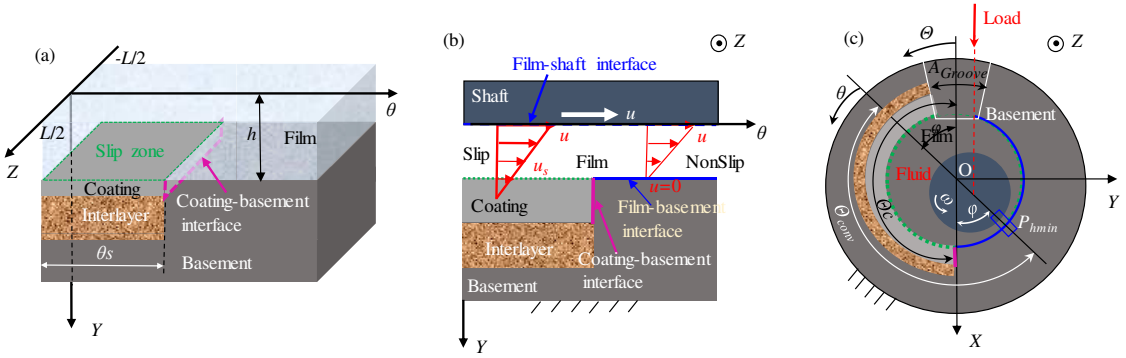


Fig. 3-1. (a) Coating, interlayer and basement, (b) structure at middle plane and (c) coordinate system of the coated journal bearings considering partial wall slip

3.3 Governing equations of the fluid

3.3.1 Generalized Reynolds equation considering slip

In the model, the lubricant is assumed to be an uncompressible Newtonian fluid under laminar flow. The viscosity change of the lubricants across the film thickness is necessary to be considered in thermal case. Therefore, the generalized Reynolds equation containing the items of slip velocity is applied as

$$\begin{aligned}&\frac{\partial}{R_s^2\partial\theta}\left(\Phi_\theta F_2\frac{\partial p}{\partial\theta}\right)+\frac{\partial}{\partial z}\left(\Phi_z F_2\frac{\partial p}{\partial z}\right)=\Phi_c\frac{\partial}{R_s\partial\theta}\left[\frac{F_1}{F_0}\left(u_0+u_s\right)\right]+\\&\Phi_c\frac{\partial}{\partial z}\left[\frac{F_1}{F_0}w_s\right]+\sigma\frac{\partial\left[\Phi_s\left(u_0+u_s\right)\right]}{R_s\partial\theta}+\sigma\frac{\partial\left[\Phi_s\left(w_s\right)\right]}{\partial z}+\xi^+p^-\end{aligned}\tag{3-1}$$

where $u=u_s$ and $w=w_s$, u_s and w_s are the slip velocities at the film-coating interface. At the film-shaft interface, $u=u_0$ and $w=w_0$, and u_0 is the velocity of the shaft surface. ξ^+ is a penalty item which is to control cavitation. This approach meets the Reynolds' boundary conditions (BCs) and thus the conservation of mass flow rate [110]. ξ^+ is an infinite positive number and $p^-=\min(p, 0)$ corresponds to the negative part of the HD pressure. σ is the standard deviation of asperity height that is set to be 1.0 μm. Other parameters are the same with that in Eq.(2-5). The others are

$$F_0=\int_0^{h(\theta,z)}\frac{\mathrm{d}y}{\mu(y)},\quad F_1=\int_0^{h(\theta,z)}\frac{y\mathrm{d}y}{\mu(y)},\quad F_2=\int_0^{h(\theta,z)}\frac{y\left(y-y_m\right)\mathrm{d}y}{\mu(y)},\quad y_m=\frac{F_1}{F_0}$$

where y is the coordinate in film thickness direction, $0\le y\le h(\theta)$. The film thickness can be expressed by

$$h(\theta)=C\left(1+\varepsilon\cos\theta\right)+\delta^m(\theta)+\delta_b^T(\theta)-\delta_s^T(\theta)\tag{3-2}$$

where δ^m and δ_b^T are the mechanical and thermal deformations of the bush surface, δ_s^T is the shaft thermal expansion which decreases the film thickness.

The nondimensional parameters of Reynolds equation are

$$\overline{z}=\frac{z}{L},(-0.5\le\overline{z}\le0.5),\quad \overline{y}=\frac{y}{h},(0\le\overline{y}\le1),\quad H=\frac{h}{C},\quad \psi=\frac{C}{R_s},\quad \frac{p}{P}=\frac{\mu_0\omega_0}{\psi^2}=\frac{\mu_0\omega_0}{(C/R)^2},$$

$$\overline{\sigma}=\frac{\sigma}{C},\quad U=\frac{u}{R_s\omega_0},\quad U_s=\frac{u_s}{R_s\omega_0},\quad W_s=\frac{w_s}{R_s\omega_0},\quad \overline{F_0}=\frac{F_0}{CH/\mu_0}=\int_0^1\frac{\mathrm{d}\overline{y}}{\overline{\mu}(\overline{y})},$$

$$\overline{F_1}=\frac{F_1}{C^2H^2/\mu_0}=\int_0^1\frac{\overline{y}\mathrm{d}\overline{y}}{\overline{\mu}},\quad y_m=\frac{F_1}{F_0}=CH\frac{\overline{F}_1}{\overline{F}_0},\ \overline{y}_m=\frac{y_m}{CH}=\frac{\overline{F}_1}{\overline{F}_0},$$

$$\overline{F_2}=\frac{F_2}{C^3H^3/\mu_0}=\int_0^1\frac{\overline{y}\left(\overline{y}-\overline{y}_m\right)\mathrm{d}\overline{y}}{\overline{\mu}\left(y\right)}\ 。$$

The nondimensional form of Eq.(3-1) is

$$\begin{aligned}&\frac{\partial}{\partial\theta}\left(\Phi_\theta H^3\overline{F_2}\frac{\partial P}{\partial\theta}\right)+\frac{R_s^2}{L^2}\frac{\partial}{\partial\overline{z}}\left(\Phi_z H^3\overline{F_2}\frac{\partial P}{\partial\overline{z}}\right)=\Phi_c\frac{\partial}{\partial\theta}\left[H\frac{\overline{F_1}}{\overline{F_2}}\left(U_0+U_s\right)\right]\\&+\frac{\sigma}{C}\frac{\partial\left[\left(U_0+U_s\right)\Phi_s\right]}{\partial\theta}+\frac{\sigma}{C}\frac{\partial\left(W_s\Phi_s\right)}{\partial z}+\frac{R^2}{C^3}\xi^+P^-\end{aligned}\tag{3-3}$$

Eq.(3-3) is solved by finite element method (FEM) which is the same with that in Section 2.2.5. The matrix elements of Eq.(2-30) are

$$\begin{cases}k_{ij}=\underset{\text{Gauss}}{\mathbf{I}}\left\{\left(\Phi_\theta H^3\overline{F_2}\frac{\partial\Re_i}{\partial\theta}\frac{\partial\Re_j}{\partial\theta}\right)+\frac{R_s^2}{L^2}\left(\Phi_z H^3\overline{F_2}\frac{\partial\Re_i}{\partial\overline{z}}\frac{\partial\Re_j}{\partial\overline{z}}\right)+\xi^+\Re_i^-\Re_j^-\right\}\\R_i=-\underset{\text{Gauss}}{\mathbf{I}}\left\{\begin{aligned}&\left(\Phi_\theta H^3\overline{F_2}\frac{\partial P_0}{\partial\theta}\frac{\partial\Re_i}{\partial\theta}\right)+\frac{R_s^2}{L^2}\left(\Phi_z H^3\overline{F_2}\frac{\partial P_0}{\partial\overline{z}}\frac{\partial\Re_i}{\partial\overline{z}}\right)+\Phi_c\frac{\partial}{\partial\theta}\left[H\frac{\overline{F_1}}{\overline{F_2}}\left(U_0+U_s\right)\right]\Re_i\\&+\frac{\sigma}{C}\frac{\partial\left[\left(U_0+U_s\right)\Phi_s\right]}{\partial\theta}\Re_i+\frac{\sigma}{C}\frac{\partial\left(W_s\Phi_s\right)}{\partial\overline{z}}\Re_i+\frac{R^2}{C^3}\xi^+\Re_i^-P_0^-\end{aligned}\right.\end{cases}\tag{3-4}$$

3.3.2 Film velocity

In order to solve the film temperature, the film velocity needs to be solved first. *u*, *v* and *w* are the film velocities in the circumferential direction *x*, the film thickness direction *y* and the axial direction *z* respectively. As shown in Fig. 3-2, mechanical analysis of the fluid microcell is

$$p\mathrm{d}y\mathrm{d}z+\left(\tau+\frac{\partial\tau}{\partial y}\mathrm{d}y\right)\mathrm{d}x\mathrm{d}z=\left(p+\frac{\partial p}{\partial x}\mathrm{d}x\right)\mathrm{d}y\mathrm{d}z+\tau\mathrm{d}x\mathrm{d}z\tag{3-5}$$

Then it can be gotten

$$\frac{\partial p}{\partial x}=\frac{\partial\tau}{\partial y}\tag{3-6}$$

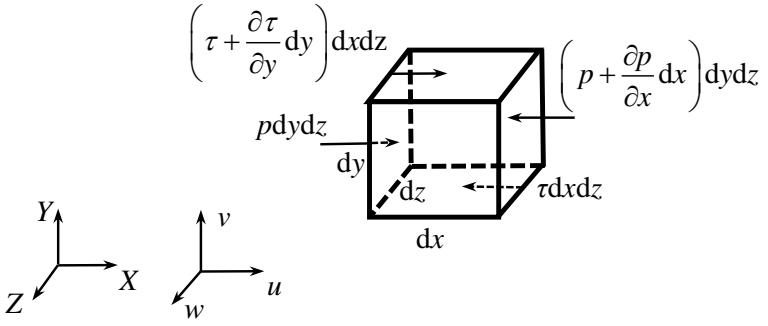


Fig. 3-2 The mechanical analysis of the fluid microcell

Combined with Newton's law of viscosity $\tau=\mu\frac{\partial u}{\partial y}$, it can be obtained

$$\frac{\partial p}{\partial x}=\frac{\partial}{\partial y}\left(\mu\frac{\partial u}{\partial y}\right) \tag{3-7}$$

Assuming that the HD pressure is constant in the film thickness direction, it can be obtained

$$\frac{\partial p}{\partial z}=\frac{\partial}{\partial y}\left(\mu\frac{\partial w}{\partial y}\right),\quad \frac{\partial p}{\partial y}=0 \tag{3-8}$$

The fluid continuity equation is

$$\frac{\partial u}{\partial x}+\frac{\partial v}{\partial y}+\frac{\partial w}{\partial z}=0 \tag{3-9}$$

Since the bush is fixed and only the slip at film-coating interface is considered, the boundary condition of the film velocity at film-shaft interface is: $u(h)=u_0$, $v(h)=v_0=0$ and $w(h)=w_0=0$, and at film-bush interface is: $u(0)=u_s$, $v(0)=0$ and $w(0)=w_s$. Integrating Eq.(3-7) and Eq.(3-8) twice in film thickness direction (y direction) and combining Eq.(3-9), the film velocity in x, y and z directions can be gotten as

$$\begin{cases} u=\dfrac{\partial p}{\partial x}\left(I-\dfrac{I_2 J}{J_2}\right)+\dfrac{u_0-u_s}{J_2}J+u_s \\ v=-\displaystyle\int_0^y\left(\frac{\partial u}{\partial\theta}+\frac{\partial w}{\partial z}\right)\mathrm{d}y \\ w=\dfrac{\partial p}{\partial z}\left(I-\dfrac{I_2 J}{J_2}\right)+\dfrac{w_0-w_s}{J_2}J+w_s \end{cases} \tag{3-10}$$

where $I=\int_0^y \frac{\varsigma}{\mu}\mathrm{d}\varsigma$, $J=\int_0^y \frac{1}{\mu}\mathrm{d}\varsigma$, $I_2=\int_0^h \frac{y}{\mu}\mathrm{d}y=\frac{C^2H^2}{\mu_0}\int_0^1 \frac{\bar{y}}{\bar{\mu}}\mathrm{d}\bar{y}=\frac{C^2H^2}{\mu_0}\bar{I}_2$,

$J_2=\int_0^h \frac{1}{\mu}\mathrm{d}y=\frac{CH}{\mu_0}\int_0^1 \frac{1}{\bar{\mu}}\mathrm{d}\bar{y}=\frac{CH}{\mu_0}\bar{J}_2$。

The nondimensional parameters are the same with Eq.(3-1), so the nondimensional film velocity is

$$\begin{cases}\bar{u}=H^2\dfrac{\partial P}{\partial\theta}\left(\bar{I}-\dfrac{\bar{I}_2}{\bar{J}_2}\bar{J}\right)+\dfrac{U_1-U_s}{J_2}\bar{J}+U_s\\ \bar{v}=-\dfrac{CH}{R_s}\displaystyle\int_0^{\bar{y}}\left(\frac{\partial\bar{u}}{\partial\theta^*}+\frac{R_s}{L}\frac{\partial\bar{w}}{\partial\bar{z}}\right)\mathrm{d}\varsigma\\ \bar{w}=\dfrac{R_s}{L}H^2\dfrac{\partial P}{\partial\bar{z}}\left(\bar{I}-\dfrac{\bar{I}_2}{\bar{J}_2}\bar{J}\right)+\dfrac{-W_s}{J_2}\bar{J}+W_s\end{cases}\tag{3-11}$$

where $\bar{I}=\int_0^{\bar{y}}\frac{\varsigma}{\bar{\mu}}\mathrm{d}\varsigma$, $\bar{J}=\int_0^{\bar{y}}\frac{1}{\bar{\mu}}\mathrm{d}\varsigma$, $\bar{I}_2=\int_0^1\frac{\bar{y}}{\bar{\mu}}\mathrm{d}\bar{y}$, $\bar{J}_2=\int_0^1\frac{1}{\bar{\mu}}\mathrm{d}\bar{y}$, $\frac{\partial}{\partial\theta^*}=\frac{\partial}{\partial\theta}-\frac{\varsigma}{H}\frac{\mathrm{d}H}{\mathrm{d}\theta}\frac{\partial}{\partial\bar{y}}$.

The boundary condition of the film velocity in film thickness direction is $\bar{v}(0)=\bar{v}(1)=0$ which should be imposed. The second order differential of velocity $\bar{v}$ is

$$\frac{\partial^2\bar{v}}{\partial\bar{y}^2}=-\frac{CH}{R_s}\frac{\partial}{\partial\bar{y}}\left(\frac{\partial\bar{u}}{\partial\theta}-\frac{\bar{y}}{H}\frac{\partial H}{\partial\theta}\frac{\partial\bar{u}}{\partial\bar{y}}+\frac{R_s}{L}\frac{\partial\bar{w}}{\partial\bar{z}}\right)\tag{3-12}$$

Eq.(3-12) can be calculated by finite difference method. The second order differential of velocity $\bar{v}$ can also be expressed by

$$\frac{\partial^2\bar{v}}{\partial\bar{y}^2}=\frac{\bar{v}(i,j+1)-2\bar{v}(i,j)+\bar{v}(i,j-1)}{\Delta\bar{y}^2}\tag{3-13}$$

where i is the *ith* node number of the element in film thickness direction; j is the *jth* node number of the element circumferential direction; Δy is the node distance along film thickness direction.

Based on Eq.(3-12) and Eq.(3-13) the velocity of the node (i, j) can be gotten

$$\bar{v}(i,j)=\left[\frac{CH}{R_s}\frac{\partial}{\partial\bar{y}}\left(\frac{\partial\bar{u}}{\partial\theta}-\frac{\bar{y}}{H}\frac{\partial H}{\partial\theta}\frac{\partial\bar{u}}{\partial\bar{y}}+\frac{R_s}{L}\frac{\partial\bar{w}}{\partial\bar{z}}\right)\Delta\bar{y}^2+\bar{v}(i,j-1)+\bar{v}(i,j+1)\right]\Big/2\tag{3-14}$$

3.3.3 Wall slip velocity

Two-component slip model [66] considering bosh slip length and critical shear stress is used to calculate the wall slip velocity. The shear stress is expressed by

$$\tau_c = \tau_{co} + \frac{\mu}{b} u_s \tag{3-15}$$

where τ_{co} is the critical shear stress at which wall slip occurs. b is the slip length. The wall slip begins when the fluid-solid shear stress is larger than the critical shear stress of τ_{co}. Then slip velocity u_s increases linearly with the increasing shear stress at a constant slip length of b.

Integrating Eq.(3-6) along film thickness direction, and submitting the boundary condition of $\tau=\tau_c$ at $y=0$, it can be obtained

$$\tau = \frac{\partial p}{\partial x} y + \tau_c \tag{3-16}$$

Combined with Newton's law of viscosity $\tau = \mu \frac{\partial u}{\partial y}$, it can be obtained

$$\frac{\partial u}{\partial y} = \frac{1}{\mu} \frac{\partial p}{\partial x} y + \frac{\tau_c}{\mu} \tag{3-17}$$

Integrating Eq.(3-17) in film thickness direction, the velocity in circumferential direction can be deduced as

$$u = u\left(y=0\right) + \frac{\partial p}{\partial x} \int_0^y \frac{\varsigma}{\mu} \mathrm{d}\varsigma + \tau_c \int_0^y \frac{1}{\mu} \mathrm{d}\varsigma = u_s + \frac{\partial p}{\partial x} I + \tau_c J \tag{3-18}$$

where $I = \int_0^y \frac{\varsigma}{\mu} \mathrm{d}\varsigma$, $J = \int_0^y \frac{1}{\mu} \mathrm{d}\varsigma$.

The boundary condition at film-bush interface of $y=h$ is $u=u_0$, $I=I_2$ and $J=J_2$. And submitting them to Eq.(3-18), the slip velocity at film-bush interface is calculated as

$$u_s = u_0 - \frac{\partial p}{\partial x} I_2 - \tau_c J_2 \tag{3-19}$$

Similarly, the slip velocity in axial direction at film-coating interface can be deduced as

$$w_s = w_0 - \frac{\partial p}{\partial z} I_2 - \tau_c J_2 \tag{3-20}$$

The nondimensional forms of Eq.(3-19) and Eq.(3-20) are

$$\begin{cases} \bar{u}_s = \bar{u}_0 - H^2 \dfrac{\partial P}{\partial \theta} \bar{I}_2 - \bar{\tau}_c H \bar{J}_2 \\ \bar{w}_s = \bar{w}_0 - \dfrac{R_s}{L} H^2 \dfrac{\partial P}{\partial \bar{z}} I_2 - \bar{\tau}_c H \bar{J}_2 \end{cases} \tag{3-21}$$

where $\tau_c = \tau_0 \bar{\tau}_c$, $\tau_0 = \dfrac{\mu_0 R_s \omega_0}{C}$, μ_0 is the oil viscosity at initial temperature, ω_0 is the rotational speed of the shaft, $\bar{u}_s = \dfrac{u_s}{R_s \omega_0}$, $\bar{w}_s = \dfrac{w_s}{R_s \omega_0}$, $I_2 = \dfrac{C^2 H^2}{\mu_0} \bar{I}_2$, $J_2 = \dfrac{CH}{\mu_0} \bar{J}_2$. Then the nondimensional form of Eq.(3-15) is

$$\bar{\tau}_c = \bar{\tau}_{c0} + \frac{\bar{\mu}}{\bar{b}} \bar{u}_s \tag{3-22}$$

Submitting Eq.(3-22) to Eq.(3-21), it can be gotten

$$\begin{cases} \bar{u}_s = \left(\bar{u}_0 - H^2 \dfrac{\partial P}{\partial \theta} \bar{I}_2 - \operatorname{sgn}\left(\bar{u}_s\right) \left|\bar{\tau}_{c0}\right| H \bar{J}_2 \right) \Big/ \left(1 + H \bar{J}_2 \dfrac{\bar{\mu}}{\bar{b}} \right) \\ \bar{w}_s = \left(\bar{w}_0 - \dfrac{R_s}{L} H^2 \dfrac{\partial P}{\partial \bar{z}} I_2 - \operatorname{sgn}\left(\bar{w}_s\right) \left|\bar{\tau}_{c0}\right| H \bar{J}_2 \right) \Big/ \left(1 + H \bar{J}_2 \dfrac{\bar{\mu}}{\bar{b}} \right) \end{cases} \tag{3-23}$$

where sgn(u_s) is the sign function for sgn(u_s>0)=1, sgn(u_s<0)=-1 and sgn(u_s=0)=0.

As shown in Eq.(3-23), the slip velocity is directly influenced by the gradient of hydrodynamic pressure dp/dx, the film thickness h, the critical shear stress τ_{co} and the slip length b.

The shear stress always has a tendency to hinder the fluid flowing on the solid surface, so if the slip velocity is opposite to the speed of solid surface, τ_c will be positive, otherwise it will be negative. Therefore, for $\bar{u}_s > 0$ or $\bar{u}_s < 0$, slip occurs in circumferential direction as shown in(3-24); for $\bar{w}_s > 0$ or $\bar{w}_s < 0$, slip occurs in axial direction as shown in (3-25).

$$\begin{cases} \dfrac{\partial P}{\partial \theta} < \left(\bar{u}_0 - \bar{\tau}_{c0} H \bar{J}_2 \right) \Big/ \left(H^2 \bar{I}_2 \right), & if \quad \bar{u}_s > 0 \\ \dfrac{\partial P}{\partial \theta} = \bar{u}_0 \Big/ \left(H^2 I_2 \right), & if \quad \bar{u}_s < 0 \\ \dfrac{\partial P}{\partial \theta} < \left(\bar{u}_0 + \bar{\tau}_{c0} H \bar{J}_2 \right) \Big/ \left(H^2 \bar{I}_2 \right), & if \quad \bar{u}_s < 0 \end{cases} \tag{3-24}$$

$$\begin{cases} \dfrac{\partial P}{\partial \bar{z}} < \left(\bar{w}_0 - \bar{\tau}_{c0} H \bar{J}_2\right) \Big/ \left(\dfrac{R_s}{L} H^2 I_2\right), & if\ \bar{w}_s > 0 \\ \bar{w}_s = 0, \quad \dfrac{\partial P}{\partial \bar{z}} = \bar{w}_0 \Big/ \left(\dfrac{R_s}{L} H^2 I_2\right), & if\ \bar{w}_s = 0 \\ \dfrac{\partial P}{\partial \bar{z}} < \left(\bar{w}_0 + \bar{\tau}_{c0} H \bar{J}_2\right) \Big/ \left(\dfrac{R_s}{L} H^2 I_2\right), & if\ \bar{w}_s > 0 \end{cases} \tag{3-25}$$

3.4 Governing equation of temperature

3.4.1 Governing equation of film temperature

The two-dimensional (2D) energy equation is used to calculate the film temperature

$$\rho_f C_f \left(u \frac{\partial T_f}{\partial x} + v \frac{\partial T_f}{\partial y}\right) = k_f \left(\frac{\partial T_f}{\partial y}\right)^2 + \mu \left(\frac{\partial u}{\partial y}\right)^2 \tag{3-26}$$

where ρ_f, C_f and k_f are the film density, specific heat and thermal conductivity respectively. v is the fluid velocity in the film thickness direction.

The nondimensional parameters are set to be $\bar{T} = T/T_0$, $\bar{\mu} = \mu/\mu_0$, $\bar{y} = \dfrac{y}{h} = \dfrac{y}{CH}$, $\left(0 \le \bar{y} \le 1\right)$. The others are the same with that in Reynolds equation. The differential operators to x, y and z are

$$\frac{\partial}{\partial x} = \frac{1}{R_s}\frac{\partial}{\partial \theta} - \frac{1}{R_s}\frac{\bar{y}}{H}\frac{\partial H}{\partial \theta}\frac{\partial}{\partial \bar{y}}, \quad \frac{\partial}{\partial y} = \frac{1}{CH}\frac{\partial}{\partial \bar{y}}, \quad \frac{\partial}{\partial z} = \frac{1}{L}\frac{\partial}{\partial \bar{z}} \tag{3-27}$$

Submitting Eq.(3-27) to Eq.(3-26) the nondimensional form of energy equation is

$$Pe\left\{\bar{u}\frac{\partial \bar{T}_f}{\partial \theta} + \left(\bar{v}\frac{R_s}{CH} - \bar{u}\frac{\bar{y}}{H}\frac{\partial H}{\partial \theta}\right)\frac{\partial \bar{T}_f}{\partial \bar{y}}\right\} = \frac{1}{H^2}\left(\frac{\partial^2 T_f}{\partial \bar{y}^2}\right) + N_d \frac{\bar{\mu}}{H^2}\left(\frac{\partial \bar{u}}{\partial \bar{y}}\right)^2 \tag{3-28}$$

where $Pe = \dfrac{\rho_f C_f \omega_0 C^2}{k_f}, N_d = \dfrac{\omega_0 R_s^2 \mu_0}{T_0 k_f}$。

The viscosity-temperature relationship is given by

$$\mu(T) = \mu_0 \exp\left(-\beta\left(T - T_0\right)\right) \tag{3-29}$$

where η_0 is the viscosity at T=T_0 and β is the thermoviscosity coefficient.

Film properties in the rupture zone are managed using the method proposed by Ref.[111]. The thermal properties in rupture zone are obtained by

$$\Phi(\theta, y) = \alpha_l \Phi_L(\theta, y) + \alpha_g \Phi_G(\theta, y) \tag{3-30}$$

where the coefficient $\alpha_l = h_{\text{rup}}/h(\theta)$ represents the proportion of the liquid; $\alpha_g = 1-\alpha_l$ represents the proportion of the gas; h_{rup} is the film thickness at the critical position of the film rupture zone, and $h(\theta)$ is the film thickness in the rupture zone. $\Phi(\theta,y)$ represents the film properties, including thermal conductivity k_f, viscosity η, specific heat c_f, and density ρ_f. The subscripts L and G represent the liquid and gas phases, respectively.

3.4.2 Governing equation of bush

The coated bearing bush includes coating, interlayer and basement. The 2D heat conduction equation is used to solve the bush temperature. The equation in the polar coordinate system is expressed as

$$0 = k\left(\frac{\partial^2 T}{\partial r^2} + \frac{1}{r}\frac{\partial T}{\partial r} + \frac{1}{r^2}\frac{\partial^2 T}{\partial \theta^2}\right) \tag{3-31}$$

The nondimensional parameters are set to be $T = T_0\overline{T}$ and $r = R_s\overline{r}$. In radial direction, the ranges of the coating, interlayer and basement are $\left(1 \le \overline{r} \le \frac{R_c}{R_s}\right)$, $\left(\frac{R_c}{R_s} \le \overline{r} \le \frac{R_i}{R_s}\right)$, and $\left(\frac{R_i}{R_s} \le \overline{r} \le \frac{R_o}{R_s}\right)$ respectively. And the nondimensional form of Eq.(3-31) is

$$0 = \left(\frac{\partial^2 \overline{T}}{\partial \overline{r}^2} + \frac{1}{\overline{r}}\frac{\partial \overline{T}}{\partial \overline{r}} + \frac{1}{\overline{r}^2}\frac{\partial^2 \overline{T}}{\partial \theta^2}\right) \tag{3-32}$$

Similarly, the weighted residual formulation of Eq. (3-32) can be deduced by the same method with section 2.2.5.

$$\iint_{\Omega_e}\left[\frac{\partial \overline{T}}{\partial \overline{r}}\frac{\partial \Re}{\partial \overline{r}} + \frac{1}{\overline{r}^2}\frac{\partial \overline{T}}{\partial \theta}\frac{\partial \Re}{\partial \theta} - \frac{1}{\overline{r}}\frac{\partial \overline{T}}{\partial \overline{r}}\Re\right]\mathrm{d}\Omega_e - \oint_{\partial\Gamma_e} -\frac{\partial \overline{T}}{\partial \overline{r}}\Re\mathrm{d}\theta + \frac{1}{\overline{r}^2}\frac{\partial \overline{T}}{\partial \theta}\Re\mathrm{d}\overline{r} = 0 \tag{3-33}$$

Then the weak formulation of the heat conduction equation can be yielded by Galerkin method as

$$\begin{cases} K_e = \iint_{\Omega_e} \left[\dfrac{\partial \Re^{\mathrm{T}}}{\partial \overline{r}} \dfrac{\partial \Re}{\partial \overline{r}} + \dfrac{1}{\overline{r}^2} \dfrac{\partial \Re^{\mathrm{T}}}{\partial \theta} \dfrac{\partial \Re}{\partial \theta} - \dfrac{1}{\overline{r}} \dfrac{\partial \Re^{\mathrm{T}}}{\partial \overline{r}} \Re \right] \mathrm{d}\Omega_e \\ \qquad - \oint_{\partial \Gamma_e} \dfrac{1}{\overline{r}^2} \dfrac{\partial \Re^{\mathrm{T}}}{\partial \theta} \Re \mathrm{d}\overline{r} - \dfrac{\partial \Re^{\mathrm{T}}}{\partial \overline{r}} \Re \mathrm{d}\theta \\ R_e = \iint_{\Omega_e} \left[\dfrac{\partial \Re^{\mathrm{T}}}{\partial \overline{r}} \dfrac{\partial \overline{T}_0}{\partial \overline{r}} + \dfrac{1}{\overline{r}^2} \dfrac{\partial \Re^{\mathrm{T}}}{\partial \theta} \dfrac{\partial \overline{T}_0}{\partial \theta} - \dfrac{1}{\overline{r}} \Re^{\mathrm{T}} \dfrac{\partial \overline{T}_0}{\partial \overline{r}} \right] \mathrm{d}\Omega_e \\ \qquad + \oint_{\partial \Gamma_e} \dfrac{1}{\overline{r}^2} \Re^{\mathrm{T}} \dfrac{\partial \overline{T}_0}{\partial \theta} \mathrm{d}\overline{r} - \Re^{\mathrm{T}} \dfrac{\partial \overline{T}_0}{\partial \overline{r}} \mathrm{d}\theta \end{cases} \tag{3-34}$$

3.4.3 Boundary conditions for temperature calculation

Because of rotation of shaft, the temperature of the shaft surface is assumed to be uniform, i.e. the boundary condition (BC) at film-shaft interface is set to be

$$\int_{\theta_I}^{\theta_o} \left. \frac{\partial T_f}{\partial y} \right|_{y=h} \mathrm{d}\theta = 0, \qquad T_f\left(y=h\right) = T_J\left(t\right) \tag{3-35}$$

where θ_I is the angle at inlet, θ_o is the angle at outlet, T_J is the temperature of shaft surface, and T_f is the film temperature.

Heat flux continuity BC is imposed at the film-coating, coating-interlayer, interlayer-basement and coating-basement interfaces as

$$k_1 \left. \frac{\partial T_1}{\partial y} \right|_{y=y_1} = k_2 \left. \frac{\partial T_2}{\partial y} \right|_{y=y_2} \tag{3-36}$$

where k_1, k_2 and T_1, T_2 and y_1, y_2 represent the thermal conductivity, temperature and coordinate of the two parts at the interface.

The heat exchange at the oil inlet ($\theta=\theta_I$) is shown in Fig. 3-3. The oil flow at the inlet includes Q_I that enters into the bearing and Q_R that recirculates from the outlet. The temperature and flow meet the relationship

$$\begin{cases} T_I = T_R & , \quad Q_R > Q_I \\ T_I = \left(\dfrac{Q_R}{Q_I} \right) T_R + \dfrac{Q_I - Q_R}{Q_I} T_s & , \quad Q_R < Q_I \end{cases} \tag{3-37}$$

where T_I is the inlet temperature, T_R is the recirculate temperature, T_s is the feeding temperature.

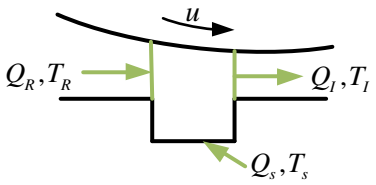


Fig. 3-3 The heat exchange in the oil groove

The inlet flow

$$Q_I = \int_{-L/2}^{L/2} \int_0^{h_{inlet}} u_{inlet} \mathrm{d}y\mathrm{d}z \tag{3-38}$$

where u_{inlet} is the film velocity at inlet, h_{inlet} is the film thickness at inlet.

Because of cavitation, the film thickness at outlet needs to be modified. Here, the flow rate at the outlet is represented by that at the film rupture position

$$Q_R = \int_{-L/2}^{L/2} \int_0^{h_{outlet}} u_{outlet} \mathrm{d}y\mathrm{d}z = \int_{-L/2}^{L/2} \int_0^{h_{rupture}} u_{rupture} \mathrm{d}y\mathrm{d}z \tag{3-39}$$

where u_{outlet} is the film velocity at outlet, and h_{outlet} is the film thickness at outlet.

The bearing bush (including coating, interlayer and basement) and the oil at the inlet and outlet meet the thermal convection boundary conditions

$$k_* \left.\frac{\partial T}{\partial \theta}\right|_{\theta=\theta_I} = H_{O^*}\left(T_*\big|_{\theta=\theta_I} - T_I\right) \text{ or } k_* \left.\frac{\partial T}{\partial \theta}\right|_{\theta=\theta_R} = H_{O^*}\left(T_I - T_*\big|_{\theta=\theta_R}\right) \tag{3-40}$$

where k_* is the thermal conductivity of bush, H_{O^*} is the heat transfer coefficient between oil and bush, T_* and T_I are the inlet oil temperature and bush temperature, and θ_R is the outlet angle.

The BC between the outside basement and atmosphere meets the heat convection BC

$$k_b \left.\frac{\partial T}{\partial r}\right|_{r=R_o} = H_{ba}\left(T\big|_{r=R_o} - T_A\right) \tag{3-41}$$

where T_A is the atmosphere temperature, H_{ba} is the heat transfer coefficient between the bush and atmosphere, k_b is the thermal conductivity of basement.

3.4.4 Deformation of the bush

The coating thickness is much smaller than the basement thickness, so mechanical displacement of the coating δ^m can be obtained by Winkler model [112] based on the

plain strain hypothesis (as shown in Eq.(3-42), neglecting the mechanical deformation of the interlayer and basement.

$$\delta^m(\theta,z)=\frac{(1+\nu_c)(1-2\nu_c)}{(1-\nu_c)}\frac{h_c}{E_c}p(\theta,z) \tag{3-42}$$

where v_c, E_c and h_c are the Poisson's ratio, elasticity modulus and thickness of the coating respectively.

The thermal deformations of the coating, interlayer and basement are not uniform, so they are solved by finite element method. The plane strain hypothesis is used. The bush is assumed to deform freely in the radial direction as shown in Fig. 3-4. The thermal load is given by

$$\{\boldsymbol{F}\}=\Delta T[1,\ 1,\ 0] \tag{3-43}$$

where ΔT is the temperature rise of the bush.

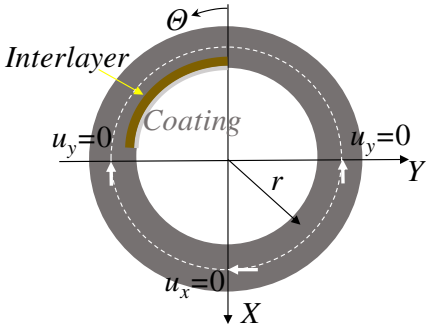


Fig. 3-4 The constrain of thermal deformation of the bush

3.5 Solution method of Finite Element Method

3.5.1 Solution of thermal deformation

Finite element method (FEM) is used to solve the thermal deformation of the bush and the plane strain hypothesis is applied. The solution domain is divided by the quadrilateral element. As shown in Fig. 3-5, the deformation of each node of the element is decomposed into θ and r directions, which are represented by δ_θ and δ_r respectively, and the corresponding thermal loads are F_θ and F_r.

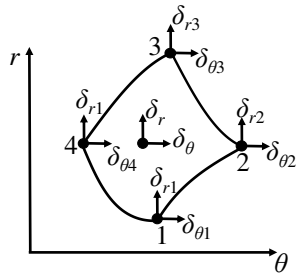


Fig. 3-5 The freedom of the element node

The deformation of the element can be yielded

$$\{\boldsymbol{\delta}\}^e = \{\delta_\theta, \delta_r\}^{\mathrm{T}} = [\mathfrak{R}_1 \ \ \mathfrak{R}_2 \ \ \mathfrak{R}_3 \ \ \mathfrak{R}_4]\{\delta_{\theta 1}, \delta_{r1}, \delta_{\theta 2}, \delta_{r2}, \delta_{\theta 3}, \delta_{r3}, \delta_{\theta 4}, \delta_{r4}\}^{\mathrm{T}} \quad (3\text{-}44)$$

where $[\mathfrak{R}_i] = \mathfrak{R}_i[I]$, $[\boldsymbol{I}] = \begin{bmatrix} 1 & 0 \\ 0 & 1 \end{bmatrix}$, $\mathfrak{R}_i$ is the shape function as shown in Eq.(2-19).

The strain matrix of the element is expressed

$$\{\varepsilon\}^{(e)} = \{\varepsilon_\theta, \varepsilon_r, \gamma_{\theta r}\}^{\mathrm{T}} = \left\{\frac{\partial \delta_\theta}{\partial \theta}, \frac{\partial \delta_r}{\partial r}, \frac{\partial \delta_\theta}{\partial r} + \frac{\partial \delta_r}{\partial \theta}\right\}^{\mathrm{T}} = [B_1 \ B_2 \ B_3 \ B_4][\boldsymbol{\delta}]^{(e)} \quad (3\text{-}45)$$

Combining Eq.(3-44), it yields

$$B_i = \begin{Bmatrix} \dfrac{\partial \mathfrak{R}_i}{\partial \theta} & 0 \\ 0 & \dfrac{\partial \mathfrak{R}_i}{\partial r} \\ \dfrac{\partial \mathfrak{R}_i}{\partial \theta} & \dfrac{\partial \mathfrak{R}_i}{\partial r} \end{Bmatrix}, \quad i = 1,2,3,4 \quad (3\text{-}46)$$

The stiffness matrix of the element is

$$\left[K_{ij}\right] = \iint_\Omega \left[B_i\right]^{\mathrm{T}} [D] \left[B_j\right] \mathrm{d}\theta \mathrm{d}r \ , \quad i, j = 1,2,3,4 \quad (3\text{-}47)$$

where [*D*] is the elastic matrix in plane strain state, and it can be expressed by

$$[\mathrm{D}] = \frac{E_*(1-\nu_*)}{(1+\nu_*)(1-2\nu_*)} \begin{bmatrix} 1 & \dfrac{\nu_*}{1-\nu_*} & 0 \\ \dfrac{\nu_*}{1-\nu_*} & 1 & 0 \\ 0 & 0 & \dfrac{1-2\nu_*}{2(1-\nu_*)} \end{bmatrix} \quad (3\text{-}48)$$

where E_* and ν_* are the elastic modulus and Poisson's ratio respectively.

Submitting Eq.(3-46) and Eq.(3-48) to Eq.(3-47), and imposed the nondimensional parameter of $r=R_o\,\overline{r}$, it yields

$$\left[K_{ij}\right]=\frac{E_*}{1-\nu_*^2}\iint_\Omega\begin{bmatrix}\dfrac{\partial\Re_i}{\partial\theta}\dfrac{\partial\Re_j}{\partial\theta}+\dfrac{1-\nu_*}{2}\dfrac{\partial\Re_i}{\partial\overline{r}}\dfrac{\partial\Re_j}{\partial\overline{r}} & \nu_*\dfrac{\partial\Re_i}{\partial\theta}\dfrac{\partial\Re_j}{\partial\overline{r}}+\dfrac{1-\nu_*}{2}\dfrac{\partial\Re_i}{\partial\overline{r}}\dfrac{\partial\Re_j}{\partial\theta}\\ \nu_*\dfrac{\partial\Re_i}{\partial\theta}\dfrac{\partial\Re_j}{\partial\overline{r}}+\dfrac{1-\nu_*}{2}\dfrac{\partial\Re_i}{\partial\overline{r}}\dfrac{\partial\Re_j}{\partial\theta} & \dfrac{\partial\Re_i}{\partial\overline{r}}\dfrac{\partial\Re_j}{\partial\overline{r}}+\dfrac{1-\nu_*}{2}\dfrac{\partial\Re_i}{\partial\theta}\dfrac{\partial\Re_j}{\partial\theta}\end{bmatrix}\mathrm{d}\theta\mathrm{d}\overline{r}\quad(3\text{-}49)$$

And transforming Eq. (3-49) to the isoperimetric coordinate system, it gets

$$\left[K_{ij}\right]=\int_{-1}^{1}\int_{-1}^{1}\begin{bmatrix}g_{11}^{ij} & g_{12}^{ij}\\ g_{21}^{ij} & g_{22}^{ij}\end{bmatrix}\det\boldsymbol{J}\mathrm{d}\xi\mathrm{d}\eta=\begin{bmatrix}k_{11}^{ij} & k_{12}^{ij}\\ k_{21}^{ij} & k_{22}^{ij}\end{bmatrix}\quad(3\text{-}50)$$

where det$\boldsymbol{J}$ is the determinant of Jacobian matrix $\boldsymbol{J}$ that can be obtained by the method in 2.2.5 as

$$\det\boldsymbol{J}=\left(\sum_{i=1}^{4}\frac{\partial\Re_i}{\partial\xi}\theta_i\cdot\sum_{i=1}^{4}\frac{\partial\Re_i}{\partial\eta}\overline{r}_i\right)-\left(\sum_{i=1}^{4}\frac{\partial\Re_i}{\partial\xi}\theta_i\cdot\sum_{i=1}^{4}\frac{\partial\Re_i}{\partial\eta}\overline{r}_i\right)$$

Then the Gaussian integral method can be applied to Eq.(3-50) as

$$\begin{cases}k_{11}^{ij}=\dfrac{E_*}{1-\nu_*^2}\displaystyle\sum_{m=1}^{2}\sum_{n=1}^{2}\left(\frac{\partial\Re_i}{\partial\theta}\frac{\partial\Re_j}{\partial\theta}+\frac{1-\nu_*}{2}\frac{\partial\Re_i}{\partial\overline{r}}\frac{\partial\Re_j}{\partial\overline{r}}\right)\det\boldsymbol{J}\cdot w_m w_n\\ k_{12}^{ij}=\dfrac{E_*}{1-\nu_*^2}\displaystyle\sum_{m=1}^{2}\sum_{n=1}^{2}\left(\nu_*\frac{\partial\Re_i}{\partial\theta}\frac{\partial\Re_j}{\partial\overline{r}}+\frac{1-\nu_*}{2}\frac{\partial\Re_i}{\partial\overline{r}}\frac{\partial\Re_j}{\partial\theta}\right)\det\boldsymbol{J}\cdot w_m w_n\\ k_{21}^{ij}=\dfrac{E_*}{1-\nu_*^2}\displaystyle\sum_{m=1}^{2}\sum_{n=1}^{2}\left(\nu_*\frac{\partial\Re_i}{\partial\overline{r}}\frac{\partial\Re_j}{\partial\theta}+\frac{1-\nu_*}{2}\frac{\partial\Re_i}{\partial\theta}\frac{\partial\Re_j}{\partial\overline{r}}\right)\det\boldsymbol{J}\cdot w_m w_n\\ k_{22}^{ij}=\dfrac{E_*}{1-\nu_*^2}\displaystyle\sum_{m=1}^{2}\sum_{n=1}^{2}\left(\frac{\partial\Re_i}{\partial\overline{r}}\frac{\partial\Re_j}{\partial\overline{r}}+\frac{1-\nu_*}{2}\frac{\partial\Re_i}{\partial\theta}\frac{\partial\Re_j}{\partial\theta}\right)\det\boldsymbol{J}\cdot w_m w_n\end{cases},\quad i,j=1,2,3,4\qquad(3\text{-}51)$$

The thermal load can be expressed as

$$\{F\}^e=\iint_\Omega[B]^T[D]\varepsilon_0\mathrm{d}\theta\mathrm{d}r\quad(3\text{-}52)$$

where ε_0 is the strain before imposing the thermal load, $\{\varepsilon_0\}=(1+\nu)\alpha_T\Delta T[1,1,0]^{\mathrm{T}}$, α_T is thermal expansion coefficient, ΔT is temperature rise.

Combining Eq.(3-46) and Eq.(3-48), it yields

$$\begin{cases}F_\theta^{ie}=\dfrac{E_*\alpha_T T_0}{1-\nu_*^2}\displaystyle\int_{-1}^{1}\int_{-1}^{1}\left(\frac{\partial\Re_i}{\partial\theta}+\nu_*\frac{\partial\Re_i}{\partial\theta}\right)\Delta\overline{T}_i\det\boldsymbol{J}\mathrm{d}\xi\mathrm{d}\eta=\dfrac{E_*\alpha_T T_0}{1-\nu_*}\displaystyle\sum_{m=1}^{2}\sum_{n=1}^{2}\frac{\partial\Re_i}{\partial\theta}\Delta\overline{T}_i\det\boldsymbol{J}\cdot w_m w_n\\ F_r^{ie}=\dfrac{E_*\alpha_T T_0}{1-\nu_*^2}\displaystyle\int_{-1}^{1}\int_{-1}^{1}\left(\nu_*\frac{\partial\Re_i}{\partial\overline{r}}+\frac{\partial\Re_i}{\partial\overline{r}}\right)\Delta\overline{T}_i\det\boldsymbol{J}\mathrm{d}\xi\mathrm{d}\eta=\dfrac{E_*\alpha_T T_0}{1-\nu_*}\displaystyle\sum_{m=1}^{2}\sum_{n=1}^{2}\frac{\partial\Re_i}{\partial\overline{r}}\Delta\overline{T}_i\det\boldsymbol{J}\cdot w_m w_n\end{cases}\qquad(3\text{-}53)$$

Based on Eq.(3-51) and Eq.(3-53), the thermal deformation equation of the element of $[K]^e\{\delta\}^e=\{F\}^e_{8\times1}$ can be obtained. By imposing the displacement constraints, the thermal deformation of the bush can be calculated.

3.5.2 Up-wind FEM for the solution of film temperature

Since the energy equation contains a convection term which causes oscillate when the shape function of Eq.(2-19) is applied, the upwind FEM is used to solve this problem [113].

The effect of the convection term can be evaluated by Peclet number of P_e

$$P_e=\frac{\rho_f C_f u_{ij} L^e_{ij}}{2k_f} \tag{3-54}$$

where u_{ij} is the film velocity at the edge containing node *i and node j*, L^e_{ij} is the edge length containing node *i* and node *j*, ρ_f is the fluid density, and C_f is the specific heat of the fluid.

Taking the shape function of the upwind FEM [114] as the weight function which can be expressed as

$$W_i=\Re_i+\alpha_i F_i \tag{3-55}$$

where F_i is the function of upwind FEM, α_i is upwind parameter. $\Re_i$ is the shape function, and the one dimensional form is

$$\Re_i(\xi)=\frac{1}{2}(1+\xi_i\xi),\quad \Re_i(\eta)=\frac{1}{2}(1+\eta_i\eta) \text{ where } i=1,2 \tag{3-56}$$

where ξ_i=1,-1 and η_i=-1, 1.

The one-dimensional function of upwind FEM is

$$F_i(\xi)=\frac{3}{4}\xi_i(1-\xi^2),\quad F_i(\eta)=\frac{3}{4}\eta_i(1-\eta^2),\quad i=1,2,3,4 \tag{3-57}$$

Therefore, the one-dimensional weight functions in ξ and η directions are

$$\begin{cases} W_i(\xi)=\frac{1}{2}(1+\xi_i\xi)+\alpha_i\cdot\frac{3}{4}\xi_i(1-\xi^2) \\ W_i(\eta)=\frac{1}{2}(1+\eta_i\eta)+\beta_i\cdot\frac{3}{4}\eta_i(1-\eta^2) \end{cases} \tag{3-58}$$

where the upwind parameters α_i and β_i in ξ and η directions can be expressed as

$$\begin{cases} \alpha_i = \coth\left(\dfrac{\gamma_{\theta i}}{2}\right) - \dfrac{2}{\gamma_{\theta i}}, \quad \gamma_{\theta i} = \dfrac{u_{\theta i} L^e_{\theta i}}{k_f} = R_s^2 \omega_0 \dfrac{\overline{u}_i \overline{L}^e_{\theta i}}{k_f} \\ \beta_i = \coth\left(\dfrac{\gamma_{yi}}{2}\right) - \dfrac{2}{\gamma_{yi}}, \quad \gamma_{yi} = \dfrac{v_{yi} L^e_{yi}}{k_f} = R_s \omega_0 CH \dfrac{\overline{v}_i \overline{L}^e_{yi}}{k_f} \end{cases} \tag{3-59}$$

where $L^e_{\theta i}, L^e_{yi}, \overline{L}^e_{\theta i}, \overline{L}^e_{yi}$ are the lengths of the element edges including ith node, $u_{\theta i}$, $v_{yi}, \overline{u}_i, \overline{v}_i$ are the dimensional and nondimensional film velocities. The subscripts of θ and y represent in θ and y directions.

The two-dimensional weight function can be gotten as [115]

$$W_i(\xi,\eta) = W_i(\xi) \cdot W_i(\eta), \quad i = 1,2,3,4 \tag{3-60}$$

Submitting Eq.(3-58) to Eq.(3-60), it yields

$$\begin{cases} W_i(\xi,\eta) = \dfrac{1}{4}\left[(1+\xi_i\xi) + \alpha_i\xi_i \cdot \dfrac{3}{2}(1-\xi^2)\right] \cdot \left[(1+\eta_i\eta) + \beta_i\eta_i \cdot \dfrac{3}{2}(1-\eta^2)\right] \\ \dfrac{\mathrm{d}W_i(\xi,\eta)}{\mathrm{d}\xi} = \dfrac{1}{4}\xi_i(1-3\alpha_i\xi) \cdot \left[(1+\eta_i\eta) + \beta_i\eta_i \cdot \dfrac{3}{2}(1-\eta^2)\right] \\ \dfrac{\mathrm{d}W_i(\xi,\eta)}{\mathrm{d}\eta} = \dfrac{1}{4}\eta_i(1-3\beta_i\eta) \cdot \left[(1+\xi_i\xi) + \alpha_i\xi_i \cdot \dfrac{3}{2}(1-\xi^2)\right] \end{cases} \tag{3-61}$$

The nondimensional temperature can be linearized based on the first-order Taylor expansion

$$\overline{T}_f = \overline{T}_{f0} + \mathrm{d}\overline{T}_f, \ \nabla\overline{T}_f = \nabla\overline{T}_{f0} + \nabla\mathrm{d}\overline{T}_f \tag{3-62}$$

where $\overline{T}_{f0}$ is the calculated temperature in the previous step, $\mathrm{d}\overline{T}_f$ is the temperature increase, and ∇ is the differential operator.

Applying the same process in section 2.2.5, the weak formulation of the matrix equations can be deduced by Galerkin method. The matrix coefficients of weak formulation of generalized Reynolds equation are

$$\begin{cases} K_e = \iint_{\Omega_e} \left\{ Pe \cdot W^{\mathrm{T}} \left[\bar{u} \dfrac{\partial W}{\partial \theta} + \left(\bar{v} \dfrac{R_s}{CH} - \bar{u} \dfrac{\bar{y}}{H} \dfrac{\partial H}{\partial \theta} \right) \dfrac{\partial W}{\partial \bar{y}} \right] + \dfrac{1}{H^2} \dfrac{\partial W^{\mathrm{T}}}{\partial \bar{y}} \dfrac{\partial W}{\partial \bar{y}} \right\} \mathrm{d}\Omega_e \\ \qquad + \oint_{\partial \Gamma_e} \dfrac{1}{H^2} W^{\mathrm{T}} \dfrac{\partial W}{\partial \bar{y}} \mathrm{d}\theta \\ R_e = -\iint_{\Omega_e} \left[Pe \cdot W^{\mathrm{T}} \left(\bar{u} \dfrac{\partial \bar{T}_{f0}}{\partial \theta} + M \dfrac{\partial \bar{T}_{f0}}{\partial \bar{y}} \right) + \dfrac{1}{H^2} \dfrac{\partial W^{\mathrm{T}}}{\partial \bar{y}} \dfrac{\partial \bar{T}_{f0}}{\partial \bar{y}} \right] \mathrm{d}\Omega_e \\ \qquad + \iint_{\Omega_e} \left(N_d \dfrac{\bar{\mu}}{H^2} \left(\dfrac{\partial \bar{u}}{\partial \bar{y}} \right)^2 \right) W^{\mathrm{T}} \mathrm{d}\Omega_e - \oint_{\partial \Gamma_e} \dfrac{1}{H^2} W^{\mathrm{T}} \dfrac{\partial \bar{T}_{f0}}{\partial \bar{y}} \mathrm{d}\theta \end{cases} \tag{3-63}$$

3.5.3 Solution procedure

Fig. 3-6 shows the flow chart of the solution procedure. The general process is

1. The generalized Reynolds equation, Eq.(3-1), is solved to obtain the pressure distribution. The fluid velocity across the film thickness and the slip velocity in Eq.(3-23) at the film-coating interface are then calculated.

2. The temperatures of the film, bush (coating, interlayer and basement), and shaft are obtained by solving Eq.(3-26) and Eq.(3-31) combined with the thermal BCs. The film viscosity and mechanical and thermal deformations are then calculated.

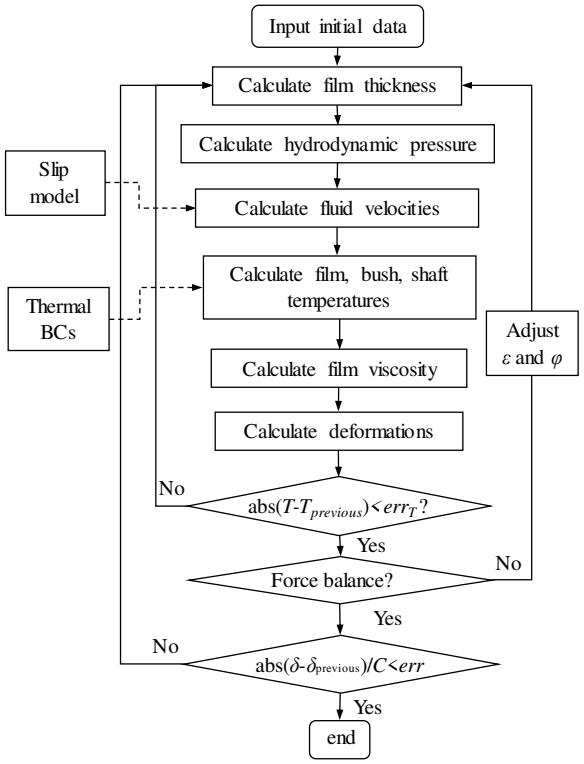


Fig. 3-6 Flow chart of the calculation procedure

Steps 1 and 2 are repeated until the temperature deviation is less than the imposed error err_T, which is set to be 2×10^{-5}.

3. Steps 1 to 3 are repeated until the hydrodynamic (HD) force is balanced with the applied load by adjusting the eccentricity ratio ε and attitude angle φ.

4. Both the mechanical and thermal deformations should be convergent by repeating the steps 1 to 4. The convergence errors of the mechanical and thermal deformations are respectively set to be 5×10^{-4}.

3.5.4 Model verification

As the model is complex, to the authors' knowledge, there is no relevant theoretical calculation and experimental research. Therefore, the model is separately verified.

The present slip model is validated by the data in Ref. [80] as shown in Fig. 3-7. The eccentricity ratio is ε=0.8, length to diameter ratio is L/D=1, and dimensionless critical shear stress is $\bar{\tau}_c = 2.0$. In present paper, the nondimensional slip length is set to be 0.0345. The nondimensional hydrodynamic pressure is noted as $P=p\psi^2/(2\mu\omega)$. It can be seen present results are in coincidence with that of Lv et al.

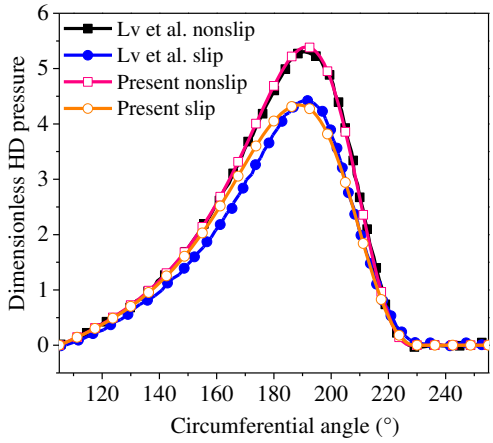


Fig. 3-7 Verification of the HD pressure distribution consider wall slip in the middle plane

In order to verify the thermal deformation of the bush containing PTFE coatings and steel basement, the validation is undertaken by considering the thermal expansion of a 2D ring, i.e. the bearing bush, modeled by ANSYS software. A uniform temperature rise of 20℃ of the bush is imposed. The other parameters of PTFE coating and steel basement are listed in Table 3-2. Thermal deformations of the inner surface of the ring (or bush) along the circumferential direction are shown in Fig. 3-8. Clearly, in both without and with a PTFE coating cases, the present results well agree with those of the ANSYS simulation.

Fig. 3-9 shows a plot of the evolution of temperature at the film-basement interface

along the circumferential direction. The simulation parameters are listed in Table 3-1 and Table 3-3. The supply oil pressure was 0.07 MPa, the shaft speed was 1600 rpm, and the applied load was 4.0 kN. In our simulation, the bush area is divided into three parts which are the coating, interlayer and basement, but the three parts are in the same material of bronze, so that our simulation conditions are the same with that in Ref.[116]. These results are in good coincidence with the experimental and simulation results of Kucinschi et al. [116].

Table 3-1 Structure parameters of the bearing

Parameter	Symbol	Value	Parameter	Symbol	Value
Shaft radius, mm	R_s	50	Radial clearance at 20℃, μm	C	123
External bearing radius, mm	R_o	100	Bush thickness, mm	h_{bush}	50
Bearing length, mm	L	80	Groove angle,°	A_{Groove}	18

Table 3-2 Properties of the coating, interlayer and basement [117]

Parameter	Coating			Interlayer	Basement
	PTFE	Graphite	DLC	Bronze	Steel
Density, kg/m^3	2200	2250	2000	8940	7850
Thermal conductivity, W/m℃	0.3	105	600	65	36
Specific heat, J/kg·℃	1200	710	970	490	486
Poisson's ratio	0.46	0.15	0.17	0.33	0.29
Elasticity modulus, GPa	0.11	25	759	120	210
Thermal expansion coefficient, ×10^{-6}	124	4.8	1.2	17	11.5
Bush/oil heat transfer coefficient, W/m^2·℃	50	700	800	700	600
Bush/air heat transfer coefficient, W/m^2·℃	-	-	-	-	100
Thickness, mm	1.0	1.0	1.0	3	46

Table 3-3 Simulation parameters

Parameter	Symbol	Value
Thermal conductivity, W/m℃	k_f, k_a, k_b, k_s	0.13, 0.026, 65, 50
Density, kg/m^3	ρ_f, ρ_a, ρ_b, ρ_s	860, 1.17, 8940, 7700
Specific heat, J/kg·℃	C_f, C_a, C_b, C_s	2000, 1006, 490, 380
Heat transfer coefficient, W/m^2·℃	H_{ba}, H_{bo}	100, 700
Poisson's ratio	v_b	0.3
Elasticity modulus, GPa	E_b	120
Fluid viscosity, Pa·s	$\eta_{30℃}$	0.05
Viscosity-temperature coefficient	β_η	0.0468
Thermal expansion coefficient, ×10^{-6}	α_T	17
Temperature, ℃	T_a, T_I	30, 30
Supply pressure, Mpa	P_s	0.07

*note: the subscripts of *f*, *a*, *b*, *s* represent *film*, *atmosphere*, *basement*, *shaft; I* represents *inlet; ba represents basement and atmosphere; bo represents basement and oil.*

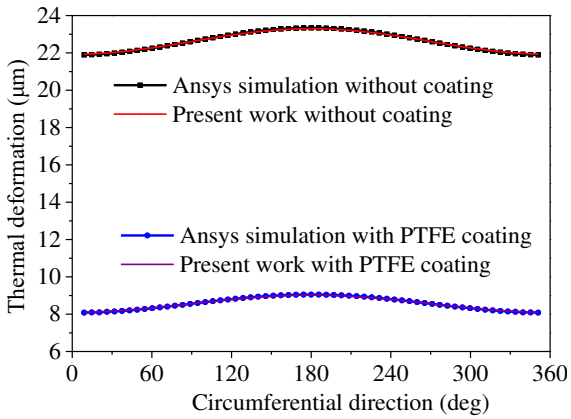


Fig. 3-8 Comparison of the thermal deformation of PTFE coating in radial direction at inner surface of bush

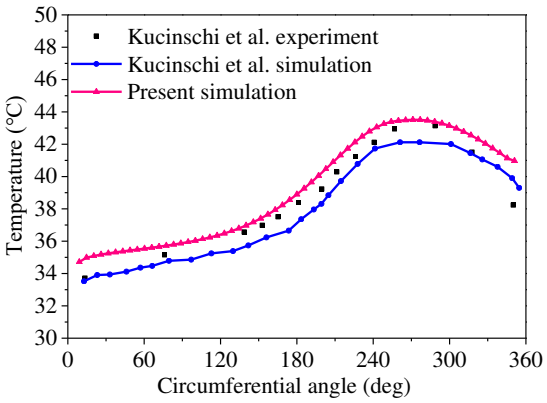


Fig. 3-9 Present result of film-bush (bronze) interface temperature compared with Kucinchi's [116]

3.6 Effect of operating conditions on thermal slip behavior

This section discusses the influence of operating conditions on the thermal slip behavior of the bearing with PTFE coating in Table 3-2. The applied load is 8.0 kN (2MPa), the shaft speed is 2k rpm. The reduction in maximum temperature ($\triangle T_{max}$) and the increase in minimum film thickness ($\triangle h_{min}$) are respectively calculated by $\triangle T_{max}=(T_{nonslip}-T_{slip})/T_{nonslip}*100\%$ and $\triangle h_{min}=-(h_{min_nonslip}-h_{min_slip})/h_{min_nonslip}*100\%$. The subscripts *slip* and *nonslip* mean the parameters calculated with and without wall slip. If the percentages are positive, it means wall slip is beneficial to decrease T_{max} and increase HD force.

3.6.1 TEHDS behavior in different relative clearances

Fig. 3-10 shows the influence of relative clearance on the maximum temperature T_{max} and minimum film thickness h_{min}. The radial clearances are set to be 100 μm, 123 μm, 145 μm and 168 μm at the initial temperature of 20℃, corresponding to relative clearances of 2.0‰, 2.5‰, 2.9‰ and 3.4‰. T_{max} decreases with the increase in relative clearance (Fig. 3-10 (a)). This is because the large relative clearance results in the increase in inlet flow rate, which can take away more heat (Fig. 3-10 (d)). As the relative clearance increases, $\triangle T_{max}$ slightly increases. When the relative clearance rises from 2.0‰ to 3.4‰, $\triangle T_{max}$ increases from 5.27% to 5.98%. Fig. 3-10 (b) shows that the h_{min} increases firstly to the maximum value at 2.9‰, in which the slip effect is most negative with $\triangle h_{min}$ reaching -2.84% (1.22 μm). Fig. 3-11 shows that the relative clearance has little influence on the temperature distribution of the film-bush (coating, interlayer and basement) area.

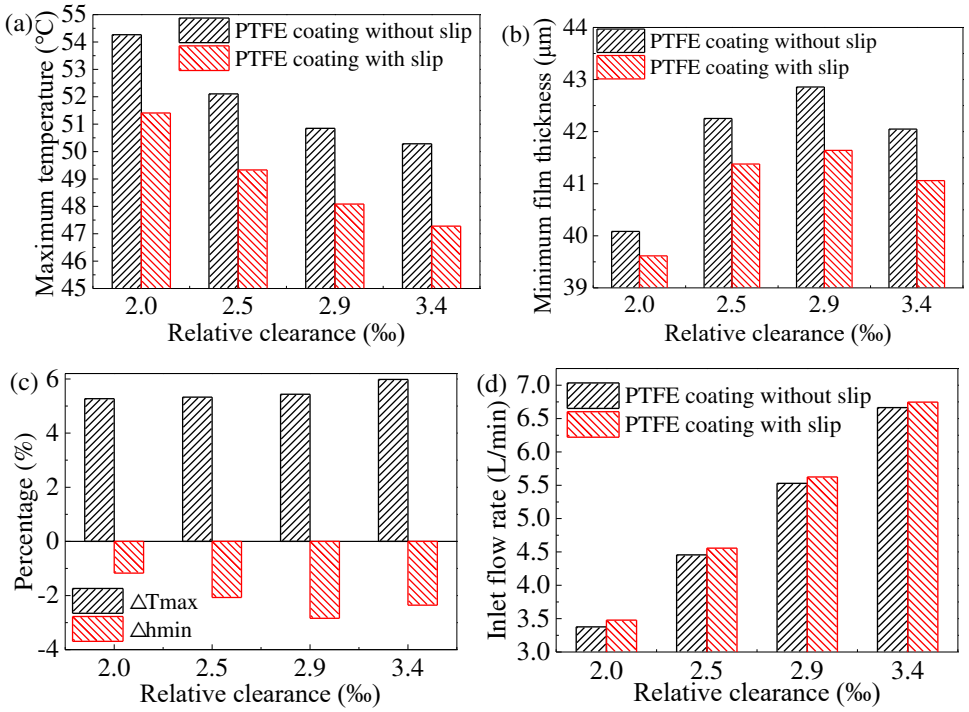


Fig. 3-10 Influence of relative clearance on (a) T_{max}, (b) h_{min}, (c) $\triangle T_{max}$ and $\triangle h_{min}$ and (d) inlet flow rate

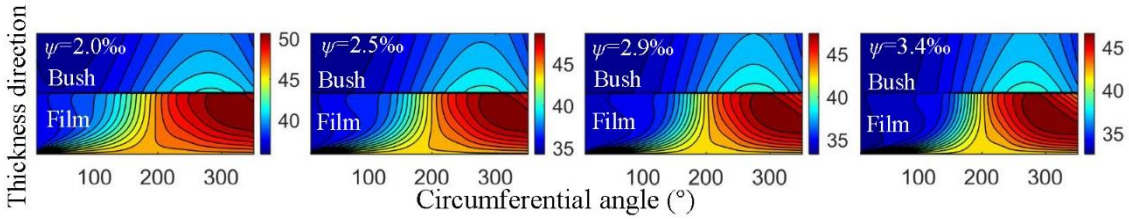


Fig. 3-11 Influence of relative clearance on temperature distribution in TEHDS regime

Fig. 3-12 shows the influence of relative clearance on the deformations of the PTFE coating in radial direction in TEHDS regime. In Fig. 3-12(a), the maximum mechanical deformation increases with the elevated relative clearance. Compared with 2.0‰, the maximum mechanical deformation of 3.4‰ rises by 0.81 μm, which

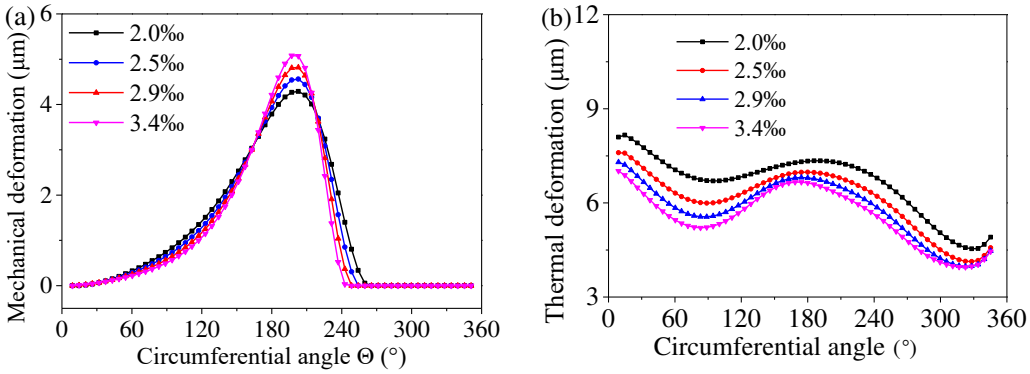


Fig. 3-12 Influence of relative clearance on (a) mechanical deformation and (b) thermal deformation of the coating in radial direction

is caused by the maximum HD pressure. Fig. 3-12(b) shows that the thermal deformation reduces with the increase in the relative clearance, which is due to the lower temperature under the larger relative clearance.

3.6.2 TEHDS behavior in different feeding temperatures

Fig. 3-13 shows the influence of the feeding temperature on the maximum temperature T_{max} and minimum film thickness h_{min}. When the feeding temperature increases from 20°C to 50°C, T_{max} increases by about 10°C, and h_{min} decreases by 14.6 μm as shown in Fig. 3-13(a) and (b). $\triangle T_{max}$ caused by wall slip decreases from 7% (3.1℃) to 4.5% (2.5℃), which indicates the slip effect becomes weaken (Fig. 3-13(c)). This is because the temperature rise caused by high feeding temperature is more obvious than the temperature reduction caused by wall slip. With the increase in feeding temperature, $\triangle h_{min}$ caused by wall slip becomes more significant. As the feeding temperature claims up to 50℃, $\triangle h_{min}$ decreases to -7.15%. Because in high feeding temperature, h_{min} is small which results in the obvious effect of the wall slip. In total, the feeding temperature should not be too high, otherwise the HD force would be weaken significantly.

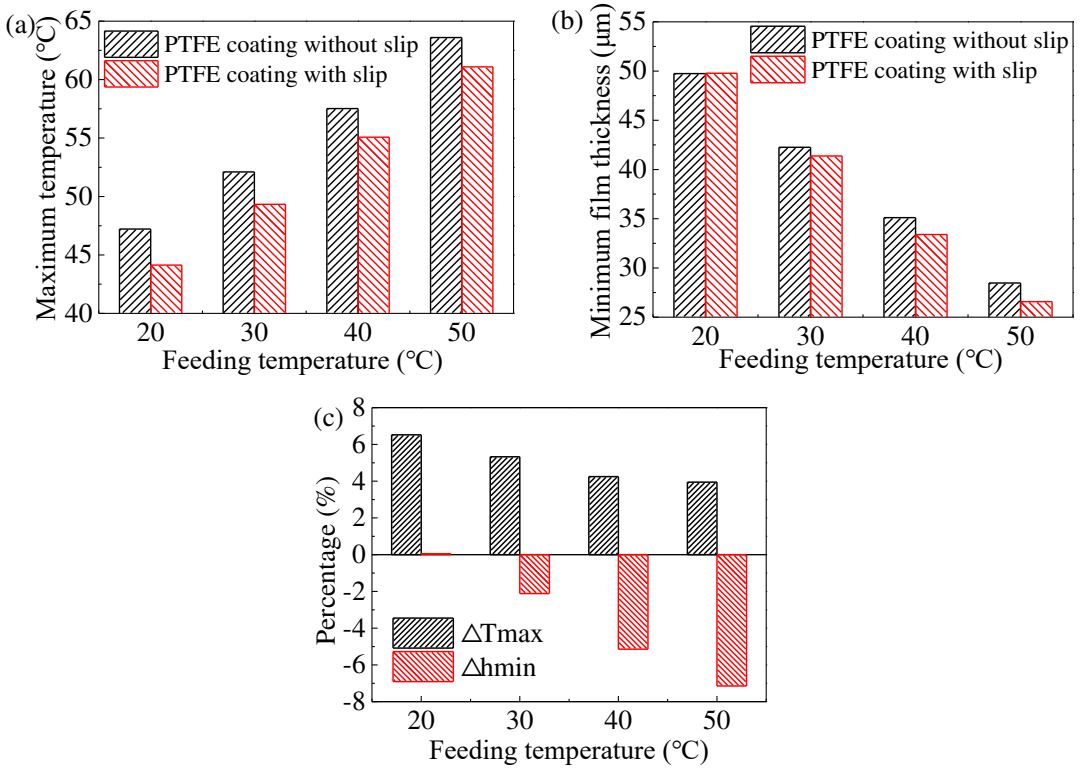


Fig. 3-13 Influence of inlet temperature on (a) T_{max}, (b) h_{min} (c) $\triangle T_{max}$ and $\triangle h_{min}$

Fig. 3-14 shows the influence of feeding temperature on deformations of the PTFE coating in radial direction in TEHDS regime. When the feeding temperature increases

from 20°C to 50°C, the maximum mechanical deformation increases by about 0.6 μm (13.3%, Fig. 3-14(a)); the average thermal deformation of the coating rises by about 5.6 μm (Fig. 3-14(b)), but the thermal expansion of the shaft increases by about 19 μm (Fig. 3-14 (c)). The mechanical deformation and thermal deformation of the coating are much smaller than the thermal expansion of the shaft, which results in the reduce in h_{min} in Fig. 3-13(b). Because of thermal insulation properties of the PTFE coating, the heat is prevented to transfer to the basement (Fig. 3-15), leading to a high T_{max} and a significant thermal expansion of the shaft.

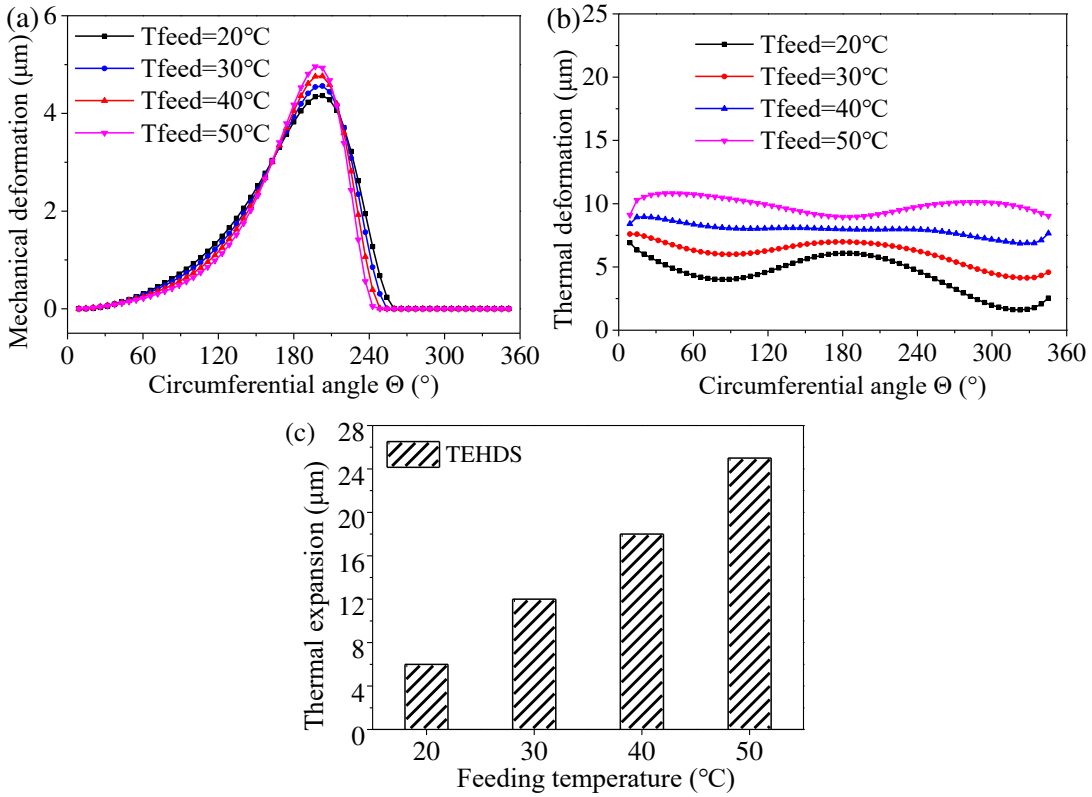


Fig. 3-14 Influence of feeding temperature on (a) mechanical and (b) thermal deformation of coating deformations in radial direction and (c) thermal expansion of shaft

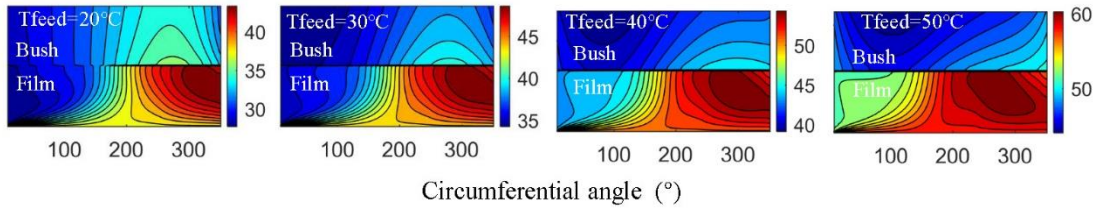


Fig. 3-15 Influence of feeding temperature on temperature distribution in TEHDS regime

3.6.3 TEHDS behavior in different shaft speeds

Fig. 3-16 shows the effect of shaft speed on the maximum temperature T_{max} and minimum film thickness h_{min}. As the shaft speed rises, both T_{max} and h_{min} increase.

Wall slip would further decrease the T_{max}, i.e. $\triangle T_{max}$ is large, in high speed, which means the slip effect on reducing T_{max} is more obvious. This is because with the increase in shaft speed, the shear stress is large, leading to the large slip velocity. At low speed (1k rpm), the slip results in a decrease in h_{min} (about -6.5%). However, at high speed (6k rpm) the slip causes an increase in h_{min} (about 3.8%) as shown Fig. 3-16(c). This is because the reduction of the temperature caused by slip effect can decrease the thermal deformation.

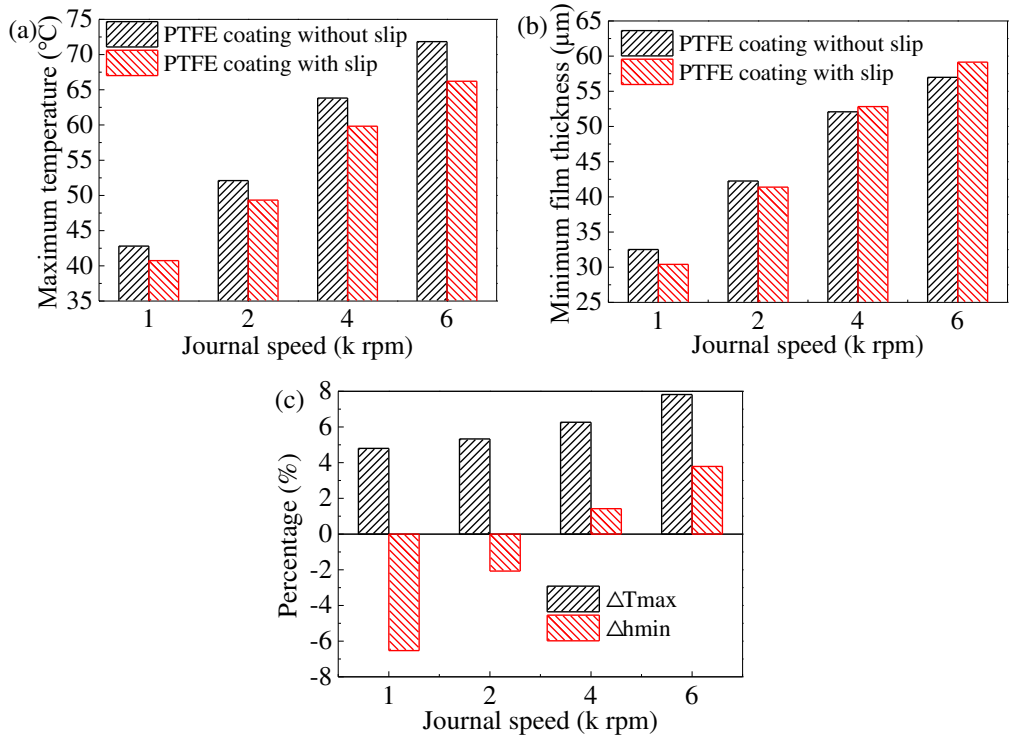


Fig. 3-16 Influence of shaft speed on (a) maximum temperature, (b) minimum film thickness and (c) $\triangle T_{max}$ and $\triangle h_{min}$

Fig. 3-17 shows the influence of shaft speed on deformations in TEHDS regime. When the shaft speed increases from 1k rpm to 6k rpm, the maximum mechanical deformation of coating decreases by about 1 μm. The average thermal deformation of coating increases by about 3.3 μm, which is three times of the mechanical deformation. Meanwhile the thermal deformation of the shaft increases by 10 μm (Fig. 3-17(c)), which is about three times of the coating deformation. Therefore, thermal deformation at high speed reduces h_{min} (Fig. 3-16(b)), but h_{min} still increase significantly due to large HD force caused by high speed. Therefore, it is necessary to comprehensively consider the effect of thermal deformation on the reduction of h_{min} and the effect of high shaft speed on the increase of hmin to determine whether the bearing seizures or not. Fig. 3-18 shows in high shaft speed the maximum temperature zone moves to the trailing edge (outlet) of the bearing.

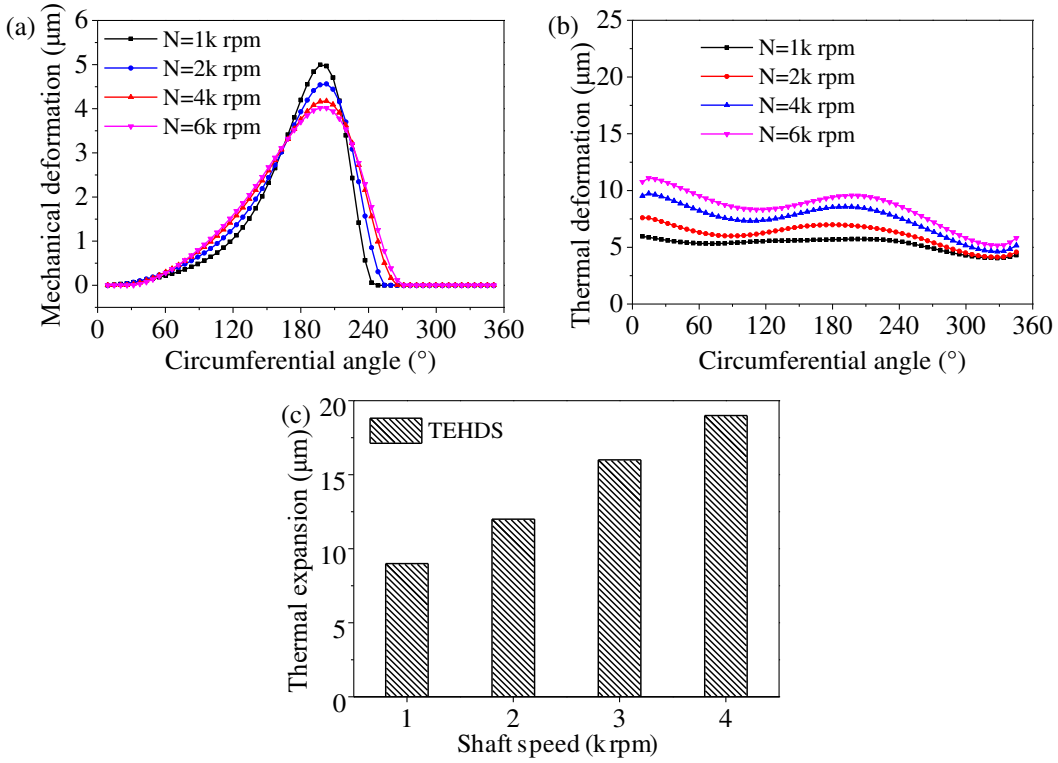


Fig. 3-17 Influence of shaft speed on (a) mechanical and (b) thermal deformations of the coating in radial direction and (c) shaft expansion in TEHDS regime

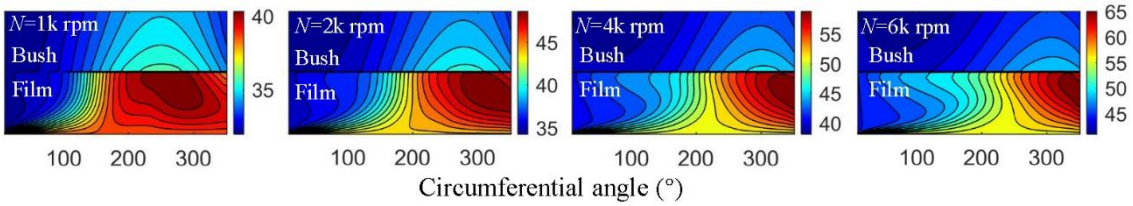


Fig. 3-18 Influence of shaft speed on temperature distribution in TEHDS regime

3.7 Conclusions

In this chapter, based on the two-component slip model, a thermoelasto-hydrodynamic (TEHD) model of coated bearings considering wall slip effect is established (TEHDS) to obtain the slip velocity distribution at film-coating interface and the temperature distribution of the film-bush (coating, interlayer, basement) area.

The thermal deformation of the bush is solved by finite element method (FEM) based on Galerkin method. The upwind FEM is applied to solve the oscillation problem caused by the convection term of the energy equation. The model is verified by the published experimental and ANSYS results.

In large relative clearance and shaft speed, the effect of wall slip on the reduction of maximum temperature is more obvious. In high speed, wall slip can even be helpful to increase the minimum film thickness. There is an relative clearance at which the wall slip would largest decrease on the minimum film thickness. In high

feeding temperature, wall slip can further decrease the minimum film thickness.

Chapter 4 Coating zone optimization and thermal slip behavior of the coated journal bearings

4.1 Introduction

The effect of slip zone on journal bearings is influenced by amounts of factors. This chapter optimizes the partial wall slip zone in high eccentricity ratios (heavy loads) by control variable method. Firstly, the optimal slip zone in isothermal cases is obtained, and then impose the selected zone to the case of constant heavy load, and obtain the selection criteria of the slip position. By analyzing the thermal slip behavior of PTFE coatings, the slip zone (coating zone) that is conducive to reducing maximum temperature and raising minimum film thickness is determined. Finally, the influence of operating conditions and coating parameters on the thermal properties is analyzed.

4.2 Geometry model

Fig. 4-1 shows the coating (slip) zone at bush surface which is symmetrical about the bearing midplane. In order to shape the slip zone, we define three coefficients:

$$\alpha=\theta_s/\theta_{hmin}\ (0\leq \alpha \leq 2),\ \lambda=L_1/L_{s1}\ (0\leq \lambda),\ \gamma=L_{s1}/L\ (0\leq \gamma \leq 1)$$

where $\theta_s=\Theta_c-\varphi$ is the length of the slip zone from θ=0° to the tailing end of the zone as shown in Fig. 3-1(c); Θ_c is the length of slip zone from Θ=0° to the tailing end of the zone; $\theta_{h\min}$ is the length from the attitude angle φ to the position of minimum film thickness $h_{\min}$, i.e. $\theta_{h\min}$=180°. α<1 and α>1 indicate that the slip zone respectively locates at the convergent region and divergent region of the film. L_{s1} and L_1 are the front width and tailing end width of the slip zone respectively. λ>1 means the tailing end width is larger than the front width.

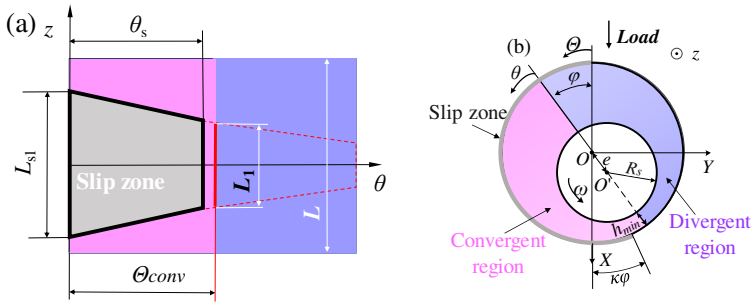


Fig. 4-1. Coating (slip) zone at bush surface (a) unfolded drawing and (b) section view

4.3 Optimization of slip (coating) zone in isothermal case

The hydrodynamic (HD) force gain is calculated by $F_G=(F_{h_slip}-F_{h_nonslip})/F_{h_nonslip}\times100\%$. The reduction in friction coefficient is calculated by $f_D=-(f_{slip}-f_{nonslip})/f_{nonslip}\times100\%$. The decrease in friction torque is calculated by $T_D=-(T_{f_slip}-T_{f_noslip})/T_{f_noslip}\times100\%$. The subscripts *slip* and *nonslip* mean the parameters calculated with and without the wall slip. These parameters are used as the evaluation criteria of the bearing performance. The positive percentage means the positive effect of the slip zone. In this section, the dynamic coordinate system θ-rz in Fig. 4-1 is used for simplification, so the attitude angle is always 0°. The used parameters of simulation are listed in Table 4-1.

Table 4-1 Parameters of simulation

Parameters	Values	Parameters	Values
Shaft radius R, mm	50	Viscosity at 40℃ η, Pa·s	0.0277
Bearing length L, mm	80	Dimensionless critical shear stress $\bar{\tau}$	0.28
Length to diameter ratio, L/D	0.8	Wall slip length b, μm	10
Radial clearance C, μm	145	Supply pressure p_s, MPa	P_s=0
Shaft speed N, rpm	4000		

The effect of wall slip in axial direction in different slip zones is shown in Fig. 4-2. The maximum slip velocity W_s in axial direction occurs at both axial ends. When the tailing end width of the slip zone is small, i.e. with a small λ, the slip velocity W_s in axial direction is quite small that can be neglected. With an increase in λ, the maximum W_s increases which results in the large leakage flow rate. Meanwhile, the circumferential slip velocity U_s acts in a larger area. The negative effect of W_s can be

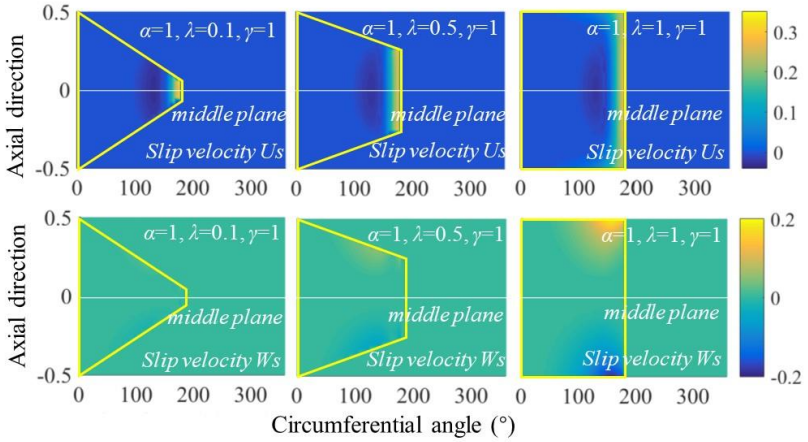


Fig. 4-2 The slip zone and the nondimensional slip velocities in circumferential direction U_s and axial direction W_s at ε=0.9

offset by the positive effect of U_s, and the effect of W_s is still small. Therefore, the influence of slip velocity in axial direction is not considered in this simulation.

4.3.1 Effect of eccentricity ratio ε on the slip behavior

Fig. 4-3 shows the effect of eccentricity ratio ε on the hydrodynamic behavior. The slip zone coefficients are chosen as α=0.85, λ=0.5 and γ=0.8. Slip length is b=10 μm. The partial slip zone behaves much better in low ε than that in high ε as shown in Fig. 4-3(a). For ε=0.1~0.8, the partial slip zone significantly increases the HD force and reduces the friction coefficient with a slight change in friction torques. However, when ε rises up to 0.9, the performance of partial slip zone turns to be negative by diminishing the HD force and increasing the friction coefficient. It can be seen in Fig. 4-3 (b), the slip velocity is large in low ε at the front part of slip zone. In high eccentricity of ε=0.9, negative slip velocity appears, i.e. the slip velocity goes into the opposite direction of the shaft speed, causing the decrease in the HD force. In order to improve the performance of the bearings, it is necessary to further optimize the slip zone coefficients in high eccentricity ratios.

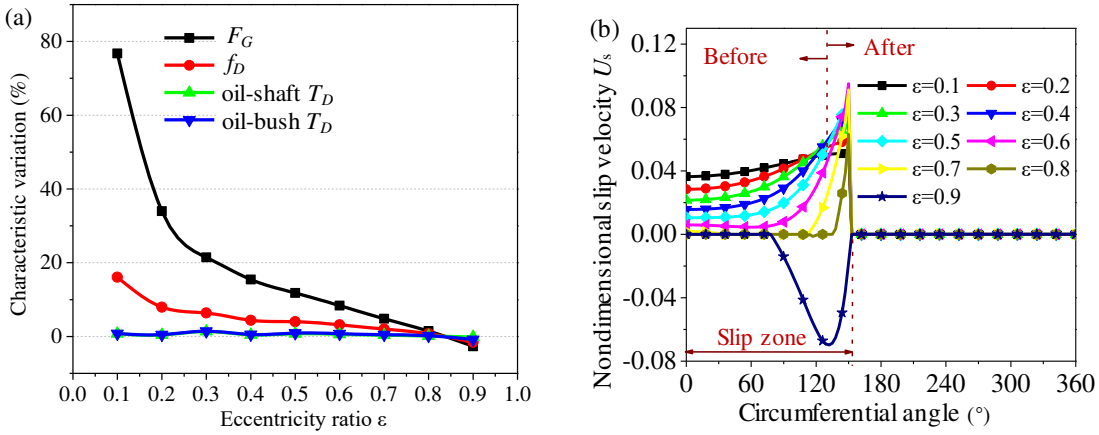


Fig. 4-3 Effect of eccentricity ratio ε on (a) HD force gain F_G, friction coefficient decrease f_D and friction torque decrease T_D, and (b) nondimensional circumferential slip velocity U_s in the middle plane

4.3.2 Optimization of slip zone in high eccentricity ratios

This part mainly focuses on the optimization of journal bearings under high eccentricity ratio. The common parameters used are eccentricity ratio ε=0.9, slip zone coefficients λ=0.5 and γ=0.8, slip length b=10 μm, dimensionless critical shear stress $\bar{\tau}_c$=0.28.

4.3.2.1 Effect of slip zone location (coefficient α) on the hydrodynamic behavior

Fig. 4-4 shows the effect of slip zone coefficient α on the hydrodynamic behavior

at the high eccentricity ratio of ε=0.9. For α>1.0, the HD force and friction coefficient are much worse than that of α<1.0 (Fig. 4-4 (a)), so it is better to set α<1.0. In the positive region of α=0.91~1.0 in Fig. 4-4 (b), slip zone could improve the HD force with the maximum gain of 4.5%, meanwhile the friction coefficient decrease of f_D rises up to the peak value of 2.4%. Fig. 4-4 (c) indicates that the oil-bush friction torque does not always decrease in the positive region, but the increment is smaller than 2%, so in high eccentricity ratio, the HD force and friction coefficient are used as the evaluation criteria to obtain the optimal partial slip zone.

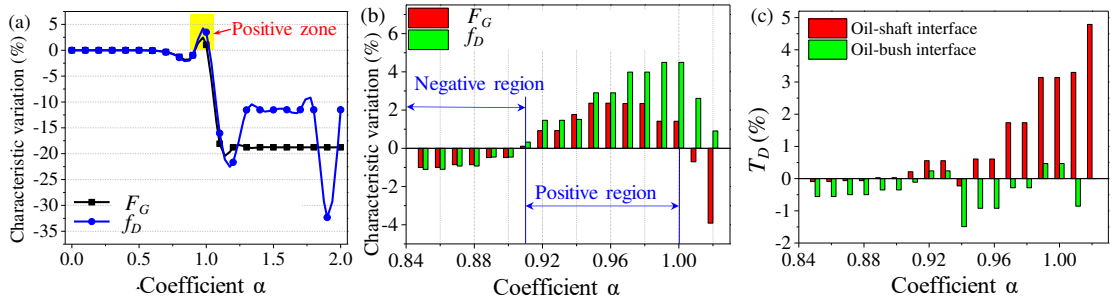


Fig. 4-4 Effect of slip zone coefficient α on the hydrodynamic behavior under high eccentricity ratio of ε=0.9, (a) the HD force gain F_G and friction coefficient decrease f_D, (b) the HD force gain F_G and friction coefficient decrease f_D in positive region, and (c) friction torque T_D decrease in positive region

4.3.2.2 Effect of slip zone shape (coefficients λ and γ) on the hydrodynamic behavior

Fig. 4-5 shows the effect of coefficient λ on the performance of journal bearings with the eccentricity ratio of ε=0.9, the slip zone coefficient of α=1.0. It can be seen that the HD force gain F_G and friction coefficient reduction f_D increase with coefficient λ (Fig. 4-5(a). F_G and f_D reach the maximum values of 4.8% and 11% respectively at λ=1.2. This means that the slip zone owing wider tailing end works better. The large coefficient λ causes a little increase in maximum HD pressure in the middle plane (Fig. 4-5(b)), because it has little influence on the slip velocity in the middle plane in Fig. 4-5 (c). Before θ=150° slip velocity is negative, while it becomes positive after θ=150° as shown in Fig. 4-5 (c).

Fig. 4-6 shows the effect of slip zone coefficient γ on the hydrodynamic behavior of journal bearings with coefficients of α=1 and λ=1/γ. For more obvious effect, larger eccentricity ratio of ε=0.92 is used. It is clear that the increasing coefficient γ can improve the HD force slightly with F_G<1%, and lower friction coefficient and friction torque with f_D<1.23% and T_D<1.4% respectively. Moreover, coefficient γ has little influence on HD pressure and slip velocity U_s in the middle plane (Fig. 4-6(b) and (c)). This is because the shape change caused by coefficient γ mainly influences the

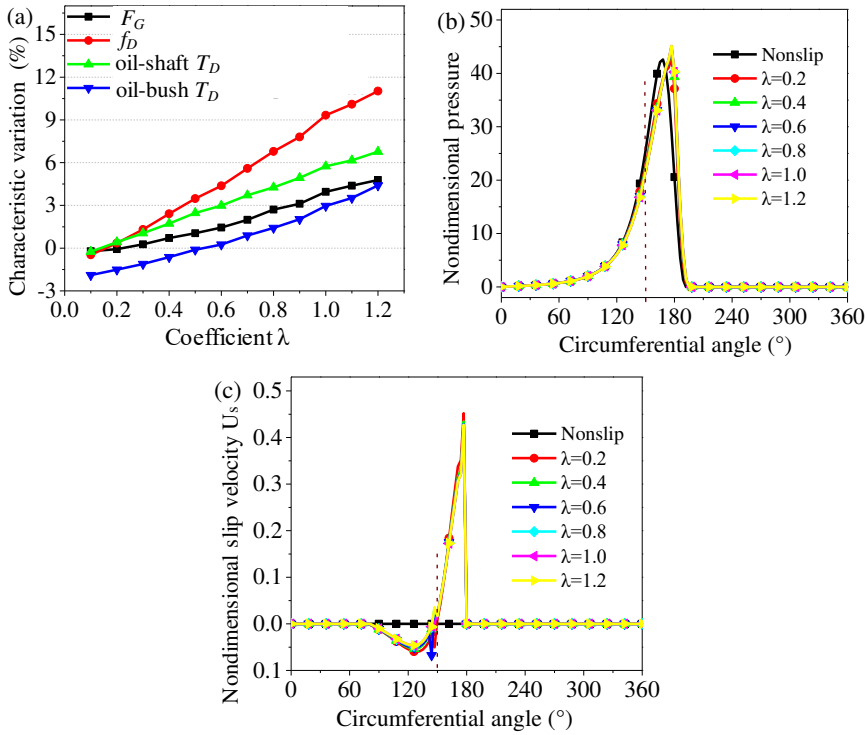


Fig. 4-5 Effect of slip zone coefficient λ on the hydrodynamic (HD) behavior of journal bearings, (a) the HD force gain F_G, friction coefficient decrease f_D, (b) the HD pressure, and (c) the slip velocity U_s in the middle

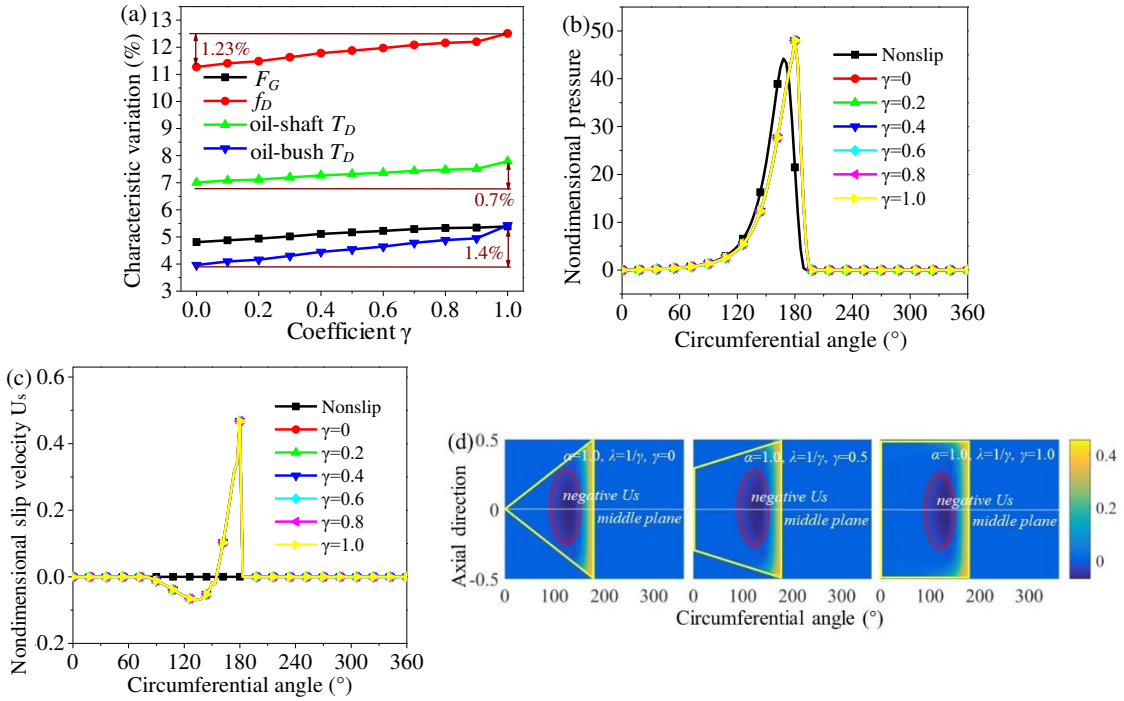


Fig. 4-6 Effect of slip zone coefficient γ on (a) the HD force gain F_G, friction coefficient decrease f_D and friction torque decrease T_D, (b) the HD pressure, (c) the slip velocity U_s and (d) the distribution of U_s at film-bush interface in high eccentricity ratio

slip zone where the slip velocity is close to zero and make little change in the pressure distribution, and the variation of γ could not offset the negative zone of slip velocity U_s (Fig. 4-6d). Despite the subtle influence of γ, it is still beneficial to widen the front size of the slip zone, i.e. enlarge L_{s1}.

The influence of slip zone shape, i.e. the coefficients of λ and γ at high eccentricity ratio is similar to that in moderate eccentricity ratio. It is helpful to increase both the coefficients of λ and γ. That is to say setting λ=1 and γ=1 and the optimal shape of the slip zone is maximum rectangular.

4.3.2.3 Hydrodynamic behavior of selected slip zone in high eccentricity ratios

Fig. 4-7 shows the effect of high eccentricity ratio on the hydrodynamic behavior with the optimized slip zone parameters of α=1, λ=1, γ=1, and slip length of b=5 μm. As shown in Fig. 4-7(a), the HD force gain F_G increases with the rise of ε. The friction coefficient decrease f_D experiences a rise and meets the largest value of 12.5% at ε=0.96. However, there is a special point of ε=0.93, whose performance is better than the two adjacent points of ε=0.92 and ε=0.94. This is because the present slip zone parameters are not optimal for all the eccentricity ratios. In this case, these parameters can best improve the performance of ε=0.93 and it is marked as a special point. For ε>0.96, F_G and f_D go lower, but it can be concluded that the rectangular slip zone can still improve the performance of journal bearings for ε=0.9~0.97. As shown in Fig. 4-7 (b) and (c) and Eq.(3-23), in slip zone 1 the pressure gradient dp/dθ is close to zero and the film thickness is high, so the slip velocity is almost zero. In slip zone 2, though film thickness becomes smaller, the slip velocity is still negative because of the increasing pressure gradient dp/dθ. In slip zone 3, the pressure gradient dp/dθ is quite large, but the film thickness also becomes small enough to offset the negative effect of dp/dθ, so there is a sharp increase in slip velocity.

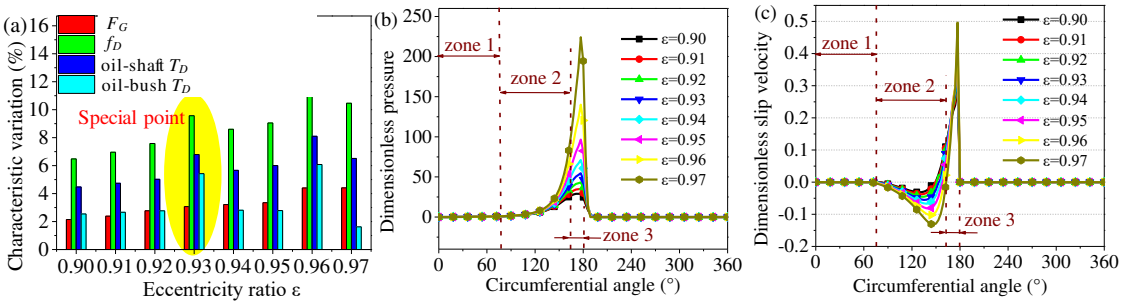


Fig. 4-7 Effect of high eccentricity ratio on (a) HD force gain F_G, friction coefficient decrease f_D, (b) HD pressure, and (c) slip velocity U_s in the middle plane

4.3.3 Optimal slip zone selection under heavy loads

In this part, the optimized slip zone coefficients of λ=1 and γ=1 are selected. The

influence of attitude angle under heavy load is considered. The fixed coordinate system of Θ-rz is applied (Fig. 4-1(b)), and its origin of Θ=0 is the vertical direction of Y=0. The slip zone starts from the system origin of Θ=0, instead of θ=0. In the fixed coordinate system Θ-rz, attitude angle φ is not zero. As the part slip zone of Θ_{slip}=0~φ locates at the end of the divergent region of the film, its influence can be neglected. Therefore, the optimal α still approximately located at 0.9~1.0. The new coefficient of κ is introduced to considering the variation of the attitude angle, the tailing end of the slip zone is noted as $\Theta_{end}=\pi+\kappa\varphi$ ($\kappa \in [0,1]$), i.e. $\Theta_c=\pi+\kappa\varphi$, $\alpha=(\Theta_c-\varphi)/\Theta_{conv}$.

The optimized parameters for ε=0.94 are selected for further exploring the performance of journal bearing with eccentricity ratios ranging from 0.4 to 0.97 as shown in Fig. 4-8. The slip length is b=5 μm. The tailing end of the slip zones are set to be $\Theta_{end}=\pi$, $\Theta_{end}=\pi+0.25\varphi$, $\Theta_{end}=\pi+0.5\varphi$, $\Theta_{end}=\pi+0.75\varphi$, and $\Theta_{end}=\pi+1.0\varphi$, corresponding to κ=0, κ=0.25, κ=0.50, κ=0.75 and κ=1.00 respectively. The nonslip attitude angle of ε=0.94 is φ=20.3°, so the corresponding values of α are 0.889, 0.915, 0.943, 0.971 and 0.999. For ε<0.94, the selected value of κ can raise the HD force and lower the friction coefficient (Fig. 4-8(a) and (b)). For κ=0.75 and κ=1.00, the slip zone better improves the bearing performance in different eccentricity ratios with the maximum F_G of 4.5% and the maximum f_D of 10%. However, for ε>0.94, except κ=0.5, the selected partial slip zones diminish the HD force in any case.

Usually with the increase in eccentricity ratio, the attitude angle drops, and the slip zone coefficient α rises. In Fig. 4-8(c), it can be seen for ε<0.94 and κ=0.5~1.0, the attitude angle goes down, so the exact value of coefficient α becomes higher. If the journal bearing always works in a constant heavy load, in order to get the optimal performance, it is better to set the partial slip zone with the coefficient κ ranging from 0.5 to 0.9.

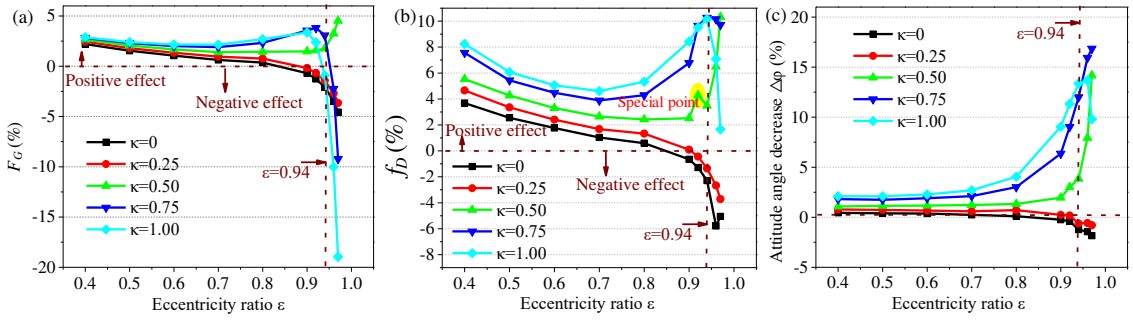


Fig. 4-8 The performance of journal bearing in partial slip zone in different eccentricity ratios, (a) the HD force gain F_G, (b) the friction coefficient decrease f_D, (c) the decrease percentage of attitude angle

4.4 Selection of PTFE coating position in thermal case

The thermal properties of the coating journal bearings are discussed in four lubrication regimes: thermohydrodynamic lubrication without/with slip (THD/ THDS) and thermoelastohydrodynamic without/with slip (TEHD/TEHDS). Because the bearing groove (Fig. 3-1(c)) is set to be 18°, the range of coating length Φ_c is 9° $\leq \Phi_c \leq$ 351°. According to the definition of coefficient α in section 4.2, its range can be calculated as -0.45 $\leq \alpha \leq$1.95. The parameters of the coating, interlayer and basement are listed in Table 3-1, Table 3-2 and Table 3-3. The applied load is 8 kN (2.0 MPa), the shaft speed is 2000 rpm, a supply pressure of zero is imposed, and the coating is set as PTFE.

Fig. 4-9 demonstrates the maximum temperature (T_{max}) and shaft temperature, and minimum film thickness (h_{min}) as a function of coating coefficient α. When the coating end is located in the film convergent region, i.e. zone 1 of α<0.8, the influence of the partial coating is quite small, with variations of T_{max} and h_{min} of less than 0.3℃ and 1.0 μm respectively (Fig. 4-9 (a)). The maximum pressure P_{max} remained constant at about 2.56 MPa (Fig. 4-9 (b)). Therefore, in the view of simulation, the THD model can be used to obtain an acceptable result in zone 1, i.e. it is acceptable to neglect the effects of wall slip and coating deformations.

When the coating end is close to the position of minimum film thickness, i.e. zone 2 of α=0.8~1.4, T_{max} can be increased in all lubrication cases at $\alpha\approx$1.0 (Fig. 4-9 (a)). In nonslip cases (THD and TEHD), T_{max} can be further raised with the increasing α, but in slip cases (THDS and TEHDS), it can be decreased by 2.0% at $\alpha\approx$1.4. This is because the partial coating can affect the heat transfer to the basement in the maximum temperature area as shown in Fig. 4-10 (for $\alpha\approx$1.0). Fig. 4-9 (b) shows that h_{min} experiences a sharp decrease by about 16% and 21% in the TEHD and TEHDS cases respectively, but this large reduction does not appear in the THD and THDS cases. It can be deduced that the sharp decrease is caused by deformations. Then this sharp decrease in h_{min} leads to a sharp increase in p_{max} (for TEHD) which can be offset by the slip (for TEHDS) as shown in Fig. 4-9(c). In summary, we prefer lower T_{max} and thicker h_{min}, so the range of α=0.8~1.4 is unacceptable or infeasible. Based on the simulation, when slip occurs, the slip and deformation are not recommended to be neglected, and TEHDS model is better to be applied.

When the coating end is located in the film divergent region, i.e. zone 3 of α > 1.4, the variations of T_{max}, h_{min} and p_{max} are quite small, so, in the point of manufacturing, it is better to prescribe full coatings. Without slip, T_{max} can be increased by about 5% (2.5℃) compared with that of α<0.8 because the PTFE coating of α>1.4 effectively

prevents the heat transfer to the basement. With slip, T_{max} can be decreased by 2% compared with that of α<0.8 because the slip velocity works on a large range (Fig. 4-11) and effectively decreases the heat generation of viscous damping. However, h_{min} and p_{max} with slip are smaller than that without slip (Fig. 4-9 (b)). Therefore, wall slip offsets the temperature rise caused by a full PTFE coating, but at the sacrifice of decreasing HD force. For zone 3, when slip occurs, it is suggested to apply the TEHDS model to obtain more accurate simulation results.

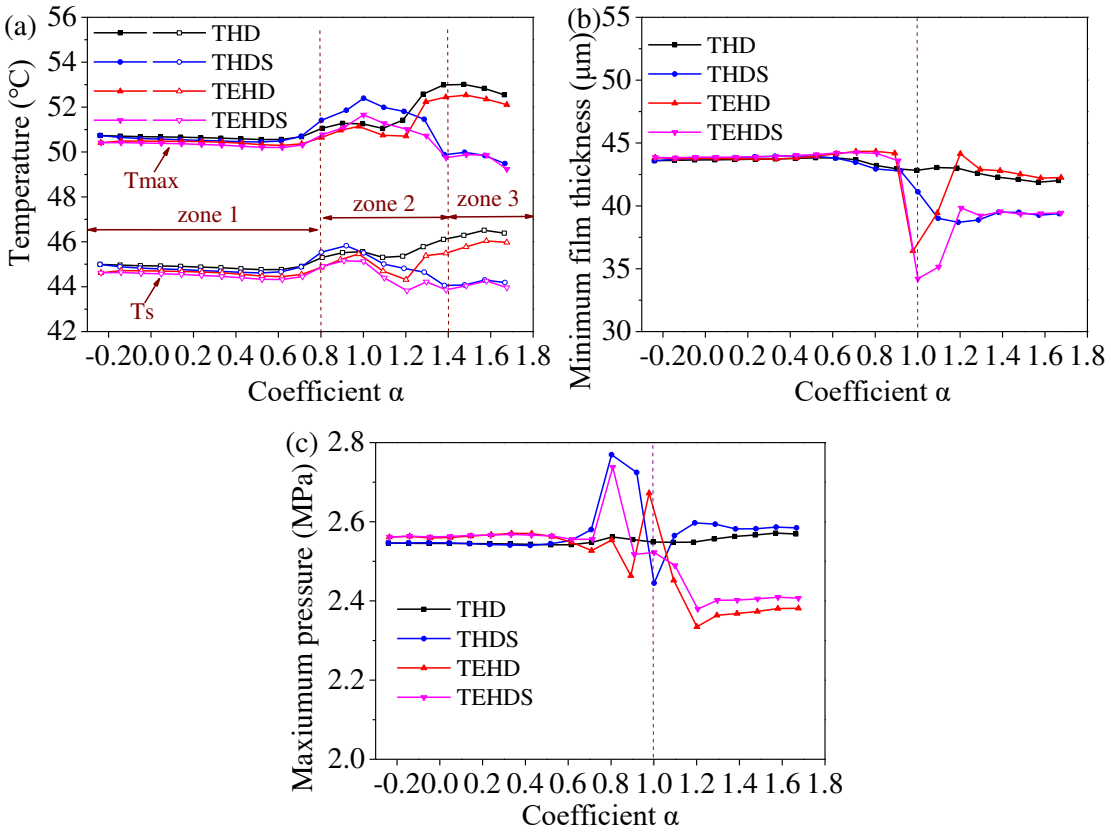


Fig. 4-9 Influence of coefficient α of PTFE coating on (a) shaft and maximum temperature T_{max}, (b) minimum film thickness h_{min} and (c) maximum pressure P_{max}

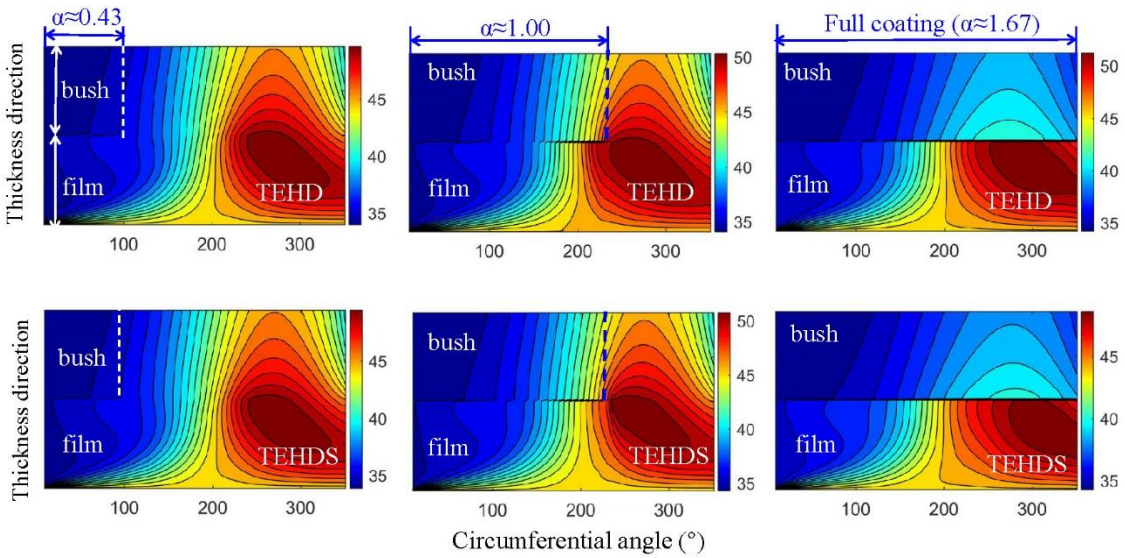


Fig. 4-10 Temperature distribution of the film-bush (coating, interlayer, basement) area

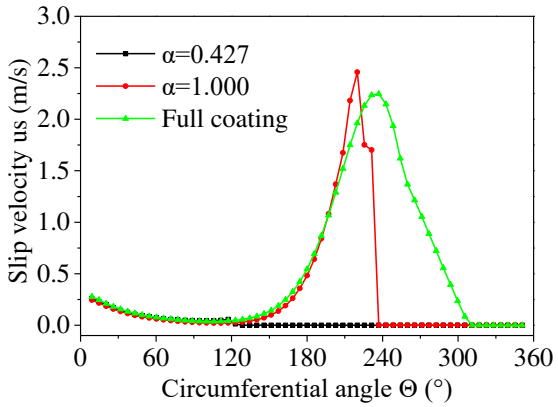


Fig. 4-11 Slip velocity in the middle plane in TEHDS regime

Fig. 4-12 shows deformations in the radial direction at the film-bush interface. In Fig. 4-12(a), the mechanical deformation of the basement is close to zero compared with the coatings because the coating (PTFE) is much softer than the basement (steel). Mechanical deformation of α=1.0 is close to that of the full coating, because almost the entire active pressure zone act on the partial coating. However, for α=0.428, the maximum mechanical deformation is 1.27 μm which is only one quarter of that for α=1.0 and the full coating because only the low pressure zone acts on the partial coating of α=0.428.

In terms of thermal deformation in Fig. 4-12(b), for α=0.428 and α=1.0, the deformation of coating is about 5~10 μm smaller than that of the basement, and a discontinuity exists at the coating-basement interface in the circumferential direction (Fig. 3-1), which can cause the partial coating to detach from the basement. Also, the large thermal deformation gap can produce a step divergent region at α≈1.0 and obviously decrease the HD force, i.e. a sharp decrease in h_{min} (in Fig. 4-9(b)). This is

also why the range of α=0.8~1.4 should be avoided. Thermal deformation of the full coating is 4~12 μm less than that without coating, although the thermal expansion coefficient of the coating is much larger than that of the basement. This is because the basement temperature is lower than that of the coating, and the lower basement thermal expansion confines thermal expansion of the coatings. Compared to the no coating and partial coatings, the thermal deformation of the bush coated by full PTFE coating is more uniform.

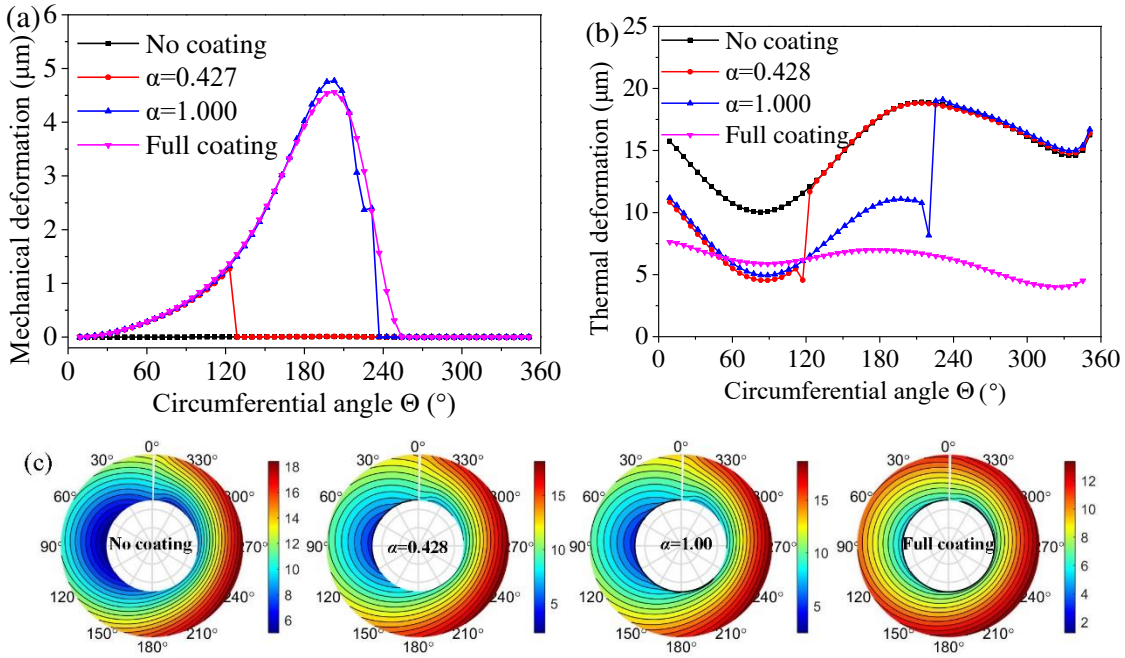


Fig. 4-12 Influence of coating coefficient α on (a) mechanical and (b) thermal deformations of the coating and (d) the temperature distribution of bush in middle plane in TEHDS regime

4.5 Effect of coating parameters on the thermal behavior

4.5.1 Thermal behavior in different coating thickness

Fig. 4-13 shows the maximum temperature T_{max}, minimum film thickness h_{min} and maximum pressure P_{max} with respect to coating thickness. Three typical values of α≈0.43, 1.0 and *full coating* are discussed. For α≈0.43, T_{max}, h_{min} and P_{max} are almost constant at 50.3℃, 50 μm and 2.56 MPa respectively for different coating thicknesses because the partial coating location is far from the maximum pressure and temperature area.

As to α≈1.0, with an increase in coating thickness, the increases of T_{max} and P_{max} are less than 1.0% and 4% respectively, but h_{min} drops significantly. For TEHDS case, when the coating thickness rises from 0.5 mm to 1.5 mm, h_{min} can be reduced from 40.5 μm to 32.4 μm (a reduction of 19.7%), resulting in a sharp decrease of HD force.

This is because with the increase in coating thickness, the thermal deformation of the partial coating decreases.

For the full coating, with an increase in coating thickness, T_{max} rises by less than 4% accompanied by a reduction of P_{max} of less than 6.2%. For h_{min}, in the TEHDS case shown in Fig. 4-13(a), the minimum film thickness of h_c=0.5 mm increases by about 2% and 5% respectively, compared with those of h_c=1.0 mm and h_c=1.5 mm; in the TEHDS case, these increments are about 2% and 4% respectively (Fig. 4-13(b)). This mainly attributes to the less thermal deformation of the thicker coating as shown in Fig. 2-14(b). It can also be deduced that the coating thickness has a larger influence on h_{min} than wall slip.

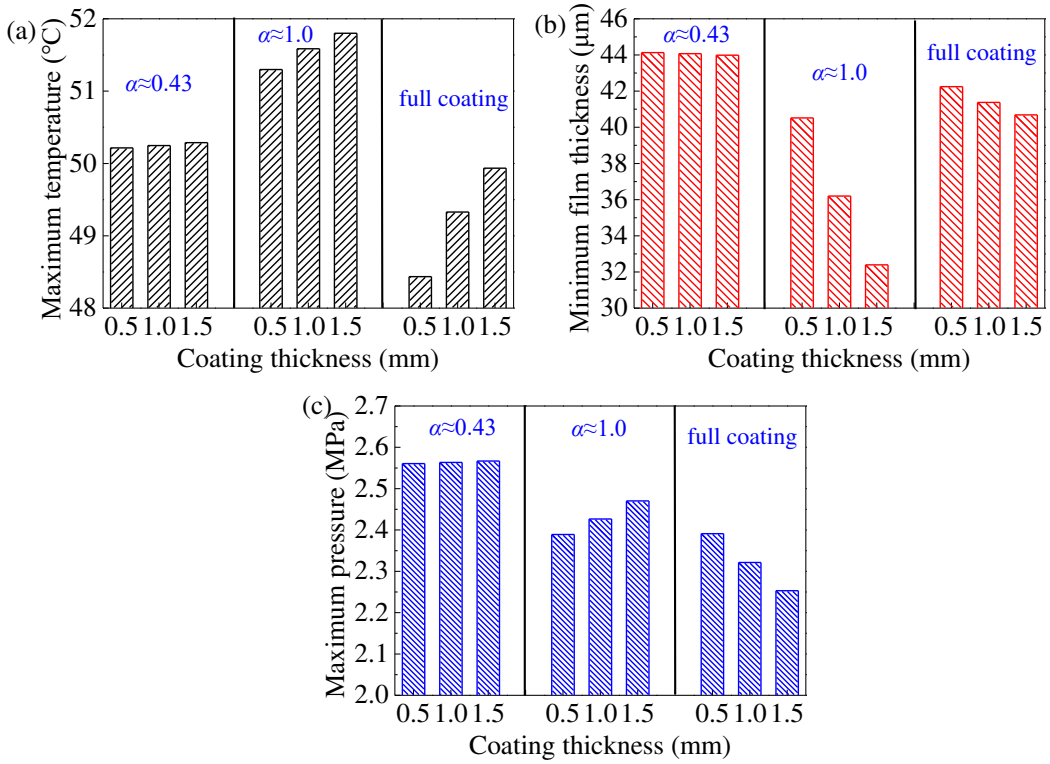


Fig. 4-13 (a) Maximum temperature T_{max}, (b) minimum film thickness h_{min} and (c) maximum pressure p_{max} in different coating thicknesses in TEHDS regime

Fig. 4-14 shows the mechanical and thermal deformations of a full coating as a function of coating thickness. Fig. 4-14(a) indicates that, for each 0.5 mm increase in coating thickness, the maximum mechanical deformation rises about 2.0 μm, which is helpful to increase h_{min}. However, a thicker coating also enlarges the reduction of thermal deformation, and can even lead to negative values (Fig. 4-14 (b)). This means that the coating shrinks into the inner circle and causes smaller h_{min}, so the bearing is much more easily damaged by seizures. Shrink of the coating is mainly caused by the significantly different thermal properties of the coating and

basement. The thermal expansion of PTFE is much larger than that of the basement, but, when confined by the basement, the coating cannot freely expand and is forced to deform in the opposite direction, i.e. shrinking into the inner circle. This shrink effect of the coating is also presented by Ref. [54].

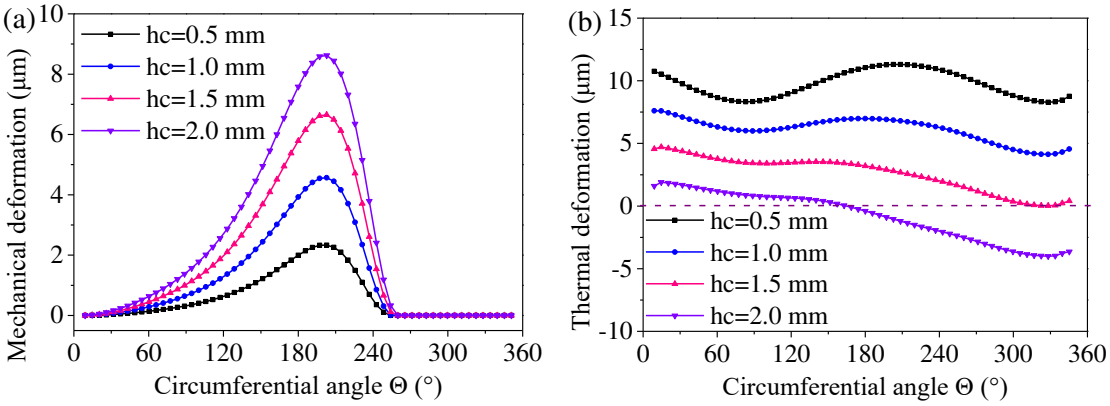


Fig. 4-14 The influence of coating thickness on (a) mechanical deformation and (b) thermal deformation in TEHDS regime

4.5.2 Thermal behavior in different coating materials

In this section, the coatings of PTFE, graphite and diamond-like carbon (DLC) are used. The parameters are listed in Table 3-2, and the working conditions are the same as described in Section 4.3.3.

Fig. 4-15 shows the temperature distribution at the film-coating-interlayer-basement zone for graphite and DLC coatings. Compared with the PTFE coating of in Fig. 4-10, graphite and DLC coatings cannot prevent heat transfer to the basement because of their better heat conduction properties, and there are no obvious temperature boundaries between the coating, interlayer and basement. The influence of the partial graphite and DLC coating of α=0.43 and 1.0 has a little influence on the temperature distribution.

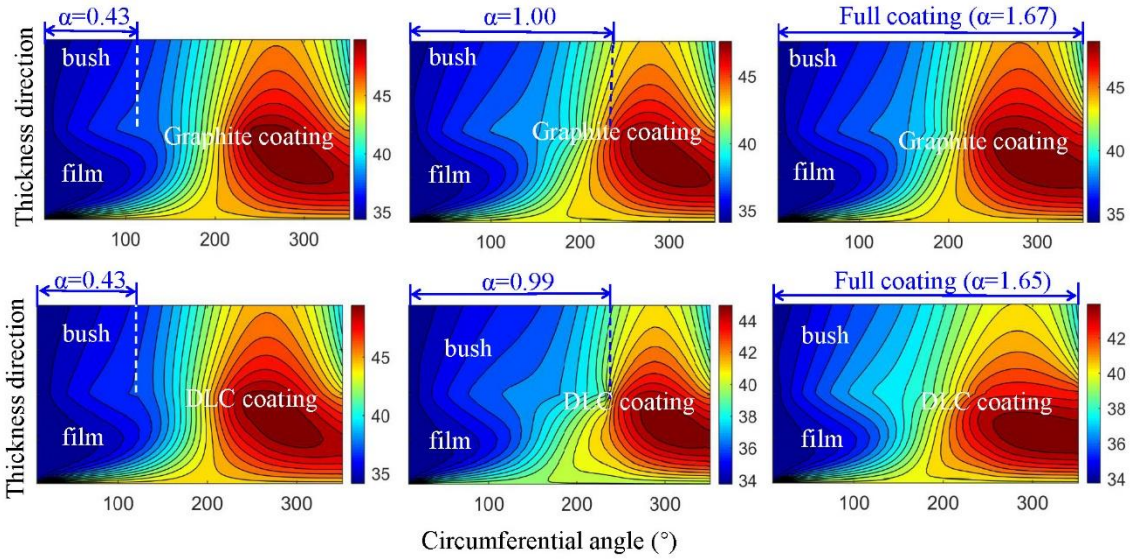


Fig. 4-15 Thermal distribution with different coating materials

Fig. 4-16 shows the comparison of maximum temperature T_{max} and minimum film thickness h_{min} for different coating materials. For $\alpha\approx0.43$, the variation of T_{max} is within 1.0% (0.5℃), so the effect of coating material on T_{max} can be neglected. For $\alpha\approx1.0$, compared with PTFE, graphite reduces T_{max} by 6% (3.0℃) and improves h_{min} by 28% (about 10.3 μm), whereas DLC further improves these two gaps to 11% (5.6℃) and 39% (14.2 μm). Similarly, a full DLC results in a reduction of T_{max} by about 15% (7.7℃) and an increment of h_{min} by about 18.5 (7.8 μm) when compared with a full PTFE coating. Therefore, both graphite and DLC improve bearing thermal behavior by decreasing T_{max} and increasing h_{min}, this is mainly attributed to the high thermal conductivities of graphite (105 W/m·℃) and DLC (600 W/m·℃)

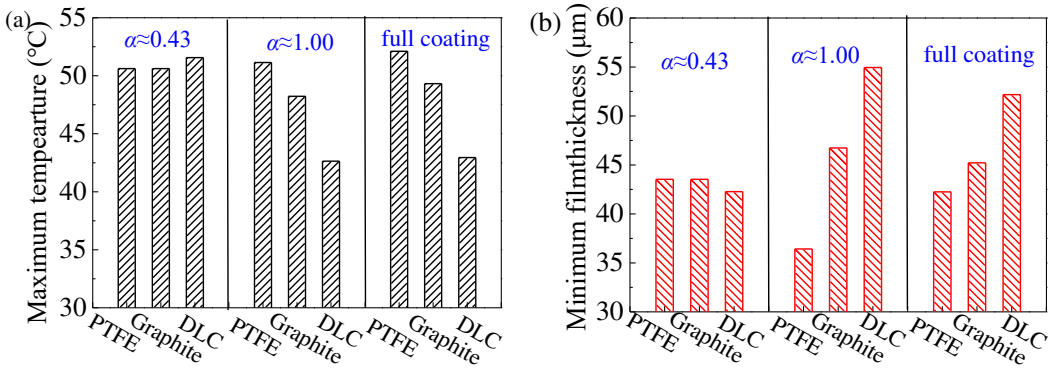


Fig. 4-16 Influence of coating material on (a) maximum temperature T_{max} and (b) minimum film thickness h_{min}

The thermal deformations of different coating materials differ significantly as shown in Fig. 4-17. For $\alpha\approx1.0$ in Fig. 4-17(a), the discontinuous deformation at the coating-basement interface of PTFE is about 10 μm larger than those of graphite and

DLC. In the full coating data shown in Fig. 4-17 (b), the thermal deformation of PTFE is 10~15 μm smaller than those of graphite and DLC, even though PTFE has a larger thermal expansion coefficient. Compared to the mechanical deformation of PTFE coating, the mechanical deformations of graphite and DLC coatings are close to zero due to the much larger elasticity modulus and have a little influence on thermal behavior.

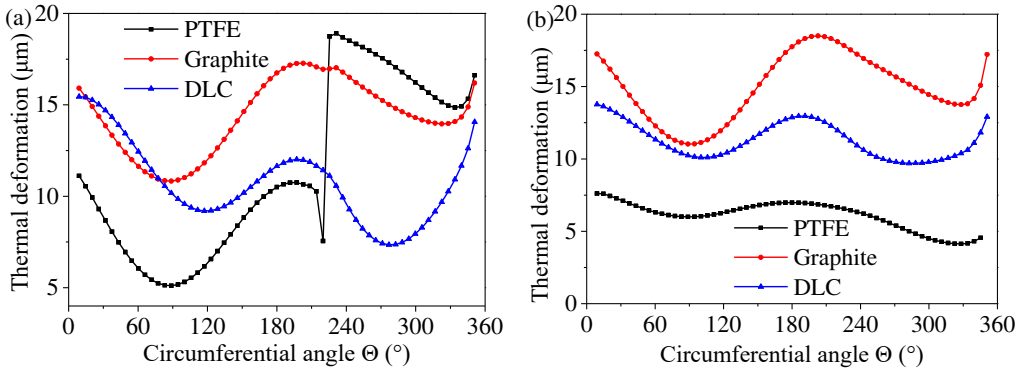


Fig. 4-17 Influence of coating material on thermal deformation at (a) α≈1.0 and (b) full coating

4.6 Conclusions

In this chapter, the influence of the slip zone on the hydrodynamic and thermal behavior of journal bearings under heavy load is analyzed. The selection method of the coating (slip) zone is given. Conclusions are as follows:

(1) In isothermal case, the axial width of the slip zone is better to be increased, that is, the slip zone is set to be a rectangle with the bearing width. Under constant heavy load, the slip zone is located within the convergence region of the film and the tailing end is close to the position of minimum film thickness (h_{min}) so that it can effectively improve the HD force.

(2) When the PTFE coating locates in the convergence region of the film and the tailing end is far away from the position of h_{min}, the influence of the coating on the maximum temperature (T_{max}) and h_{min} is quite small. When the tailing end of the coating locates in the divergence region of the film and is far away from the position of h_{min}, wall slip can reduce T_{max} but also decreases HD force. It is infeasible or unacceptable, without further texture design, to locate the tailing end close to the position of h_{min}.

(3) Thick PTFE coating thickness increases T_{max} and reduces h_{min}. If the coating is too thick, it will deform inward, which increases the risk of bearing seizure failure. Graphite and DLC coatings with better thermal conductivity can lower the film temperature.

Chapter 5 Experimental tests of the thermal properties of the coated tilting pad journal bearings

5.1 Introduction

In this chapter, the experimental research on the coated tilting pad journal bearings (CTPJBs) in both steady state and start-stop process are carried out. Firstly, the influence of relative clearance, operating conditions and coating materials on large-clearance coated bearings is studied. Then tests are conducted in steady stationary for micro-clearance coated bearings to observe the thermal and worn properties of PTFE, graphite and Ag coatings. Finally, the influence of relative clearance, acceleration and initial temperature on the temperature during startup is discussed to obtain the conditions that are conducive to the safe startup of CTPJBs.

5.2 Test rig and instrumentation

5.2.1 The construction of test rig

The experiment is carried on a self-built test rig of journal bearings. As shown in Fig. 5-1, the construction of the experimental platform is mainly divided into four parts: the power system, the lubrication system, signal acquisition system and mechanical system. The motorized spindle is driven by the frequency converter. The advantage is that the step-less speed regulation of the motorized spindle can be realized by adjusting the frequency of the frequency converter. The lubrication of the tested CTPJBs and supporting rolling bearings is realized by the lubrication system; the signal data of temperature, rotation speed and vibration are collected through corresponding sensors and NI data acquisition system. Data processing and storage are performed using the virtual device LabView. The photo of the test rig is show in Fig. 5-2.

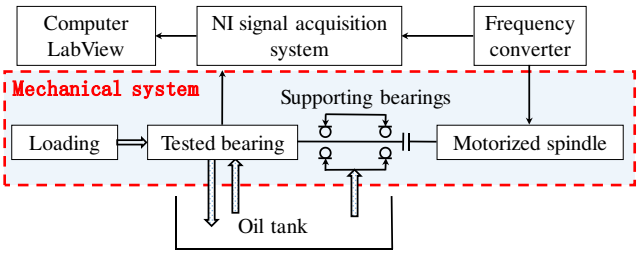


Fig. 5-1 Schematic representation of the test rig

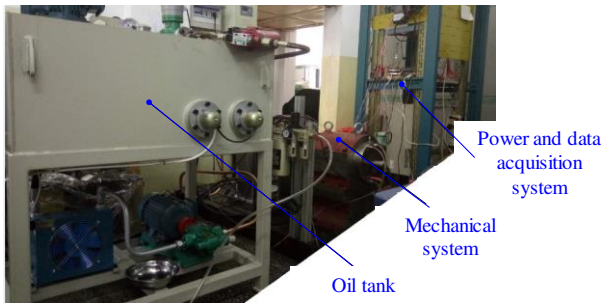


Fig. 5-2 Photo of the test rig of the journal bearings

The mechanical system realizes the power transmission and the normal running of the bearing. It mainly includes the motorized spindle, the coupling, the supporting rolling bearings, the loading device and the tested bearing device as shown in Fig. 5-3. The speed of the motorized spindle can be up to 12k rpm and rotates in both forward and reverse directions. It is connected with the shaft of the tested bearing by a flexible coupling. In order to reduce the deformation of the rotating shaft under heavy loads, two supporting rolling bearings are arranged on the same side of the tested bearing. The tested bearing is placed in the loading ring, which is limited by two guide rail sliders fixed on the temporary oil tank to ensure the loading direction. The load in the vertical direction is applied on the loading ring by a hydraulic cylinder, and it is transmitted to the tested bearing by the loading ring.

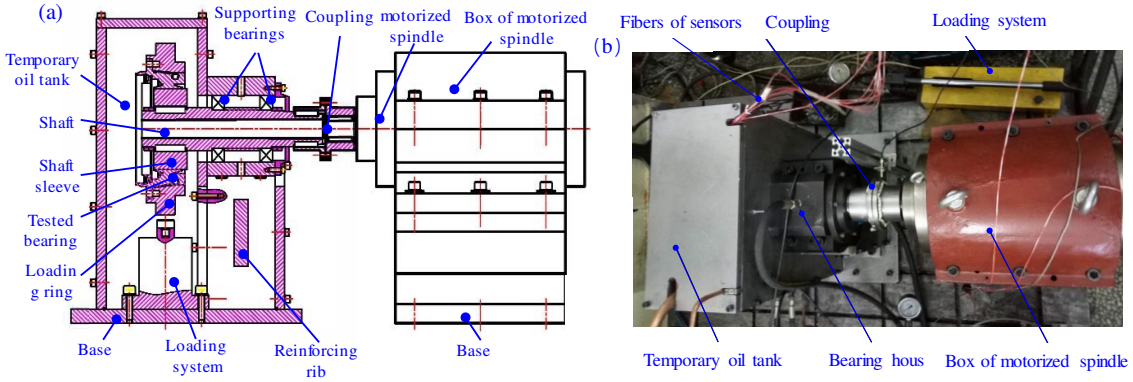


Fig. 5-3 (a) assembly drawing and (b) photo of the mechanical system of the test rig of the journal bearings

5.2.2 The geometry of the tilting pad journal bearing

The experimental object is a six-pad CTPJB, the photo of which is shown in Fig. 5-4. Fig. 5-4 a) shows the single coated pad, and the coatings are sintered to the pad surface through the interlayer of copper which is used to enhance the bonding force. Fig. 5-4 b) shows the six pads are installed in the loading ring which is arranged on the shaft. Under the loading ring, the hydraulic cylinder is used to load. The weight of the ring is balanced by the extra applied load.

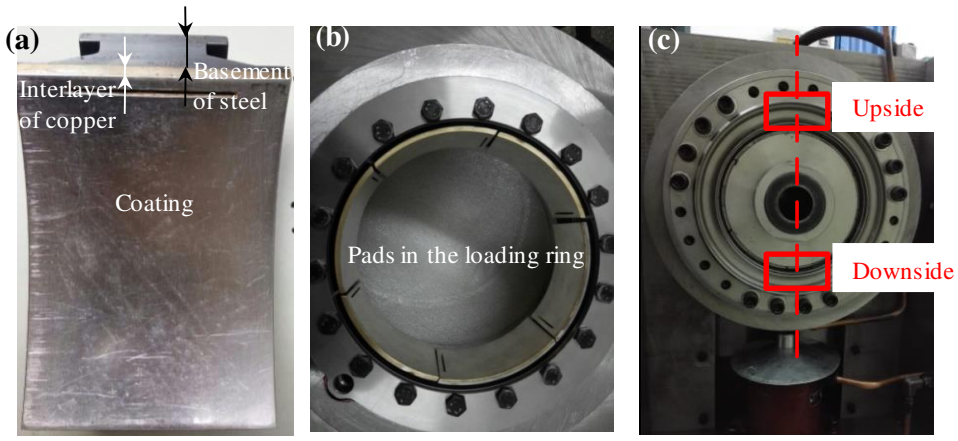
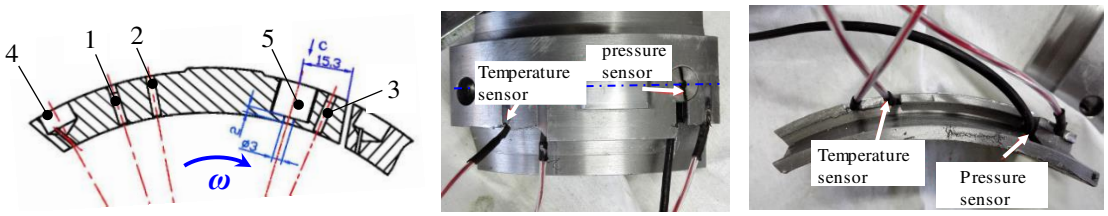


Fig. 5-4 Photo of the six-pad CTPJB, (a) single coated pad, (b) pads in the loading ring and (c) loading mode

5.2.3 Sensors position on the pads

Three temperature sensors (No. 1, 2 and 3) and one pressure sensor (No. 5) are installed in the axial center of the bearing pad as shown in Fig. 5-5. From the leading edge to the trailing edge of pad, the positions of sensors 1, 2, 3, and 5 are imposed respectively at 16.5°, 23.5°, 55.5° and 49.5° along the rotational speed. No. 4 is the oil supply port.



1,2,3-Temperature sensors, 4-Oil supply port, 5-Pressure sensors

Fig. 5-5 Location of the sensors in the pad

The geometrical parameters of the bearing, the lubricant and parameters of the bearing used in the experiments are shown in Table 5-1 and

Table 5-2 respectively.

Table 5-1 Geometrical parameters of the bearing at 20°C

Parameters	Value	Parameters	Value
Internal pad radius, mm	85.015	Preload coefficient	0
External pad radius, mm	98	Pad thickness, mm	12.985
Bearing length, mm	60	Angular extent of pad i,°	58.5
Radius of pad pivot, mm	99	Pivot position in pad i, A_i/B_i,	0.672
External radius of loading ring, mm	199	Pivot position in the bearing i,°	6+60*(i-1)

Table 5-2 Lubricant characteristics (ISO T32)

Parameters	Value	Parameters	Value
Feeding and bath temperatures, ℃	40	Density at 40℃, kg/m^3	860
Supply pressure, MPa	0.3	Thermal conductivity, W/(m·K)	0.13
Dynamic viscosity at 40 ℃, mPa·s	27.52	Specific heat, J/(kg·K)	2000
Dynamic viscosity at 100 ℃, mPa·s	4.644		

5.3 Geometry model of the coated tilting pad journal bearing

Fig. 5-6 shows the geometry of the coated tilting pad journal bearing (CTPJB) with six pads. Θ=0 of the fixed coordinate system Θ-rz starts from vertical direction, and the constant applied load is in the direction of X. The number of each pad is marked. Compared to the plain journal bearing, the construction of CTPJB is much more complex. As shown in Fig. 5-6, R_s is the shaft radius, $R_{p\ int}$ is the internal radius of the pad, $R_{p\ ext}$ is the external radial of the pad， R_h is the distance from shaft center to the pad pivot, A_i is the pivot position in the pad, B_i is the length of the pad, i represents the ith pad. The governing equations of pressure and temperature and the boundary conditions (BDs), as well as the solving method, are the same as Chapter 3, but the film thickness of each pad is necessary to be recalculated.

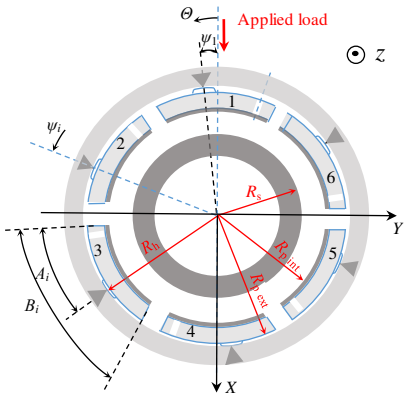


Fig. 5-6 Geometry of the tilting pad journal bearing

The film thickness of the ith pad:

$$h_i(\Theta) = C_p - (C_p - C_b)\cos(\Theta - \psi_i) - (R_s + h_p)\delta_i \sin(\Theta - \psi_i) + e\cos(\Theta - \varphi) + \delta_{Ri} \tag{5-1}$$

where e is the bearing eccentricity, φ is the attitude angle, C_b is the bearing clearance, C_p is the clearance of the pad， C_p=R_p-R_s, ψ_i is the pivot position the in the bearing, δ_i is the tilting angle of the pad, δ_{Ri} is the pad deformation in radial direction, and h_p

is the pad thickness.

The nondimensional film thickness is expressed as

$$H_i(\Theta)=1-m\cos(\Theta-\psi_i)-\left(\frac{R_s+d}{C_p}\right)\delta^i\sin(\Theta-\psi_i)+\frac{C_b}{C_p}\varepsilon\cos(\Theta-\varphi) \quad (5\text{-}2)$$

where $\varepsilon=e/C_p$, $m=(C_p-C_b)/C_p$.

Fig. 5-7 shows the mechanics analysis of shaft, and it can be given as

$$\begin{cases}-\sum_{n=1}^{N}F_{hn}\cos(\Theta)-W=0\\ \sum_{n=1}^{N}F_{hn}\sin(\Theta)=0\end{cases} \quad (5\text{-}3)$$

where F_{hn} is the hydrodynamic (HD) force at the nth element, m is shaft mass, N is the total number of the element, W is the applied load.

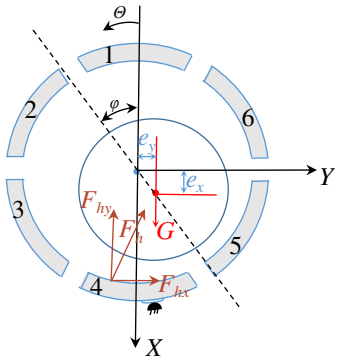


Fig. 5-7 Mechanics analysis of the shaft

Unlike plain journal bearings, besides meeting the condition of force equilibrium, the CTPJB also needs to satisfy the condition of moment equilibrium. For a single pad, the mechanics analysis is shown in Fig. 5-8. The moment equation of the ith pad can be expressed as

$$\begin{cases}0=F_{ihx}+F_{iNx}\\ 0=F_{ihy}-F_{iNy}+m_pg\\ 0=m_pgx_g+F_{ihx}y_h+F_{ihy}x_h\end{cases} \quad (5\text{-}4)$$

where F_{ihx} and F_{ihy} are the HD force of the ith pad in x and y directions, F_{iNx} and F_{iNy} are the support force of the pivot of the ith pad in x and y directions. m_p is the pad mass. x_h and y_h are the distance between the HD force and the pivot in x and y

directions. x_g is the centroid of the pad to the pivot in y direction.

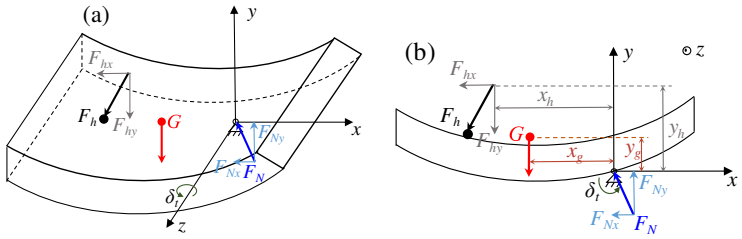


Fig. 5-8 Mechanics analysis of each pad (a) 3D view and (b) front view

Fig. 5-9 shows the solution process of CTPJB:

Step 1. Firstly, given the initial operating parameters, bearing parameters and the initial position of the shaft center.

Step 2. Calculate the film thickness of each pad by Eq.(5-1), obtain the HD pressure by solving Reynolds equation and calculate the HD force of the bearing, then calculate the moment of each pad.

Step 3. Adjust the tilting angle of each pad through the moment equilibrium of Eq.(5-4), and repeat step 1 until the moment balance of each pad is achieved, i.e. the resultant moment is less than the imposed error.

Step 4. Solve the mechanical and thermal deformations of the pads, obtain the film and pad temperatures by solving energy and heat conduction equations, then repeat steps 2 to 4 until the convergence of the temperature.

Step 5. Determine whether the force of shaft is equilibrium or not by Eq.(5-3) If it is unbalanced, adjust the position of the shaft center and repeat steps 2 to 4 until it is balanced.

Step 6. Determine whether the deformations (including mechanical deformation and thermal deformation) are convergent or not. If it is not convergent, repeat steps 2 to 6 until the convergences are met. Finally, the positions of the pads and the shaft center, the HD pressure and film thickness, temperature distribution and deformations can be obtained.

5.4 Thermal properties of the large-clearance coated bearings

In this section, the relative clearance of the coated bearings is set to be above 1.0‰. The silver (Ag) CTPJBs are firstly tested under stationary operating conditions for the Ag coating. The theoretical analysis is conducted to obtain the thermal properties of the bearing in stable cases.

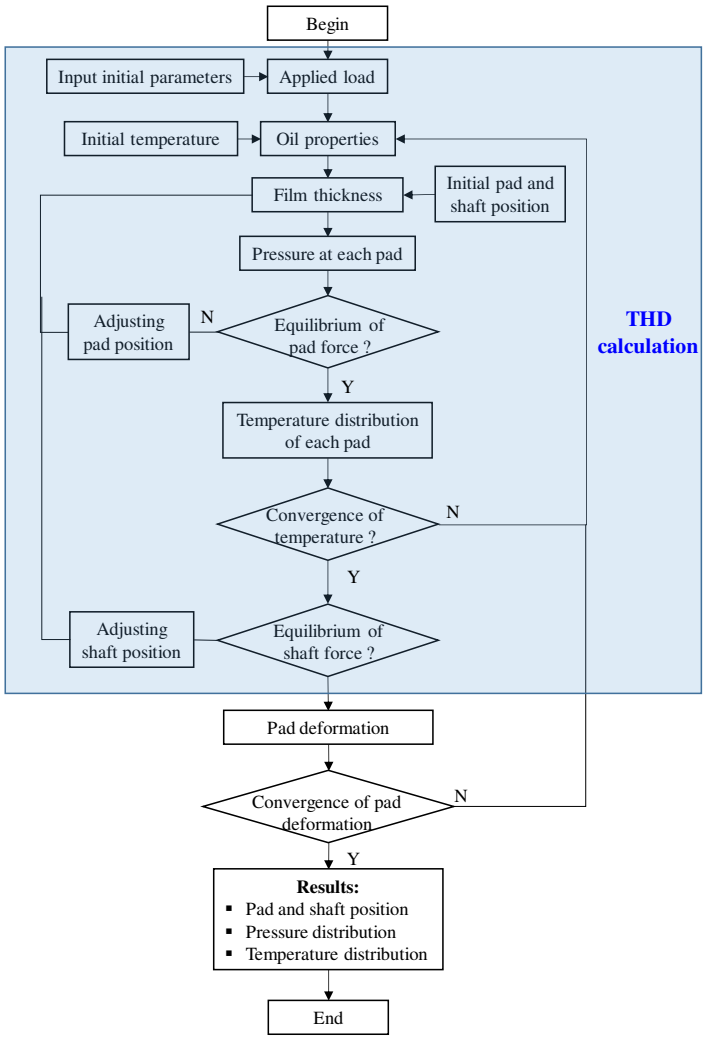


Fig. 5-9 Solution process of the CTPJBs

5.4.1 TEHD behavior in different relative clearances

CTPJBs with different relative clearances are designed for high-speed heavy-load tests and theoretical analysis. The clearance values are shown in Table 5-3. The coating material is Ag. The designed clearance values are listed in Table 5-3, and the large-clearance bearings are that of C1, C2 and C3.

Table 5-3 Parameters of bearing clearance

Parameters	Initial clearance C0	Clearance C1	Clearance C2	Clearance C3
Internal bearing diameter, mm	$170.03^{+0.04}_{0}$			
Shaft diameter, mm	$170.0^{0}_{-0.025}$	$169.88^{0}_{-0.025}$	$169.83^{0}_{-0.025}$	$169.78^{0}_{-0.025}$
Bearing radius clearance, μm	15~47.5	75~107.5	100~132.5	125~157.5
Relative clearance, ‰	0.18~0.56	0.88~1.26	1.18~1.56	1.47~1.86

The simulation and test temperatures are compared as shown in Fig. 5-10. The simulation parameters are listed in Table 3-2. The applied load is 7.5 kN, the speed is 8.8k rpm, and temperature of the 3# sensor in Fig. 5-5 is used. It can be seen the simulation and experimental results are almost consistent. The temperature of each pad decreases in large relative clearance. The temperatures of the pad 3 and pad 4 in the loading side are highest by reaching up to about 100 ℃, followed by the temperature of the pad 5. The temperatures of others are relatively uniform and can reach up to 95°C.

Fig. 5-11 shows the film thickness and pressure of the CTPJB in different relative clearances. Unlike plain journal bearings, each pad of CTPJB has formed a convergence film region, and there is no divergence region, so cavitation effect does not occur. With the increasing clearance, the minimum film thickness becomes larger, and the maximum pressure decreases. Since stable pressure is formed on each pad, the HD force can be offset by each other. Therefore, though there is a high HD pressure in small clearance, the whole HD force is not larger than that in large clearance.

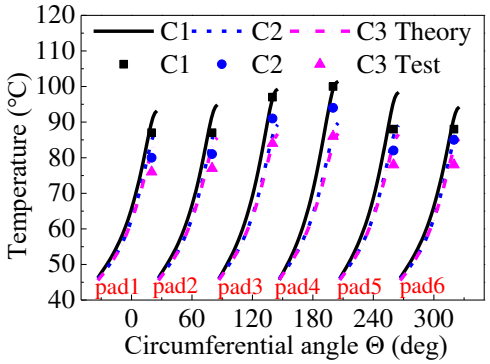


Fig. 5-10 Effect of relative clearance on temperature of each pad

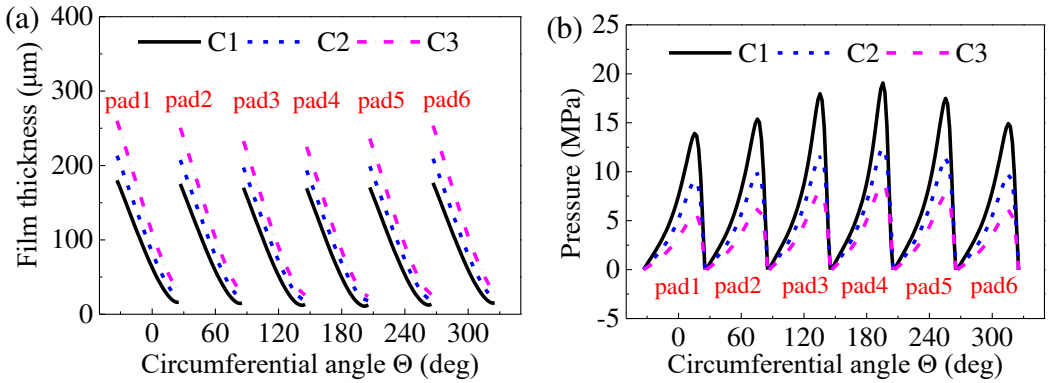


Fig. 5-11 Effect of relative clearance on (a) film thickness and (b) pressure of the CTPJB

Fig. 5-12 shows the radial thermal deformation of each pad of the coating in different clearances. The maximum deformations can reach more than 20 μm at both

leading and trailing edges of each pad. The deformation at the leading edge is negative, i.e. pad expands inward which results in the film thickness smaller, but the negative deformation has little effect on the film thickness because of the large clearance at the leading edge. On the contrary, the deformation of the trailing edge is positive, i.e., the pad expands outward which results in the film thickness larger, so the thermal deformation has a greater impact on the film thickness because of the small clearance at the trailing edge. Fig. 5-13 shows the thermal deformation distribution of each pad in the clearance of C2. The positive and negative radial deformations are caused by the constraint of the pad pivot, at which at displacement is constrained to be zero.

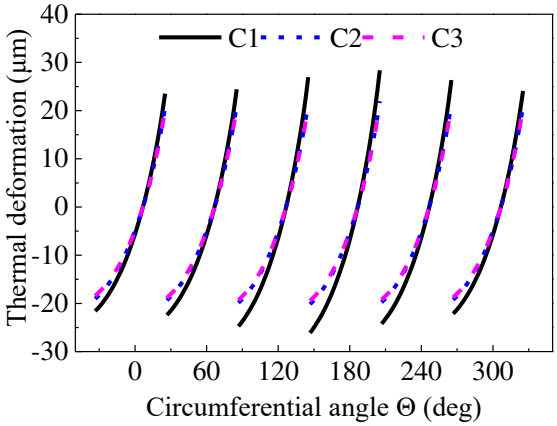


Fig. 5-12 Effect of relative clearance on the thermal deformation in radial direction

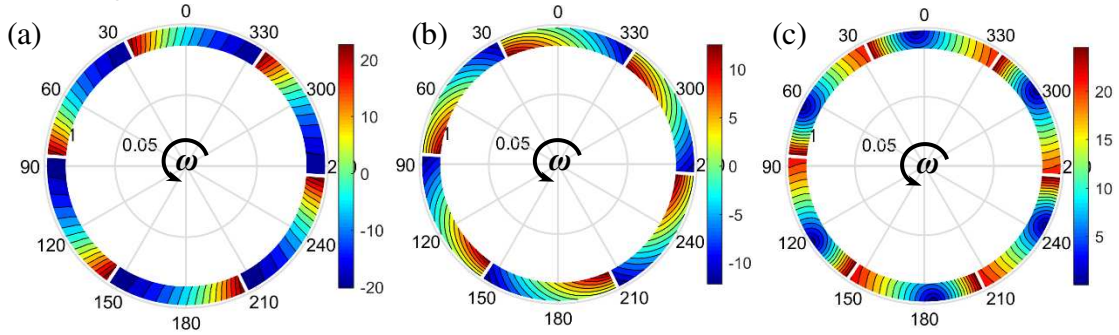


Fig. 5-13 Thermal deformation (μm) of each Ag coated pad in the clearance of C2, (a) in radial direction, (b) in circumferential direction and (c) total deformation

5.4.2 TEHD behavior in different coating materials

Fig. 5-14 shows the thermal properties of CTPJBs with Ag, graphite and PTFE coatings. The applied load is 7.5 kN, the shaft speed is 8k rpm and the relative clearance is C2 in Table 5-3. Fig. 5-14(a) presents the temperature of PTFE coating is slightly lower than graphite and Ag coatings at the leading edge, but at the trailing edge its temperature is about 20℃ which is higher than the other two coatings (in

Fig. 5-14(b)). The maximum radial thermal deformation of PTFE coating is about 10 μm which is obviously smaller than the other two coatings (Fig. 5-14(c)). In Fig. 5-14(d), the maximum pressure p_{max} of Ag coating is about 7.0 MPa which is 3.0% higher than graphite coating, and 11.1% higher than PTFE coating. Though the h_{min} of PTFE coating is small, its maximum HD pressure p_{max} is not high because of the formation of active HD pressure on each pad.

Fig. 5-15 shows the temperature distribution of different coatings in the middle plane of the bearing. Similar to 4.5.2, it is clear that the PTFE coating hinders the heat transfer to the basement which lead to a colder pad. The graphite and Ag coatings do not hinder the heat transfer to the pad.

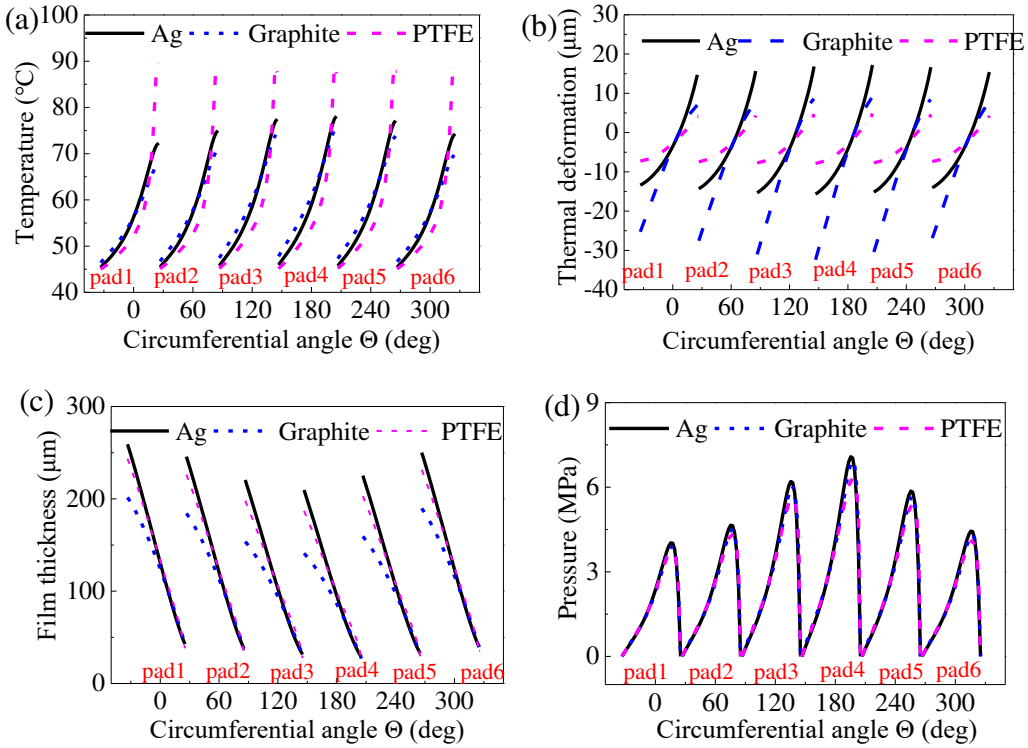


Fig. 5-14 Effect of coating materials on (a) temperature, (b) radial thermal deformation, (c) film thickness and (d) HD pressure of CTPJBs

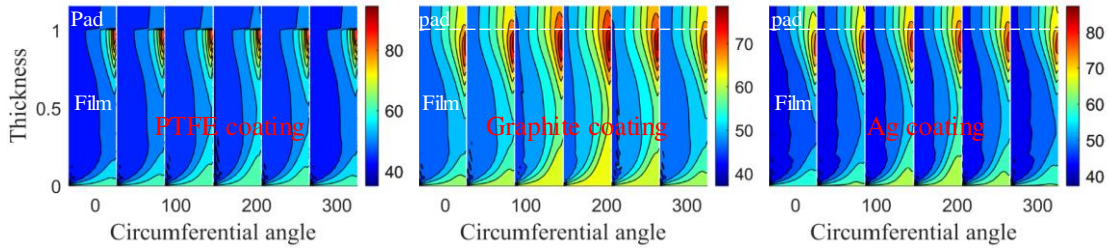


Fig. 5-15 Temperature distribution in the middle plane of CTPJBs

5.4.3 Effect of operating conditions on temperature

Fig. 5-16 shows influence of shaft speed on the temperature and HD pressure of six-pad CTPJBs. The applied load is 5kN and the bearing clearance is C1 in Table 5-3. The high speed leads to the high maximum temperature of the oil film at each pad (Fig. 5-16 (a)) and great the peak HD pressure of each pad (Fig. 5-16 (b)).

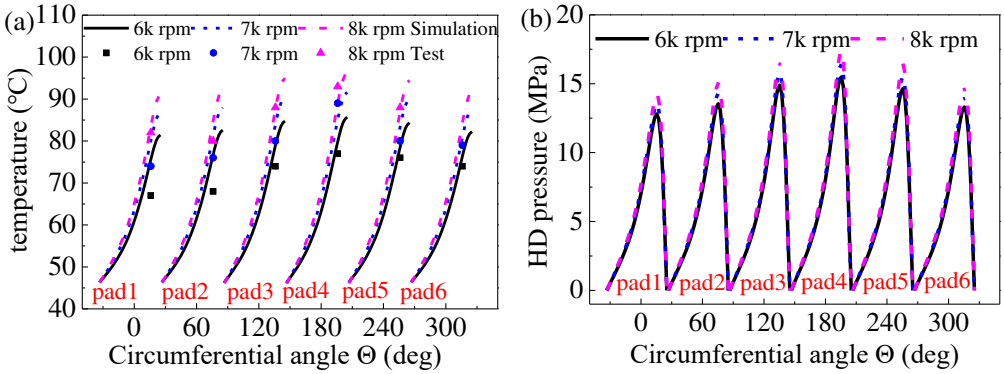


Fig. 5-16 (a) Temperature and (b) HD pressure of CTPJBs at different shaft speeds

Fig. 5-17 demonstrates the thermal hydrodynamic properties of CTPJBs at film-coating interface under different applied loads. The shaft speed is 6k rpm and the bearing clearance is C1 in Table 5-3. It can be seen that the maximum temperature is higher in heavier load. For the HD pressure, the slight load (5kN) can generates a larger maximum pressure at pad 1, 2, and 6. In total, the differences of temperature and pressure in different loads are quite slight.

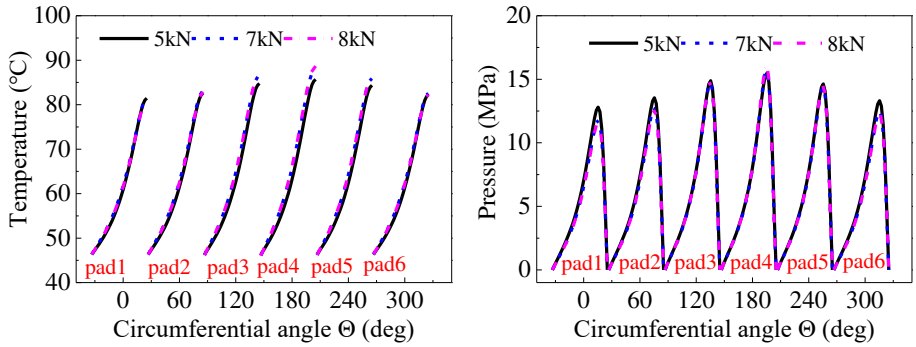


Fig. 5-17 (a) Temperature and (b) HD pressure of CTPJBs under different applied loads

5.5 Thermal and wear properties of micro-clearance coated bearings

In order to understand the characteristics of coated bearings in micro-clearance (less than 1.0‰), this section aims to test the temperature of different coated bearings, including PTFE coating, silver (Ag) coating and graphite coating. The adopted bearing clearance is the initial clearance C0 in Table 5-3.

5.5.1 Test of PTFE coated bearing

The pads of the polymer-coated hydrodynamic bearings are prone to be burn in micro-clearance because of the rapid temperature rise. As shown in Fig. 5-18, the temperature and pressure of the PTFE coated bearing with the applied load of 4 kN and shaft speed of 6k rpm are tested. The relative clearance after installation is 0.38‰. The temperature of the 3# sensor in Fig. 5-5 is used. As shown in Fig. 5-18(a), the pad temperature continues to rise due to the continuous increase in the temperature of the feeding temperature. The temperature of pad 3 and pad 4 on the loading side is the highest, followed by pad 5.

Moreover, it can be seen in Fig. 5-18(b) that each pad does not generate a stable HD pressure. After the experiment, the PTFE coating on the pads are worn seriously with the coating peeling off from the basement (Fig. 5-19). It can be deduced that the stable hydrodynamic lubrication is not formed, and the bearing has been working in the mixed lubrication regime, because the quite small relative clearance leads to high temperature and results in bearing seizures. In this case, the simulation is also unable to obtain a convergence result due to the negative film thickness caused by the thermal deformations. In view of this, the PTFE coated bearing in micro-clearance is unsuitable for high speed and heavy load tests.

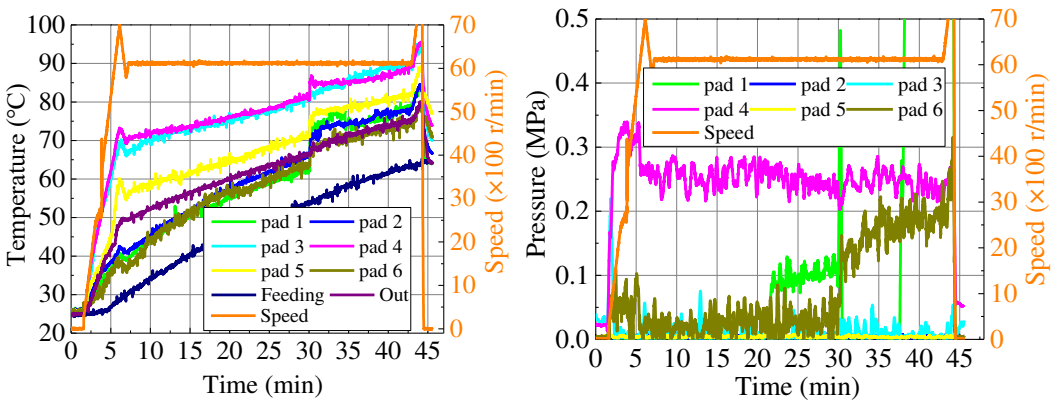


Fig. 5-18 (a) Temperature and (b) HD pressure of the PTFE coated pads under 6k rpm and 4 kN

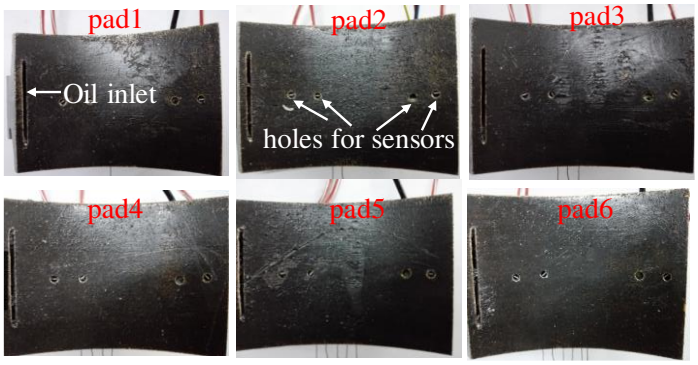


Fig. 5-19 Surface topography of the PTFE coated pads after several tests

5.5.2 Test of Graphite coated bearing

In order to understand the wear of the graphite coated bearing, the temperature of each pad is shown in Fig. 5-20. The applied load is 5 kN and the temperature of the 3# sensor in Fig. 5-5 is used. The bearing start-stop several times. In Fig. 5-20 (a), at 6k rpm of the shaft speed, it can be seen the temperature of each pad is stable, even though the temperature of pad 4 is as high as 160℃ and the temperature of pad 3 also reaches 150℃, so the bearing can run normally. In Fig. 5-20 (b), when the speed is lifted up to 7k rpm, the temperature cannot be stabilized. It can be inferred that the bearing cannot operate normally at higher speed due to the high temperature. The bearing coating and shaft have undergone large thermal deformation which lead to smaller bearing clearance, and the oil film cannot be formed.

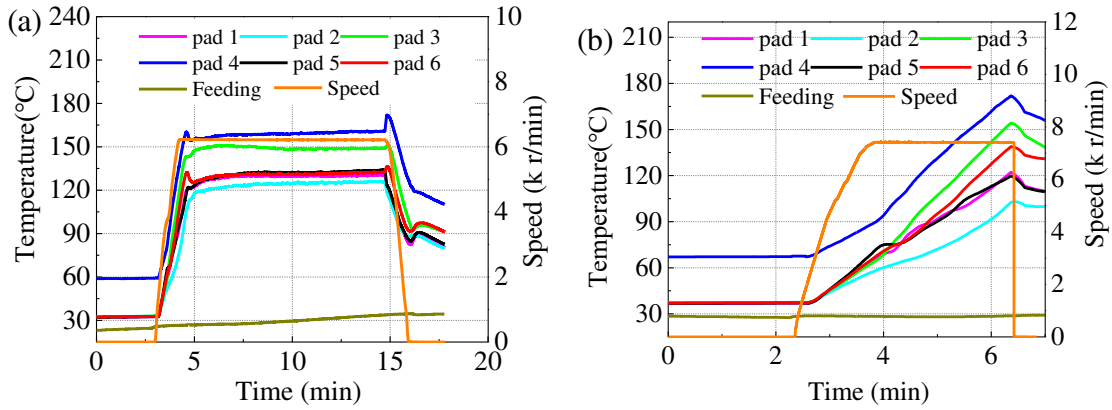


Fig. 5-20 Temperature of different Graphite coated pads at (a) 6k rpm and (b) 7k rpm

After several tests, the surface topography of the graphited bearing is shown in Fig. 5-21. The wear and scratch on the pad surfaces are obvious, and cracks can be seen on the worn surfaces. Also, the wear debris are accumulated on the pad surfaces. The failure mode is quite different from that of the PTFE coating in Fig. 5-19.



Fig. 5-21 Surface topography of graphite coated pads after several test

5.5.3 Test of silver (Ag) coated bearing

Fig. 5-23 shows the temperature of Ag coated pads. The applied load is 7.5 kN, the shaft speed is 8k rpm, and temperature of the 3# sensor in Fig. 5-5 is used. The temperature of each pad can be stable and the bearing is running under hydrodynamic lubrication. Similar to the PTFE and graphite coated bearings, the temperature of pad 4 and pad 3 on the loading side are relatively high. For Ag coated bearing, the bearing in micro-clearance can operate normally.

After several start-stop and cumulative test, the surface morphology of each pad is shown in Fig. 5-23. Scratches appeared on the surface of each pad, and serious wear occurred at the edge of each pad and the oil inlet, and the interlayer copper was exposed. Since the wear in hydrodynamic lubrication is quite small, and it can be inferred that the wear on the surface of the bearing pad is caused by solid contact during the startup and shutdown.

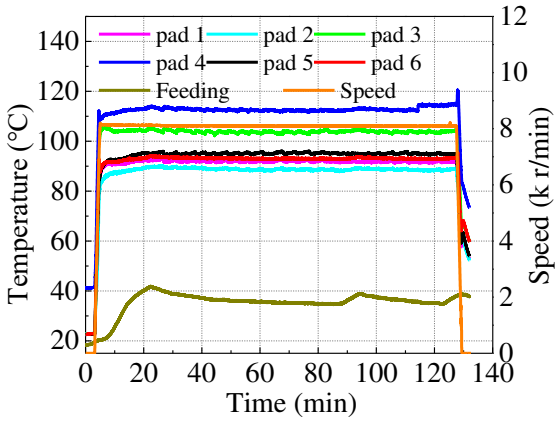


Fig. 5-22 Temperature of different Ag coated pads



Fig. 5-23 Surface topography of Ag coated pads after several test

Generally, the PTFE coating is widely used in the bearings, but it presents worse performance in micro-clearance cases during starting up under applied load. This because the PTFE coating is easily peeled off from the interlayer under the surface contact, and the abrasive grain easily block the inlet resulting in the unformed film. Though the graphite and Ag coatings are also worn, they can still enable the bearing to run.

5.6 Thermal behavior of the coated bearings during startup

Based on the micro-clearance bearing test in Section 5.4.1, even if the coated bearing can operate normally in a stationary state, there are still obvious scratches or wear appear on the pad surfaces, because the shaft and the pads contact with each other during the startup process under heavy load. In this section, the thermal behavior during startup process of the bearing is studied.

5.6.1 Temperature rise in different relative clearances

It can be seen in section 5.5 that the temperature rise of pad 3 and pad 4 on the loading side is the largest, so in this section the temperature rise of pad 3 and pad 4 is discussed during startup.

Fig. 5-24 shows the effect of relative clearance on the temperature rise during startup. The applied load is 7.5 kN. The shaft speed takes 2.2 min to increase from zero to 8k rpm. The small relative clearance generates the fast increase in temperature rise and yields the high stable temperature. The temperatures in different relative clearances almost reach the stable temperature at the same time. This is because the bearing with large clearance has a large amount of oil flow in the clearance, and the oil takes away more heat. Also, the shear rate of oil film in large film thickness of large clearance is small, so that the generated heat is less. The fluctuation of the temperature in stationary state is caused by the fluctuation of the feeding temperature.

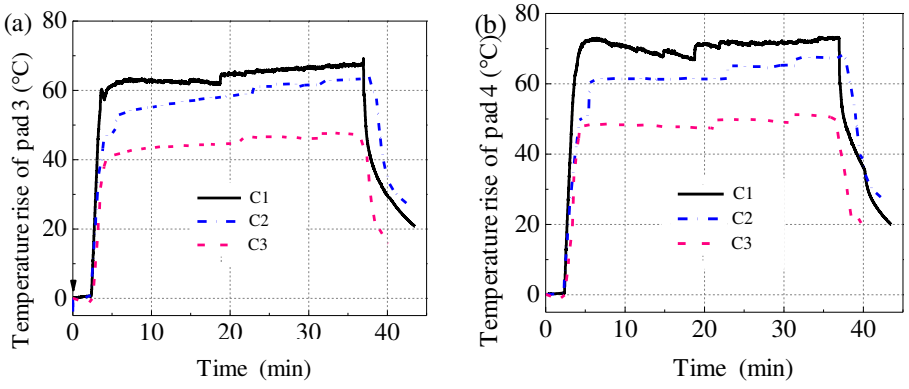


Fig. 5-24 Temperature rise of (a) pad 3 and (b) pad 4 during startup in different relative clearances

5.6.2 Temperature rise in different accelerations

Fig. 5-25 shows the variation of the shaft speed and temperature of pad 3 in different linear accelerations during start-stop process. The applied load is 5 kN and the relative clearance is C1 in Table 5-3. The shaft accelerates from zero to 7.3 rpm in 70 s, 150 s and 204 s corresponding to Acceleration 1, 2 and 3 as shown in Fig. 5-25 (a).

In Fig. 5-25 (b) and (c), it can be seen that the period of rapid temperature rise is consistent with the acceleration time. The great acceleration causes the fast temperature rise during startup. It easily causes bearing seizures because the heat cannot transfer to the bush in time. After the acceleration process is completed, the temperature increases slowly, and the temperature rise is almost same in stationary state. During shutdown, because the temperature decreases, which cannot cause thermal failures of the bearing, we mainly discuss the startup process.

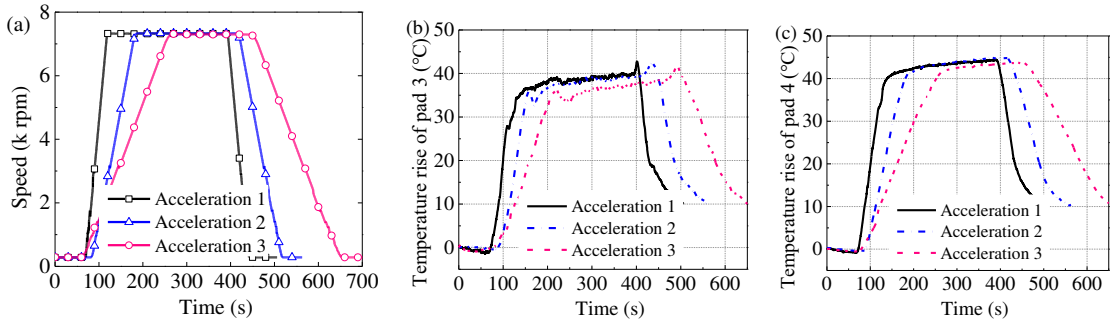


Fig. 5-25 Effect of acceleration on temperature rise of pad 3 and pad 4, (a) shaft speed, (b) temperature rise of pad 3 and (c) temperature rise of pad 4

Fig. 5-26 shows the variation of the shaft speed and temperature of pad 3 in different acceleration modes during start-stop process. The applied load is 5 kN and the bearing clearance is C1 in Table 5-3. It shows that the shaft accelerates from zero to 7.3k rpm (or decelerates from 7.3k rpm to zero) in 150 seconds in acceleration mode of linear and cosine respectively. The difference of these two modes is that the linear acceleration is constant, but for cosine acceleration mode, the acceleration first increases and then decreases, and the acceleration is zero at the beginning and end of acceleration.

It can be seen in Fig. 5-26 that the temperature rises in the same mode with the acceleration of the shaft speed, i.e. the temperature rises along the shaft speed in linear or cosine mode. The acceleration mode has little influence on the steady temperature. In order to avoid the temperature rises fast at the very beginning of startup, the selection of a cosine type acceleration mode with small initial acceleration is beneficial to thermal startup.

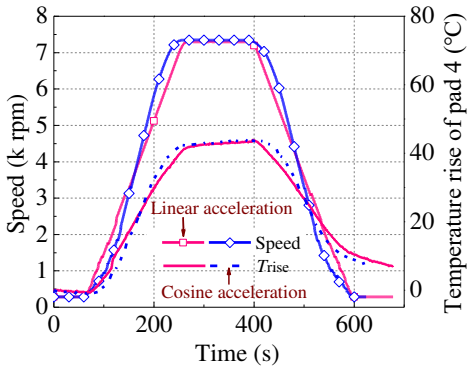


Fig. 5-26 Effect of acceleration mode on temperature rise of pad 4

5.6.3 Temperature rise in different initial temperatures

Fig. 5-27 shows the influence of initial temperature on the temperature rise during startup. The shaft starts up linearly from zero to 8.8k rpm in 1.8 minutes. The relative clearance is the value C3 in Table 5-3, and the applied load is 7.5 kN. The oil feeds into the static bearing in the first 2.5 min. In the high initial temperature, the feeding temperature is 35℃ and the temperature of each pad is about 42℃. In the low initial temperature, the feeding temperature is 25℃ and the temperature of each pad is about 26℃. the temperature difference of the pads of the two initial states is 16℃. The bearings arrive at the steady temperature almost at the same time. The temperature rise of pad 4 in high initial temperature is about 47.1℃ which is about 12.3℃ lower than that in low initial temperature. It can be deduced that the temperature rises faster in low initial temperature.

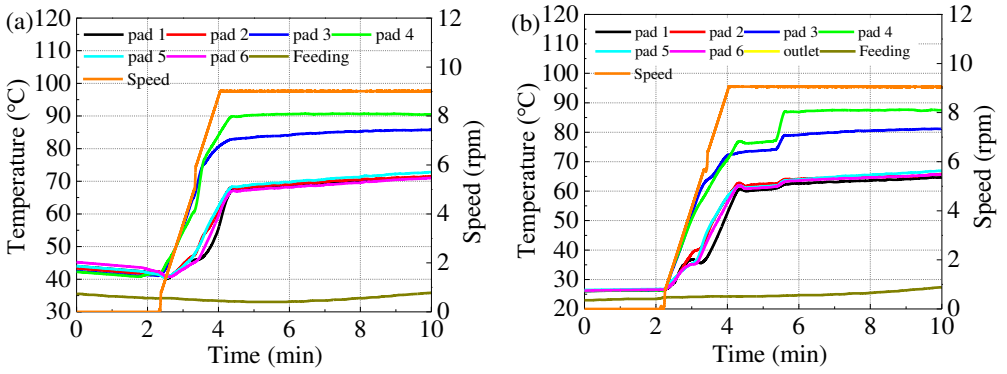


Fig. 5-27 Influence of initial temperature on temperature rise during startup, (a) high initial temperature and (b) low initial temperature

5.7 Conclusions

This chapter studies the thermal and wear properties of the six-pad CTPJBs in both steady and star-stop state under heavy loads. The conclusions are

(1) During startup under heavy load, coatings are obviously worn, and the temperature of the pad in the loading side rises quickest and the stable temperature is also highest. The oil temperature of the PTFE coated bearing is the highest, which easily causes bearing failure. The temperature difference of Ag and graphite coatings is small, but the Ag coating is more likely to enable the bearing to run under extreme conditions.

(2) Theoretically, the convergence film region at each pad is formed, i.e. there is no cavitation, and the HD force of each pad can offset with each other. The relative gap has obvious impact on the maximum HD pressure, but the influence of shaft speed and applied load is small.

(3) During startup, the temperature of CTPJBs increases fast in small relative clearance and low initial temperature cases. The temperature increases in the same way with shaft speed. The great acceleration causes the fast temperature rise. The acceleration mode only affects the form of temperature increase, and has no influence on the stable temperature. Large relative clearance, small acceleration (or small initial acceleration) and high initial temperature are conducive to the safe thermal startup of the CTPJBs.

Conclusions

Aiming at the coated journal bearings that start up and shut down under heavy load without hydrostatic supporting, the transient contact behavior is analyzed firstly, and the worn properties are presented. Then the thermal slip behavior at film-coating interface is analyzed, and the selection method of the slip zone (coating zone) under heavy load in isothermal condition and considering thermal slip behavior is given. The experiments are conducted to explore the stationary and transient thermal behavior of the coated tilting pad journal bearings (CTPJBs) used in gas turbine.

The key conclusions of this work are as follows:

(1) A mixed lubrication model is established considering both surface contact and hydrodynamic lubrication during startup and shutdown of plain journal bearings. The transient contact behavior and worn problem of the shaft-bush surface under applied load are analyzed. The results show that the contact zone during startup can be as large as 8 times, and the volume wear (in the order of 10^{-4} mm^3) is 10^3 times of that during shutdown. The contact and wear mainly occur in the early period of startup. Smooth surface and large relative clearance are helpful to reduce contact zone and volume wear during startup. Smooth surface and small relative clearance are beneficial to reduce surface wear during shutdown.

(2) During startup, small acceleration generates small contact zone, but there exists an optimal acceleration to minimize the volume wear. During shutdown, small deceleration results in large contact zone and volume wear. When the deceleration is small enough, the shaft will slide along the bush surface for a while then rolling to the standstill position, and the contact zone and volume wear rise up to the same order with that during startup. When the deceleration is large enough, the shaft will purely roll to the standstill, and the contact zone and volume which occur close to the standstill position are so small that can be neglected.

(3) Based on the two-component slip model, a thermoelastohydrodynamic (TEHD) model considering slip effect (TEHDS) is established. The temperature distributing across the film-coating-interlayer-basement area is obtained. The influence of operating conditions on the thermal properties of coated bearings is analyzed. The results show that the slip effect is more effective to reduce the maximum temperature (T_{max}) in large relative clearance and high speed, but this effect is weaken in high feeding temperature. Wall slip is possible to elevate the minimum film thickness (h_{min}) in high shaft speed.

(4) The influence of the slip zone on the hydrodynamic (HD) behavior of the journal bearing is analyzed, and the selection criteria for the slip zone under heavy load in isothermal case is determined. The axial width of the slip zone should be increased, that is, the width of the slip zone should be set as the width of the bearing. In heavy load, the slip zone should be located within the convergence region of the film in the circumferential direction and the tailing end of the zone is close to the position of h_{min} to increase the HD force and decrease the friction coefficient.

(5) The influence of PTFE coating position on the thermal slip behavior of the journal bearing under constant load is discussed. When the coating zone is located in the convergence film region and the tailing end is far from the position of h_{min}, the coatings have very slight effect on the T_{max} and h_{min}. When the coating tailing end is located in the film divergence gap and far away from the position of h_{min}, the slip effect can reduce the T_{max}, but it also decreases h_{min} which would lead to the reduction in HD force. Without further texture design, the tailing end of the coating should be avoided imposing close to the position of h_{min}. If the PTFE coating is too thick, the coating can deform inwardly, which increases the risk of bearing seizures. Graphite and DLC coatings with better thermal conductivity can further improve this drawback.

(6) According to the test analysis of coated tilting pad journal bearing (CTPJB), it can be seen that the PTFE, graphite and silver (Ag) coatings are obviously worn during startup under heavy loads. The temperature of PTFE coated bearing is the highest and the worn coating can enable the bearing failure. The temperature difference between the Ag coating and the graphite coating is small, but the silver coating is more likely to enable the bearing to run in extreme conditions. Theoretically, each pad forms a convergent film, the cavitation does not appear, and the HD force of each pad can offset with each other. The relative clearance has an obvious impact on the P_{max}, while the influence of speed and applied load are small.

(7) During startup, in small relative clearance and low initial temperature, the temperature increases fast. The temperature rise is in consistent with the acceleration. The large acceleration leads to the fast increase in temperature. If the speed accelerates in linear or cosine mode, the temperature will rise in linear or cosine mode. Large relative clearance, small acceleration and high initial temperature are conducive to safe thermal startup of the CTPJBs.

The Perspectives are as follows

Based on the optimized slip zone selected in this paper, the manufacturing and texture design of the wall slip zone can be carried out, and low-viscosity lubricating oil can be developed to test the hydrodynamic and thermal performance of the journal bearings.

Reference

[1] Gertzos K P, Nikolakopoulos P G, Chasalevris A C, et al. Wear identification in rotor-bearing systems by measurements of dynamic bearing characteristics[J]. Computers & Structures, 2011, 89(1): 55-66.

[2] Dufrane K F, Kannel J W. Thermally induced seizures of journal bearings[J]. Journal of Tribology, 1989, 111(2): 288-292.

[3] Zhi Z. Analysis and Treatment on the high temperature of titling - pad bearing of 630MW Steam Turbine[J]. Science & Technology Vision, 2018, 000(003):153-154.

[4] Kango, S., Shukla, D.K., Sharma, N., Arif, M.: Implication of surface texture and alip on hydrodynamic fluid film bearings: a comprehensive survey, Tribology Online, 2020, 15, 265-282

[5] Jin J, Zhang G.X, Wang X.J., Experiment and simulations on lubrication performance of EMP journal bearing. Journal of Shanghai University (English Edition), 2004, 8(1): 85-89.

[6] Monmousseau P, Fillon M. Transient thermoelastohydrodynamic analysis for safe operating conditions of a tilting-pad journal bearing during startup[J]. Tribology International, 2000, 33(3–4): 225-231.

[7] Conway-Jones J M, Leopard A J. Plain bearing damage[C]//Proc. 4'"Turbomachinery Symposium. 1975: 59-63.

[8] Gustafson R E. Behavior of a Pivoted-Pad Thrust Bearing During Startup[J]. J. of Lubrication Tech, 1967, 89(2): 134-142.

[9] Mokhtar M. O. A., R. B. Howarth, P. B. Davies. Wear characteristics of plain hydrodynamic Journal bearings during repeated starting and stopping[J]. Tribology Transactions, 1977, 20(3):191-194.

[10] Mokhtar M O A, Howarth R B, Davies P B. The behavior of plain hydrodynamic journal bearings during starting and stopping[J]. ASLE Transactions, 1977, 20(3): 183-190.

[11] Fillon, Michel, Bligoud, JeanClaude, Frene, Jean. Experimental study of tilting-pad journal bearings-Comparison with theoretical thermoelastohydrodynamic results[J]. Journal of Tribology, 1992, 114(3): 587-588.

[12] Desbordes H, Fillon M, Wai C C H, et al. Dynamic analysis of tilting-pad journal bearing-influence of pad deformations[J]. Journal of Tribology, 1994,

116(3): 621-628.

[13] Monmousseau P, Fillon M, Frene J. Transient thermoelastohydrodynamic study of tilting-pad journal bearings—Comparison Between Experimental Data and Theoretical Results[J]. Journal of Tribology, 1997, 119(3): 401-407.

[14] Kucinschi B, Fillon M. An Experimental Study of Transient Thermal Effects in a Plain Journal Bearing[J]. Journal of Tribology, 1999, 121(2): 327-332.

[15] Harnoy A. Model-Based Investigation of Friction During Startup of Hydrodynamic Journal Bearings[J]. Journal of Tribology, 1995, 117(4): 667-673.

[16] Kucinschi B R, Fillon M, Frêne J, et al. A Transient Thermoelasto-hydrodynamic Study of Steadily Loaded Plain Journal Bearings Using Finite Element Method Analysis[J]. Journal of Tribology, 2000, 122(1): 219-226.

[17] Ettles C M, Knox R T, Ferguson J H, et al. Test results for PTFE-faced thrust pads, with direct comparison against Babbitt-faced pads and correlation with analysis[J]. Journal of Tribology, 2003, 125(4): 814-823.

[18] Wang X, Zhang Z, Pan J. A Transient Thermoelastohydrodynamic Analysis of a Tilting-Pad Thrust Bearing During Startup[C]// 3rd World Tribology Congress, Washington, USA. 2005: 149-150.

[19] Lu X, Khonsari M M. On the Lift-off Speed in Journal Bearings[J]. Tribology Letters, 2005, 20(3-4): 299-305.

[20] Lu X, Khonsari M M. An Experimental Investigation of Grease-Lubricated Journal Bearings[J]. Journal of Tribology, 2007, 129(1): 84-90.

[21] Bouyer J, Fillon M. Behaviour of a hydrodynamic journal bearing: torque measurement during startup[C]// ROTRIB ’07, 10th International conference of tribology, Bucharest, Romania, 2007: 53-57.

[22] Bouyer J, Fillon M. Experimental measurement of the friction torque on hydrodynamic plain journal bearings during startup[J]. Tribology International, 2011, 44(7–8): 772-781.

[23] Bouyer J, Fillon M. Experimental Investigation on the influence of surface roughnesses and bearing materials on the friction coefficient during startup[C]// Proceedings of the STLE Annual Meeting and Exhibition, LasVegas, NV, USA, 2010, 1–3.

[24] Bouyer J, Fillon M, Valle V. Stick-slip phenomenon induced by friction in a plain journal bearing during startup[C]// 4th World tribology congress, Kyoto, Japan. 2009, 101.

[25] Adatepe H, Durak E, Biyiklioğlu A. Experimental study of the effect of additive on the tribological properties journal bearing under running-in and

startup or shutdown stages[J]. Industrial Lubrication & Tribology, 2008, 60(3): 138-146.

[26] Mehala K, Bendaoud N, Youcefi A. Evolution of the lubrication regime of a cylindrical journal bearing in the starting phase[J]. Industrial Lubrication & Tribology, 2014, 66(3): 379-386.

[27] Liu H C, Guo F, Zhang B B, et al. Behavior of hydrodynamic lubrication films under non-steady state speeds[J]. Tribology International, 2016, 93:347-354.

[28] Sang M C, Khonsari M M. Wear simulation for the journal bearings operating under aligned shaft and steady load during startup and coast-down conditions[J]. Tribology International, 2016, 97: 440-466.

[29] Cristea A F, Bouyer J, Fillon M, et al. Transient Pressure and Temperature Fields Measurements in a Lightly Loaded Circumferential Groove Journal Bearing from Startup to Steady-State Thermal Stabilization[J]. Tribology Transactions, 2017, 60(6): 988-1010.

[30] Xiang G, Han Y. Study on the tribo-dynamic performances of water-lubricated microgroove bearings during startup[J]. Tribology International, 2020, 151: 106395.

[31] Xiang G, Han Y, He T, et al. A Dynamic Wear Model for Micro-Grooved Water-Lubricated Bearings Under Transient Mixed Lubrication Condition[J]. Journal of Tribology, 2020, 142(7): 071701.

[32] Xiang G, Han Y, He T, et al. Transient tribo-dynamic model for journal bearings during startup considering 3D thermal characteristic[J]. Tribology International, 2020, 144: 106123.

[33] Zhang D, Ho J K L, Dong G, et al. Tribological properties of Tin-based Babbitt bearing alloy with polyurethane coating under dry and starved lubrication conditions[J]. Tribology International, 2015, 90: 22-31.

[34] Cao J, Yin Z, Li H, et al. Tribological studies of soft and hard alternated composite coatings with different layer thicknesses [J]. Tribology International, 2017, 110: 326-332.

[35] Simmons J E L, Knox R T, Moss W O. The development of PTFE (polytetrafluoroethylene)-faced hydrodynamic thrust bearings for hydrogenerator application in the United Kingdom[J]. Proceedings of the Institution of Mechanical Engineers, Part J: Journal of Engineering Tribology, 1998, 212(5): 345-352.

[36] Babu M V S, Krishna A R, Suman K N S. Review of journal bearing materials and current trends[J]. American Journal of Materials Science and Technology, 2015, 4(2): 72-83.

[37] Zhou J, Blair B, Argires J, et al. Experimental performance study of a high speed oil lubricated polymer thrust bearing[J]. Lubricants, 2015, 3(1): 3-13.

[38] Swann M K, Watkins J, Bornstein K R. Present limits of operation of product lubricated and magnetic bearings in pumps[C]// Proceedings of the 14th International Pump Users Symposium. Texas A&M University. Turbomachinery Laboratories, 1997, 113-127.

[39] Lan P, Meyer J L, Vaezian B, et al. Advanced polymeric coatings for tilting pad bearings with application in the oil and gas industry[J]. Wear, 2016, 354-355: 10-20.

[40] Bashandeh K, Lan P, Meyer J L, et al. Tribological performance of graphene and PTFE solid lubricants for polymer coatings at elevated temperatures[J]. Tribology Letters, 2019, 67(3): 1-14.

[41] Glavatskih S B. Evaluating thermal performance of a PTFE-faced tilting pad thrust bearing[J]. J. Trib., 2003, 125(2): 319-324.

[42] McCarthy D M C, Glavatskih S B, Sherrington I. Oil-film thickness and temperature measurements in PTFE and babbitt faced tilting-pad thrust bearings[J]. Proceedings of the Institution of Mechanical Engineers, Part J: Journal of Engineering Tribology, 2005, 219(3): 179-185.

[43] McCarthy D M C, Glavatskih S B. Assessment of polymer composites for hydrodynamic journal‐bearing applications[J]. Lubrication Science, 2009, 21(8): 331-341.

[44] Fillon M, Glavatskih S B. PTFE-faced centre pivot thrust pad bearings: Factors affecting TEHD performance[J]. Tribology International, 2008, 41(12): 1219-1225.

[45] Glavatskih S B, Fillon M. TEHD analysis of thrust bearings with PTFE-faced pads[J]. Journal of Tribology, 2006, 128(1): 49-58.

[46] Mahieux C A. Experimental characterization of the influence of coating materials on the hydrodynamic behavior of thrust bearings: a comparison of Babbitt, PTFE, and PFA[J]. Journal of Tribology, 2005, 127(3): 568-574.

[47] Katsaros K, Bompos D A, Nikolakopoulos P G, et al. Thermal–Hydrodynamic Behaviour of Coated Pivoted Pad Thrust Bearings: Comparison between Babbitt, PTFE and DLC[J]. Lubricants, 2018, 6(2): 50.

[48] Weissbacher C, Kiefel A, Blumenthal H, et al. Performance of a Direct Bonded Sub-Millimeter Peek Coating for Hydrodynamic Plain Bearings [J]. Journal of Tribology, 2021, 143(10): 101801.

[49] Jahanmir S, Hunsberger A Z, Heshmat H. Load capacity and durability of H-DLC coated hydrodynamic thrust bearings[J]. Journal of Tribology, 2011,

133(3): 031301.

[50] Hong Y S, Lee S R, Kim J H, et al. Application of a DLC-Coating for improving hydrostatic piston shoe bearing performance under mixed friction conditions[J]. International Journal of Precision Engineering and Manufacturing, 2015, 16(2): 335-341.

[51] Rodriguez-Lelis J M, Vela-Arvizo D, Abundez-Pliego A, et al. Effect on the Film Pressure Distribution on a Hydrodynamic Tilting Pad Bearing Caused by the Coating of the Journal With DLC by Triboadhesion[C]// ASME-STLE International Joint Tribology Conference, San Diego, USA. 2007, 48108: 281-283.

[52] Prase B, Leidich E. Characteristics of hydrodynamic plain bearings with bonded coating[C]// Nordtrib-2016, 17th Nordic Symposium on Tribology, Aulanko, Finland. 2016, 1-5..

[53] Thomsen K, Klit P. A study on compliant layers and its influence on dynamic response of a hydrodynamic journal bearing[J]. Tribology International, 2011, 44(12): 1872-1877.

[54] Pap B, Fillon M, Guillemont M, et al. Experimental and Numerical Analysis on the Seizure of a Carbon-Filled PTFE Central Groove Journal Bearing during Startup Period[J]. Lubricants, 2018, 6(1): 14.

[55] Summer F, Grün F, Offenbecher M, et al. Challenges of friction reduction of engine plain bearings–Tackling the problem with novel bearing materials[J]. Tribology International, 2019, 131: 238-250.

[56] Stephan K, Holzer A, Megahed S, et al. Investigation of the coating of hydrodynamic plain bearing contact surfaces by means of Extreme High-Speed Laser Material Deposition (EHLA)[C]// IOP Conference Series: Materials Science and Engineering. IOP Publishing, 2021, 1097(1): 012016.

[57] Vandoni L, Demir A G, Previtali B, et al. Wear behavior of fiber laser textured TiN coatings in a heavy loaded sliding regime[J]. Materials, 2012, 5(11): 2360-2382.

[58] Zhang G, Yuan X, Dong G. The tribological behavior of Ni–Cu–Ag-based PVD coatings for hybrid bearings under different lubrication conditions[J]. Tribology International, 2010, 43(1-2): 197-201.

[59] Mubarok F, Armada S, Fagoaga I, et al. Thermally sprayed SiC coatings for offshore wind turbine bearing applications[J]. Journal of thermal spray technology, 2013, 22(8): 1303-1309.

[60] Grün F, Gódor I, Gärtner W, et al. Tribological performance of thin overlays for journal bearings[J]. Tribology international, 2011, 44(11): 1271-1280.

[61] Neto C, Evans D R, Bonaccurso E, et al. Boundary slip in Newtonian liquids: a review of experimental studies[J]. Reports on progress in physics, 2005, 68(12): 2859-2897.

[62] Girared PS. Mémoires de la classe des Sciences Mathématiques et Physiques de l'Institut Impérial de France, 1815, 14: 329.

[63] Prony R. Recherches physico-mathématiques sur la théorie des eaux courantes[M]. Imprimerie impériale, 1804.

[64] Ma, G.J., Wu, C.W., Zhou, P.: Wall slip and hydrodynamics of two-dimensional journal bearing[J]. Tribology International, 2007, 40: 1056-1066

[65] Thompson P A, Troian S M. A general boundary condition for liquid flow at solid surfaces[J]. Nature, 1997, 389: 360-362.

[66] Spikes H, Granick S. Equation for Slip of Simple Liquids at Smooth Solid Surfaces[J]. Langmuir, 2003, 19(12): 5065-5071.

[67] Wang J Y, Betelu S, Law B M. Line tension approaching a first-order wetting transition: experimental results from contact angle measurements[J]. Physical Review E Statistical Nonlinear & Soft Matter Physics, 2001, 63(1): 031601.

[68] Sbragaglia M, Prosperetti A. A note on the effective slip properties for microchannel flows with ultrahydrophobic surfaces[J]. Physics of Fluids, 2007, 19(4): 43603.

[69] Guo, L., Wong, P.L., Guo, F.: Boundary yield stress and interfacial potential energy barrier in thin film hydrodynamic lubrication[J]. Triboloy Letters, 2016, 62(1): 1-8.

[70] Yu X, Meng Y, Tian Y, et al. Measurement of lubricant viscosity and detection of boundary slip at high shear rates[J]. Tribology International, 2016, 94: 20-25.

[71] Lili W. Study on Wall Slip and Cavitation Mechanism of a High Speed Journal Bearing [D]. Shandong University, Jinan China, 2012,

[72] Kalin M, Velkavrh I, Vižintin J. The Stribeck curve and lubrication design for non-fully wetted surfaces[J]. Wear, 2009, 267(5–8): 1232-1240.

[73] Evans R.D., Cogdell J.D., Richter G.A. , et al. Traction of lubricated rolling contacts between thin-film coatings and steel[J]. Tribology Transactions, 2008, 52(1): 106-113

[74] Choo J.H., Glovnea R.P., ForrestA.K., et al. A low friction bearing based on liquid slip at the wall[J] Journal of Tribology, 2007, 129(3): 611–620.

[75] Zhang H , Liu Y , Hafezi M, et al. A distribution design for circular concave textures on sectorial thrust bearing pads[J]. Tribology International, 2019, 149: 105733.

[76] Bailey N Y, Cliffe, K A, Hibberd S et al.. Dynamics of a high speed coned thrust bearing with a Navier slip boundary condition[J]. Journal of Engineering Mathematics, 2016, 97: 1-24.

[77] Tauviqirrahman M, Ismail R, Jamari J, et al. Combined effect of texturing and boundary slippage in lubricated sliding contacts[J]. Tribology International, 2013, 66: 274-281.

[78] Fatu A, Maspeyrot P, Hajjam M. Wall slip effects in (elasto) hydrodynamic journal bearings[J]. Tribology International, 2011, 44(7-8): 868-877.

[79] Ma G J, Wu C W, Zhou P. Influence of Wall Slip on the Dynamic Properties of a Rotor-Bearing System[J]. Tribology Transactions, 2008, 51(2): 204-212.

[80] Lv F, Rao Z, Ta N, et al. Mixed-lubrication analysis of thin polymer film overplayed metallic marine stern bearing considering wall slip and journal misalignment[J]. Tribology International, 2017, 109: 390-397.

[81] Ismail S, Sarangi M. Effects of texture shape and fluid–solid interfacial slip on the hydrodynamic lubrication performance of parallel sliding contacts[J]. Proceedings of the Institution of Mechanical Engineers Part J Journal of Engineering Tribology, 2014, 228(4): 382-396.

[82] Rao P, Agarwal S. Effect of permeability and different slip velocities at both the porous interface using couple stress fluids on the slider bearing load carrying mechanism[J]. Proceedings of the Institution of Mechanical Engineers, Part J: Journal of Engineering Tribology, 2016, 230(2): 196-201.

[83] Rao T V V L N, Rani A M A, Wang M, et al. Stability evaluation of three-layered journal bearing with slip/partial slip[J]. Industrial Lubrication and Tribology, 2017, 69 (3): 334-341.

[84] Bhattacharya A, Dutt J K, Pandey R K. Influence of hydrodynamic journal bearings with multiple slip zones on rotordynamic behavior[J]. Journal of Tribology, 2017, 139(6): 061701.

[85] Cheng F, Ji W A. Velocity-slip model for analysis of the fluid film in the cavitation region of a journal bearing[J]. Tribology International, 2016, 97: 163-172.

[86] Jao H C, Chang K M, Chu L M, et al. A Modified Average Reynolds Equation for Rough Bearings with Anisotropic Slip[J]. Journal of Tribology, 2016, 138(1): 011702.

[87] Song Z, Guo F, Liu Y, et al. Investigation of slip/no-slip surface for two-dimensional large tilting pad thrust bearing[J]. Industrial Lubrication and Tribology, 2017, 69(6): 995-1004.

[88] Zhu B, Li Y P, Wang W G, et al. Boundary slippage modeling and optimization

of hydrophobic tilting pad thrust bearing with elastic deformation[J]. Tribology International, 2019, 136: 299-316.

[89] Chen H, Zhang Y. Hydrodynamic journal bearing with slippage sleeve surface[J]. Australian Journal of Mechanical Engineering, 2019, 19(2): 143-152.

[90] Salant R F, Fortier A E. Numerical analysis of a slider bearing with a heterogeneous slip/no-slip surface[J]. Tribology Transactions, 2004, 47(3): 328-334.

[91] Zhang H, Hua M, Dong G, et al. Boundary slip surface design for high speed water lubricated journal bearings[J]. Tribology International, 2014, 79: 32-41.

[92] Rao T V V L N. Analysis of single-grooved slider and journal bearing with partial slip surface[J]. Journal of Tribology, 2010, 132(1): 014501

[93] Fortier A E, Salant R F. Numerical analysis of a journal bearing with a heterogeneous slip/no-slip surface[J]. Journal of Tribology, 2005, 127(4): 820-825.

[94] Wang L L, Lu C H, Ge P Q, et al. Study on the influence of critical shear stress on wall slip of spiral oil wedge journal bearing[J]. Proceedings of the Institution of Mechanical Engineers, Part J: Journal of Engineering Tribology, 2012, 226(5): 362-376.

[95] Rao T V V L N, Rani A M A, Nagarajan T, et al. Analysis of slider and journal bearing using partially textured slip surface[J]. Tribology International, 2012, 56(12):121–128.

[96] Senatore A, Rao T. Partial slip texture slider and journal bearing lubricated with Newtonian fluids: a review[J]. Journal of Tribology, 2018, 140(4): 040801

[97] Arif M, Shukla D K, Kango S, et al. Implication of Surface Texture and Slip on Hydrodynamic Fluid Film Bearings: A Comprehensive Survey[J]. Tribology Online, 2020, 15(4): 265-282.

[98] Jamari J, Muchammad M, Hilmy F, et al. Effect of inertia on the cavitation phenomena of hydrodynamic textured bearings considering slip[J]. Journal of the Brazilian Society of Mechanical Sciences and Engineering, 2019, 41(9): 1-14.

[99] Tauviqirrahman M, Jamari J, Wibowo B S, et al. Multiphase computational fluid dynamics analysis of hydrodynamic journal bearing under the combined influence of texture and slip[J]. Lubricants, 2019, 7(11): 97.

[100] Tauviqirrahman M, Afif M F, Paryanto P, et al. Investigation of the Tribological Performance of Heterogeneous Slip/No-Slip Journal Bearing

Considering Thermo-Hydrodynamic Effects[J]. Fluids, 2021, 6(2): 48.

[101] Feng W, Han Y, Xiang G, et al. Hydrodynamic lubrication analysis of water-lubricated bearings with partial microgroove considering wall slip[J]. Surface Topography: Metrology and Properties, 2021, 9(1): 015019.

[102] Jin J, Chen X, Fu Y, et al. Optimal design of the slip–texture on a journal-bearing surface[J]. Industrial Lubrication and Tribology, 2020, 73(2): 230-237.

[103] Li W L, Huang Z H, Lin C S, et al. On the linear stability analysis of journal bearings–Consideration of coupled effects of anisotropic slip and surface roughness[J]. Tribology International, 2019, 137: 254-266.

[104] Greenwood J A, Williamson J B P. Contact of nominally flat surfaces[J]. Proceedings of the Royal Society A: Mathematical, Physical and Engineering Sciences, 1966, 295(1442): 300-319.

[105] Varney P, Green I. Rough Surface Contact of Curved Conformal Surfaces: An Application to Rotor–Stator Rub. J Tribol 2016; 138(4): 041401.

[106] Wu C, Zheng L. An Average Reynolds Equation for Partial Film Lubrication with a Contact Factor[J]. Journal of Tribology, 1989, 111(1): 83-90.

[107] Patir N, Cheng HS. An average flow model for determining effects of three-dimensional roughness on partial hydrodynamic lubrication [J]. J of Lubrication Tech 1978; 100(1): 12-17.

[108] Patir N, Cheng HS. Application of average flow model to lubrication between rough sliding surfaces [J]. Journal of Lubrication Technology, 101(2): 220-229.

[109] Dobrica M B, Fillon M, Maspeyrot P. Influence of mixed-lubrication and rough elastic-plastic contact on the performance of small fluid film bearings[J]. Tribology Transactions, 2008, 51(6): 699-717.

[110] Habchi W, Eyheramendy D. Vergne P, et al. Stabilized fully-coupled finite elements for elastohydrodynamic lubrication problems [J]. Advances in Engineering Software, 2012, 46(1):4-18.

[111] Pierre I, Fillon M. Influence of geometric parameters and operating conditions on the thermohydrodynamic behaviour of plain journal bearings [J]. Proceedings of the Institution of Mechanical Engineers, Part J: Journal of Engineering Tribology, 2000, 214(5): 445-457.

[112] Radeş M. Dynamic analysis of an inertial foundation model [J]. International Journal of Solids and Structures, 1972, 8(12), 1353-1372.

[113] Heinrich J C, Huyakorn P S, Zienkiewicz O C, et al. An ‘upwind’ finite element scheme for two‐dimensional convective transport equation [J]. International Journal for Numerical Methods in Engineering, 1977, 11(1):

131-143

[114] Zienkiewicz O C, Gallagher R H, Hood P. Newtonian and non-Newtonian viscous incompressible flow. Temperature induced flows. Finite element solutions [J]. The Mathematics of Finite Elements and Applications II MAFELAP, Academic Press, London, 1975, 235-267.

[115] Kim J, Alan B P, and Ravindra K. G. TEHD analysis for tilting-pad journal bearings using upwind finite element method [J]. Tribology Transactions, 1994, 37(4): 771-783.

[116] Kucinschi B R, Fillon M, et al. A Transient Thermoelastohydrodynamic Study of Steadily Loaded Plain Journal Bearings Using Finite Element Method Analysis[J]. Journal of Tribology, 2000, 122(1): 219-219.

[117] Zhang P, Lee K H, Lee C H. Friction characteristics of magneto-rheological fluid on DLC-and PTFE-coated surfaces[J]. Proceedings of the Institution of Mechanical Engineers, Part J: Journal of Engineering Tribology, 2017, 231(8): 1007-1015.

Extended Abstract

Chapter 1 Introduction

In special cases, the hydrodynamic bearings used in high-power gas turbines own compact size and micro relative clearance, and often start up and shut down frequently under heavy load without hydrostatic supporting system, which easily cause bearing seizure and worn failure. Self-lubrication coatings are becoming an alternative way to improve the friction performance of the bearing. The slip properties at lubricant-coating interface are quite different from those of traditional bearing friction pairs. Also the thermal properties of the self-lubrication coatings, such as polytetrafluoroethylene (PTFE), are quite different from those of metals, which are easy to cause bush burn during startup. Therefore, this paper focuses on understanding and improving the contact performance of the journal bearings that start up and shut down under heavy load to explain how the operating conditions affect the wear during startup and shutdown. And this paper also focuses on studying on the thermal slip effect at film-coating interface of the journal bearing at heavy load and high speed to explore the possible way that reduces the probability that bearing seizure occurs.

Startup and shutdown behavior of hydrodynamic bearings

In the early 1960s, the start-stop behavior of hydrodynamic bearings was conducted through experimental study by the U.S. Naval Fleet Engineering Laboratory. In 1970s, there are seldom experimental researches on the startup and shutdown behavior by Mokhtar et al. Until the late 1980s, Fillon et al. conducted systematic experiments and theoretical research about the start-stop behavior of hydrodynamic bearings, and their research extends to the recent years. They found the wear location of the bearing is mainly caused by the sliding of the shaft along the bush surface during startup. The wear location is greatly affected by the bearing clearance, surface finish, and bearing roundness. During startup, the friction coefficient increased with the increase of roughness. The pressure field built faster than the temperature field during startup. The startup torque is greatly affected by the feeding temperature, and the maximum friction torque is linear to the static load applied.

Generally speaking, in the aspect of experiments, the influences of the applied load, journal speed, acceleration, feeding temperature, surface roughness and bearing structure on the motion of journal center, transient film thickness, transient temperature, friction torque, friction coefficient, startup torque, lift-off speed are

separately studied during startup. In terms of simulations, the elastohydrodynamic (EHD) model that takes into account the elastic deformation of solids, the thermohydrodynamic (THD) model that considers the effect of temperature, and the thermoelastichydrodyanmic (TEHD) model that considers both thermal deformation and solid elastic deformation are separately built to study the startup and shutdown behavior of hydrodynamic bearings.

Self-lubricated coatings in hydrodynamic bearings

Bearings are prone to boundary or mixed lubrication under extreme conditions such as startup and shutdown period, heavy load or starved lubrication. In order to cope with the various extreme conditions, a variety of self-lubricated coatings have been applied to the surface of the bush. The traditional plastic coatings such as polytetrafluo-roethylene (PTFE) and polyetheretherketone (PEEK) have been proved to be applicable. The diamond-like carbon (DLC) coating was also studied with low friction coefficient. Some other composite coatings, such as metal matrix composite (316L+TiC/316L+SiC) coating, WC/C coating, SiC coating, polyperfluo-roalkoxyethylene (PFA) and aromatic thermosetting polyester (ATSP) based coatings, show the prospective application of hydrodynamic bearings.

In total, present research mainly focuses on the pin-on-disk friction and wear test in mixed lubrication and the tests show excellent performance and promising applications of the polymer coatings in sliding bearings, but in the complex engineering applications, the composite coatings also show some drawbacks that influence the application.

Slip behavior of hydrodynamic bearing

Wall slip, also known as interface slip or boundary slip, refers to the relative motion at fluid-solid interface. As long as the shear stress is large enough, it is possible to overcome the interaction between solid and liquid molecules to produce slip.

The slip phenomenon of the journal hydrodynamic bearing under low and high viscosity lubricants is studied by the target velocity tracking method. The slip length of perfluoropolyethers (PFPE) coated sample tested by the rheometer remoter can be in the order of 10 μm. The critical shear stress at the oil-PTFE interface of a plastic journal bearing is about 1126.94 Pa. The critical shear rate of water was higher than that of PC and 3# mineral oil. The friction coefficient decreases and the minimum friction coefficient shifts to the right in hydrodynamic lubrication with slip. In mixed lubrication, the friction coefficient would be reduced less with slip. In hydrodynamic lubrication.

The modified Reynolds equation deduced based on the Navier-Stokes equation,

critical shear stress slip model and two-component slip model are used to analyze the influence of wall slip on the hydrodynamic behavior and to optimize the wall slip parameters to improve the hydrodynamic behavior. Also the comprehensive effect of the slip behavior and surface texture is explored.

Summarily, present studies of experiments mainly focuses on discovering the wall slip phenomenon for various fluid-solid interface and then establishing the wall slip model. The numerical analysis for bearings are focused on deriving the Reynolds equation considering wall slip, and then analyzing the influence of wall slip on the hydrodynamic behavior.

Chapter 2 Contact behavior of the loaded hydrodynamic journal bearings during startup and shutdown

The geometry model for startup and shutdown is shown in Fig.E-1. Before starting up, the applied load is supported completely by the asperity contact force. After accelerating, the hydrodynamic (HD) force of F_h and film thickness increase with the increasing journal speed and the corresponding asperity contact force of F_c decreases. The journal is completely separated with the bearing surface when F_c drops to zero. The contact time of t_c is defined as the period during which two surfaces are in contact. Shutdown is a reverse process.

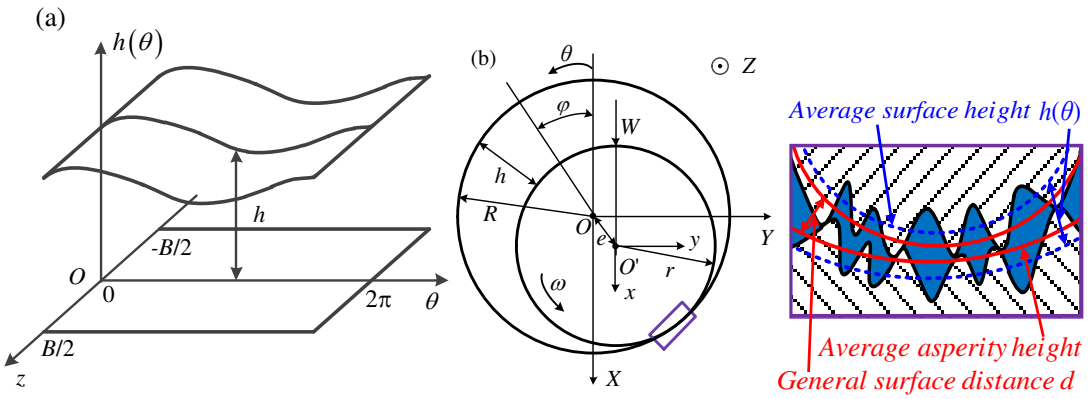


Fig.E-1 (a) The coordinate system and (b) the movement and the asperity contact property during startup

The asperity height of the rough surface meets the Gaussian distribution. The Greenwood-Williamson (GW) contact model is applied to calculate the contact pressure. The wear volume is obtained by Archard model. The average Reynolds equation considering surface roughness is used to calculate the hydrodynamic (HD) pressure. The motion equation of the journal center is

$$\begin{cases} m\ddot{x} = F_{cx}(t) + F_{hx}(t) + F_{fx}(t) + W \\ m\ddot{y} = F_{cy}(t) + F_{hy}(t) + F_{fy}(t) \end{cases} \tag{1-1}$$

where F_c, F_h and F_f respectively represent contact force, HD force and friction force. The subscripts of x and y represent in X and Y directions. t represents time. m is the equivalent mass, $m=W/g$; W is the applied force, g is acceleration of gravity.

The solution procedure of the model is

(1) At beginning of t=0, the journal is in a steady-state position, and the initial average oil film thickness is determined according to the balance of contact force and external load balance for startup (or the balance of HD force and external load for shutdown).

(2) With the increasing (decreasing) journal speed during startup (shutdown), HD pressure and HD force are obtained. Meanwhile, the contact pressure and the asperity contact force are obtained by calculating GW model.

(3) The motion of the journal center at each time step are calculated by solving the motion equations using Newmark method.

(4) The HD force, asperity contact force and the motion properties are calculated iteratively until the end of the acceleration of the bearing during startup.

The journal speed rises linearly up to 1000 rpm during startup or decreases linearly from 1000 rpm to zero during shutdown within 0.1 second. The surface roughness is in isotropic orientation. The other parameters are listed in Table E-1.

Table E-1 The simulation parameters

Parameters	Symbols	Values	Parameters	Symbols	Values
Shaft radius (mm)	R_s	50	Areal asperity density (asp/m^2)	D_{sum}	5e11
Bearing length (mm)	B	60	Standard deviation of surface roughness (μm)	σ	1.0
Density of oil (kg/m^3)	ρ	860	Equivalent modulus (GPa)	$E_{1,2}$	210
Oil viscosity at 20℃ (Pa·s)	μ	0.027	Poisson's ratio	$v_{1,2}$	0.29
Asperity radius (μm)	R_p	2	External load (kN)	W	4

The influence of standard deviation of asperity height σ on the contact behavior during startup is presented in Fig.E-2. Small σ leads to a sharp increase in HD force, resulting in a short contact time and a low lift-off speed (Fig.E-2(a)). The small σ leads to the less contact zone (Fig.E-2(b)) and volume wear (Fig.E-2(c)). For the contact behavior during shutdown in Fig.E-3, both the contact zone and volume wear increase with the increasing σ, and the wear position is very close to the static position of the journal. The volume wear is in the order of 10^{-7} mm^3 which can be neglected compared to that (in the order of 10^{-4} mm^3) during startup. In total, the smooth surface is beneficial to reduce the wear zone and wear volume during startup and shutdown.

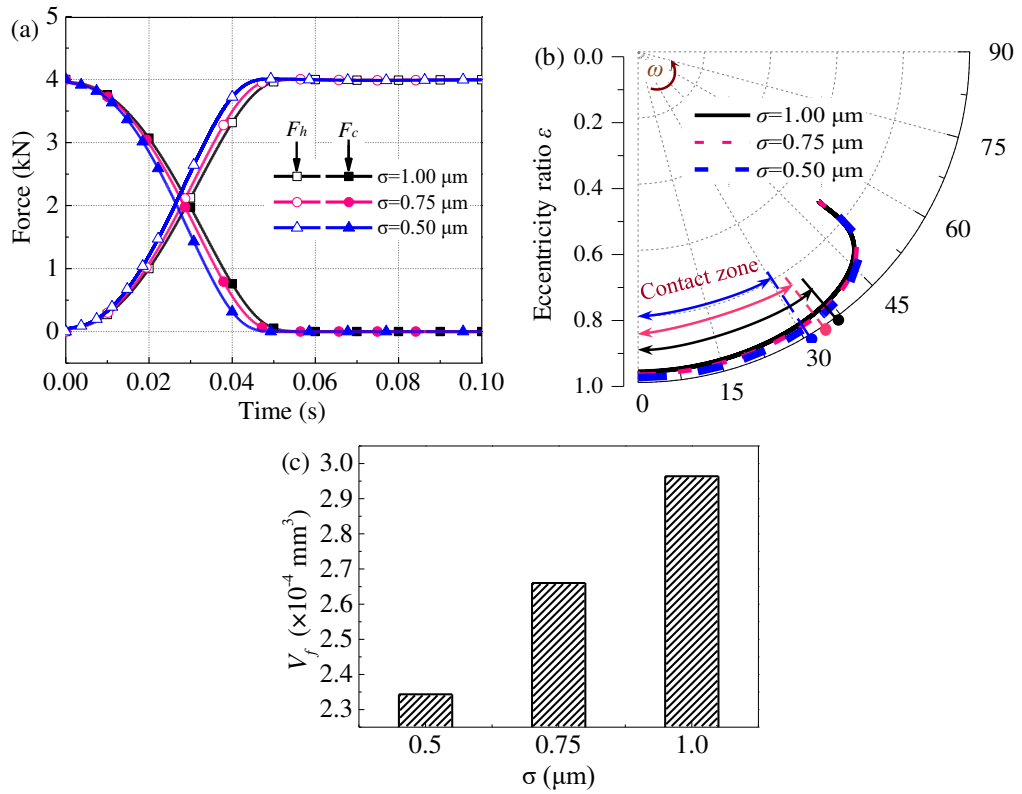


Fig.E-2 Influence of standard deviation of asperity height σ on (a) the HD force F_h and contact force F_c, (b) contact zone and (c) volume wear V_f during startup

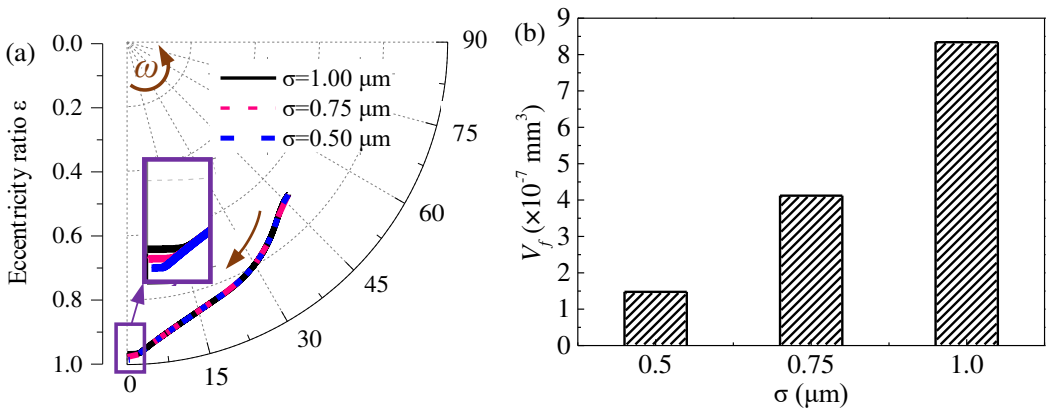


Fig.E-3 Influence of standard deviation of asperity height σ on (a) contact zone and (b) volume wear during shutdown

Fig.E-4 shows the influence of relative clearance on the contact behavior during startup. With the increase in relative clearance, both the contact zone and the volume wear are significantly enlarged. This is because the curvatures of the journal and bush are almost same in small relative clearance, which easily results in the contact of the two surfaces. The contact zone and volume wear during shutdown can be neglected compared to that during startup.

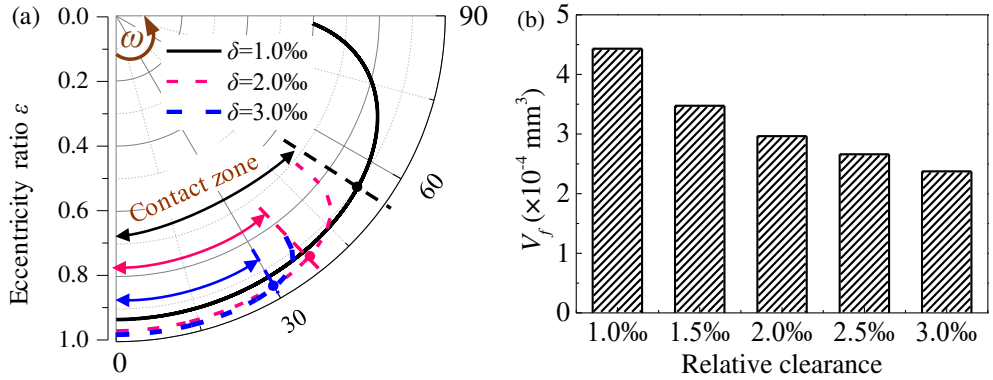


Fig.E-4 Influence of relative on (a) contact zone and (b) volume wear V_f during startup

Fig.E-5 shows the influence of acceleration time on contact behavior during startup. The acceleration time is the time that the journal accelerates from zero to 1000 rpm. With acceleration time increases from 0.1s to 0.5s, the contact time climbs up 0.057s to 0.129s, but the contact zone goes down. Meanwhile, the volume wear experiences a lowest value of 2.91×10^{-4} mm^3 at the acceleration time of 0.3 s. For the shutdown process in Fig.E-6, the contact zone is obvious in long acceleration time. When the deceleration time reaches 10 s, the volume wear is in the order of 10^{-4} mm^3 which is same with that during startup, i.e. when the deceleration is small, the wear during shutdown cannot be neglected. In order to reduce the wear zone and volume, there exists an optimal acceleration for startup, but for shutdown the large deceleration is better.

Chapter 3 Thermoelastohydrodynamic model of partly coated journal bearings considering wall slip

The geometry model of the partly coated bearings considering wall slip at film-coating interface is shown in Fig.E-7. An interlayer is used to enhance the bonding force between the coating and basement. In Fig.E-7(c), Θ is the fixed coordinate system, θ is the dynamic coordinate system, and $\theta=\Theta-\varphi$, where φ is the attitude angle.

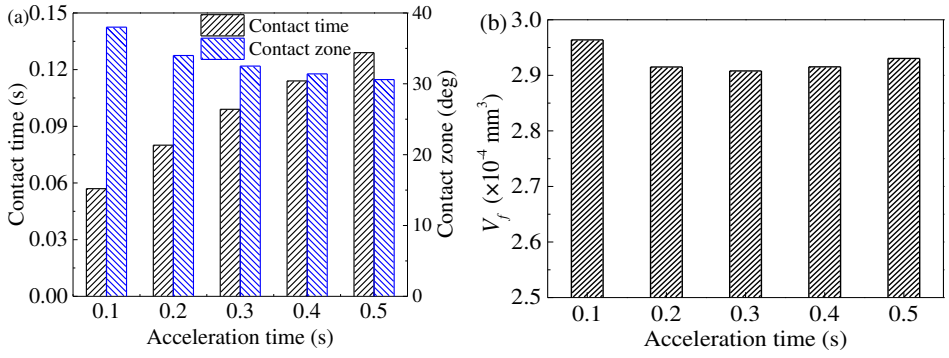


Fig.E-5 Influence of acceleration time on (a) contact time and contact zone and (b) volume wear V_f during startup

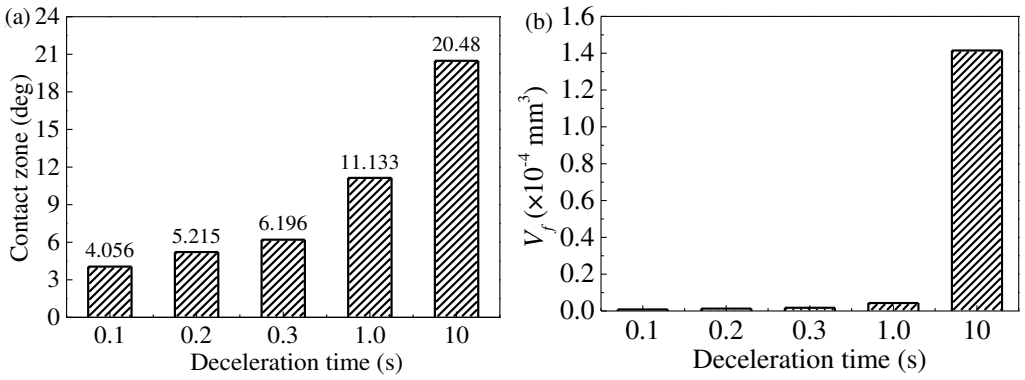


Fig.E-6 Influence of acceleration time on (a) contact zone and (b) volume wear V_f during shutdown

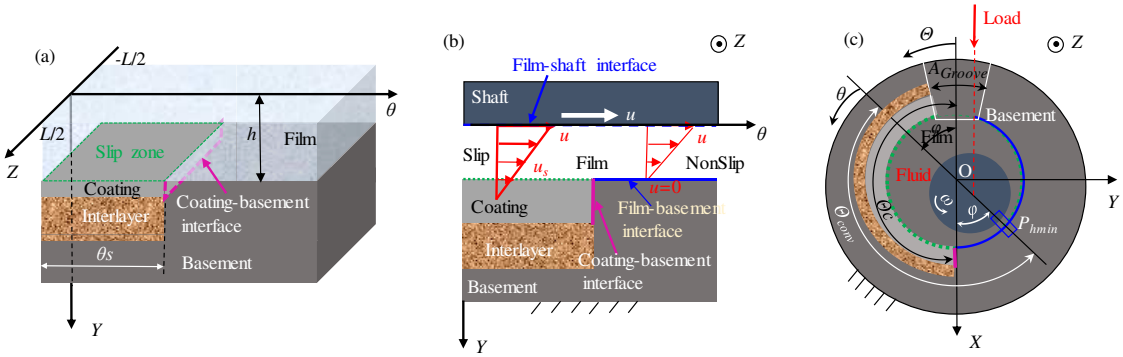


Fig.E-7 (a) Coating, interlayer and basement, (b) structure at middle plane and c) coordinate system of the coated journal bearings considering partial wall slip

The generalized Reynolds equation considering slip is applied

$$\frac{\partial}{R_s^2\partial\theta}\left(\Phi_\theta F_2\frac{\partial p}{\partial\theta}\right)+\frac{\partial}{\partial z}\left(\Phi_z F_2\frac{\partial p}{\partial z}\right)=\Phi_c\frac{\partial}{R_s\partial\theta}\left[\frac{F_1}{F_0}\left(u_0+u_s\right)\right]+$$
$$\Phi_c\frac{\partial}{\partial z}\left[\frac{F_1}{F_0}w_s\right]+\sigma\frac{\partial\left[\Phi_s\left(u_0+u_s\right)\right]}{R_s\partial\theta}+\sigma\frac{\partial\left[\Phi_s\left(w_s\right)\right]}{\partial z}+\xi^+p^- \tag{E-2}$$

where u_s and w_s are the slip velocities. ξ^+p^- is a penalty item which means the control cavitation. ξ^+ is an infinite positive number and p^-=min (p, 0) corresponds to the negative part of the HD pressure.

Two-component slip model is used to calculate the wall slip velocity. The shear stress is expressed by

$$\tau_c=\tau_{co}+\frac{\mu}{b}u_s \tag{E-3}$$

The energy equation and the heat conduction equation are used to solve the film and bush temperature.

Fig.E-8 shows the flow chart of the solving process as follows:

1. The generalized Reynolds equation is solved to obtain the pressure distribution. Then the fluid velocity across the film thickness and the slip velocity at the film-

coating interface are calculated.

2. The temperatures of the film, bush (coating, interlayer and basement), and shaft are obtained by solving energy and heat conduction equation combined with the thermal BCs. The film viscosity and mechanical and thermal deformations are then calculated. Steps 1 and 2 are repeated until the temperature deviation is less than the imposed error err_T, which is set to be 2×10^{-5}.

3. Steps 1 to 3 are repeated until the hydrodynamic (HD) force is balanced with the applied load by adjusting the eccentricity ratio ε and attitude angle φ.

4. Both the mechanical and thermal deformations should be convergent by repeating the steps of steps 1 to 4. The convergence errors of the mechanical and thermal deformations are respectively set to be 5×10^{-4}.

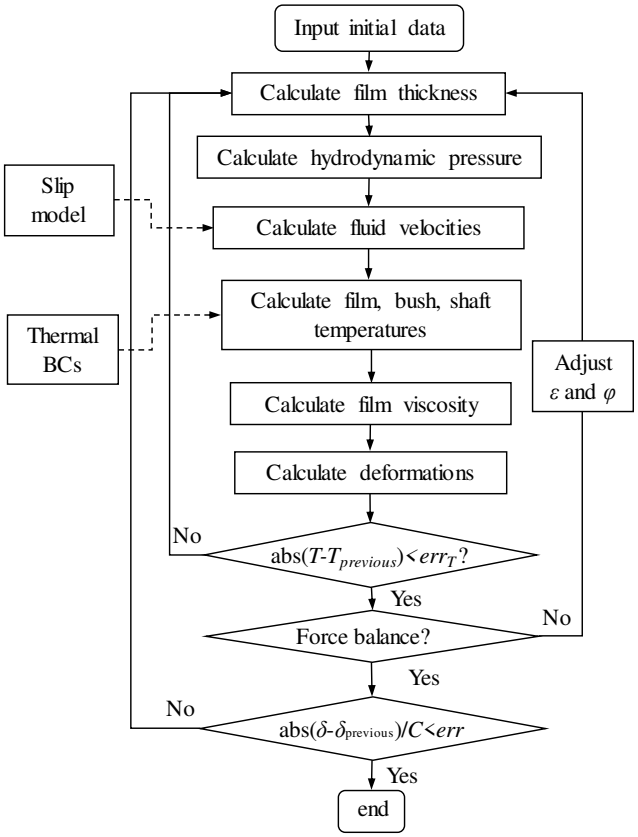


Fig.E-8 Flow chart of the calculation procedure

The simulation parameters are listed in Table E-2, Table E-3 and Table E-4.

Table E-2 Structure parameters of the bearing

Parameter	Symbol	Value	Parameter	Symbol	Value
Shaft radius, mm	R_s	50	Radial clearance at 20℃, μm	C	123
External bearing radius, mm	R_o	100	Bush thickness, mm	h_{bush}	50
Bearing length, mm	L	80	Groove angle, deg	A_{Groove}	18

Table E-3 Properties of the coating, interlayer and basement

Parameter	Coating			Interlayer	Basement
	PTFE	Graphite	DLC	Bronze	Steel
Density, kg/m^3	2200	2250	2000	8940	7850
Thermal conductivity, W/m℃	0.3	105	600	65	36
Specific heat, J/kg·℃	1200	710	970	490	486
Poisson's ratio	0.46	0.15	0.17	0.33	0.29
Elasticity modulus, GPa	0.11	25	759	120	210
Thermal expansion coefficient, ×10^{-6}	124	4.8	1.2	17	11.5
Bush/oil heat transfer coefficient, W/m^2·℃	50	700	800	700	600
Bush/air heat transfer coefficient, W/m^2·℃	-	-	-	-	100
Thickness, mm	1.0	1.0	1.0	3	46

Table E-4 Simulation parameters

Parameter	Symbol	Value
Thermal conductivity, W/m℃	k_f, k_a, k_b, k_s	0.13, 0.026, 65, 50
Density, kg/m^3	ρ_f, ρ_a, ρ_b, ρ_s	860, 1.17, 8940, 7700
Specific heat, J/kg·℃	C_f, C_a, C_b, C_s	2000, 1006, 490, 380
Heat transfer coefficient, W/m^2·℃	H_{ba}, H_{bo}	100, 700
Poisson's ratio	v_b	0.3
Elasticity modulus, GPa	E_b	120
Fluid viscosity, Pa·s	$\eta_{30℃}$	0.05
Viscosity-temperature coefficient	β_η	0.0468
Thermal expansion coefficient, ×10^{-6}	α_T	17
Temperature, ℃	T_a, T_I	30, 30
Supply pressure, Mpa	P_s	0.07

*note: the subscripts of *f*, *a*, *b*, *s* represent *film*, *atmosphere*, *basement*, *shaft; I* represents *inlet; ba represents basement and atmosphere; bo represents basement and oil.*

The wall slip behavior in different operating conditions is shown in Fig.E-9. The reduction in maximum temperature and the increase in film thickness are calculated by $\triangle T_{max}=(T_{nonslip}-T_{slip})/T_{nonslip}*100\%$ and $\triangle h_{min}=-(h_{min_nonslip}-h_{min_slip})/h_{min_nonslip}*100\%$ respectively. The large relative clearance and high journal speed lead to the large $\triangle T_{max}$, which means the wall slip effect can more obviously decrease the T_{max}. Usually the slip effect weakens the HD force with resulting in the low h_{min}. However, when the speed is larger than 4k rpm, the slip is helpful to increase h_{min} by owing a positive $\triangle h_{min}$. This because compared to the nonslip case at 4k rpm, the slip can be explained by the small thermal deformation caused by the low T_{max} in slip case.

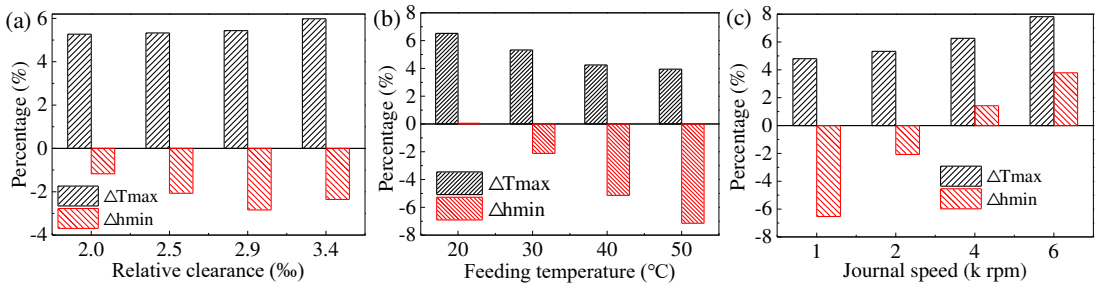


Fig.E-9 Influence of (a) relative clearance, (b) feeding temperature and (c) journal speed on the thermal wall slip behavior of the PTFE coated bearing

Chapter 4 Coating zone optimization and thermal slip behavior of the coated journal bearing

Fig.E-10 shows the coating (slip) zone at bush surface which is symmetrical about the bearing middle plane. In order to locate the slip zone, the coefficient of $\alpha=(\Theta_c-\varphi)/\Theta_{conv}$ ($-\varphi/\Theta_{conv} \le \alpha \le 2$) is defined. where Θ_c is the length of slip zone from $\Theta=0$ deg to the tailing end of the zone; Θ_{conv} is the length from the attitude angle φ to the position of minimum film thickness h_{min}, i.e. the film convergent region of $\Theta_{conv}=180$ deg. $\alpha<1$ and $\alpha>1$ indicate that the slip zone locates at the convergent region and divergent region of the film respectively.

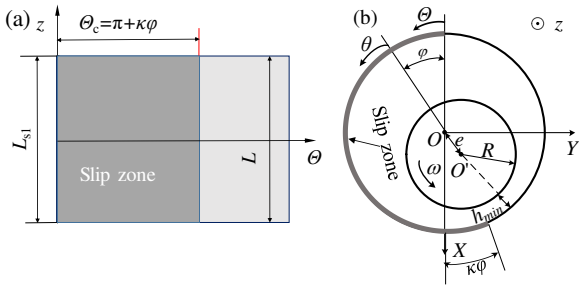


Fig.E-10 Coating (slip) zone at bush surface

The HD gain is calculated by $F_G=(F_{h_slip}-F_{h_nonslip})/F_{h_nonslip}\times 100\%$. The reduction in friction coefficient is calculated by $f_D=-(f_{slip}-f_{nonslip})/f_{nonslip}\times 100\%$. The positive values of F_G and f_D mean positive effect of the slip zone. Based on the study of the slip zone shape in isothermal cases, the axial width of the slip zone should be increased, that is, the slip zone should be set to a rectangle with the bearing width. In high eccentricity (heave load), the optimal α is better to be imposed 0.9~1.0. The coefficient κ is introduced to describe the slip length as $\Theta_c=\pi+\kappa\varphi$ ($\kappa\in[0,1]$) under heavy constant load.

The optimized parameters of $\varepsilon=0.94$ are selected for further exploring the performance of journal bearing with eccentricity ratios ranging from 0.4 to 0.97 as shown in Fig.E-11. The nonslip attitude angle of $\varepsilon=0.94$ is $\varphi=20.3°$. The slip length is 5 μm and the critical shear stress is 1024 Pa. For $\varepsilon<0.94$, all the selected slip zone

of κ=0.5, 0.75, and 1.0 can raise the HD force and lower the friction coefficient (Fig.E-11(a) and (b)). For ε>0.94, except κ=0.5, the other selected partial slip zones diminish the HD force. That means the selected zone that can works better in the load of ε=0.94 can also improve the bearing performance in the loads smaller than ε=0.94.

The thermal properties of the coating journal bearings are discussed in four lubrication regimes: thermohydrodynamic lubrication without/with slip (THD/ THDS) and thermoelastohydrodynamic without/with slip (TEHD/TEHDS). The bearing groove is set to be 18 deg, so the range of α is calculated as $-0.45 \leq \alpha \leq 1.95$. The parameters are listed in Table E-2, Table E-3 and Table E-4. The applied load is 8 kN (2.0 MPa), the journal speed is 2000 rpm.

Fig.E-12 demonstrates the influence of PTFE coating coefficient α on the temperature and minimum film thickness. When the tailing end of the coating locates in the film convergent region, i.e. zone 1 of α<0.8, the influence of the coating is quite small, with variations of temperature and h_{min} of less than 0.3℃ and 1.0 μm. When the tailing end of the coating is close to the position of h_{min}, i.e. zone 2 of α=0.8~1.4, T_{max} increases in all lubrication cases at α≈1.0 (Fig.E-12 (a)). h_{min} experiences a sharp decrease by about 16% and 21% in the TEHD and TEHDS cases respectively, but this large reduction does not appear in the THD and THDS cases. It can be deduced that the sharp decrease is caused by deformations. We prefer lower T_{max} and thicker h_{min}, so the range of α=0.8~1.4 is unacceptable or infeasible. When the tailing end of the coating locates in the film divergent region, i.e. zone 3 of α > 1.4, the variations of T_{max} and h_{min} are quite small, so in the point of manufacturing it is better to prescribe full coatings. Without slip, T_{max} can be increased by about 5% (2.5℃) compared to that of α<0.8. The slip can effectively decrease T_{max} by 2% compared with that of α<0.8.

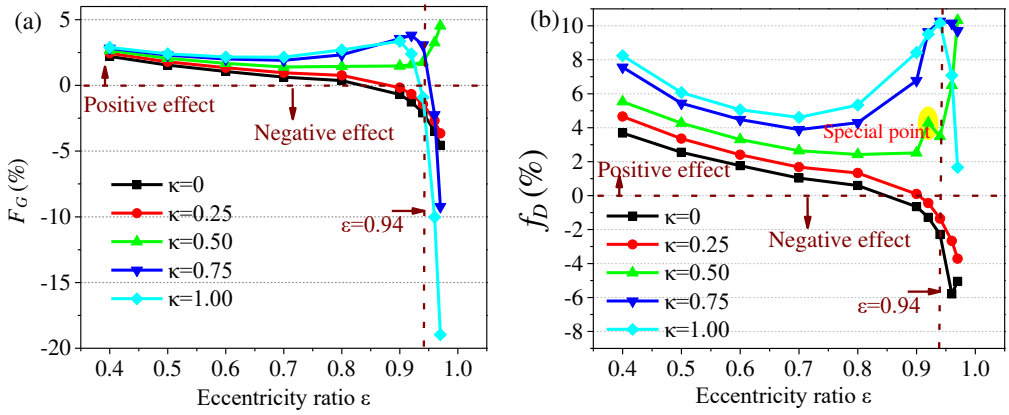


Fig.E-11 The performance of journal bearing in partial slip zone in different eccentricity ratios, (a) the HD force gain F_G and (b) the friction coefficient decrease f_D

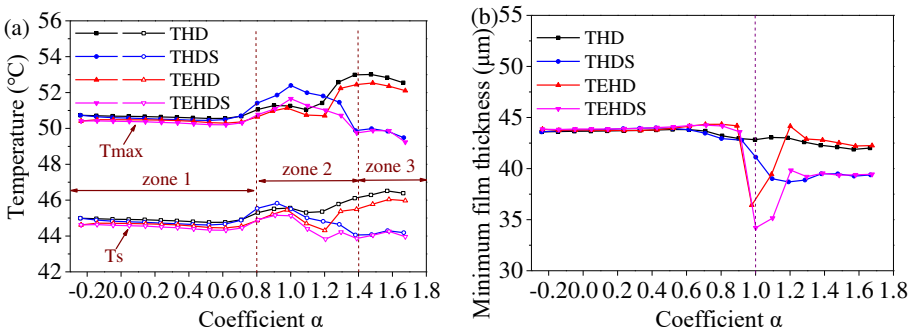


Fig.E-12 Influence of coefficient α of PTFE coating on (a) journal and maximum temperature T_{max}, (b) minimum film thickness h_{min}

Fig.E-13 shows the temperature distribution at the film-coating-interlayer-basement zone for PTFE, graphite and DLC coatings. The TEHD case is considered. The parameters are listed in Table E-3. In full coating, the T_{max} of PTFE coating is highest, and the T_{max} of DLC coating is lowest. Compared with the PTFE coating, graphite and DLC coatings cannot prevent heat transfer to the basement because of their better heat conduction properties, and there are no obvious temperature boundaries between the coating, interlayer and basement. The influence of the partial graphite and DLC coating of α=0.43 and 1.0 has a little influence on the temperature distribution.

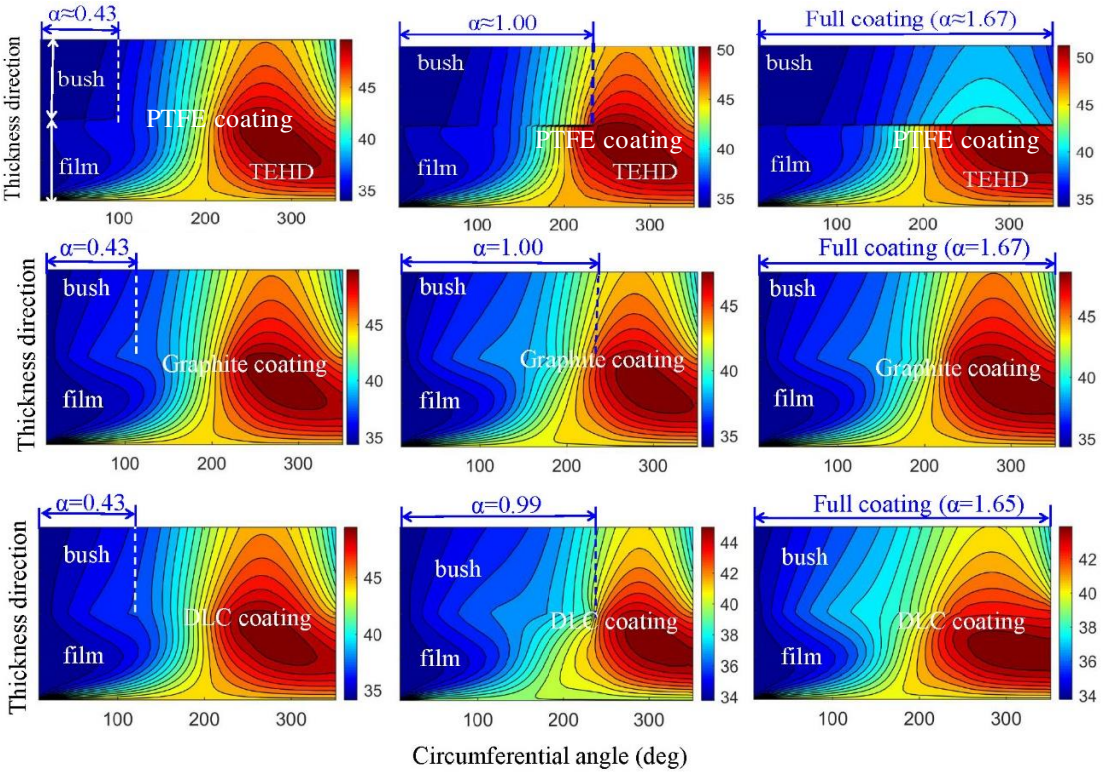


Fig.E-13 Thermal distribution with different coating materials

Chapter 5 Experimental tests of the thermal properties of the coated tilting pad journal bearing

The mechanical system of the test bench mainly includes the motorized spindle, the coupling, the supporting role bearings, the loading device and the tested bearing device as shown in Fig.E-14. The motorized spindle can be up to 12k rpm. It is connected with the tested bearing journal by a flexible coupling. In order to reduce the deformation of the rotating shaft under heavy loads, two supporting rolling bearings are arranged on the same side of the tested bearing. The tested bearing is placed in the loading ring, which is limited by two guide rail sliders fixed on the temporary oil tank. The load in the vertical direction is applied on the loading ring by a hydraulic cylinder, and it is transmitted to the tested bearing by the loading ring.

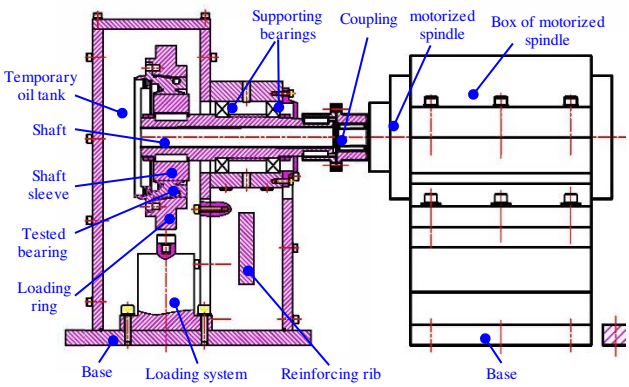


Fig.E-14 Assembly drawing of the test bench

The geometry of the six-pad coated tilting pad journal bearing (CTPJB) is shown in Fig.E-15, the photo is shown in Fig.E-16. The temperature sensors are installed as shown in Fig.E-17. The parameters used are listed in Table E-5 and Table E-6 and Table E-7.

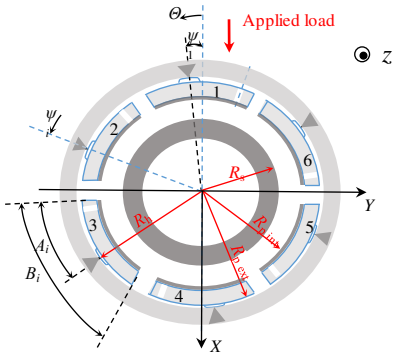


Fig.E-15 Geometry model



Fig.E-16 Pads in the loading ring

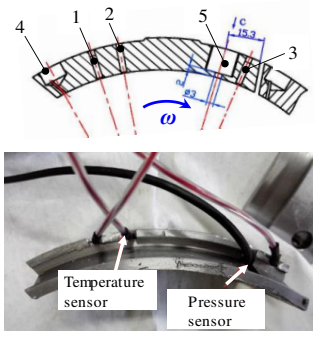


Fig.E-17 Location of the sensors in the pad

Table E-5 Geometrical parameters of the bearing at 20°C

Parameters	Value	Parameters	Value
Internal pad radius, mm	85.015	Preload coefficient	0
External pad radius, mm	98	Pad thickness, mm	12.985
Bearing length, mm	60	Angular extent of pad *i*, deg	58.5
Radius of pad pivot, mm	99	Pivot position of pad *i*, A_i/B_i,	0.672
External radius of loading ring, mm	199	Pivot position of pad *i*, deg	6+60*(*i*-1)

Table E-6 Lubricant characteristics (ISO T32)

Parameters	Value	Parameters	Value
Feeding and bath temperatures, ℃	40	Density at 40℃, kg/m^3	860
Supply pressure, MPa	0.3	Thermal conductivity, W/(m·K)	0.13
Dynamic viscosity at 40 ℃, mPa·s	27.52	Specific heat, J/(kg·K)	2000
Dynamic viscosity at 100 ℃, mPa·s	4.644		

Table E-7 Parameters of bearing clearance

Parameters	Initial clearance C0	Clearance C1	Clearance C2	Clearance C3
Internal bearing diameter, mm	$170.03^{+0.04}_{0}$			
Shaft diameter, mm	$170.0^{0}_{-0.025}$	$169.88^{0}_{-0.025}$	$169.83^{0}_{-0.025}$	$169.78^{0}_{-0.025}$
Bearing radius clearance, μm	15~47.5	75~107.5	100~132.5	125~157.5
Relative clearance, ‰	0.18~0.56	0.88~1.26	1.18~1.56	1.47~1.86

In micro-relative clearance that is lower than 1.0‰, the temperature of the PTFE, Graphite and Ag coated bearings is tested during startup. The tests show in PTFE coating the bearing cannot form steady temperature The Graphite can run under 5kN and 6k rpm, but when the speed rises up to 7k rpm, the bearing seizure occurs. The sliver (Ag) coated bearing can normally run under 7.5 kN and 8k rpm. In all cases, the bush surface is obviously worn. When the relative clearance is enlarged to 1.18‰~1.56‰, the coated bearings can run under 7.5 kN and 8k rpm, even though causing the worn at the bush surface.

The Ag coating is tested. Because the temperature rise of pad 4 on the loading side is the largest, so the temperature rise of pad 4 is discussed during startup. Fig.E-18 shows the effect of relative clearance on the temperature rise during startup. The applied load is 7.5 kN. The journal speed takes 2.2 min to increase from zero to 8k rpm. The small the relative clearance generates the fast increase in temperature and yields the high stable temperature. The temperatures in different relative clearances

almost reach the stable temperature at the same time. This is because the bearing with large clearance has a large amount of oil flow in the clearance, and the oil takes away more heat. Also it generates lower friction due to a higher average film thickness, i.e. lower shear rate in large clearance.

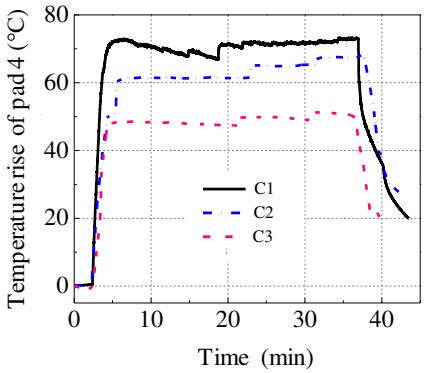


Fig.E-18 Influence of relative clearance on temperature rise of Ag CTPJBs

The influence of acceleration on temperature rise is shown in Fig.E-19. Acceleration 1 is the largest following by the acceleration 2 and 3. The period of rapid temperature rise is consistent with the acceleration time. In Fig.E-19(a), the great acceleration causes the fast temperature rise during startup, so in large acceleration it easily causes bearing seizures because the heat cannot transfer to the bush in time. The temperature rises in the same mode with the acceleration of the journal speed, i.e. the temperature rises along the journal speed in linear and cosine modes (Fig.E-19 (b)). After the acceleration process is completed, the temperature increases slowly, and the temperature rise is almost same in stationary state.

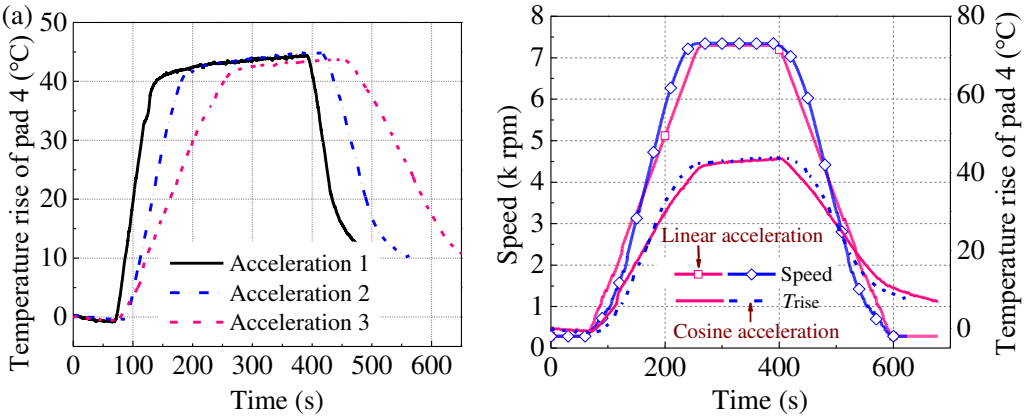


Fig.E-19 Influence of (a) acceleration and (b) acceleration mode on temperature rise of Ag CTPJBs

Fig.E-20 shows the influence of initial temperature on the temperature rise during startup. The journal starts up linearly from zero to 8.8k rpm in 1.8 minutes. The

relative clearance is the value C3 in Table E-7, and the applied load is 7.5 kN. The oil feeds into the static bearing in the first 2.5 min. In the high initial temperature, the feeding temperature is 35℃ and the temperature of each pad is about 42℃. In the low initial temperature, the feeding temperature is 25℃ and the temperature of each pad is about 26℃. The temperature difference of the pads of the two initial states is 16℃. The bearings arrive at the steady temperature almost at the same time. The temperature rise of pad 4 in high initial temperature is about 47.1℃ which is about 12.3℃ lower than that in low initial temperature. It can be deduced that the temperature rises faster in low initial temperature. Therefore, the high initial temperature is helpful for the thermal startup.

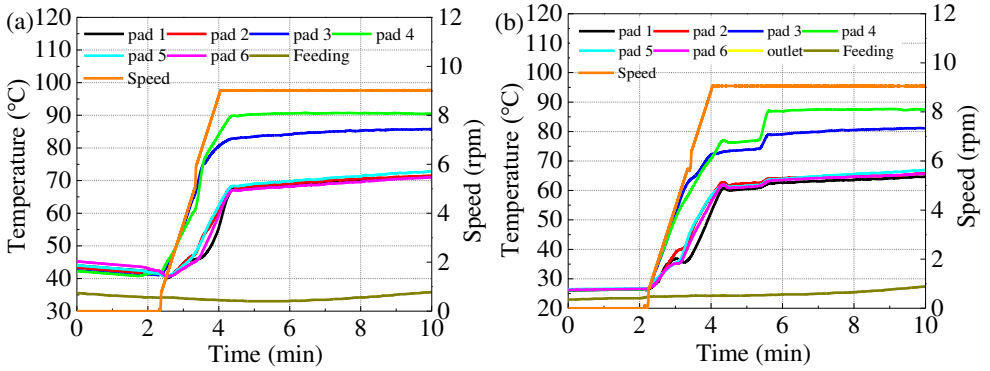


Fig.E-20 Influence of initial temperature on temperature rise of Ag CTPJBs, (a) high initial temperature and (b) low initial temperature

Conclusions

Aiming at the coated journal bearings that starts up and shuts down under heavy load, the transient contact zone and the worn properties are presented. Then the thermal wall slip behavior at film-coating interface are analyzed, and the effect of slip zone is discussed. The experiments are conducted to explore the stable and transient thermal behavior of the coated tilting pad journal bearings (CTPJBs).

The key conclusions of this work are as follows:

(1) The wear zone and volume during startup is much larger than that during shutdown. Smooth surface generates small wear zone and volume during startup. Large relative clearance decreases the wear zone and volume during startup. During startup, large acceleration increases the wear zone, but there exists an optimal acceleration to enable the volume wear lowest. During shutdown, when the deceleration is too small, the wear zone and volume can be in the same order with that during startup, and the wear cannot be neglected.

(2) In large relative clearance and high journal speed, the slip effect is more effective to reduce the maximum temperature (T_{max}), but high feeding temperature

enables this effect less obvious. At high journal speed, wall slip is more beneficial to the minimum film thickness (h_{min}).

(3) In isothermal case, the axial width of the slip zone is better to be increased. In heavy load, the slip zone should be located within the convergence region of the film and the tailing end of the zone is close to the position of h_{min}.

(4) When the PTFE coating zone is located in the convergence region of the film and the tailing end is far from the position of h_{min}, the coatings have very slight effect on the T_{max} and h_{min}. When the coating tailing end is located in the film divergence region and far away from the position of h_{min}, the slip effect can reduce the T_{max} accompanying with decreasing h_{min}. The tailing end of the coating should be avoid imposing close to the position of h_{min}. Graphite and DLC coatings with better thermal conductivity owing low T_{max} without preventing the oil heat transferring to the bush.

(5) The PTFE, graphite and silver (Ag) coatings are obviously worn during startup under heavy loads. The temperature of PTFE coated bearing is the highest and the worn coating can easily make the bearing failure. The silver coating is more likely to enable the bearing to run in extreme conditions.

(6) During startup, in small relative clearance and low initial temperature, the temperature increases fast. The temperature rise is in consistent with the speed acceleration. The large acceleration leads to the fast increase in temperature. Large relative clearance, small acceleration and relatively high initial temperature are conducive to safe starting of the bearing.

Résumé étendu

Chapitre 1 Introduction

Dans des cas particuliers, les paliers hydrodynamiques utilisés dans les turbines à gaz haute puissance possèdent une taille compacte et un faible jeu relatif, et démarrent et s'arrêtent fréquemment sous une charge élevée et sans système de sustentation hydrostatique, ce qui provoque facilement un grippage des paliers et des défaillances par usure. Les revêtements autolubrifiants constituent une alternative pour améliorer les performances de frottement du palier. Les propriétés de glissement à l'interface lubrifiant-revêtement sont assez différentes de celles des matériaux de friction de paliers traditionnels. De plus, les propriétés thermiques des revêtements autolubrifiants, tels que le polytétrafluoroéthylène (PTFE), sont assez différentes de celles des métaux, qui provoquent plus facilement de forts échauffements lors du démarrage. Par conséquent, ces travaux de thèse se concentrent sur la compréhension et l'amélioration des performances de contact des paliers lisses opérant à l'arrêt et au démarrage sous forte charge afin d'expliquer comment les conditions de fonctionnement affectent l'usure lors de ces phases transitoires. Ils portent également sur l'étude de l'effet de glissement thermique à l'interface du revêtement de film du palier lisse à forte charge et à grande vitesse pour explorer la manière possible de réduire la probabilité qu'un grippage se produise.

Comportement au démarrage et à l'arrêt des paliers hydrodynamiques

Au début des années 1960, des études expérimentales sur le comportement au démarrage et à l'arrêt des paliers hydrodynamiques ont été menées par le «Naval Fleet Engineering Laboratory» aux États-Unis. Dans les années 1970, il y a quelques rares recherches expérimentales sur le comportement au démarrage et à l'arrêt parmi lesquelles celles de Mokhtar et al. Jusqu'à la fin des années 1980, Fillon et al. ont mené des expériences systématiques et des recherches théoriques sur le comportement en régime transitoire des paliers hydrodynamiques, et leurs recherches se sont poursuivies jusqu'à ces dernières années. Ils ont découvert que l'empreinte d'usure du palier est principalement causée par le glissement de l'arbre seul sur la surface du coussinet lors du démarrage. Les caractéristiques du défaut d'usure sont grandement affectées par le jeu radial du palier, la finition des surfaces et la circularité du palier. Au démarrage, le coefficient de frottement augmente avec l'augmentation de la rugosité. Le champ de pression apparait plus rapidement que le

champ de température lors du démarrage. Le couple de démarrage est fortement affecté par la température d'alimentation et le couple de friction maximal varie linéairement avec la charge statique appliquée.

De manière générale, du point de vue expérimental, les influences de la charge appliquée, de la vitesse de l'arbre, de l'accélération, de la température d'alimentation, de la rugosité de la surface et de la structure portante sur la trajectoire du centre de l'arbre, l'épaisseur du film transitoire, la température transitoire, le couple de frottement, le coefficient de frottement, couple maximal au démarrage, vitesse de décollage sont étudiées séparément lors du démarrage. En termes de simulations, le modèle élastohydrodynamique (EHD) qui prend en compte la déformation élastique des solides, le modèle thermohydrodynamique (THD) qui considère l'effet de la température, et le modèle thermoélastohydrodynamique (TEHD) qui considère à la fois la déformation thermique et la déformation élastique solide sont construits séparément pour étudier le comportement des paliers hydrodynamiques lors des phases de démarrage et d'arrêt.

Revêtements autolubrifiés dans les paliers hydrodynamiques

Les paliers sont sujets à une lubrification limite ou mixte dans des conditions extrêmes telles que les phases de démarrage et d'arrêt, une charge élevée ou une sous-alimentation en lubrifiant. Afin de faire face aux diverses conditions extrêmes, une variété de revêtements autolubrifiés ont été déposés dans l'alésage du coussinet. Les revêtements polymères (plastiques) traditionnels tels que le polytétrafluoroéthylène (PTFE) et le polyétheréthercétone (PEEK) se sont avérés applicables. Le revêtement en carbone de type diamant (DLC) possédant un faible coefficient de frottement a également été étudié. Certains autres revêtements composites, tels que les revêtements composites à matrice métallique (316L+TiC/316L+SiC), les revêtements WC/C, les revêtements SiC, les revêtements à base de polyperfluoroalcoxyéthylène (PFA) et de polyester thermodurcissable aromatique (ATSP), révèlent des caractéristiques permettant des applications potentielles sur des paliers hydrodynamiques.

Au final, les recherches actuelles se concentrent principalement sur les essais de frottement et d'usure du type pion-disque en lubrification mixte et ces tests montrent d'excellentes performances et des applications prometteuses des revêtements polymères dans les paliers lisses ; cependant, pour des applications d'ingénierie complexes, les revêtements composites montrent également quelques inconvénients qui influencent leur utilisation.

Comportement au glissement du palier hydrodynamique

Le glissement de paroi, également connu sous le nom de glissement d'interface ou de glissement de limite, fait référence au mouvement relatif à l'interface fluide-solide. Tant que la contrainte de cisaillement est suffisamment grande, il est possible de surmonter l'interaction entre les molécules solides et liquides pour produire un glissement.

Le phénomène de glissement dans les paliers hydrodynamiques pour des lubrifiants à faible et haute viscosité est étudié par la méthode de vitesse de cibles. La longueur de glissement de l'échantillon revêtu de perfluoropolyéthers (PFPE) testé par le rhéomètre distant peut être de l'ordre de 10 μm. La contrainte de cisaillement critique à l'interface huile-PTFE d'un palier lisse en plastique est d'environ 1126,94 Pa. Le taux de cisaillement critique de l'eau était supérieur à celui du PC et de l'huile minérale 3#. Le coefficient de frottement diminue et le coefficient de frottement minimum se déplace vers la droite en lubrification hydrodynamique avec glissement. En lubrification mixte, la baisse du coefficient de frottement est moins affectée par la présence du glissement. En lubrification hydrodynamique, le glissement des parois peut diminuer le coefficient de frottement.

L'équation de Reynolds modifiée déduite sur la base de l'équation de Navier-Stokes, du modèle de glissement de contrainte de cisaillement critique et du modèle de glissement à deux composants est utilisée pour analyser l'influence du glissement de paroi sur le comportement hydrodynamique et pour optimiser les paramètres de glissement de paroi afin d'améliorer les performances du palier hydrodynamique. L'effet global du comportement de glissement et de la texture de surface est également exploré.

En résumé, les études expérimentales actuelles se concentrent principalement sur la découverte du phénomène de glissement de paroi pour diverses interfaces fluide-solide, puis sur l'établissement du modèle de glissement de paroi. L'analyse numérique des systèmes de guidage se concentre sur la dérivation de l'équation de Reynolds en considérant le glissement de paroi, puis sur l'analyse de l'influence du glissement de paroi sur le comportement hydrodynamique.

Chapitre 2 Comportement de contact des paliers lisses hydrodynamiques chargés au démarrage et à l'arrêt

Le modèle géométrique pour le démarrage et l'arrêt est montré dans Fig. F-1. Avant le démarrage, la charge appliquée est entièrement supportée par la force de contact des aspérités. Après accélération, la force hydrodynamique (HD) de F_h et l'épaisseur du film augmentent avec l'augmentation de la vitesse du tourillon et la force de contact d'aspérité correspondante de F_c diminue. Le tourillon est complètement

séparé de la surface d'appui lorsque F_c devient nulle. Le temps de contact de t_c est défini comme la période pendant laquelle deux surfaces sont en contact. L'arrêt est un processus inverse.

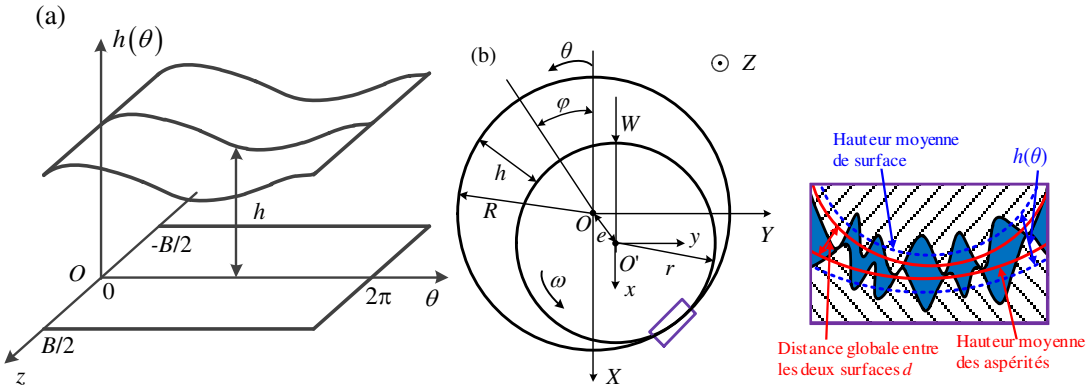


Fig. F-1 (a) Le système de coordonnées et (b) le mouvement et la propriété de contact d'aspérité lors du démarrage

La hauteur d'aspérité de la surface rugueuse rencontre la distribution gaussienne. Le modèle de contact Greenwood-Williamson (GW) est appliqué pour calculer la pression de contact. Le volume d'usure est obtenu par le modèle d'Archard. L'équation de Reynolds moyenne tenant compte de la rugosité de surface est utilisée pour calculer la pression hydrodynamique (HD). L'équation du mouvement du centre du journal est

$$\begin{cases} m\ddot{x} = F_{cx}(t) + F_{hx}(t) + F_{fx}(t) + W \\ m\ddot{y} = F_{cy}(t) + F_{hy}(t) + F_{fy}(t) \end{cases} \tag{1-4}$$

où F_c, F_h et F_f représentent respectivement la force de contact, la force HD et la force de frottement. Les indices de x et y représentent les composantes dans les directions X et Y. t représente le temps. m est la masse équivalente $m=W/g$; W est la force appliquée, g est l'accélération de la pesanteur.

La procédure de résolution du modèle est :

(1) Au début de t=0, le tourillon est dans une position stable, et l'épaisseur moyenne initiale du film d'huile est déterminée en fonction de l'équilibre de la force de contact et de l'équilibre de charge externe pour le démarrage (ou l'équilibre de force HD et externe charge pour l'arrêt).

(2) Avec la vitesse croissante (décroissante) de l'arbre pendant la phase de démarrage (arrêt), la pression hydrodynamique HD et la force HD sont obtenues. Pendant ce temps, la pression de contact et la force de contact d'aspérités sont

obtenues en calculant le modèle de Greenwood et Williamson (GW).

(3) La trajectoire du centre du journal à chaque pas de temps est calculée en résolvant les équations de mouvement en utilisant la méthode de Newmark.

(4) La force HD, la force de contact d'aspérité et la trajectoire sont calculés de manière itérative jusqu'à la fin de l'accélération de l'arbre pour la phase de démarrage.

La vitesse du tourillon augmente linéairement jusqu'à 1000 tr/min pendant le démarrage ou diminue linéairement de 1000 tr/min à zéro pendant l'arrêt en 0,1 seconde. La rugosité de surface est d'orientation isotrope. Les autres paramètres sont répertoriés dans le Tableau F-1.

Tableau F-1 Les paramètres de simulation

Paramètres	Symboles	Valeurs	Parameters	Symboles	Valeurs
Rayon de l'arbre (mm)	Rs	50	Densité surfacique des apérités (asp/m^2)	D_{sum}	5e11
Longueur du coussinet (mm)	B	60	Écart type de la rugosité de surface (μm)	σ	1.0
Densité de l'huile (kg/m^3)	ρ	860	Module d'Young équivalent (GPa)	$E_{1,2}$	210
Viscosité de l'huile à 20℃ (Pa·s)	μ	0,027	Coefficient de Poisson	$v_{1,2}$	0,29
Rayon des aspérités (μm)	R_p	2	Charge externe appliquée (kN)	W	4

L'influence de l'écart type de la hauteur d'aspérité σ sur le comportement de contact au démarrage est présentée sur la Fig. F-2. Une faible valeur de σ entraîne une forte augmentation de la force HD, entraînant un temps de contact court et une faible vitesse de décollage (Fig. F-2(a)). Une petite valeur de σ conduit à la diminution de la zone de contact (Fig. F-2 (b)) et du volume d'usure (Fig. F-2(c)). Pour le comportement du contact pendant l'arrêt (Fig. F-3), la zone de contact et le volume d'usure augmentent avec l'augmentation de σ, et la position de la zone d'usure est très proche de la position statique du tourillon. Le volume d'usure est de l'ordre de 10^{-7} mm^3 qui peut être négligé par rapport à celui déterminé lors du démarrage (de l'ordre de 10^{-4} mm^3). Au total, la surface lisse est bénéfique pour réduire la zone d'usure et le volume d'usure se produisant lors des phases du démarrage et de l'arrêt.

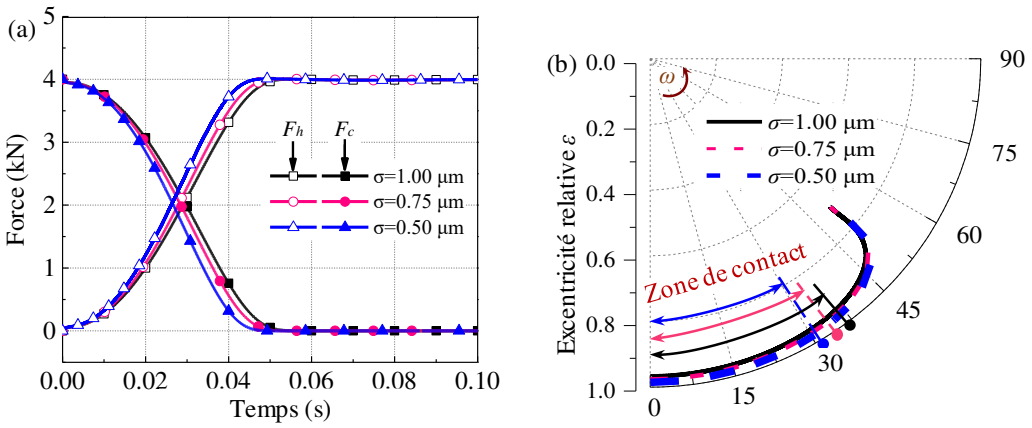


Fig. F-2 Influence de l'écart type de la hauteur d'aspérité σ sur (a) le LCC F_h et la force de contact F_c, (b) la zone de contact et (c) le volume d'usure V_f au démarrage

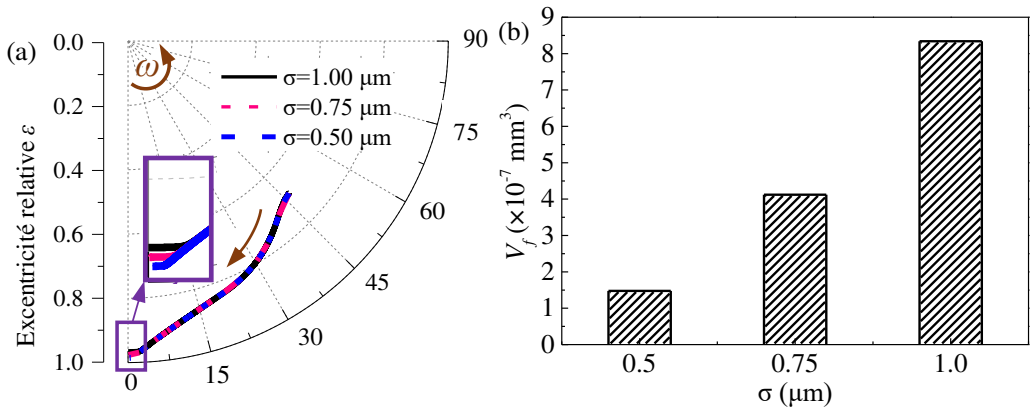


Fig. F-3 Influence de l'écart type de la hauteur d'aspérité σ sur (a) la zone de contact et (b) le volume d'usure pendant l'arrêt

La Fig. F-4 montre l'influence du jeu relatif sur le comportement du contact lors du démarrage. Avec l'augmentation du jeu relatif, la zone de contact et le volume d'usure sont considérablement augmentés. C'est parce que les courbures du tourillon

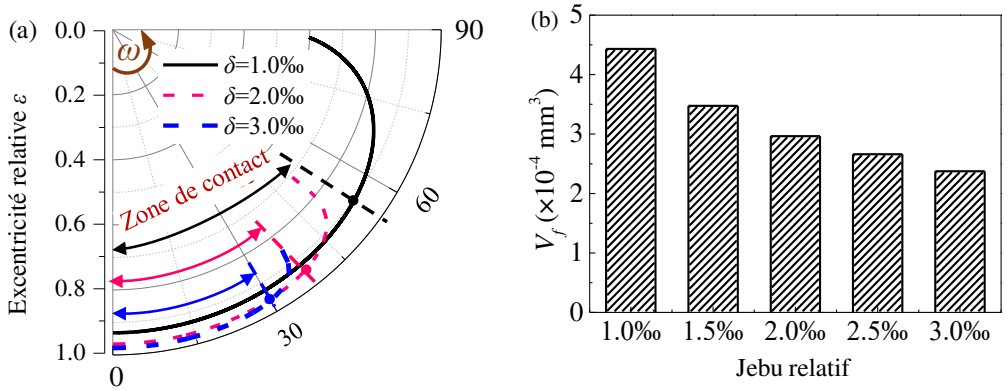


Fig. F-4 Influence de l'usure relative sur (a) la zone de contact et (b) le volume d'usure V_f au démarrage

et de la douille sont presque identiques pour un petit jeu relatif que le contact des deux surfaces se réalise plus facilement. Le volume d'usure de la zone de contact pendant l'arrêt peut être négligé par rapport à celui calculé durant la phase de démarrage.

La Fig. F-5 montre l'influence du temps d'accélération sur le comportement du contact pendant le démarrage. Le temps d'accélération est le temps pendant lequel le tourillon accélère de zéro à 1000 tr/min. Lorsque le temps d'accélération passe de 0,1 s à 0,5 s, le temps de contact augmente de 0,057 s à 0,129 s, mais la zone de contact diminue. Pendant ce temps, l'usure du volume connaît une valeur la plus basse de 2.91×10^{-4} mm^3 au temps d'accélération de 0,3 s. Pour le processus d'arrêt de la Fig. F-6, le temps de décélération est le temps pendant lequel le tourillon décélère de 1000 tr/min à zéro. La zone de contact est évidente en temps de décélération long. Lorsque le temps d'accélération atteint 10 s, l'usure volumique est de l'ordre de 10^{-4} mm^3 ce qui est identique à celle au démarrage, c'est-à-dire que lorsque l'accélération est faible, l'usure à l'arrêt ne peut être négligée. Afin de réduire la zone d'usure et le volume, il existe une accélération optimale pour le démarrage, mais pour l'arrêt la grande décélération est meilleure.

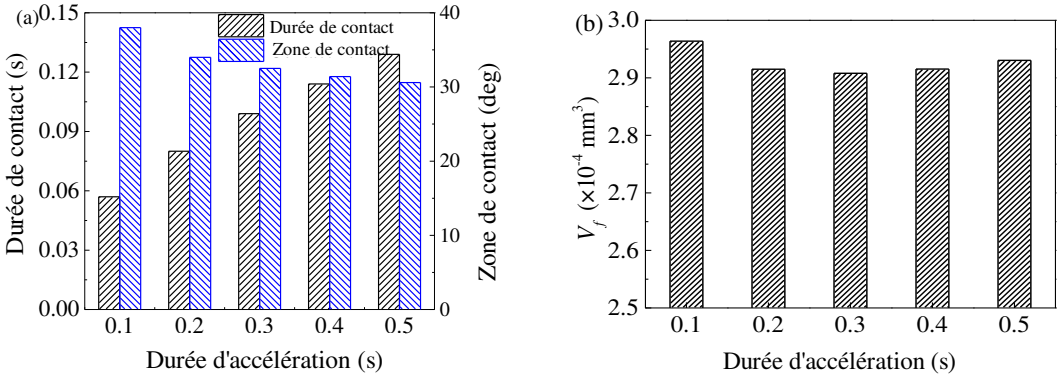


Fig. F-5 Influence du temps d'accélération sur (a) le temps de contact et la zone de contact et (b) le volume d'usure V_f au démarrage

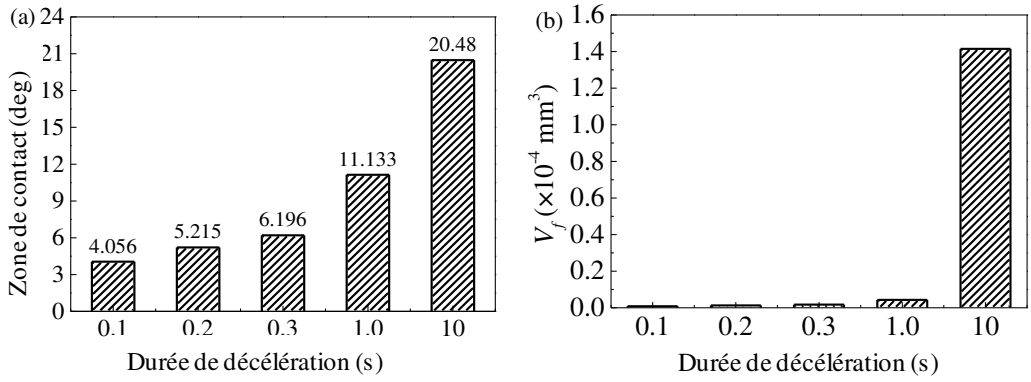


Fig. F-6 Influence du temps décélération sur (a) la zone de contact et (b) le volume d'usure V_f lors de l'arrêt

Chapitre 3 Modèle thermoélastohydrodynamique (TEHD) des paliers lisses partiellement revêtus tenant compte du glissement à la paroi

Le modèle géométrique des paliers partiellement revêtus tenant compte du glissement à la paroi au niveau de l'interface film-revêtement est illustré à la Fig. F-7. Une couche intermédiaire est utilisée pour améliorer la force de liaison entre le revêtement et le substrat. Dans la Fig. F-7 (c), Θ est le système de coordonnées fixe, θ est le système de coordonnées dynamique, et $\theta=\Theta-\varphi$, où φ est l'angle de calage.

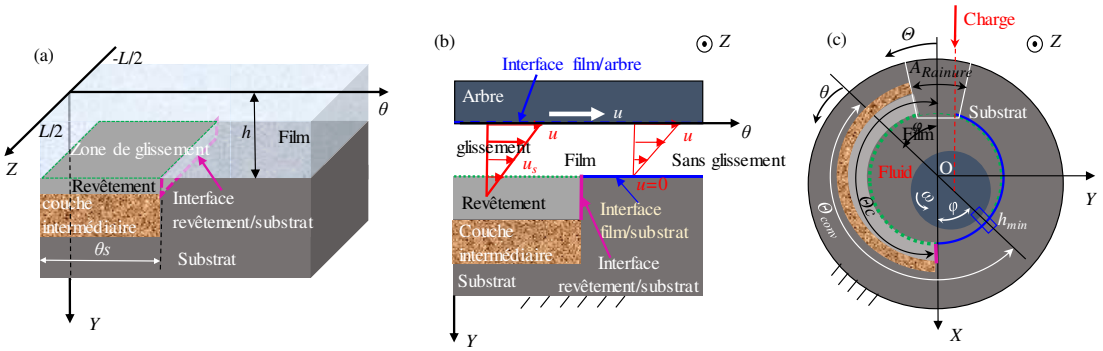


Fig. F-7 (a) Revêtement, couche intermédiaire et substrat, (b) structure au niveau du plan médian et c) système de coordonnées des paliers lisses revêtus compte tenu du glissement partiel à la paroi

L'équation de Reynolds généralisée considérant le glissement est appliquée

$$\frac{\partial}{R_s^2\partial\theta}\left(\Phi_\theta F_2\frac{\partial p}{\partial\theta}\right)+\frac{\partial}{\partial z}\left(\Phi_z F_2\frac{\partial p}{\partial z}\right)=\Phi_c\frac{\partial}{R_s\partial\theta}\left[\frac{F_1}{F_0}\left(u_0+u_s\right)\right]+ \Phi_c\frac{\partial}{\partial z}\left[\frac{F_1}{F_0}w_s\right]+\sigma\frac{\partial\left[\Phi_s\left(u_0+u_s\right)\right]}{R_s\partial\theta}+\sigma\frac{\partial\left[\Phi_s\left(w_s\right)\right]}{\partial z}+\xi^+p^- \tag{E-5}$$

où u_s et w_s sont les composantes de la vitesse de glissement. ξ^+p^- est un élément de pénalité qui est un moyen de contrôler la cavitation. ξ^+ est un nombre positif infini et $p^-=\min(p, 0)$ correspond à la partie négative de la pression hydrodynamique (HD).

Un modèle de glissement à deux composants est utilisé pour calculer la vitesse de glissement à la paroi. La contrainte de cisaillement est exprimée par

$$\tau_c=\tau_{co}+\frac{\mu}{b}u_s \tag{E-6}$$

L'équation d'énergie et l'équation de la chaleur sont résolues afin calculer la température dans le film et dans le coussinet.

La Fig. F-8 montre l'organigramme du processus de résolution comme suit :

1. L'équation de Reynolds généralisée est résolue pour obtenir la distribution de

pression dans le film lubrifiant. Ensuite, la vitesse du fluide à travers l'épaisseur du film et la vitesse de glissement à l'interface film-revêtement sont calculées.

2. Les températures du film, du coussinet (revêtement, couche intercalaire et substrat) et de l'arbre sont obtenues en résolvant les équations de l'énergie et de la chaleur en prenant en compte les conditions aux limites (BC) sur la température. La viscosité du film et les déformations mécaniques et thermiques sont ensuite calculées. Les étapes 1 et 2 sont répétées jusqu'à ce que l'écart de température soit inférieur à l'erreur imposée err_T, qui est fixée à 2×10^{-5}.

3. Les étapes 1 à 3 sont répétées jusqu'à ce que la force HD soit équilibrée avec la charge appliquée en ajustant l'excentricité relative ε et l'angle de calage φ.

4. Les déformations mécaniques et thermiques doivent être convergentes en répétant les étapes des étapes 1 à 4. Les erreurs de convergence des déformations mécaniques et thermiques sont respectivement fixées à 5×10^{-4}.

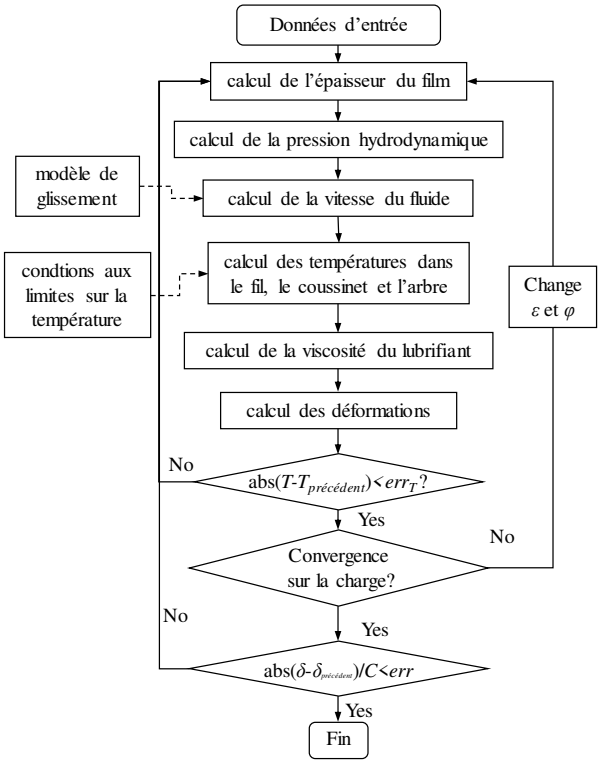


Fig. F-8 Organigramme de la procédure de calcul

Les paramètres de simulation sont répertoriés dans le Tableau F-2, Tableau F-3 et Tableau F-4.

Tableau F-2 Paramètres dimensionnels du palier

Paramètres	Symboles	Valeurs	Paramètres	Symboles	Valeurs
Rayon de l'arbre, mm	R_s	50	Jeu radial à 20℃, μm	C	123
Rayon externe du coussinet, mm	R_o	100	Epaisseur du coussinet, mm	h_{bush}	50
Longueur du coussinet, mm	L	80	Angle de la rainure, deg	A_{Groove}	18

Tableau F-3 Propriétés du revêtement, de la couche intercalaire et du substrat

Paramètres	Revêtement			Couche intercalaire	Substrat
	PTFE	Graphite	DLC	Bronze	Acier
Densité, kg/m^3	2200	2250	2000	8940	7850
Conductivité thermique, W/m℃	0.3	105	600	65	36
Chaleur spécifique, J/kg·K	1200	710	970	490	486
Coefficient de Poisson	0,46	0,15	0,17	0,33	0,29
Module d'Young, GPa	0,11	25	759	120	210
Coefficient de dilatation thermique, ×10^{-6}	124	4,8	1,2	17	11,5
Coeff. d'échange thermique film/coussinet, W/m^2·K	50	700	800	700	600
Coeff. d'échange thermique air/coussinet, W/m^2·K	-	-	-	-	100
Epaisseur, mm	1,0	1,0	1,0	3	46

Tableau F-4 Paramètres de simulation

Paramètres	Symboles	Valeurs
Condutcivité thermique, W/m·K	k_f, k_a, k_b, k_s	0,13, 0,026, 65, 50
Densité, kg/m^3	ρ_f, ρ_a, ρ_b, ρ_s	860, 1,17, 8940, 7700
Chaleur spécifique, J/kg·K	C_f, C_a, C_b, C_s	2000, 1006, 490, 380
Coefficient d'échange thermique, W/m^2·K	H_{ba}, H_{bo}	100, 700
Coefficient de Poisson	v_b	0,3
Module d'Young, GPa	E_b	120
Viscosité dynamique, Pa·s	$\eta_{30℃}$	0,05
Coefficient de thermoviscosité	β_η	0,0468
Coefficient de dilatation thermique, ×10^{-6}	T_a, T_l	30, 30
Température, ℃	α_T	17
Pression d'alimentation, MPa	P_s	0,07

*note : les indices *f*, *a*, *b*, *s* représentent *le film, l'ambiant, le substrat et l'arbre ; I* représente *l'entrée ; ba* représente *le substrat et l'ambiant ; bo* représente *le substrat et l'huile.*

Le comportement de glissement à la paroi est illustré à la Fig. F-9 pour différentes conditions de fonctionnement. La réduction de la température maximale et l'augmentation de l'épaisseur du film sont calculées à l'aide des relations $\triangle T_{\max}=(T_{\text{nonslip}}-T_{\text{slip}})/T_{\text{nonslip}}*100\%$ et $\triangle h_{\min}=-(h_{\min_\text{nonslip}}-h_{\min_\text{slip}})/h_{\min_\text{nonslip}}*100\%$, respectivement. Le grand jeu relatif et la vitesse élevée de l'arbre conduisent à un

$\triangle T_{max}$, important, ce qui signifie que l'effet de glissement à la paroi peut réduire plus clairement le T_{max}. Habituellement, l'effet de glissement affaiblit la force HD, ce qui entraîne une faible h_{min}. Cependant, lorsque la vitesse est supérieure à 4 000 tr/min, le glissement est utile pour augmenter h_{min} en devenant un $\triangle h_{min}$ positif. Ceci peut s'expliquer par rapport à la configuration sans glissement : à 4 000 tr/min, la déformation thermique est faible car la température T_{max} dans la configuration avec glissement reste peu élevée.

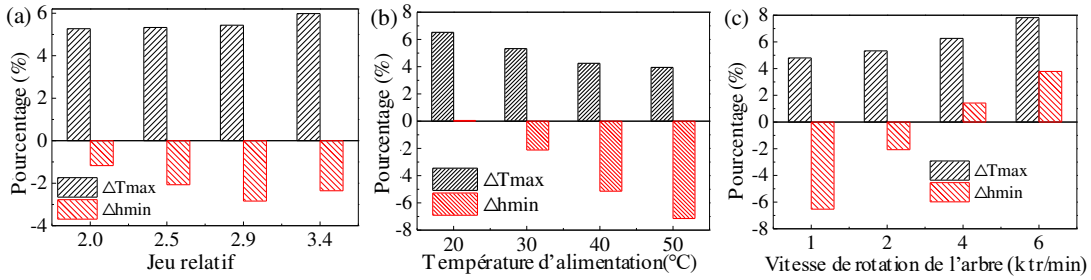


Fig. F-9 Influence (a) du jeu relatif, (b) de la température d'alimentation et (c) de la vitesse du tourillon sur le comportement de glissement thermique à la paroi du palier revêtu de PTFE

Chapitre 4 Optimisation de la zone de revêtement et comportement au glissement thermique du palier lisse revêtu

La Fig. F-10 montre la zone de revêtement (glissement) à la surface du coussinet qui est symétrique par rapport au plan médian du palier. Afin de localiser la zone de glissement, le coefficient $\alpha=(\Theta_c-\varphi)/\Theta_{conv}$ ($-\varphi/\Theta_{conv} \leq \alpha \leq 2$) est défini. Θc est la longueur de la zone de glissement de $\Theta=0$ jusqu'à l'extrémité arrière de la zone; Θ_{conv} est l'angle entre l'angle de calage et la position angulaire de l'épaisseur minimale du film h_{min}, c'est-à-dire la région convergente du film de $\Theta_{conv}=180°$. $\alpha<1$ et $\alpha>1$ indiquent que la zone de glissement se situe respectivement au niveau de la région convergente et de la région divergente du film.

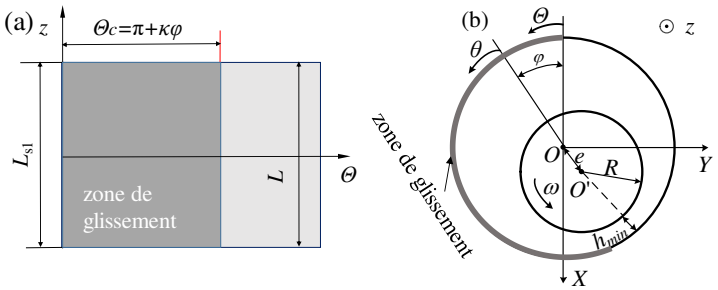


Fig. F-10 Zone de revêtement (de glissement) à la surface du coussinet

Le gain de capacité de charge est calculé par $F_G=(F_{h_slip}-F_{h_nonslip})/F_{h_nonslip}\times 100\%$. La réduction du coefficient de frottement est calculée par $f_D=-(f_{slip}-f_{nonslip})/f_{nonslip}\times$

100%. Les valeurs positives de F_G et f_D signifient un effet positif de la zone de glissement. Sur la base de l'étude de la forme de la zone de glissement dans les cas isothermes, la largeur axiale de la zone de glissement doit être augmentée, c'est-à-dire que la zone de glissement doit être définie sur un rectangle avec la largeur du roulement. Pour des cas d'excentricités élevées (charges élevées), la valeur optimale de α se situe dans l'intervalle 0,9~1,0. Le coefficient κ est introduit pour décrire la longueur de glissement comme $\Theta_c=\pi+\kappa\varphi$ ($\kappa \in [0,1]$) sous une forte charge constante.

Les paramètres optimisés obtenus pour ε=0,94 sont sélectionnés pour explorer davantage les performances des paliers lisses avec des rapports d'excentricité allant de 0,4 à 0,97, comme indiqué sur la Fig. F-11. L'angle de calage pour le cas de non glissement de ε=0,94 est de φ=20,3°. La longueur de glissement est de 5 μm et la contrainte de cisaillement critique est de 1024 Pa. Pour ε<0,94, toute la zone de glissement sélectionnée de κ=0,5, 0,75 et 1,0 peut augmenter la force HD abaisser le coefficient de frottement (Fig. F-10(a) et (b)). Pour ε>0,94, sauf κ=0,5, les autres zones de glissement partiel sélectionnées diminuent la force HD. Cela signifie que la zone sélectionnée qui peut mieux fonctionner pour la charge de ε=0,94 peut également améliorer les performances de palier pour des charges inférieures à ε=0,94.

Les propriétés thermiques du revêtement des paliers lisses sont discutées pour quatre régimes de lubrification : lubrification thermohydrodynamique sans/avec glissement (THD/THDS) et thermoélastohydrodynamique sans/avec glissement (TEHD/TEHDS). La rainure du palier est fixée à 18°, de sorte que la plage de α est -0,45 ≤ α ≤1,95. Les paramètres sont répertoriés dans le Tableau F-2, le Tableau F-3 et le Tableau F-4. La charge appliquée est de 8 kN (2,0 MPa) et la vitesse de rotation de l'arbre est de 2 000 tr/min.

Fig. F-12 montre l'influence du coefficient de revêtement PTFE sur la température et l'épaisseur minimale du film. Lorsque la fin du revêtement se situe dans la région convergente du film, c'est-à-dire la zone 1 de α<0,8, l'influence du revêtement est assez faible, avec des variations de température et de h_{min} inférieures à 0,3℃ et 1,0 μm. Lorsque la fin du revêtement est proche de la position de h_{min}, c'est-à-dire la zone 2 de α=0,8~1,4, Tmax augmente dans tous les cas de lubrification à α≈1,0 (Fig. F-12 (a)). h_{min} subit une forte diminution, d'environ 16% et 21% respectivement dans les cas TEHD et TEHDS, mais cette réduction importante n'apparaît pas dans les cas THD et THDS. On peut en déduire que la forte diminution est causée par des déformations. Nous préférons un T_{max} inférieur et un h_{min} plus épais, de sorte que la plage de α= 0,8 ~ 1,4 est inacceptable ou infaisable. Lorsque l'extrémité arrière du revêtement se situe dans la région divergente du film, c'est-à-dire la zone 3 de α> 1,4,

les variations de T_{max} et h_{min} sont assez faibles, il est donc préférable, au stade de la fabrication, de prescrire des revêtements complets. Sans glissement, T_{max} peut être augmenté d'environ 5% (2,5℃) par rapport à celui de α<0,8. Le glissement peut effectivement diminuer T_{max} de 2 % par rapport à celui de α<0,8.

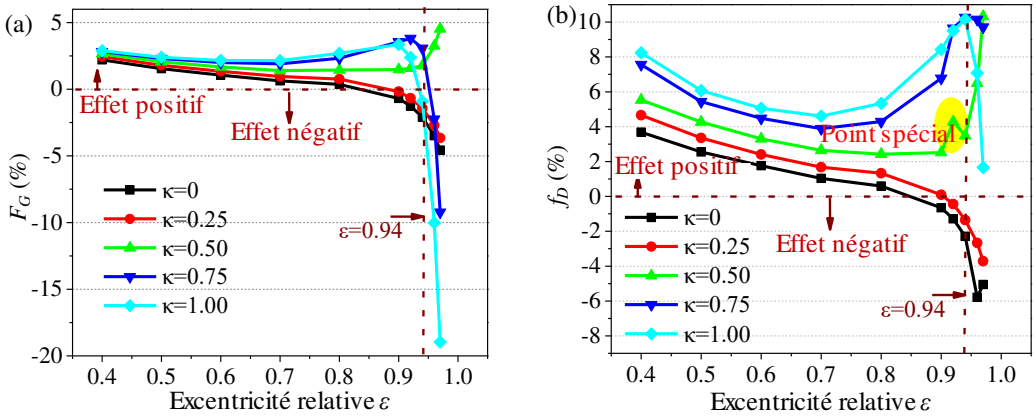


Fig. F-11 Les performances du palier lisse dans la zone de glissement partiel dans différents rapports d'excentricité, (a) le gain de capacité de charge F_G et (b) la diminution du coefficient de frottement f_D

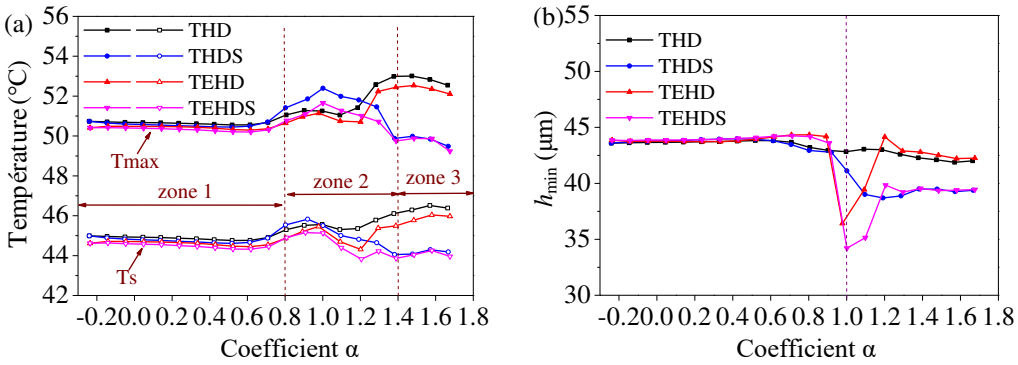


Fig. F-12 Influence du coefficient α du revêtement PTFE sur (a) la température de l'arbre T_s et la température maximale T_{max}, (b) l'épaisseur minimale du film h_{min}

La Fig. F-13 montre la distribution de la température dans la zone de revêtement-intercouche-substrat pour les revêtements PTFE, graphite et DLC. Le cas TEHD est considéré. Les paramètres sont répertoriés dans le Tableau F-3. Pour un revêtement complet, la température T_{max} du revêtement PTFE est la plus élevée et celle du revêtement DLC est la plus faible. Par rapport au revêtement PTFE, les revêtements graphite et DLC ne peuvent pas empêcher le transfert de chaleur vers le substrat en raison de la meilleure conduction thermique de ces matériaux, et il n'y a pas de limites de température évidentes entre le revêtement, la couche intercalaire et le substrat. Les cas du graphite partiel et du revêtement DLC de α= 0,43 et 1,0 ont une petite influence sur la distribution de la température.

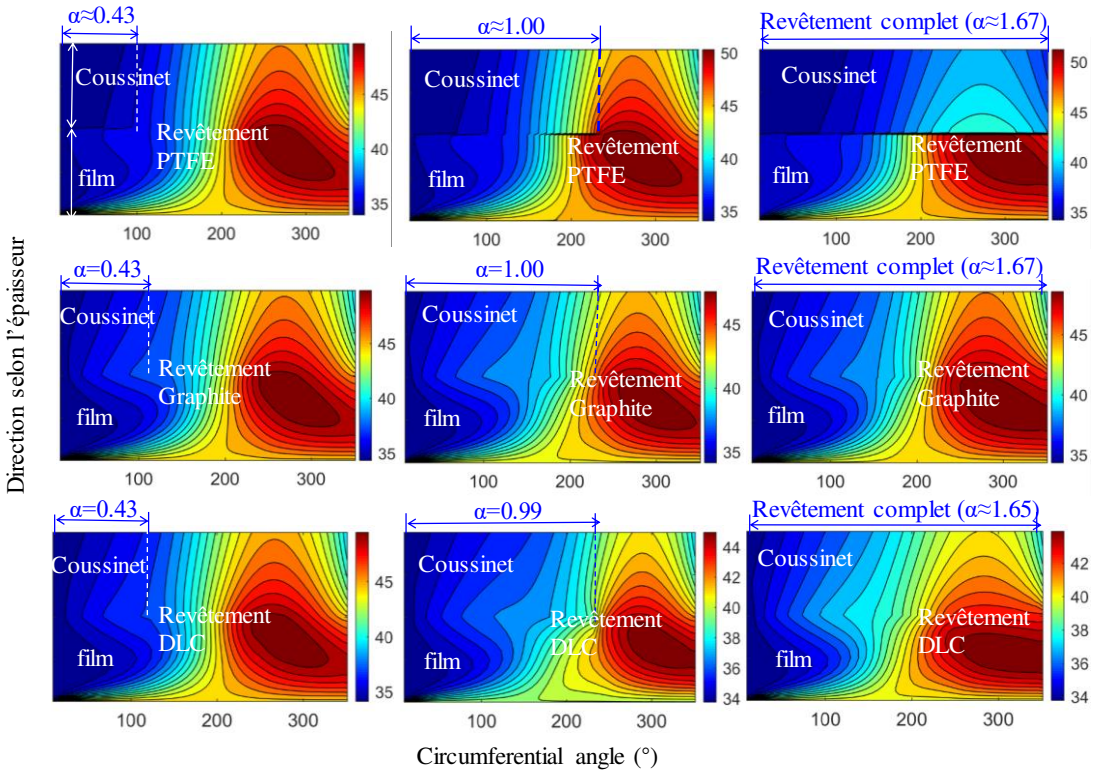


Fig. F-13 Distribution thermique avec différents matériaux de revêtement

Chapitre 5 Essais expérimentaux des propriétés thermiques du palier à patins oscillants revêtus

Le système mécanique du banc d'essai comprend principalement la broche motorisée, l'accouplement, les roulements de guidage de l'arbre d'essais, le dispositif de chargement et la cellule du palier testé comme indiqué dans Fig. F-14. La broche motorisée peut aller jusqu'à 12 000 tr/min. Elle est reliée à l'arbre d'essais par un accouplement flexible. Afin de réduire la déformation de l'arbre tournant sous de fortes charges, deux roulements de guidage sont disposés du même côté du palier testé. Le palier d'essais est placé dans l'anneau de chargement, et l'anneau de chargement est limité par deux glissières (rail de guidage) fixées sur le réservoir d'huile temporaire. La charge dans le sens vertical est appliquée sur l'anneau de chargement par un vérin hydraulique, et elle est transmise au palier testé par l'anneau de chargement.

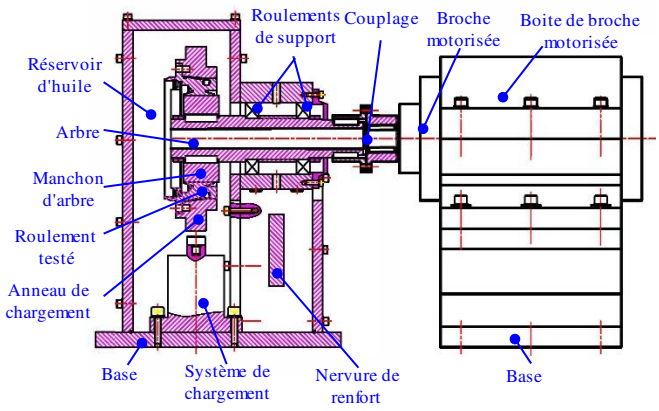


Fig. F-14 Plan de montage du banc d'essai

La géométrie du palier à patins oscillants revêtus à six patins (CTPJB) est illustrée à la Fig. F-15, la photo est illustrée à la Fig. F-16, et les capteurs de température sont installés comme illustré à la Fig. F-17. Les paramètres sont répertoriés dans le Tableau F-5, le Tableau F-6 et le Tableau F-7.

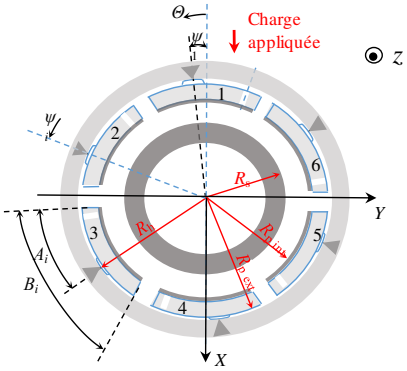


Fig. F-15 Modèle géométrique



Fig. F-16 Patins dans l'anneau de chargement

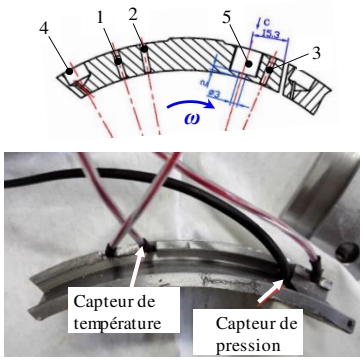


Fig. F-17 Emplacement des capteurs dans le patin

Tableau F-5 Paramètres géométriques du palier à 20°C

Paramètres	Valeurs	Paramètres	Valeurs
Rayon interne des patins, mm	85,015	Coefficient de précharge	0
Rayon externe des patins, mm	98	Epaisseur du patin, mm	12,985
Longueur du palier, mm	60	Amplitude angulaire du patin *i*, deg	58,5
Rayon du pivot, mm	99	Position angulaire relative du pivot *i*, A_i/B_i,	0,672
Rayon externe de l'anneau de chargement, mm	199	Position angulaire pivot i dans le palier, deg	6+60*(*i*-1)

Tableau F-6 Caractéristiques du lubrifiant (ISO T32)

Paramètres	Valeurs	Paramètres	Valeurs
Températures d'alimentation et de bain, ℃	40	Densité à 40℃, kg/m3	860
Pression d'alimentation, MPa	0,3	Conductivité thermique, W/(m·K)	0,13
Viscosité dynamique à 40℃, mPa·s	27,52	Chaleur spécifique, J/(kg·K)	2000
Viscosité dynamique à 100 ℃, mPa·s	4,644		

Tableau F-7 Paramètres de jeu de paliers

Paramètres	Jeu radial initial C0	Jeu radial C1	Jeu radial C2	Jeu radial C3
Diamètre interne des patins, mm	$170.03^{+0.04}_{0}$			
Diamètre de l'arbre, mm	$170.0^{0}_{-0.025}$	$169.88^{0}_{-0.025}$	$169.83^{0}_{-0.025}$	$169.78^{0}_{-0.025}$
Jeu radial, μm	15~47,5	75~107,5	100~132,5	125~157,5
Jeu relatif, ‰	0,18~0,56	0,88~1,26	1,18~1,56	1,47~1,86

La température des paliers revêtus de PTFE, de graphite et d'Ag avec un jeu relatif inférieur à 1,0‰ est mesurée pendant la phase de démarrage. Les tests montrent que pour le revêtement PTFE, le palier ne peut pas avoir une température et une pression constantes pour le cas de charge appliquée de 4kN et de vitesse 6 000 tr/min. Le Graphite peut fonctionner avec les conditions de charge de 4kN et de vitesse 6 000 tr/min, mais lorsque la vitesse monte jusqu'à 7 000 tr/min, le grippage du palier se produit. Le palier revêtu d'argent (Ag) peut normalement fonctionner sous 7,5 kN et 8 000 tr/min. Dans tous les cas, la surface des patins est visiblement usée. Lorsque le jeu relatif est augmenté à 1,18‰~1,56, les paliers revêtus peuvent fonctionner sous 7,5kN et 8 000 tr/min, même s'ils provoquent l'usure à la surface des patins.

Le revêtement Ag est testé. Étant donné que l'élévation de température du patin 4, le patin le plus chargé, est la plus importante, l'élévation de température de ce patin 4 est discutée pendant le démarrage. La Fig. F-18 montre l'effet du jeu relatif sur l'élévation de température au démarrage. La charge appliquée est de 7,5 kN. La vitesse de rotation de l'arbre prend 2,2 minutes pour passer de zéro à 8 000 tr/min. Le faible jeu relatif génère une augmentation rapide de l'élévation de température et donne une température stable élevée, après une vingtaine de minutes. Les températures dans le patin 4 avec des différents jeux relatifs atteignent la température stable presque en même temps. C'est parce que le palier avec un jeu important possède une grande quantité d'huile dans le jeu que l'huile évacue plus de chaleur,

sachant aussi que le frottement est plus faible (grâce à un taux de cisaillement plus faible que celui du palier à faible jeu).

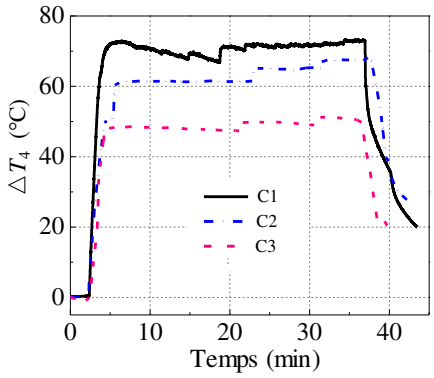


Fig. F-18 influence du jeu relatif sur la montée en température du patin 4 ($\triangle T_4$) en fonction du temps des paliers à patins oscillants revêtus d'argent, Ag CTPJBs

L'influence de l'accélération sur l'élévation de température est illustrée à la Fig. F-19. L'accélération 1 est la plus grande, suivie par les accélérations 2 et 3. La période d'élévation rapide de la température est cohérente avec le temps d'accélération. Sur la Fig. F-19 (a), la grande accélération provoque une élévation rapide de la température pendant le démarrage, donc en cas d'accélération importante, elle provoque facilement des grippages de paliers car la chaleur ne peut pas être transférée à la bague support des patins suffisamment rapidement. La température augmente de la même façon que l'accélération de la vitesse du tourillon, c'est-à-dire que la température augmente avec la vitesse du tourillon en modes linéaire et cosinus (Fig. F-19 (b)). Une fois le processus d'accélération terminé, la température augmente lentement et l'élévation de température est presque la même à l'état stable (en régime stationnaire).

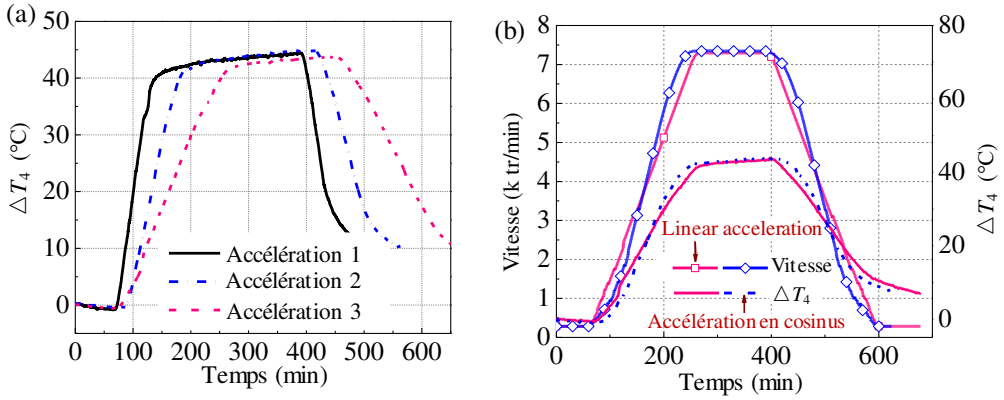


Fig. F-19 Influence de (a) l'accélération et (b) du mode d'accélération la montée en température du patin 4 ($\triangle T_4$) en fonction du temps des paliers à patins oscillants revêtus d'argent, Ag CTPJBs

La Fig. F-20 montre l'influence de la température initiale sur l'échauffement au démarrage. Le journal démarre linéairement de zéro à 8,8 000 tr/min en 1,8 minutes. Le jeu relatif est la valeur C3 Tableau E-7, et la charge appliquée est de 7,5 kN. L'huile alimente le palier statique au cours des 2,5 premières minutes. Pour la température initiale élevée, la température d'alimentation est de 35℃ et la température de chaque patin est d'environ 42℃. Pour la basse température initiale, la température d'alimentation est de 25℃ et la température de chaque patin est d'environ 26℃. La différence de température entre les deux états initiaux est de 16℃. Les paliers atteignent une température constante presque en même temps. L'élévation de température du patin 4 à une température initiale élevée est d'environ 47,1 ℃, ce qui est environ 12,3℃ inférieur à celui d'une température initiale basse. On peut en déduire que la température monte plus vite à basse température initiale. Par conséquent, la température initiale élevée est utile pour un démarrage plus en douceur, conduisant ainsi une élévation de température plus progressive et évitant tout risque de serrage des paliers.

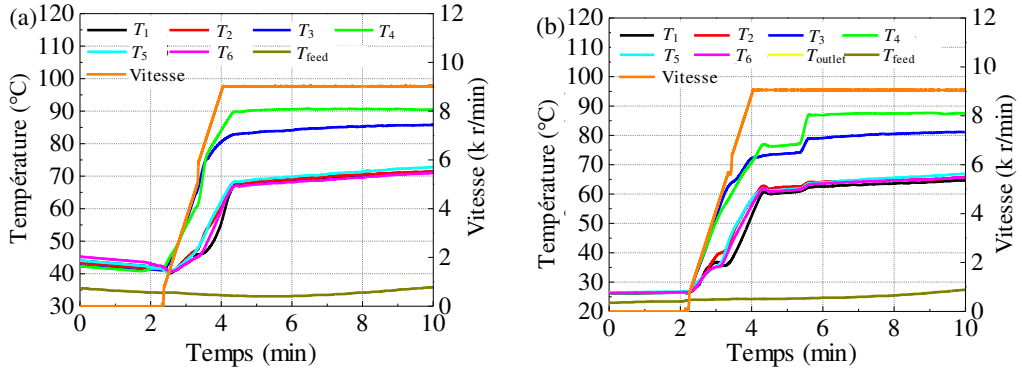


Fig. F-20 Influence de la température initiale sur l'élévation de température des Ag CTPJBs, (a) température initiale élevée et (b) température initiale basse

Conclusion

En ciblant les paliers lisses revêtus qui démarrent et s'arrêtent sous forte charge, la zone de contact transitoire et les propriétés d'usure sont présentées. Ensuite, le comportement de glissement thermique de la paroi à l'interface film-revêtement est analysé et l'effet de la zone de glissement est discuté. Les expériences sont menées pour explorer le comportement thermique régimes stationnaire et transitoire des paliers à patins oscillants revêtus (CTPJBs).

Les principales conclusions de ce travail sont les suivantes :

(1) La zone et le volume d'usure dans la phase de démarrage sont beaucoup plus importants que ceux observés lors de la phase d'arrêt. La surface lisse génère une

petite zone d'usure et un petit volume d'usure lors du démarrage. De même, un jeu relatif important diminue la zone et le volume d'usure lors du démarrage. Lors de cette phase, une forte accélération augmente la zone d'usure, mais il existe une accélération optimale qui permet d'atteindre le volume d'usure le plus faible. Dans la phase d'arrêt, lorsque l'accélération est trop faible, la zone d'usure et le volume peuvent être du même ordre qu'au démarrage, et l'usure ne peut plus être négligée.

(2) Pour un grand jeu relatif et une vitesse du tourillon élevée, l'effet de glissement est plus efficace pour réduire la température maximale (T_{max}), mais une température d'alimentation élevée réduit cet effet. À une vitesse de tourillon élevée, le glissement de paroi est plus avantageux pour l'épaisseur minimale du film (h_{min}).

(3) Pour le cas isotherme, il vaut mieux augmenter la largeur axiale de la zone de glissement. En cas de forte charge, la zone de glissement doit être située dans la région de convergence du film et l'extrémité arrière de la zone doit être proche de la position de h_{min}.

(4) Lorsque la zone de revêtement de PTFE est située dans la région de convergence du film et que l'extrémité arrière est éloignée de la position de h_{min}, les revêtements ont un très léger effet sur la température maximale T_{max} et l'épaisseur minimale du film h_{min}. Lorsque la fin du revêtement est située dans la région de divergence du film et loin de la position de h_{min}, l'effet de glissement peut réduire le T_{max} accompagnant la diminution de h_{min}. Il convient donc d'éviter d'imposer la fin du revêtement à proximité de la position de h_{min}. Les revêtements graphite et DLC possèdent une meilleure conductivité thermique conduisent à un faible T_{max} grâce au transfert de chaleur de l'huile vers le coussinet.

(5) Les revêtements PTFE, graphite et argent (Ag) sont évidemment usés lors du démarrage sous fortes charges. La température du palier revêtu de PTFE est la plus élevée et le revêtement usé peut facilement provoquer la défaillance du palier. Le revêtement en argent est plus susceptible de permettre au palier de fonctionner dans des conditions extrêmes.

(6) Lors du démarrage, pour un faible jeu relatif et une faible température initiale, la température augmente rapidement. La montée en température est en cohérence avec l'accélération de la vitesse. La grande accélération entraîne une augmentation rapide de la température. Un jeu relatif important, une faible accélération et une température initiale relativement élevée favorisent un démarrage sûr du palier.

Publications

Published papers

[1] **Shuhui Cui**, Le Gu, Liqin Wang, Bo Xu, Chuanwei Zhang. Numerical analysis on the dynamic contact behavior of hydrodynamic journal bearings during startup[J]. Tribology International, 2018, 121: 260-268.

[2] **Shuhui Cui**, Le Gu, Michel Fillon, Liqin Wang, Chuanwei Zhang. The effects of surface roughness on the transient characteristics of hydrodynamic cylindrical bearings during startup[J]. Tribology International, 2018, 128: 421-428.

[3] **Shuhui Cui**, Chuanwei Zhang, Michel Fillon, Le Gu. Optimization performance of plain journal bearings with partial wall slip[J]. Tribology International, 2020, 145: 106137.

[4] **Shuhui Cui**, Le Gu, Michel Fillon, Chuanwei Zhang. Thermohydrodynamic behavior of partially coated plain journal bearings with/without considering wall slip[J]. P I Mech Eng J-J Eng/Proceedings of the Institution of Mechanical Engineers Part J-Journal of Engineering Tribology. (under review)

Conference

[1] **Shuhui Cui**, Le Gu, Michel Fillon. Optimization performance of plain journal bearings with partial wall slip [C]. Leeds-Lyon international syposium，France Lyon: 2019.

[2] **Shuhui Cui**, Le Gu, Michel Fillon, Chuanwei Zhang. Effect of partial wall slip on the THD behavior of high-loaded plain journal bearings [C]. EDF-Pprime work shop, Pairs: 2019.

[3] **Shuhui Cui**, Le Gu, Chuanwei Zhang, Liqin Wang. Effect of surface textures on startup behaviors of plain journal bearings [C]. Word Tribology Conference, Beijing: 2017.